Appropriate modelling of climate change impacts on river flooding

Samenstelling promotiecommissie:

prof. dr. ir. H.J. Grootenboer	Universiteit Twente, voorzitter/ secretaris
prof. dr. ir. C.B. Vreugdenhil	Universiteit Twente, promotor
prof. dr. ir. W. van Leussen	Universiteit Twente
prof. dr. C.J.E. Schuurmans	Universiteit Utrecht
prof. dr. ir. A. Stein	Wageningen Universiteit
prof. dr. P.A. Troch	Wageningen Universiteit
prof. dr. ir. H.G. Wind	Universiteit Twente

ISBN 90-365-1711-7

APPROPRIATE MODELLING OF CLIMATE CHANGE IMPACTS ON RIVER FLOODING

PROEFSCHRIFT

ter verkrijging van

de graad van doctor aan de Universiteit Twente,

op gezag van de rector magnificus,

prof. dr. F.A. van Vught,

volgens besluit van het College voor Promoties

in het openbaar te verdedigen

op vrijdag 12 april 2002 te 13.15 uur.

door

Martijn Jan Booij

geboren op 27 oktober 1972

te Geldrop

Dit proefschrift is goedgekeurd door de promotor:

prof. dr. ir. C.B. Vreugdenhil

In dierbare herinnering aan mijn vader

Voorwoord

Het is 27 oktober 1972, de dag waarop ik ben geboren. Het is laagwater in de Maas, iets wat me op dat moment waarschijnlijk niets interesseert. Dat is meer dan twee decennia later, op 31 januari 1995, wel anders. Ik studeer inmiddels 'iets met water' en voor de tweede keer in drie jaar vinden er grote overstromingen van de Maas plaats. Tegelijkertijd begint algemeen het besef door te dringen dat klimaatveranderingen wel eens werkelijkheid zouden kunnen worden. Een eerste aanleiding van dit onderzoek is ontstaan. Niet veel later, het is februari 2002, ben ik dit voorwoord aan het schrijven. Een nieuwe hoogwatergolf is Itteren en Borgharen gepasseerd, gelukkig zonder al te veel schade aan te richten. Maar hoe zal het de volgende keer of over 50 jaar aflopen? Het benadrukt eens te meer de relevantie van water gerelateerd onderzoek. De afgelopen vier jaar heb ik getracht hieraan mijn steentje bij te dragen met als resultaat dit proefschrift. De steun en hulp van vele mensen is daarbij heel belangrijk geweest. Deze mensen wil ik hier bedanken.

Als eerste wil ik mijn promotor en dagelijkse begeleider Kees Vreugdenhil van harte bedanken. Hij heeft mij de mogelijkheid geboden in alle vrijheid aan mijn onderzoek te werken en zijn ideeën omtrent 'model appropriateness', een belangrijke tweede aanleiding van dit onderzoek, vorm te geven. Keek ik in eerste instantie wat raar aan tegen vragen als 'hoe goed moet het eigenlijk?' en 'is dit echt nodig?', de laatste tijd stel ik deze vragen op mijn beurt steeds vaker aan anderen. Kees, nogmaals bedankt voor alle aangename discussies, kritische vragen en prettige samenwerking.

Gedurende mijn onderzoek heb ik met verschillende mensen samengewerkt. Een aantal van hen wil ik hier speciaal bedanken. Met Paul Torfs van Wageningen Universiteit heb ik een aantal boeiende discussies gehad over hoofdstuk 3, dankzij het commentaar en de adviezen van Cor Schuurmans van de Universiteit Utrecht is hoofdstuk 4 aanzienlijk verbeterd en het afstudeerwerk van Koen van der Wal heeft een belangrijke bijdrage geleverd aan hoofdstuk 6. De samenwerking met Marcel de Wit, Mauk Burgdorffer en Hendrik Buiteveld van het RIZA, voor en tijdens Koen's afstudeerproject, heb ik als zeer prettig ervaren.

A lot of people are acknowledged for their help with the provision of data, models and other information. Luc Debontridder of the Belgian Meteorological Institute and Christophe Dehouck from Météo France provided the observed climate data for Belgium and France respectively. David Viner of the Climate Impacts LINK Project and George Boer of the Canadian Center for Climate Modelling and Analysis made the HadCM3/ HadRM2 and CGCM1 climate model data available. Ole Bøssing Christensen of the Danish Climate Center and Janice Bathols of CSIRO Atmospheric Research prepared and helped a lot with the HIRHAM4 and CSIRO9 climate model data respectively. Bob Jones of the European Soil Bureau and Malene Bruun of the

European Environmental Agency supplied me with the soil and land use data. Eric Sprokkereef of RIZA gave me essential Meuse basin data and Joop Gerretsen of Rijkswaterstaat Limburg made discharge data available. Finally, Sten Bergström of the Swedish Hydrological and Meteorological Institute kindly provided the HBV model.

De woon-werk situatie heeft geresulteerd in aardig wat kilometers met de betrouwbare vierwieler N. Sunny. Alsof de auto wilde aangeven dat vier jaar onderzoek wel genoeg was geweest, begaf die het net voor het gereedkomen van dit boekwerk. Menigmaal vroegen collega's verwonderd of ik nog steeds op en neer tufte tussen de Rijn en de Dinkel. Jazeker, en dat tuffen was de moeite waard. Ik heb een hele leuke tijd gehad met mijn collega's en hoop dat nog even voort te zetten. Een aantal van hen wil ik speciaal noemen. Ik wil Anke bedanken voor de talloze hand- en spandiensten en lekkere koffie die altijd klaar stond. René, bedankt voor je hulp bij het bewerken en omzetten van allerhande databestanden met soms wel erg rare 'formats'. Tenslotte wil ik mijn (voormalige) kamergenoten bedanken voor hun gezelschap. Jean-Luc, Chris en Caroline gedurende de eerste jaren en Michiel sinds een paar maanden. Een groot deel van de tijd deelde ik mijn kamer met één van mijn paranimfen. Frans, bedankt voor je prettige gezelschap, je gevoel voor humor en de goede discussies.

Gelukkig was er de afgelopen jaren voldoende tijd voor andere dingen dan promotieonderzoek. Weekendjes weg, feesten en partijen dichtbij en ver weg, goede gesprekken in de Vlaam of een tripje naar Heeze of Delden. Beste (schoon)familie en vrienden, bedankt voor alle gezelligheid en plezier deze jaren en natuurlijk de interesse in mijn onderzoek. Ik hoop dat het door dit proefschrift duidelijker wordt, waar ik al die jaren mee bezig ben geweest.

Dit promotieonderzoek wordt op 12 april 2002 afgesloten met de verdediging van het proefschrift. Wim van Leussen, Cor Schuurmans, Alfred Stein, Peter Troch en Herman Wind, bedankt voor het lezen van mijn proefschrift. Ik voel me vereerd dat jullie mijn opponenten zijn tijdens de verdediging.

Elsbeth en Frans, bedankt dat jullie mijn paranimfen willen zijn en mij willen helpen en steunen voorafgaand en tijdens de verdediging.

Mijn laatste dank gaat uit naar twee personen. Mamma, bedankt voor alle steun en vertrouwen, niet alleen tijdens dit promotietraject, maar ook gedurende heel mijn leven daarvoor. Lieve Simone, ondanks dat je zelf zegt dat je niet zo veel hebt bijgedragen aan dit boekwerk, denk ik toch dat je heel belangrijk bent geweest. Als steun en toeverlaat, reisgenoot en beste maatje. Dank je wel hiervoor.

Martijn Booij

Wageningen, februari 2002

Contents

Chapter 1

Introduction

1.1 General introduction

1.1.1 Climate change and hydrology

Global climate change induced by increases in greenhouse gas concentrations is likely to increase temperatures, change precipitation patterns and probably raise the frequency of extreme events (IPCC, 1996; 2001). This phenomenon is recognised by the scientific community and is beginning to penetrate into society and governmental bodies, who are presently negotiating about greenhouse gas emission reduction (e.g. in The Hague in 2001). Climate change may have serious impacts on society, for example on coastal areas through sea level rise (Warrick *et al*., 1993), on agricultural areas because of shifts in growing seasons and changes in water availability (Mearns *et al*., 1997) and in river deltas because of both sea level rise and an increased occurrence of flooding events (Jacobs *et al*., 2000).

The impact on the hydrological cycle may be considerable, influencing phenomena such as river flooding, drought and low flows. Subsequently, these changes can have an effect on all kinds of functions in a river basin. Low flows may have serious impacts on navigation, ecosystem behaviour and water quality, droughts will influence agriculture and drinking water availability and flooding events may cause enormous economical, social and environmental damage and even loss of human lives. For example the 1997 Oder flood causes the loss of 54 lives and an economical damage of 2-4 billion dollar (Kundzewicz *et al*., 1997) and even worse the 1998 Yangtze flood killed 4,000-10,000 people and resulted in gigantic economical damage (Zong and Chen, 2000). In the Netherlands, the 1993 and 1995 floods in Rhine and Meuse caused hundreds of millions Dutch guilders of economical damage and forced the evacuation of 200,000 people (Wind *et al*., 1999). Projected changes in climate may only increase the occurrence of these severe floods. This necessitates the application of robust and accurate flood estimation procedures to provide a strong basis for investments in flood protection measures with climate change.

River flood protection measures in Dutch society include dikes, polders and deepening of flood plains. They are designed to prevent flooding associated with a so-called design discharge. The design discharge is the discharge with a probability of occurrence once in a very long period. The design criterion for dikes alongside the non-tidal part of the Rhine branches and Meuse in the Netherlands is 1/1250 per year. This criterion was set in 1977 after an extensive economical analysis on possible damage due to floods on the one hand and construction costs on the other hand (Commissie Rivierdijken, 1977). The criterion was not adjusted after a similar analysis in 1993 which showed that the

situation in the Netherlands had not changed since 1977 (Commissie Boertien I, 1993). The design criterion is subject for discussion and a technical committee is currently developing a new safety approach with three criteria for deliberation: an individual risk criterion, a societal risk criterion and an economical cost-benefit analysis (TAW, 2000). The current design criterion of 1/1250 per year will be assumed throughout this thesis.

The design discharge associated with the design criterion can be determined in a purely statistical way or in a more physically based way. Statistical flood frequency analysis involves fitting of an extreme value probability distribution to a series of observed peak discharges. The resulting probability distribution relates exceedance probabilities (return periods) and peak discharges and thus the design discharge can be determined (e.g. Vogel *et al*., 1997; Gerretsen, 2001). Physically-based flood frequency analysis incorporates meteorological and hydrological information. This means that a meteorological model generates weather and its probability of occurrence, and a river basin model uses this as input to simulate peak discharges and their probability of occurrence. This approach can be carried out with analytical methods (e.g. Goel *et al*., 2000) or with Monte Carlo simulation (e.g. Sivapalan *et al*., 1990). The first method uses simple, analytically solvable equations, for example intensity-duration-frequency (IDF) curves (Blöschl and Sivapalan, 1997; Koutsoyiannis *et al*., 1998) in the meteorological part and derived flood frequency distributions in the hydrological part (Kurothe *et al*., 1997; Goel *et al*., 2000). The second method involves the generation of synthetic meteorological time series (Moon *et al*., 1994; Wilks, 1998) as input to a rainfall-runoff model (Abrahart *et al*., 1996; Lamb, 1999) to derive discharge series. An extreme value distribution function can then be fitted to the peak discharges as in the statistical approach.

Flood estimation incorporating climate change can not be done with the purely statistical approach. This is because extreme value distributions may change in future and thus distributions fitted to observed peak discharges can not be used anymore. Therefore, one of the physically-based approaches should be used. Diermanse (2001) has identified two drawbacks when applying analytical methods, namely that the spatial heterogeneity of inputs and processes is not incorporated, and secondly that the interaction of different flood generating mechanisms is not contained in these methods. One of the reasons is that equations can not be too complex, because they should be solved analytically. The Monte Carlo approach does not have this requirement and can be used here. Moreover, with the latter approach an uncertainty assessment can be done to evaluate the validity of the estimated floods with climate change. The impact of climate change on river flooding is further discussed in section 1.3.

1.1.2 Model complexity

To use the physically-based flood frequency analysis, a selection of a meteorological model (i.e. a rainfall model) and river basin model should be made. A broad palette of models is available ranging from simple, lumped black-box models to complex, distributed models including lots of physics and mathematics. Meteorological output with climate change include direct output from General Circulation Models (GCMs) (e.g. Boer *et al*., 2000a; 2000b; Gordon *et al*., 2000), dynamically downscaled output (e.g. Jones *et al.*, 1995; Christensen *et al.*, 1996) and empirically downscaled output (e.g. Bardossy, 1997; Wilby and Wigley, 2000). River basin models encompass empirical models (e.g. unit hydrograph method; Sherman, 1932), conceptual models

(e.g. Stanford watershed model; Crawford and Linsley, 1966) and physically-based models (e.g. Système Hydrologique Européen; Abbot *et al*., 1986). These divisions are somewhat arbitrary and hybrid forms exist in which for example dynamical and empirical downscaling methods are combined. The complexity of models does not only depend on the model class to which they belong, but also on the processes incorporated, the process formulations used and the different space and time scales employed. More complex models have larger data requirements and computational costs, and, although it can not be guaranteed, uncertainties in model outcomes and associated costs will generally be less. It would seem that an optimum model complexity associated with minimum total costs or total uncertainty exists. This raises the question what such an appropriate model should look like given the specific modelling objective and research area. More specifically, which physical processes and data should be incorporated and which mathematical process formulations should be used and at which spatial and temporal scale, to obtain an appropriate model level? This issue of model appropriateness is further considered in section 1.2.

1.2 Model appropriateness

Different approaches with respect to model appropriateness have been suggested. They can be classified according to the specific part of the model which is evaluated, such as output, processes, formulations, scales or models as a whole.

Evaluation with respect to the output implies using one of the common criteria for model evaluation, e.g. the coefficient of efficiency (Nash and Sutcliffe, 1970), coefficient of determination (square of the Pearson's product-moment correlation coefficient) or index of agreement (Wilmott, 1981) and comparing it with a predefined threshold. Legates and McCabe (1999) compared these goodness-of-fit measures and concluded that correlation based measures should not be used, because high correlations can be achieved by poor model simulations. Instead of the coefficient of efficiency, the index of agreement and additionally, the mean squared error or mean absolute error should be used. Weglarczyk (1998) investigated many goodness-of-fit criteria and pointed out that care should be taken in applying these measures because of their (frequent) interdependencies. Examples in climatological and hydrological literature are numerous and include single model validation (Boer *et al*., 2000a; Chiew and McMahon, 1994) and multiple model validation or model intercomparison (Kittel *et al*., 1998; Yang *et al*., 2000). This kind of evaluation is used as a kind of uncertainty analysis as well. It only assesses model appropriateness for a specific situation (time period, region, climate) and thus no extrapolations to other situations can be made. Furthermore, only the output is concerned and consequently the model appropriateness in simulating internal processes can not be evaluated.

Smith (1996) describes a qualitative procedure to incorporate additional processes or omit redundant ones dependent on e.g. the scale at which data are available and results are needed. Jakeman and Hornberger (1993) used time series techniques to determine how many parameters are appropriate to describe the rainfall-runoff relationship in the case that only rainfall, temperature and streamflow data are available. They found that after modulating the measured rainfall using a nonlinear loss function, the rainfall-runoff response of a variety of catchments is well represented using a two-component linear model with four parameters. This is in agreement with other investigations on this

subject (e.g. Loague and Freeze, 1985; Beven, 1989). This suggests that runoff behaviour can be described by two processes; surface and sub-surface runoff. The latter process is often sub-divided into groundwater flow and subsurface storm flow, supported by the different inherent mechanisms and spatial and temporal scales (Blöschl and Sivapalan, 1995). Although this kind of analyses gives some indication on the processes to be incorporated in a model, it is rather qualitative and conclusions are strongly related to the problem, region and space and time scales considered. The determination of dominant processes will be further discussed in chapter 4 and 5.

Process formulation appropriateness is again related to the problem, region and space and time scales considered. Numerous studies have been conducted to identify the appropriate formulation for a specific process. For example, comparative studies with respect to flood routing methods (Todini, 1991; Moussa and Bocquillon, 1996a) and evapotranspiration estimations (Kite and Droogers, 2000) have been performed. This will be considered in more detail in chapter 5.

The issue of appropriate spatial and temporal scales has received wide attention. Bear (1972) introduced the concept of the Representative Elementary Volume (REV) in fluid dynamics as the order of magnitude where the porosity varies only smoothly with changing volume. In analogy, Wood *et al*. (1988) introduced the term Representative Elementary Area (REA) in catchment hydrology as an appropriate scale at which a simple description of the rainfall-runoff process could be obtained. They give as one of the definitions of the REA 'the smallest discernable point which is representative of the continuum' and arrived at an area of approximately 1 km^2 analysing a catchment of 17 km^2 using TOPMODEL (Beven and Kirkby, 1979). These studies determined appropriate model scales using simulations with a specific model. A second approach is to determine the appropriate model scale without simulation with a specific model. An example is the use of hydrological response units (HRU). An HRU is an area which is considered to be homogeneous for modelling purposes. Areas with similar land use and physical characteristics are grouped into HRUs. They are assumed to exhibit a similar relationship between model inputs and outputs and can consequently be modelled with the same set of parameters (e.g. Kite and Kouwen, 1992). A third approach is to assess the appropriate scale of a separate variable without simulation. One way is the use of fractals and scaling, examples are studies considering the fractal nature of rainfall (Lovejoy and Schertzer, 1985), catchment topography (Nikora, 1994) and channel networks (Moussa and Bocquillon, 1996b). Another way is the application of similarity and dimensional analysis dealing with scales (e.g. Sivapalan et al., 1990). A third way is the use of relations between scales and statistical quantities. Western and Blöschl (1999) used such relations to determine thresholds for scales to be employed when analysing statistics accepting a specific bias. This latter approach will be extensively described in section 2.3.

The above mentioned approaches consider some specific part(s) of the appropriateness problem. There is a need for an integrated approach to determine an appropriate model for a specific modelling objective and research area. Moreover, one would preferably determine the dominant processes, appropriate formulations and scales before model construction and application. Chapter 2 will pay attention to this issue.

1.3 Climate change and river flooding in the Meuse basin

1.3.1 Global and regional climate change

As a result of human activities, atmospheric concentrations of some of the natural greenhouse gases are increasing, and entirely new man-made greenhouse gases have been introduced into the atmosphere as well. In this respect, most important natural greenhouse gases are carbon dioxide (CO_2), methane (CH_4) and nitrous oxide (N_2O). New man-made greenhouse gases are chlorofluorcarbons (CFCs) or halocarbons. The pre-industrial atmospheric concentration (1750-1800), current atmospheric concentration (1998) and current rate of annual atmospheric accumulation are for CO_2 278 parts per million by volume (ppmv), 365 ppmv and 1.5 ppmv/yr (0.4 %) (IPCC, 2001). This increase in the atmospheric greenhouse effect will change the radiative balance of the earth and is likely to increase temperatures, change precipitation patterns and probably raise frequencies of extreme events (IPCC, 1996; 2001).

Fully coupled Atmosphere-Ocean General Circulation Models (AOGCMs) incorporating land- and sea-ice dynamics and land-surface processes are used to simulate current climate and predict future climate. For these predictions, scenarios for future greenhouse gas and aerosol concentrations are used (e.g. Carter *et al*., 1999). Atmospheric GCMs currently have a typical horizontal resolution of around 300 km and have 10-20 vertical levels (Hartmann, 1994). At these resolutions, treatment of local climatic forcings which are important at the catchment scale (10-100 km) are not captured (Giorgi, 1995). A first approach to include these local forcings is the use of a global GCM with variable resolution (e.g. Déqué and Piedelievre, 1995), which gave promising results. A second approach is the application of statistical relationships to downscale large-scale GCM variables to local surface variables. This includes factor methods (where the observed series are multiplied with a factor; Gellens and Roulin, 1998), regression methods (Wilby and Wigley, 2000), classification methods (Bardossy and Plate, 1992), re-sampling methods (Wojcik *et al*., 2000) and conditional methods (e.g. weather generators, stochastic rainfall models; Jothityangkoon *et al*., 2000). A third approach is the utilisation of a high-resolution regional climate model (RCM) nested inside the global GCM. The initial and boundary conditions necessary to drive the RCM are provided by the output of GCM global simulations. With this technique, horizontal resolutions of 20 km (Marinucci *et al*., 1995) to about 50 km (Jones *et al*., 1995; Christensen *et al*., 1996) up to 70 km (Marinucci and Giorgi, 1992) are achieved. In applying one-way nested models to regional climates, there is an assumption that the development of systems within the model domain is constrained by the forcing of the GCM boundary conditions. As with the statistical techniques, the reliability of the GCMs therefore largely determines the value of the downscaling techniques. Comparisons between different downscaling techniques do not agree about which method to chose (e.g. Wilby and Wigley, 1997; Kidson and Thompson, 1998; Murphy, 1999). While in future direct use of dynamical downscaled climate variables in hydrological models may be possible, for practical reasons statistical methods are necessary (Beersma *et al*., 2000).

Simulations obtained with climate models generally are in reasonable agreement with observations of the present climate for a variety of key dynamic and thermodynamic climate variables. However, this does not mean that climate models are capable of accurately predicting the response of the climate to a natural or anthropogenic

perturbation. This is because a large number of adjustable constants is introduced in the parameterisations for the sub-grid-scale phenomena and processes. These constants often can not be determined on the basis of fundamental principles, but rather are set to values that give the most realistic-looking simulation of climate. More confidence in predictability of climate models can be gained by testing the models in great detail and their components separately, and by testing their response to prescribed forcings for which the response is known such as the diurnal and annual cycles of solar heating, or boundary conditions of earlier times (e.g. Renssen *et al*., 1996; Ganopolski *et al*., 1998). In model validation, key climate variables are the surface air temperature and precipitation. Model validation should be quantitative and has to deal with means, variances and extremes. Deficiencies of concern common to many models are the 'cold bias' of several degrees in the tropical troposphere, the underestimation of the intensity of weather systems, the poor simulation of clouds and the smoothing of the topography (McGregor *et al*., 1993). When comparing different models, agreement is necessary on the method of diagnosis, the forcing conditions (solar heating, composition atmosphere), the data set for verification (length, period) and the horizontal resolution (Schuurmans, pers. comm.). Important uncertainties of estimates of climate change are the response of cloud radiative properties, the changes in ice and snow cover, the oceanic response, the shifts in regional climate patterns and the changes in variability (Dickinson, 1989; Mearns *et al*., 1997).

Several model intercomparisons have been performed for the simulation of the present climate (model validation) and the future climate (climate prediction) (e.g. Gates, 1999; IPCC, 1996; Räisänen, 1997; Kacholia and Reck, 1997; Kittel *et al*., 1998 Meehl, 2000). They found global mean temperature and precipitation biases of respectively 1.1 °C and around 10 % and a good simulation of large-scale features. Validation over Europe with individual models (Marinucci and Giorgi, 1992 (RCM); Marinucci *et al*., 1995 (RCM), Jones *et al*., 1995 (RCM); Gregory and Mitchell, 1995 (GCM)) resulted in approximately equal performances; temperature differences of 1-4 °C and precipitation within 50 % of observed values. Christensen *et al*. (1997) found for seven RCMs for Europe positive and negative biases for temperature (2-4 °C) and mainly positive ones for precipitation (1-5 mm/day).

The models agree on large-scale features of climate change, but their agreement on smaller scales is substantially worse. The majority of the GCMs predicts a change in global mean temperature and precipitation of respectively +1 to +4.5 °C and –35 to +120 % in 2100 (large regional differences) (IPCC, 1996; Kittel *et al*, 1998). Individual GCM-studies indicate for Europe an average temperature increase of respectively 3.5, 6 and 4.4 °C with CO_2 doubling (Giorgi *et al*., 1992; Gregory and Mitchell, 1995; Jones *et al*., 1997). Three RCMs produce for Europe an average temperature increase of respectively 3.6, 2.8 and 4.0 °C (Giorgi *et al*., 1992; Rotach *et al*., 1997; Jones *et al*., 1997). Precipitation predictions vary from model to model. Many models suggest an increase of rainfall intensity and frequency of extreme events and a decrease of moderate rainfall with climate change (e.g. for Europe: Gregory and Mitchell, 1995; Cubasch *et al*., 1995). Katz and Brown (1994) indicate that extreme events are relatively more sensitive to changes in climate variability than to changes in climate means. However, the emphasis has been placed on analysing changes in the latter statistic. Some attention has been given to the variability and negligible attention to extremes.

1.3.2 Impact on hydrology and river flooding

The climate variables downscaled to 'hydrological' scales are used as input in hydrological models (empirical, conceptual or physically-based) to assess the impact of climate change on the hydrology of a catchment. The earliest studies (e.g. Nemec and Schaake, 1982) used hypothetical climate change scenarios (factor methods) in combination with statistical relations or hydrological models to assess these impacts. In the mid 80s and beginning of the 90s, results from GCMs became available as direct or indirect input in hydrological models. For example Gleick (1987) used several hypothetical and GCM climate change scenarios together with the hydrological Sacramento model for climate impact assessment in California. He found major decreases in summer runoffs and increases in winter runoffs for all eighteen climate scenarios. Similar approaches for Europe (Belgium, Switzerland, Greece) resulted in similar conclusions with respect to high and low flows (Bultot *et al*., 1988; 1992; Mimikou *et al*., 1991). From then on, also other approaches (stochastic rainfall models, synoptic scale hydrological models) were used for climate impact assessment (e.g. Wilby *et al*., 1994; Blazkova and Beven, 1997). An alternative approach is to use paleoclimatic and paleoflood data to analyse climate impacts. Results from this approach suggest that even modest climatic changes (temperature 1-2 °C and precipitation 10-20 %) can result in very important changes in the magnitudes and recurrence frequencies of floods (Knox, 1993; Knox and Kundzewicz, 1997). However, the majority of the studies uses factor-like methods for climate change scenarios and conceptual hydrological models to mainly assess changes in average variables.

In the 90s studies for the Rhine basin (Kwadijk, 1993) and the Meuse basin (Middelkoop and Parmet, 1998) were carried out. For these basins an increase of peak discharges of 15-20 % by the end of the 21st century was found, using the factor method for climate scenario construction and GIS-based hydrological models with a time step of 10 days. The peak discharges were obtained employing two different methods for downscaling 10-day discharges to daily discharges. Gellens and Roulin (1998) used seven climate scenarios in combination with the factor method and the daily conceptual model IRMB to assess the impact of climate change on streamflow for eight small catchments in Belgium (four in the Meuse basin). They found for all but one scenario a rise in the frequency of floods in winter for the catchments where surface flow prevails. Wit *et al*. (2001) studied the impact of climate change on low flows in the Meuse basin and selected sub-catchments with two climate scenarios and three different hydrological models. They found an increase of the average monthly discharge in spring and a decrease of the average monthly discharge in autumn. Only small changes in maximum monthly average discharges (winter) were found. Overall, it seems that climate change will result in an increase of flood frequencies for the Meuse basin. However, this issue is only roughly considered in previous studies. No attempt has been made to simulate discharge behaviour on a daily basis using spatially and temporally changed climate patterns.

In a review, Leavesley (1994) pointed out some major problems in the modelling of the effects of climate change on water resources. These included the measurement and estimation of parameters over a wide range of scales and the quantification of uncertainty in model parameters and results. The mismatch between different scales (from hill slope to GCM grid scale, from storm duration to climate change scale), the uncertainty assessment and additionally the response of extreme values still are major

problems in hydrological impact assessment (Beersma *et al*., 2000). These issues are briefly considered below.

Gleick (1986) pointed out the problem of the mismatch of scales when using coarse scale GCM projections for impact assessment at the catchment scale. Sub-grid scale hydrological processes are not resolved by the coarse scale GCMs and must therefore be parameterised in the GCMs. Moreover, these GCMs deliver climate variables at such a scale that, in particular for precipitation, too little variability is introduced in the hydrological system and as a result the discharge regime is less variable than the observed one. Because of this, methodologies are used to downscale variables at the GCM-scale to the scale required for impact studies. These downscaling methodologies have been briefly reviewed in section 1.3.1. An alternative approach is to employ GCM-data together with macroscale hydrological models (10^5-10^6 km^2). For example Kite and Haberlandt (1999) used the conceptual SLURP model to simulate the hydrological response to GCM and other coarse scale atmospheric data for two large basins in North America. They found that the agreement between observed and modelled discharge became better with increasing drainage area. This emphasises that the applicability of this kind of method is restricted to very large basins where only the discharge at the outlet is of interest. Other macroscale models simulate streamflow for basins in a whole continent (Arnell, 1999) or even in the whole world (Arora and Boer, 2001). These models often are strongly related to the hydrological parameterisations within GCMs or are equal to these parameterisations. Ideally, GCMs are used to describe the hydrological response to climate change directly. For the time being this can only be done for very large basins and average quantities, and even then model outcomes should be handled with care due to the crude hydrological parameterisations in GCMs.

The problem of uncertainty associated with model outcomes is a phenomenon common to all scientific areas where approximations of reality by means of models are of interest. A whole cascade of uncertainties is present in hydrological impact assessment ranging from uncertainties about future greenhouse gas emissions and responses of the climate system to uncertainties in physical catchment characteristics and hydrological models. Numerous studies have assessed these different uncertainties (e.g. Uhlenbrook *et al*., 1999; Visser *et al*., 2000), but apparently no serious attempts have been made to evaluate the whole uncertainty cascade associated with the impact of climate change on river flooding. Given the complexity of especially GCMs this seems to be very difficult if not impossible to do, but at least some range of possible outcomes should accompany a climate impact study (e.g. Carter *et al*., 1999). This range can then be compared with changes in hydrological variables to evaluate the reliability of these changes. Such an evaluation probably reveals that uncertainties are equal to or larger than predicted changes and nothing can be concluded at all. However, at least some confidence can be placed upon the direction of change and the range of possible changes provided that no 'surprises' such as the collapse of the thermohaline circulation in the North Atlantic (Ganopolski *et al*., 1998) or the disintegration of the West Antartic Ice Sheet (Oppenheimer, 1998) will occur.

Hydrological responses of particular interest are extremes like low flows and floods. Floods are of interest in this thesis and their practical relevance has been illustrated in section 1.1. Despite this practical relevance, applications of statistical extreme value theory to climate and climate impact analysis are rare given the vast amount of literature on climate change in general (Katz, 1999). This deficiency is difficult to explain taking

into account the frequent applications found in engineering design issues and its practical relevance. An explanation may be that the spatial and temporal resolutions should be sufficiently fine on the one hand and the temporal domain should be sufficiently long on the other hand to obtain reliable estimates of extreme responses. This combined with the complexity of GCMs and the variable responses within river basins can make assessments (seemingly) infeasible. Another explanation may be the belief that GCMs are incapable to provide meaningful information about changes in extremes at appropriate spatial and temporal scales (Beersma *et al*., 2000). This belief may act as a barrier to an exploration of the potential of GCMs to provide useful information. However, for example daily data and multiple GCM simulations can partly solve this problem. It must be mentioned that the other responses (low and average flows) should not be forgotten when focusing on a particular response (high flows), because the general hydrological behaviour ought to be realistic as well.

1.3.3 Meuse river basin

The implications of climate change for the important Dutch rivers has already been highlighted in the preceding sections. The Meuse basin has been chosen as research area, because less climate impact studies have been performed than e.g. for the Rhine basin (e.g. Kwadijk, 1993; Grabs, 1997; Middelkoop *et al*., 2001). Moreover the Water Resources Group of the University of Twente has some experience in other, related research fields in the Meuse area (e.g. Wind *et al*., 1999; Gerretsen, 2001). A brief description of the Meuse basin will be given here.

The Meuse is a river with a length of about 900 km from the source in France to the North Sea. Its basin covers an area of approximately 33,000 km^2 including parts of France, Luxembourg, Belgium, Germany and the Netherlands (see Figure 1.1). The main tributaries of the Meuse are the Chiers, Semois, Lesse, Sambre, Ourthe, Amblève, Vesdre and Rur. The Meuse basin can be subdivided into three major geological zones: the Lotharingian Meuse, the Ardennes Meuse and the Dutch Meuse. The Lotharingian Meuse goes from the source to the mouth of the Chiers and mainly transects sedimentary Mesozoic rocks. Its catchment is lengthy and narrow, the gradient is small and the major bed is wide. The discharge regime is therefore relatively flat. The Ardennes Meuse is situated between the mouth of the Chiers and the Dutch border and transects Paleozoic rock of the Ardennes Massif. This gives a narrow river valley and a big slope. Together with the poor permeability, this results in a quick response to precipitation. The Dutch section of the Meuse goes through the Dutch and Flemish lowlands consisting of Cenozoic unconsolidated sedimentary rocks. This section is sometimes split up into a relatively steep stretch from the border to Maasbracht and a flat stretch from Maasbracht to the mouth (Berger, 1992).

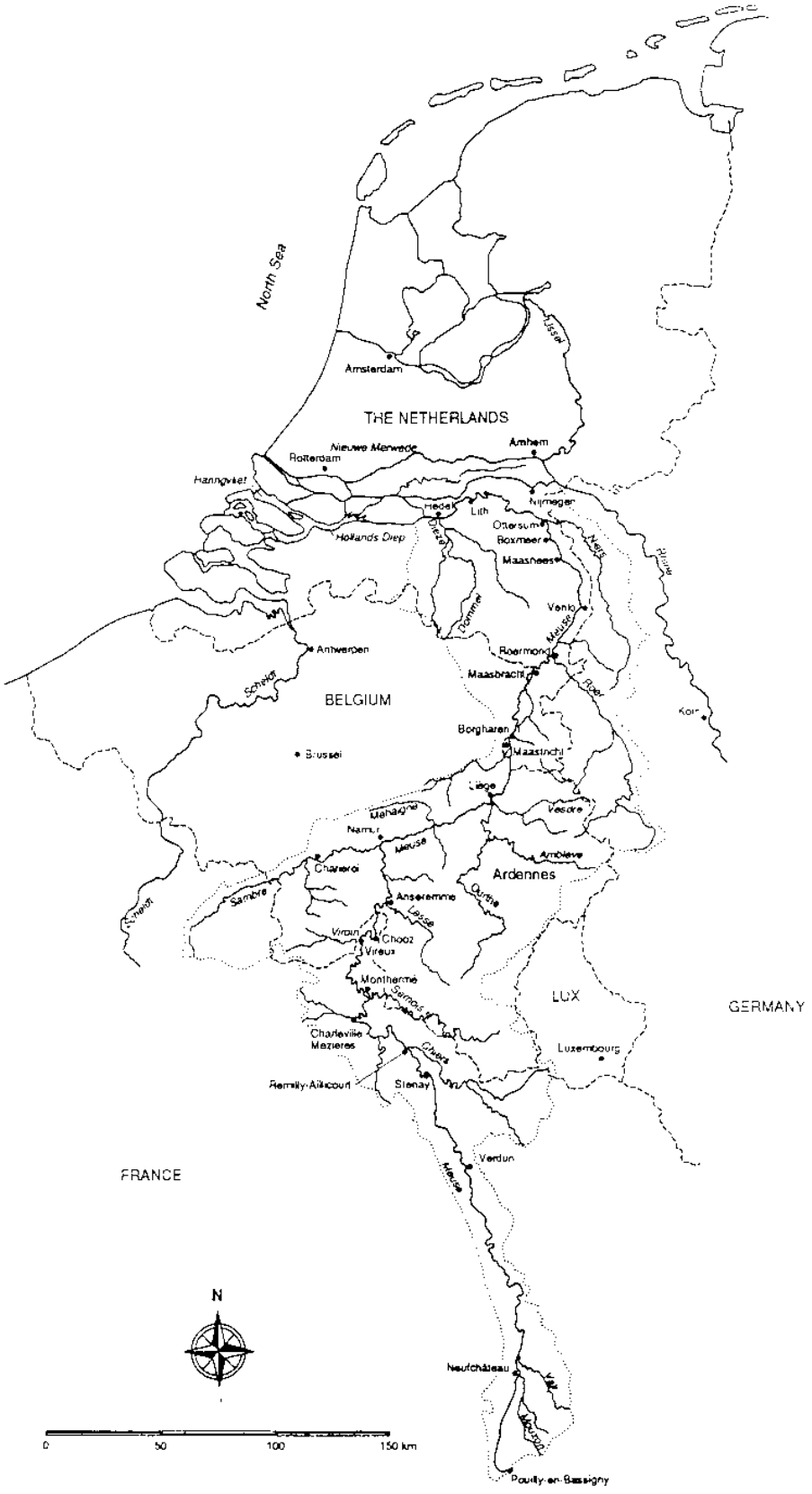

Figure 1.1 The Meuse river basin (Berger, 1992).

Precipitation is evenly distributed throughout the year. Low discharges mainly coincide with the peak of evapotranspiration during summer months and high discharges mostly occur during the winter months when evaporation is small. In Figure 1.2 the discharge regime of the Meuse is compared with the discharge regime of other rain-fed rivers of comparable size located in Northwest Europe. The figure shows that the discharge regime of the Meuse is more variable than the regime of other rivers. This implies that the Meuse has a relatively fast response to precipitation and is therefore sensitive to floods and droughts and changes in these properties due to climate change. The floods in 1993 and 1995 were the second and third largest observed peak discharges in the 20th century after the flood of 1926. Figure 1.3 gives the observed annual peak discharges at Borgharen for 1911-2000 and does not show a clear trend. When looking in more detail, a slightly increasing, but not significant trend can be observed. No attempt has been made to relate increases in greenhouse gas concentrations observed in the 20th century and accompanying temperature increases to this slightly increasing annual peak discharge series.

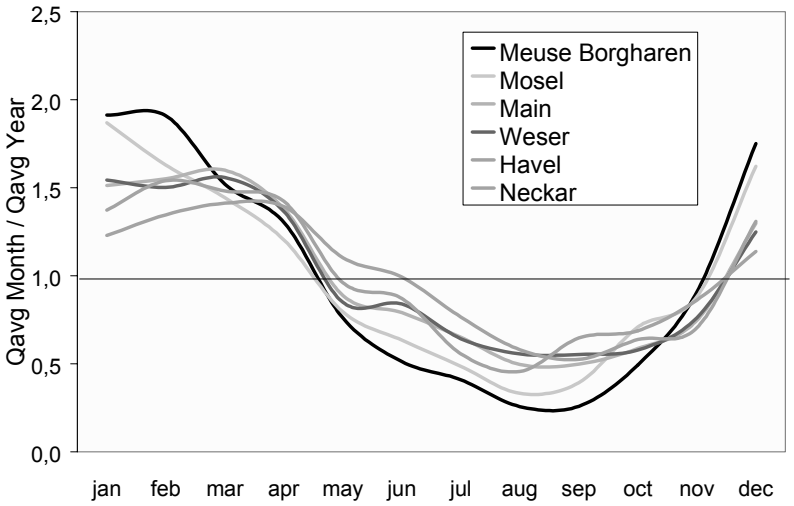

Figure 1.2 Normalised monthly discharge regimes for some Northwest European rivers (Wit et al., 2001).

The Meuse is used for a variety of functions including domestic, industrial and agricultural water supply, navigation, ecological functioning and recreation. During periods of low or high flows these functions can conflict with each other. Downstream of Liège there are a number of canals fed by water of the Meuse, the most important are the Albertkanaal, Zuid Willemsvaart and Julianakanaal. These canals are used for navigation and water supply. Reservoirs can be found in the upper branches of some tributaries and are used for electricity production, drinking water supply and flow regulation. These reservoirs are too small to have a major effect on the discharge regime of the Meuse, except for the Rur reservoir (Berger, 1992).

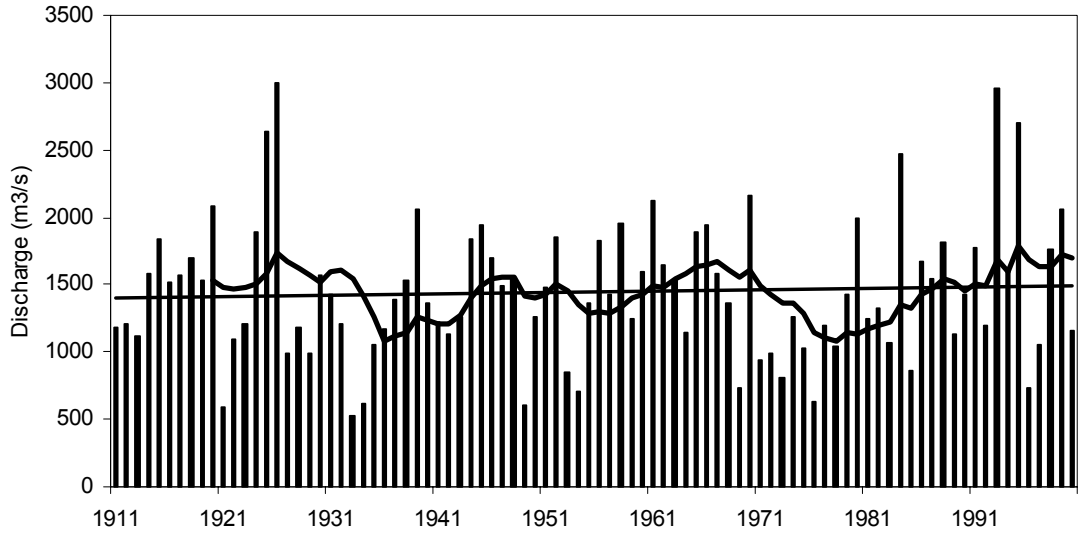

Figure 1.3 Annual peak discharges measured at Borgharen for 1911-2000 (bars), 10-year moving average (continuous line) and linear regression (straight line).

1.4 Research objectives and approach

1.4.1 Research objectives and questions

Two important research topics have been raised in the preceding sub-sections, namely the issue of appropriate models and the effect of climate change on river flooding. The corresponding research objectives are the following:

I. What is the appropriate model complexity for a specific modelling objective and research area?
II. What is the impact of climate change on river flooding in the Meuse?

Research objective I can be roughly subdivided into three research questions:
1. Which processes are dominant with respect to the research objective and area, and which variables are related to these processes?
2. Which spatial and temporal scales should be used to describe these processes and variables appropriately?
3. Which mathematical process formulations are appropriate for the description of the dominant processes at appropriate scales?

The answers to these questions will result in appropriate model components, which can be implemented into an existing modelling framework to obtain an appropriate model or can be used to build a new appropriate model.

Research objective II can be split up in two research questions:
4. How does climate change look like in terms of changes in precipitation and temperature?
5. What is the impact of this climate change on river flooding in the Meuse basin?

The second question can be dealt with by using the appropriate model from research objective I.

1.4.2 Research approach

The five mentioned research questions are considered in this thesis. Research questions 1, 2 and 3 are dealt with in chapter 2, 3, 4 and 5 and constitutes the main part of this research. Research questions 4 and 5 are mainly treated in chapter 6. An outline of the research questions and the related chapters is given in Figure 1.4 and described below.

In chapter 2, a preliminary model appropriateness procedure is set up and applied to investigate the possibilities of such a procedure and to identify the limitations and drawbacks. These latter disadvantages serve as a guide for the development of the final model appropriateness procedure. Uncertainty and scale aspects related to this procedure are described more extensively in the remainder of this chapter. In chapter 3, the effect of different spatial and temporal input and model scales on extreme river discharges is considered to further explore the issue of scales. This has been done by employing a stochastic rainfall model and a dimensionless river basin model with varying scales. In chapter 4, climate data from several sources are compared to assess the appropriate scales for the key climatic input variables. Moreover, this analysis reveals climate data under current and changed conditions to be used in the impact assessment in chapter 6. In chapter 5, river basin data from several sources are compared and literature is reviewed to derive the dominant processes, appropriate scales and appropriate process formulations to be used in the appropriate river basin model. Additionally, this analysis results in river basin data to be adopted in chapter 6. In chapter 6, the impact of climate change on river flooding is assessed by employing another stochastic rainfall model and the appropriate river basin model. This appropriate model has been obtained by implementing the appropriate model components derived in the preceding chapters into an existing modelling framework. Moreover, two additional models of differing complexities are used to check the sensitivity of the results to model complexity and to verify the model appropriate procedure. Finally in chapter 7, the answers to the research questions are formulated and the results from the preceding five chapters are collectively discussed.

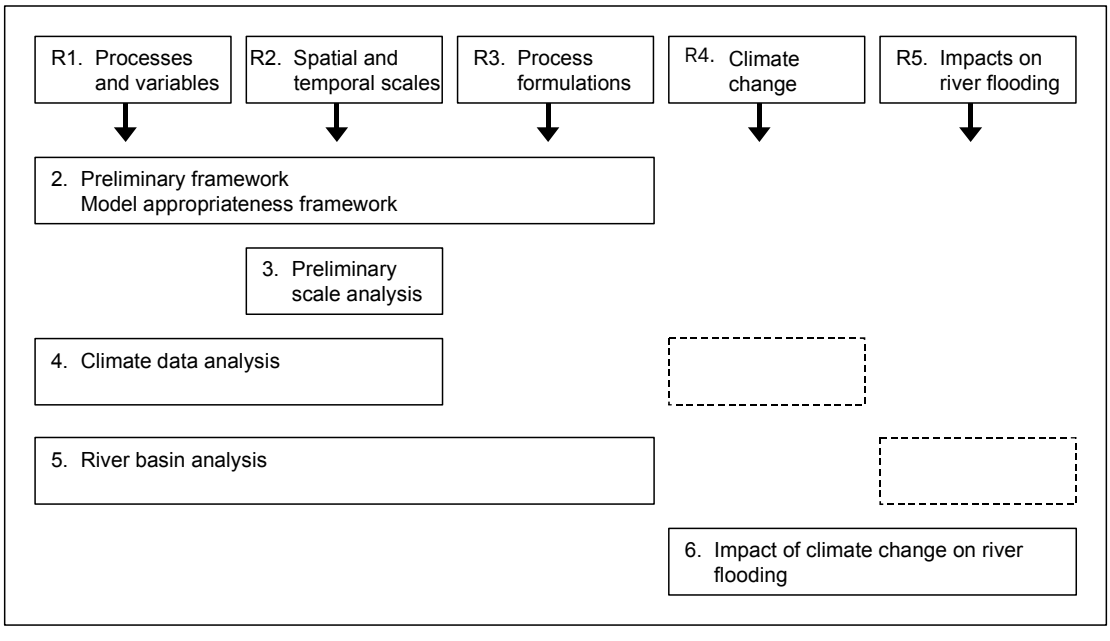

Figure 1.4 Research questions 1, 2, 3, 4 and 5 (R1-R5) and related chapters (2-6). Dashed boxes indicate that chapters aid in answering the research questions (e.g. by providing data).

Chapter 2

Model appropriateness framework

2.1 Preliminary approach

2.1.1 Introduction

Many studies consider one specific part of the appropriateness problem, e.g. the determination of the relevant processes for a problem or the assessment of appropriate spatial resolutions. As stated in chapter 1, there is a need for a more integrated approach to determine an appropriate model for a specific modelling objective and research area.

In this section a first step is taken by developing and applying a preliminary framework for the analysis and improvement of model appropriateness. The framework has been applied to a river basin model meant to assess the impact of climate change on flooding in the Meuse. This is to illustrate the above-mentioned approach, rather than to obtain an appropriate model for the specific modelling objective. The objective is achieved by developing a stochastic rainfall model for rainfall generation and using a simple, water balance based river basin model as a 'starting model' in the appropriateness framework. The rainfall model is developed, because under climate change conditions only rainfall on a coarse grid is available and thus climate change statistics should be used in a stochastic model. The river basin model outputs of particular interest are the extreme discharges, here extrapolated to the design discharge. The direction of model appropriateness improvement is determined by a cost function dependent on model output uncertainty. This model output uncertainty is assessed by means of sensitivity and uncertainty analysis with respect to the main inputs, parameters and process descriptions. Finally, the point of minimum costs should be approached to a certain extent sufficient for the user or it is found that this point will not be reached at all. This final stage is not the main objective and is beyond the scope of this section.

In 2.1.2 an outline of the procedure for the analysis and improvement of model appropriateness is given. In 2.1.3 the stochastic rainfall model is described and the river basin model is briefly considered, the latter model is extensively described in chapter 3. Results are discussed in 2.1.4 and an introduction to the final framework is given in 2.1.5. This final framework is partly considered in section 2.2, dealing with model uncertainty analysis, and in section 2.3, discussing statistical and scale issues.

Part of this chapter has been published as:

Booij, M.J., 2000. Model appropriateness for simulation of climate change and river flooding. In: L.R. Bentley, J.F. Sykes, C.A. Brebbia, W.C. Gray and G.F. Pinder (Eds.), *Computational methods in water resources*. Balkema, Rotterdam, 1169-1176.

2.1.2 Model appropriateness procedure

Analysis of model appropriateness

A cost function dependent on model output uncertainty is assumed. This cost function consists of two components, the model costs necessary to obtain a specific uncertainty level for the input, parameters or model (e.g. model development, data exploration) and the expected construction costs as a result of the output uncertainty (in water management e.g. damage, constructions). A model is assumed to be appropriate for a specific research objective when the output uncertainty results in minimal total costs. This is illustrated in Figure 2.1 for a situation with relatively small model costs and a situation with large model costs. The construction costs are generally much larger than the model costs and there is a lower limit with respect to the output uncertainty that can be obtained. The model cost function is assumed to be discontinuous due to new model technologies. These technologies require large investments with slight decreases in uncertainty on the short term, but possibly considerable decreases in uncertainty with small additional costs on the long term. The appropriate model complexity associated with minimal total costs depends largely on the relative magnitudes of the construction and model costs (compare a and b). The appropriateness criterion can be reduced to an uncertainty criterion when the costs functions are roughly known. Then, a model is assumed to be appropriate when its output uncertainty is less than a specified criterion G.

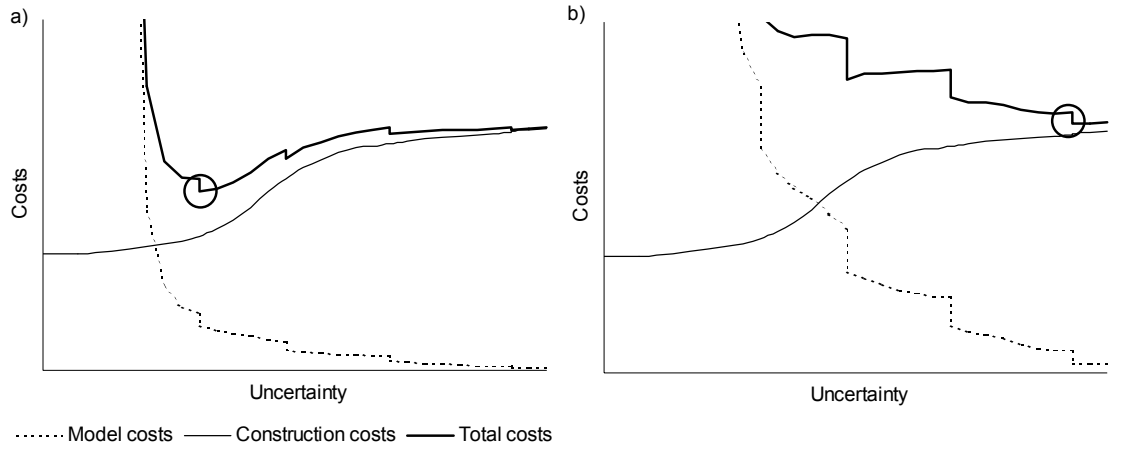

Figure 2.1 Costs as a function of output uncertainty for a situation with small model costs (a) and a situation with large model costs (b).

It is assumed that the model to be used is approximately smooth and linear and the inputs are independent. Model output uncertainty is then expressed as (e.g. Morgan and Henrion, 1990)

$$\sigma_Y^{\,2} = \sum_{i=1}^{N} \left(\frac{\partial Y}{\partial x_i} \right)_{\mathbf{X_0}}^2 \sigma_{x_i}^{\,2} \qquad (2.1)$$

where $\mathbf{X} = (x_1, x_2, \ldots\ldots, x_N)$ are the relevant inputs, parameters and processes in the model, $\mathbf{X_0}$ are the expected values of $\mathbf{X}$ and $\sigma_{\mathbf{X}}^2 = (\sigma_{x1}^2, \sigma_{x2}^2, \ldots.., \sigma_{xN}^2)$ are the variances of $\mathbf{X}$. These variances are described by a spatio-temporal semivariogram. The spherical model proposed by Hoosbeek (1998) was used here

$$\sigma_{x_i}^2(h,k) = c_0 + c_1 S_L(h) + c_2 S_T(k) \tag{2.2}$$

where

$$S_L(h) = 1.5\left(\frac{h}{L_S}\right) - 0.5\left(\frac{h}{L_S}\right)^3 \qquad h \le L_S \tag{2.3}$$

$$S_L(h) = 1 \qquad h > L_S$$

$$S_T(k) = 1.5\left(\frac{k}{T_S}\right) - 0.5\left(\frac{k}{T_S}\right)^3 \qquad k \le T_S \tag{2.4}$$

$$S_T(k) = 1 \qquad k > T_S$$

Here, h is the lag distance or model scale in space, k is the lag distance or model scale in time, c_0 is the nugget variance or the microvariability at a scale smaller than the separation distance between the closest measurement points, c_1 is the spatial variance contribution, c_2 is the temporal variance contribution, L_S is the spatial range and T_S is the temporal range. All these parameters are dependent on input, parameter and process x_i. An example of a spatio-temporal semivariogram showing $\sigma_{xi}^2(h,k)$ for arbitrary c_0, c_1, c_2, L_S and T_S is given in Figure 2.2.

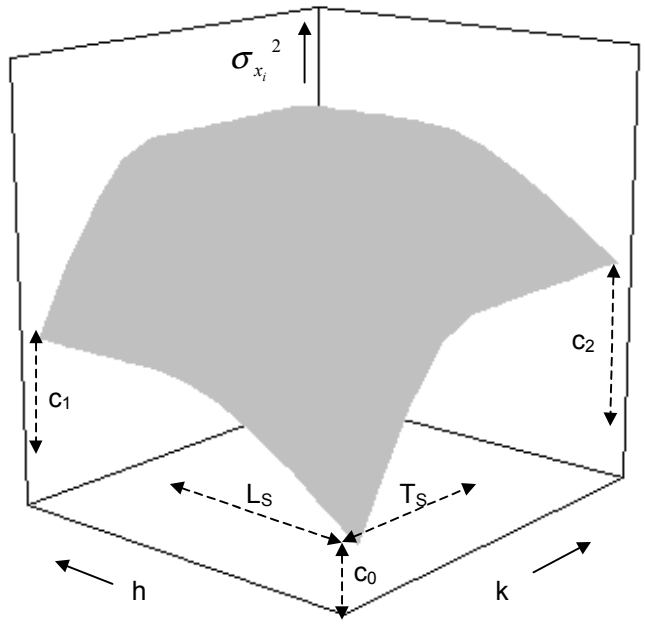

Figure 2.2 Spatio-temporal semivariogram showing $\sigma_{xi}^2(h,k)$ for arbitrary c_0, c_1, c_2, L_S and T_S.

Improvement of model appropriateness

Model output uncertainty usually will be much larger than G and consequently, reduction of uncertainties is required. This reduction can be obtained through a variety of techniques. The here applied procedure of model uncertainty reduction and accompanying model appropriateness increase will briefly be described. Starting-point is a simple river basin model, which transforms rainfall to runoff. The processes, accompanying parameters and inputs to be incorporated in the model are determined by comparing simulations from model versions including varying numbers of processes with observations through the model efficiency coefficient (Nash and Sutcliffe, 1970) and the discharge regime. These processes remain incorporated throughout the entire procedure, however process descriptions can be adapted as will be shown below. The squared sensitivities $(\partial y/\partial x_i)_{\mathbf{X0}}^2$ for these relevant processes, parameters and inputs x_i are determined by varying their values within a specific range and simulating the effect on the output Y. Then uncertainties σ_{xi}^2 according to equation (2.2) are determined and multiplied with the squared sensitivities to obtain the partial contributions to the output uncertainty σ_Y^2. Sensitivities are assumed to be only dependent on research area and process description and not on data availability and model scales. On the other hand, uncertainties are assumed to be dependent on all these aspects, resulting from equation (2.2), (2.3) and (2.4) as well. The dependence of the sensitivity and the uncertainty on the mentioned aspects is shown in Table 2.1.

Table 2.1 Presence of dependence of sensitivity ($\partial Y/\partial x_i$) and uncertainty (parameters/ variables from (2.2), (2.3) and (2.4) L_S, T_S, c_0, c_1, c_2, h, k) on aspects (research area, process description, data availability, model scale) indicated with X.

Aspect	Sensitivity	Uncertainty		
	$\partial Y/\partial x_i$	L_S, T_S	c_0, c_1, c_2	h, k
Research area	X	X	X	X
Process description	X		X	X
Data availability			X	X
Model scales				X

The largest partial contributions to the output uncertainty should be reduced taking into account Table 2.1. This means for a fixed research area that uncertainties associated with large sensitivities should be reduced through adapting process descriptions, increasing data availability and changing model scales. Which adaptations take place depend for a specific process, parameter or input on the uncertainty contributions of the nugget part c_0, spatial part $c_1 S_L(h)$ and temporal part $c_2 S_T(k)$ of equation (2.2). Sensitivities should be recalculated when process descriptions are adapted (see Table 2.1). The uncertainty reduction should proceed until uncertainty level G associated with an appropriate model for a specific situation is reached.

The procedure will be applied to a simple river basin model. This application is meant to illustrate the procedure, rather than to derive an appropriate river basin model to assess the impact of climate change on flooding in the river Meuse.

2.1.3 Rainfall and river basin model

Stochastic rainfall model

The stochastic rainfall model used is a multivariate autoregressive lag-one model AR(1). This model incorporates main statistical characteristics of observed precipitation to generate spatially and temporally varying rainfall series. The model assumptions are:

- The rainfall process is a stationary one, i.e. its statistics do not change with time.
- The rainfall process has a uniform character, i.e. its statistics do not vary in space.
- There is correlation in time and space between rainfall amounts.

The multivariate AR(1) model is described by

$$\mathbf{Z}(t) = \mathbf{A}\mathbf{Z}(t-\Delta t) + \mathbf{B}\boldsymbol{\varepsilon}(t) \tag{2.5}$$

where the vector $\mathbf{Z}(t)$ is composed of n different but interdependent rainfall time series for different locations, $\mathbf{A}$ and $\mathbf{B}$ are $n \times n$ parameter matrices and the vector $\boldsymbol{\varepsilon}(t)$ consists of n uncorrelated random numbers originating from a symmetrical three-parameter gamma distribution (reflected with respect to the y-axis). It is assumed that $\mathbf{A}$ is a diagonal matrix with uniform non-zero elements equal to a_t determining the temporal correlation $r(k)$ and transition probabilities from wet to wet days *WW*, dry to dry days *DD* etc.. Elements b_{ij} of $\mathbf{B}$ are obtained through a function relating distance between two locations $|(x, y)_i\text{-}(x, y)_j|$ and parameter b_s determining the spatial correlation $r(h)$ [see e.g. Stol (1972)]

$$b_{ij} = \exp\left[-b_s \left|(x,y)_i - (x,y)_j\right|\right] \tag{2.6}$$

The vector $\mathbf{Z}(t)$ is adjusted to obtain (positive) rainfall $\mathbf{P}(t)$

$$\begin{aligned} &\mathbf{P}(t) = \mathbf{Z}(t) && \mathbf{Z}(t) > 0 \\ &\mathbf{P}(t) = 0 && \mathbf{Z}(t) \le 0 \end{aligned} \tag{2.7}$$

The symmetrical gamma distribution is given by

$$f(x) = \frac{1}{\beta_{gs}^{\alpha_{gs}}\Gamma(\alpha_{gs})}\left|x-\xi_{gs}\right|^{\alpha_{gs}-1}\exp\left[-\frac{\left|x-\xi_{gs}\right|}{\beta_{gs}}\right] \tag{2.8}$$

with $-\infty < x < \infty$. The shape parameter α_{gs}, scale parameter β_{gs} and location parameter ξ_{gs} determine respectively the extreme behaviour of rainfall (represented by the kurtosis γ_2), the average rainfall μ and the ratio wet to dry days *W/D*. The five parameters (a_t, b_s, α_{gs}, β_{gs} and ξ_{gs}) have been determined in such a way that the above mentioned statistics of observed rainfall are approximated in a right way.

The rainfall model is applied to the Meuse basin upstream of Borgharen (near the Belgian-Dutch border) which has a surface area of about 21 10^3 km^2. Its parameter values have been obtained by means of observed rainfall (Stol, 1972; Berger, 1992; NOAA, 1999). Daily rainfall series for n = 64 points on a regular square grid (distance between points is approximately 20 km) for a 30-year period have been generated.

River basin model

A simple river basin model with variable spatial and temporal resolution has been used as the 'starting model' in the appropriateness procedure. The model consists of a number of catchment cells N and river cells $\sqrt{N}$. Different resolutions are obtained by multiplying N with 4^n depending on the actual N. These varying resolutions do not change model output for uniform and stationary input and parameters. The model structure for $N = 16$ is illustrated in Figure 2.3. This figure shows that each catchment cell in strip j receives effective precipitation (PE') and discharges this precipitation to the adjacent cell in strip j in the river direction. The catchment cell that borders a river cell discharges into this river cell in strip j, from this river cell the water is transported further to the river cell in strip j+1 and finally to the outflow point. The water movement is described by means of a water balance for the catchment cells and the river cells in a dimensionless form in order to reduce the number of parameters. The dimensionless form is obtained through scaling with a spatial correlation length, a temporal correlation length, the surface area of the basin and the mean effective rainfall. A comprehensive description of the model is given in chapter 3.

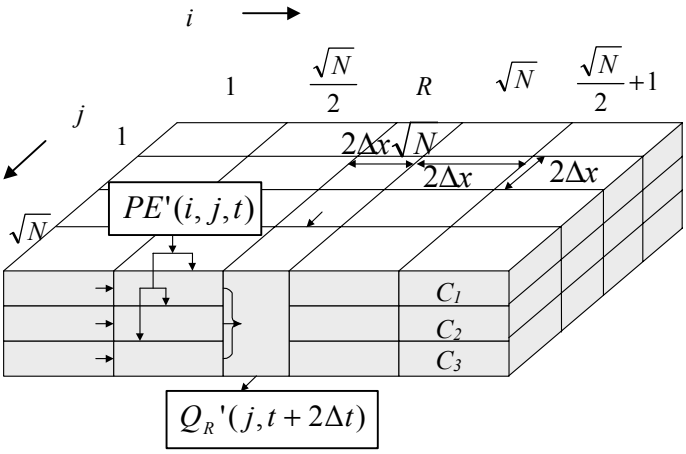

Figure 2.3 River basin model with catchment cell position expressed in i and j, river cell position (R) expressed in j and cell dimensions expressed in Δx. The input PE' (i, j, t), output Q_R' (j, t+2Δt) and water flow directions are illustrated for an arbitrary catchment and river cell (the figure has not been drawn to scale).

The 'starting model' of the Meuse basin is the most simple one, namely when $N = 1$. This gives, with a spatial correlation length of 140 km and a temporal correlation length of 1 day, dimensionless model scales of $\Delta x' = 0.52$ and $\Delta t' = 1$. Processes incorporated in this 'starting model' and parameter values used have been determined by using an observed daily rainfall-runoff series. The observed rainfall series is from a station near the center of the Meuse basin (Charleville-Mézières) for the period 1994-1997 (NOAA, 1999). The observed discharge series is from the station Borgharen at the outflow point of the river basin model for the period 1994-1997 (Rijkswaterstaat, 1998). Runoff coefficients are assumed to be monthly means and have been obtained from observed rainfall and discharge during the period 1951-1980 (Berger, 1992).

The design discharge Q_p' is derived by fitting a Gumbel distribution to the annual maximum discharges (see section 2.3). The annual maximum discharges are obtained

from a simulated daily Borgharen discharge series for a 30-year period by using one or more of the generated daily rainfall series.

2.1.4 Results and discussion

Stochastic rainfall model

Parameter values for the rainfall model and related observed and simulated statistics are summarised in Table 2.2. It is found that observed and simulated statistics correspond good enough for the research purpose. Only the differences between observed and simulated temporal correlation $r(k)$ and kurtosis γ_2 are substantial. The first difference is because the parameter a_t determines besides the temporal correlation also the transition probabilities. Therefore a_t had to be chosen in such a way that the three statistics are jointly simulated as good as possible. The second difference (γ_2) is due to the gamma distribution used. This distribution simulated the rainfall extremes quite well, however it was not able to reproduce the extremes of the extremes. These are small disadvantages of the rainfall model and should be kept in mind when interpreting the results.

Table 2.2 Parameter values for the rainfall model and related observed and simulated rainfall statistics.

Parameter	Value of parameter	Statistic	Unit	Value of statistic	
				Observed	Simulated
a_t	0.45	$r(k)$ (1 day)	-	0.24*	0.38
		WW	-	0.69*	0.66
		DD	-	0.71*	0.66
b_s	1.5	$r(h)$ (25 km)	-	0.84**	0.93
		$r(h)$ (50 km)	-	0.75**	0.85
		$r(h)$ (100 km)	-	0.64*,**	0.63
α_{gs}	0.15	γ_2	$(mm/d)^4$	19*	11
β_{gs}	100	μ	mm/d	2.56***	2.55
ξ_{gs}	0	*W*/*D*	-	0.92*	0.99

* From daily observed rainfall of 3 stations in and around the Meuse basin (Charleville-Mézières, Metz and St. Dizier) during the period 1994-1998 (NOAA, 1999).

** From spatial correlations between daily observed rainfall in the eastern part of the Netherlands (Stol, 1972).

*** From observed rainfall in the Meuse basin during the period 1951-1980 (Berger, 1992).

River basin model appropriateness procedure

First the processes to be incorporated throughout the whole procedure were determined. Models with a different number of processes were obtained by varying the number of reservoirs in a catchment cell from $m = 1$ through $m = 3$. Simulations with these models (with calibrated parameters) resulted in model efficiency coefficients of respectively 0.81, 0.84 and 0.85. A value of 1 would have implied perfect correspondence between observed and simulated discharge. On the basis of these coefficients no decision can be made. However, when comparing the discharge regimes associated with the three simulations, the one for $m = 1$ showed a too extreme behaviour. Therefore, two reservoirs were incorporated in the river basin model. The incorporated input, processes and parameters are summarised in Table 2.3. The processes in this table are effective rainfall (*PE*'), the fractions of effective rainfall infiltrating in reservoirs 1 and 2 (p_1 and

p_2), the total discharge from the adjacent catchment cells into a river cell (Q_1' and Q_2') and the discharge of the river basin (Q_R'). The parameters are a time-dependent runoff coefficient **rc** = (rc_1, rc_2,…., rc_w), initial values for fractions p_1 and p_2 [$p_{C1}(i, j, 0)$ and $p_{C2}(i, j, 0)$], the ratio of the lag constant of reservoir C_m to the lag constant of reservoir R (K_1 and K_2) and the lag constant of reservoir R in the river cell (k_R').

Table 2.3 Incorporated input, processes and parameters and associated parameter values in the model.

Input	Process	Parameter	Value
P			
	PE'	**rc**	monthly mean
	p_1	$p_{C1}(i, j, 0)$	0.5
		$p_{C2}(i, j, 0)$	0.5
		K_2	0.05
	p_2	$p_{C1}(i, j, 0)$	0.5
		$p_{C2}(i, j, 0)$	0.5
		K_2	0.05
	Q_1'	K_1	0.5
	Q_2'	K_2	0.05
	Q_R'	k_R'	0.5

The above described model (N =1 and 2 reservoirs) is the 'starting model' for the model appropriateness procedure. The input is a daily rainfall series for one point (near the basin center) for a 30-year period. The parameter values of the spatio-temporal semivariogram described by (2), (3) and (4) for each input, process and parameter have been roughly estimated and are given in Table 2.4. Approximately, the right ratios between the different parameter values for the different variables were estimated, partly on the basis of literature (e.g. Blöschl and Sivapalan, 1995; Kitanidis, 1997; Hoosbeek, 1998). The parameters L_S and h are scaled with respect to the spatial correlation length (140 km) and the parameters T_S and k are scaled with respect to the temporal correlation length (1 day). The root of the parameters c_0, c_1 and c_2 are relative to their corresponding input, process or parameter value.

Table 2.4 Parameter values $\sqrt{c_0}$, $\sqrt{c_1}$, L_S, h, $\sqrt{c_2}$, T_S, k for input, process descriptions and parameters used in start simulation (dimensionless).

Input/ process/ parameter	Nugget	Spatial			Temporal		
	$\sqrt{c_0}$	$\sqrt{c_1}$	L_S	h	$\sqrt{c_2}$	T_S	k
P	0.2	0.2	1.43	1.04	0.3	4	1
PE'	0.2	0	0.36	1.04	0.2	90	1
p_1	0.3	0.025	0.036	1.04	0.4	8	1
p_2	0.3	0.025	0.036	1.04	0.4	8	1
Q_1'	0.2	0.05	0.036	1.04	0.4	4	1
Q_2'	0.1	0.05	0.36	1.04	0.3	50	1
Q_R'	0.1	0.05	2.14	1.04	0.4	15	1
rc	0.1	0.1	0.36	1.04	0.3	90	30
p_{C1}(i, j, 0)	0.2	0.3	0.036	1.04	0.1	8	100
p_{C2}(i, j, 0)	0.2	0.3	0.036	1.04	0.1	8	100
K_1	0.2	0.3	0.036	1.04	0.1	4	100
K_2	0.1	0.1	0.36	1.04	0	50	100
k_{R0}'	0.05	0.1	2.14	1.04	0.1	15	100

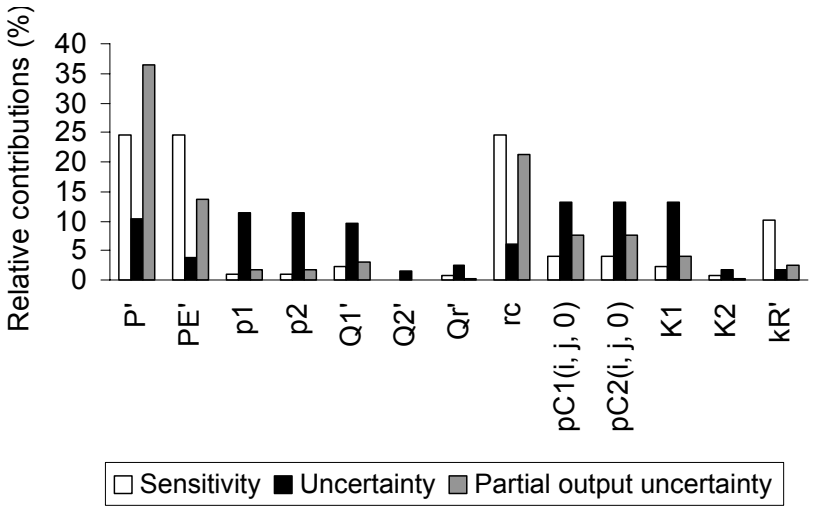

Figure 2.4 Relative contributions of input, process descriptions and parameters to sensitivity, uncertainty and output uncertainty.

1. The resulting sensitivity from equation (2.1) of the model output Q_p' (scaled with its reference value) with respect to the input, process descriptions and parameters (scaled with their reference values) is given in Figure 2.4. The sensitivities are given relative to each other and consequently their sum amounts to 100 %. When determining these sensitivities, it was found that Q_p' behaved approximately linearly with different values for input, processes and parameters.
2. The uncertainty from equation (2.2) of the input, process descriptions and parameters (scaled with their reference values) relative to each other is given in Figure 2.4 as well.
3. Finally, the partial output uncertainty contributions from equation (2.1) of the input, process descriptions and parameters relative to each other is given in Figure 2.4. The relative model output uncertainty σ_Y/Q_p' (%) is in this case 69 % as could be expected from the very simple model used. It is emphasised that the parameters in Table 2.4 are roughly chosen and thus uncertain. The dimensionless model output Q_p' is 11.9. In the following, three steps of the model appropriateness improvement procedure are presented.

Step 1. The largest partial contribution to the output uncertainty stems from **P'**. The nugget, spatial and temporal uncertainty contributions are comparable (not shown here). It has been decided to decrease the spatial contribution by including rainfall series from all stations (n = 64) in the simulations. An accompanying decrease of parameter $\sqrt{c_1}$ for **P'** from 0.2 to 0.1 was assumed. The resulting σ_Y/Q_p' is 65 % meaning a decrease of 'only' 4 % in the output uncertainty. However, Q_p' has changed dramatically to 7.7 due to the averaging effect of the input (average over 64 points).

Step 2. The changed relative contributions similar to Figure 2.4 are calculated. The partial contribution from **P'** is still the largest one, but the partial contribution from **rc** is considerable as well. The temporal uncertainty contribution of this latter parameter is the largest one, and therefore, this contribution has been decreased by modelling **rc** day-dependent (w = 365) instead of month-dependent (w = 12) through a sine function. This

resulted in a decrease of parameter *k* for **rc** from 30 to 1. The resulting σ_Y/Q_p' is 60 % (5 % decrease) and Q_p' remains relatively unchanged.

Step 3. The undesirable averaging effect of the input on the output in step 1 was assumed to decrease when the model scales (*h* and *k*) would be decreased. Parameter *h* was changed from 1.04 to 0.26 for all processes and **P'** and parameter *k* was changed from 1 to 0.25 for all processes and **rc**. This change in both parameters preserves the same constant ratio between the space and the time scale of the model. The resulting σ_Y/Q_p' is 58 %, only a 2 % decrease in output uncertainty. However, Q_p' has changed considerably (to 13.2, close to its original value), which seems to be more plausible when comparing with the observed Q_p' of 14.9 (or 4050 m^3s^{-1} based on the annual maxima for 1911-1999).

2.1.5 Discussion and introduction to framework

The results of the stochastic rainfall model indicate that a relatively simple model is able to produce realistic rainfall statistics. The only substantial departure from observed statistics was found for the temporal correlation. However, when a higher spatial resolution for the rainfall is needed, another stochastic rainfall model should be used as the quality of the simulated statistics decreases dramatically for higher resolutions (not shown here).

The application of the model appropriateness procedure showed that the procedure could give a good indication in which direction (input, process descriptions or parameters as well as nugget, spatial or temporal part) most profit can be gained when an appropriate model is required for a specific research area and objective. It was found that for this or a similar research area and objective, two reservoirs in the catchment cell already seem to be sufficient. Furthermore, the results indicated that a decrease of input uncertainty and uncertainties associated with the transformation of rainfall to effective rainfall were of particular importance.

It is again emphasised that the application was meant to illustrate the procedure rather than to derive an appropriate model designed to assess the impact of climate change on flooding in the Meuse. The results should therefore be interpreted with caution because of the following reasons:

- The uncertainties in the parameters of the spatio-temporal semivariogram are substantial.
- When including more non-linear process descriptions to decrease output uncertainty, these process descriptions should still be linearised to maintain linearity necessary for the determination of the output uncertainty. Otherwise this output uncertainty should be determined in a different, more advanced manner.
- The determination of the output uncertainty is based on the independency of inputs, processes and parameters. This assumption will not hold in reality. In fact, it does not even apply to this river basin model as there are many interdependencies, e.g. between the initial infiltration parameters and the lag constants.

Another disadvantage of this approach is the necessity of selecting a model before the start of the analysis and improvement procedure. Moreover, it is rather doubtful that this often simple starting model would be able to indicate where possible improvements should be made. It is therefore preferable to determine the characteristics of an

appropriate model (relevant processes, appropriate scales and accompanying process formulations) beforehand and implement these characteristics into an existing or a new model.

Therefore, the framework will be adapted and improved in order to apply it to a more sophisticated model with which the appropriate model level for the research objective can be determined. The main concepts behind this adapted approach are:

- The criterion for model appropriateness remains the same; i.e. a model is appropriate if its output uncertainty is less than a specified value (G).
- The characteristics of the appropriate model are determined beforehand and can then be implemented into an existing or a new model. First, the dominant climatological processes (section 4.1) and hydrological processes (section 5.2) in a river basin under flooding conditions are determined. Then, appropriate spatial and temporal scales are determined for these dominant processes or associated variables. Several scale issues are therefore described in a more general way (section 2.3) and applied to the climatological processes (remainder of chapter 4) and hydrological processes (section 5.3). Finally, appropriate process formulations dependent on scale are dealt with (section 5.4).
- The resulting appropriate model is then used to assess the model output uncertainty which is compared with G. The output uncertainty is not assessed with the simple method of equation (2.1), because of the non-linearity and interdependence problems. A more elaborate uncertainty analysis method is used, which is chosen from a variety of uncertainty analysis methods (section 2.2).

In this way an internally consistent model is obtained, because the dominant processes are suitably formulated at appropriate scales. However, it depends on the criteria for the appropriateness of scales, the formulations used and the data availability whether the complete model is also appropriate for the research objective. This can be revealed by comparing the output uncertainty with the specific criterion. When comparing the appropriateness framework in this section and the one described in the next chapters, it is found that besides an output uncertainty criterion, an internal consistency criterion is part of the framework. The appropriateness framework will be mainly based on this consistency criterion; the uncertainty criterion will be checked in chapter 6 of this thesis.

2.2 Model uncertainty analysis

2.2.1 Introduction

Uncertainty is a constant companion of scientists and decision-makers involved in climate change and impact research and management. This uncertainty arises from two quite different sources, incomplete knowledge and unknowable knowledge about the future (Hulme and Carter, 1999). Although it is recognised that it is of major concern to treat all uncertainties in climate change impact assessments (e.g. Boorman and Sefton, 1997; Guo and Ying, 1997), a systematic quantification of uncertainties and uncertainty propagation is rarely performed. This has to do among other things with the complex models particularly used in climate change modelling. Uncertainty analysis consists of several, general accepted steps:

- Definition of the main uncertainty sources
- Assessment of additional uncertainty sources due to the mismatch of different process, measurement and model scales
- Estimation of propagation of uncertainty
- Communication of uncertainty

Different scale issues will be considered in section 2.3. Even if the problem of the quantification of uncertainties could be resolved, it would remain to communicate these uncertainties to the decision and policy makers as well as to the general public (Morgan and Henrion, 1990). A detailed discussion about this subject is beyond the scope of this thesis. The two remaining steps will be considered in this section, namely the definition of the main uncertainty sources (2.2.2) and the quantification and propagation of uncertainty (2.2.3).

2.2.2 Sources of uncertainty

The primary sources of uncertainty defined by Morgan and Henrion (1990) are measurement errors, variability and model structure. Measurement errors can have a random nature (imprecision of the instrument) or a systematic nature (e.g. miscalibration). Variability is inherent in all natural processes exhibiting systematic and random variations. The spatial and temporal scales employed are related to this. The model structure introduces additional uncertainties, e.g. by simplifying relations between variables or by leaving out important variables. Another division of uncertainty sources is given by De Blois (2000). He defines model imprecision as the effect of three different sources, namely sources of uncertainty, inaccuracy and incompleteness. Uncertainty is caused by a lack of data or knowledge, or by the natural variability of the model input or model parameters, inaccuracy is caused by errors in the model schematisation and incompleteness is caused by leaving out certain model parts or relations between model parts. Lei and Schilling (1996) distinguish conceptual uncertainty due to incompleteness of the model structure and inaccuracy of the model formulations, parameter uncertainty and input data uncertainty. Numerous other divisions can be found in literature (e.g. Beck, 1987; Melching *et al*., 1990). In principle, it does not matter which division is used, the main point is that all dominant uncertainties are considered when determining the model output uncertainty.

Although some would make a distinction between variability and uncertainty and for example De Blois uses model imprecision, the term uncertainty will be used here to identify all kinds of uncertainty sources and their summation. A slightly modified version of the division of Melching *et al*. (1990) is used and given in Table 2.5. It seems that all divisions are similar and more or less fit in this table. Table 2.5 also shows the relation with the model appropriateness framework through the different components (processes, scales-statistics and formulations). Model parameter uncertainty is not explicitly considered in the framework, but is an artefact of the model formulations and the calibration data used. In the remainder of this section some of most dominant uncertainty sources in climate models and hydrological models are reviewed.

Table 2.5 Different sources of uncertainty and their relation to the model appropriateness framework.

Source	Sub-source	Appropriateness framework
Natural uncertainty	Randomness	Scales
	Scaling issues	Scales
Data uncertainty	Measurement errors	Scales
	Inadequacy of data	Scales
Model parameter uncertainty		Scales/ Formulations
Model structure uncertainty	Model incompleteness	Processes
	Model inaccuracy	Formulations

Climate models

The uncertainty in future climate simulated by climate models is large, in particular for variables such as precipitation. Dickinson (1989) considered four main sources of uncertainty in climate projections: (1) sources of atmospheric composition, (2) aspects of the geochemical cycles of carbon, (3) the calculation of the radiative forcing and (4) the response of the climate system to this forcing. He focused his review on the latter source of uncertainty and identified four uncertainties of main concern: the transient adjustment to changing forcing controlled by ocean heat uptake, the response of cloud radiative properties, the changes in the cover of ice and snow in high latitudes and the shifts in regional climate patterns. These sub-sources seem to be mainly related to the model parameters and structure. The focus on the response of the climate system is quite common in climate change uncertainty analysis. Sources 1, 2 and 3 are often aggregated and represented by scenarios for future radiative forcing (e.g. Carter *et al*., 1999), although strictly speaking these scenarios only represent different emission scenarios The scenarios can then be used as input in global climate models. Additional sources of uncertainty are ‘surprises’ and climate change projections for specific regions. Surprises are rapid, non-linear responses of the climate system to anthropogenic forcing, e.g. reorganisation of the thermohaline circulation (Ganopolski *et al*., 1998) and rapid deglaciation (Oppenheimer, 1998). None of these are explicitly simulated in climate models, nevertheless the conditions for surprises exist (Hulme and Carter, 1999). This accumulation of uncertainty has been described as an uncertainty explosion (Henderson-Sellers, 1993).

Hulme and Carter (1999) consider four sources of uncertainty as well: the global system predictability (future emissions; sources 1, 2 and 3), the climate sensitivity, the climate system predictability and the sub-grid scale climate variability. The second and third source are largely related to model structure and the latter one also refers to scaling issues. The climate sensitivity can be compared with Dickinson’s response of the

climate system. Visser *et al*. (2000) used the integrated assessment model DIALOGUE to analyse the four sources of Dickinson and concluded that the key source of uncertainty in climate change projections is found to be the uncertainty in radiative forcing models (source 3). Including all these sources in the projected range of global warming give ranges beyond those projected by the IPCC (1996) (3.7 °C). Additionally, Jones (2000) came up with an even larger range of regional scenarios.

Hydrological models

The use of rainfall-runoff models to assess the response of a catchment to climate change inevitably introduces additional uncertainties. The division of sources of uncertainty in Table 2.5 applies quite well to hydrological models, as it stems from a framework for the reliability analysis of watershed models (Melching *et al*., 1990). It is common practice in estimating model output uncertainty to presume that model calibration explains all sources of uncertainty. Then, means and variances of the parameters are calculated after calibration with multiple events and then propagated through the model (e.g. Binley and Beven, 1991; Lei and Schilling, 1994). In this way model structure uncertainties are not included and the total uncertainty is underestimated. In particular these model structure uncertainties are difficult to estimate (as for the climate models). They can be assessed for example by model validation and intercomparison (Ye *et al*., 1997), including all kinds of events (dry-wet, smooth-peaky etc.) in the calibration that trigger all relevant processes (Lei and Schilling, 1996) or including besides flux variables also state variables such as groundwater levels in the model calibration and validation (Lamb *et al*., 1999).

2.2.3 Quantification and propagation of uncertainty

Once the main uncertainty sources have been identified, they should be quantified and propagated through the model system to obtain the model output uncertainty. Uncertainty can be quantified through simple ranges (minimum-maximum), statistical moments, quantiles or complete cumulative distribution functions and probability density functions. These statistics and related scale issues will be dealt with in section 2.3. An overview of the commonly employed uncertainty propagation methods will be given below approximately in increasing order of complexity. Applications to climatological or hydrological problems will be simultaneously considered.

The model output Y (random variable) is a function of a n-dimensional independent random vector $\mathbf{X} = (x_1, x_2,\ldots,x_n)$, $Y = f(\mathbf{X})$. The essence of uncertainty propagation analysis is to explore the statistical properties of Y based on the statistical properties of $\mathbf{X}$. Generally, the complete probability density function of Y can not be derived a-priori from the probability density functions of $\mathbf{X}$ (if these are known), however often first and second moments of Y can be obtained from statistical properties of $\mathbf{X}$.

Model validation and intercomparison

Model validation involves comparison of statistics of model output Y_m and observations Y_o. The propagation of input, model and parameter uncertainties is therefore not explicitly taken into account, but only implicitly through the observations. A more thorough validation is achieved by comparing statistics of model input and model variables $\mathbf{X_m}$ with observations $\mathbf{X_o}$ as well. An example is the comparison of modelled and observed groundwater levels in a rainfall-runoff model when only catchment runoff

is of interest. Applications of this type of validation are less frequent, an example being Lamb *et al*. (1999) who used spatially distributed water table observations to constrain uncertainty.

Model intercomparison is similar to model validation and implies comparison of output statistics from model 1 and model 2 (Y_{m1} and Y_{m2}). This should always be accompanied with model validations to see differences with observations. Model validation and intercomparison only give a range of possible model outcomes, but neither give uncertainties in the strict sense as probability distributions nor as standard errors or deviations. Intercomparison is particularly popular in climate modelling and has been done in large projects as AMIP (atmospheric model intercomparison project) (Gates, 1999) and CMIP (coupled model intercomparison project) (Meehl, 2000). The usefulness of these comparisons has to do with the fact that the models are relatively similar and the data, initial and boundary conditions often are prescribed. On the other hand hydrological model intercomparisons often consider completely different model structures and formulations of various complexities (e.g. Loague and Freeze, 1985). It then becomes quite difficult to compare different models and almost impossible to assess uncertainties, because many components are compared at the same time.

Sensitivity and scenario analysis

Sensitivity analysis involves the analysis of the changes in Y due to changes in $\mathbf{X}$. The most common form is univariate sensitivity analysis in which only one component of $\mathbf{X}$ (x_i) at the same time is allowed to vary and the others remain constant (e.g. Mearns *et al*., 1997). This approach is particularly useful for the assessment of the individual role of a component in determining Y. Additionally, information about the importance of the different uncertainty contributions can be obtained. Bivariate sensitivity analysis implies the variation of two components of $\mathbf{X}$ keeping the others at a constant value. This kind of analysis is particularly useful in determining the interdependence between different components. Multivariate sensitivity analysis embraces the exploration of in particular the parameter part of the vector space $\mathbf{X}$ in order to find an optimal set of parameters (e.g. Seibert, 1997). As with model validation and intercomparison, sensitivity analysis gives ranges of model outcomes, but has the advantage of explicitly incorporating the contributions of different uncertainty sources.

Scenario analysis is strongly related to sensitivity analysis and is treated separately because it is the technique mostly used in climate research today. The distinction between these two is more related to how the information is used than to the tools involved. Scenario analysis is intended to be policy relevant and comprises a specific, consistent set of $\mathbf{X}$. Several of these scenarios with many varying components x_i can be used to establish a range of model outputs. The recent IPCC assessment made use of several, strongly differing scenarios to assess a range in future climate (Carter *et al*., 1999).

First-order analysis

First-order analysis is derived from Taylor's linear approximation of Y around the mean of $\mathbf{X}$ $\mu(\mathbf{X})$ in which linear components are truncated

$$(2.9) \qquad Y = f(\mathbf{X}) \cong f[\mu(\mathbf{X})] + \frac{\partial f(\mathbf{X})}{\partial \mathbf{X}}[\mathbf{X} - \mu(\mathbf{X})]$$

and the first and second moments are respectively

$$(2.10) \qquad \mu(Y) \cong f[\mu(\mathbf{X})]$$

$$(2.11) \qquad \sigma^2(Y) \cong \sum_{i=1}^{n}\left[\frac{\partial f(\mathbf{X})}{\partial x_i}\right]^2 \sigma^2(x_i)$$

Equation (2.11) is equal to equation (2.1) which has been used to assess the model output uncertainty in section 2.1. The main advantages of first-order analysis are its simplicity, the partitioning of the model output uncertainty into its various contributions and the two moments of Y expressed as functions of the moments of $\mathbf{X}$. The disadvantages have been discussed in 2.1.5 and were found to be the assumptions of linearity in the region around $\mu(\mathbf{X})$ and the independence of the different components x_i. Hydrological applications of first-order uncertainty analysis are numerous, an example being Melching *et al*. (1990). They applied data, parametric and model structural advanced first-order second moment uncertainty analysis to the HEC-1 rainfall-runoff model. The main conclusion was that the major prediction uncertainty is from rainfall excess estimation. Climatological applications of first-order analysis were not found in literature.

Monte Carlo analysis

Monte-Carlo analysis involves the random sampling of components x_i from the input vector $\mathbf{X}$ and the determination of the model output Y. The quality of the probability distribution of Y obviously depends on the sampling number for which a generally valid value hardly can be given. The use of an efficient sampling technique can restrict the number of simulations needed. An example is Latin Hypercube sampling in which probability distributions of $\mathbf{X}$ are divided into intervals and samples are randomly (standard) or regularly (midpoint) taken from each interval (Morgan and Henrion, 1990). Advantages of the Monte-Carlo analysis are the general applicability for estimation of response statistics of any nonlinear and/or discontinuous model and the possibility to obtain probability distributions of Y given the probability distributions of $\mathbf{X}$. Disadvantages of the Monte-Carlo analysis are the computational demand and the inability to show uncertainty contributions of each component. This latter disadvantage can be partly overcome by applying several techniques such as scatterplots, regression analysis and correlation analysis. Examples of hydrological applications (e.g. Harlin and Kung, 1992; Uhlenbrook *et al*., 1999) can be found more frequently than climatological applications, an exception being a study of Shackley *et al*. (1998) that includes Monte Carlo analysis in modelling the global carbon cycle.

Other analysis methods

Other uncertainty analysis methods include Rosenblueth uncertainty analysis (Binley *et al*., 1991), statistical linearisation (Lei and Schilling, 1994), Bayesian uncertainty analysis (Patwardhan and Small, 1992; Tol and Vos, 1998), response surface methods (Morgan and Henrion, 1990) and stochastic differential equations (Zapert *et al*., 1998).

These methods partly have aspects of the described methods and partly introduce new concepts. They will not be considered here and the uncertainty analysis method to be employed in chapter 4 for the climatological analysis and in chapter 6 for the combined climatological-hydrological analysis will be chosen from the methods described.

Choice of methods

The choice of the uncertainty analysis methods will be based on the following criteria:

- Uncertainty about the model structure; the relative importance of parameter uncertainty vs. model structure uncertainty
- Nature of the model; magnitude of uncertainties and kind of behaviour (e.g. complexity)
- Requirements of the analysis; research purpose and statistical quantity required
- Previous comparisons of uncertainty analysis methods
- Time and computational resources available

The complexity of general circulation models (GCMs) largely determines the choice of a method for the climatological uncertainty analysis. First-order analysis is impossible because of the highly non-linear relations in a GCM and Monte Carlo analysis infeasible due to computational problems. Moreover, the availability of only GCM output restricted the choice to model validation and intercomparison in stead of sensitivity or scenario analysis. This model validation and intercomparison with respect to the most important variables from the hydrological point of view will be performed in chapter 4.

The method for the climatological-hydrological uncertainty analysis is less dependent on the complexity of the (hydrological) model. However, first-order analysis seems to be less appropriate due to some non-linearities such as rainfall infiltration and quick runoff and the interdependence of input and parameters (see section 2.1). Sensitivity analysis and model validation and intercomparison do not seem to be enough in this case, because more than just averages and variances are of importance. An additional (stratified) Monte Carlo analysis should be performed to obtain necessary information about the tails and shape of the probability distribution. Several comparisons between different uncertainty analysis methods and Monte Carlo analysis have been performed (e.g. Garen and Burges, 1981; Melching, 1992; Nandakumar and Mein, 1997). All these comparisons favour application of Monte Carlo techniques as well, but emphasise the disadvantages mentioned (computational burden and inability to show uncertainty contributions). Therefore, a simplified, stratified sampling analysis and an additional sensitivity analysis have been performed.

2.3 Statistics and scales

2.3.1 Spatial and temporal scales

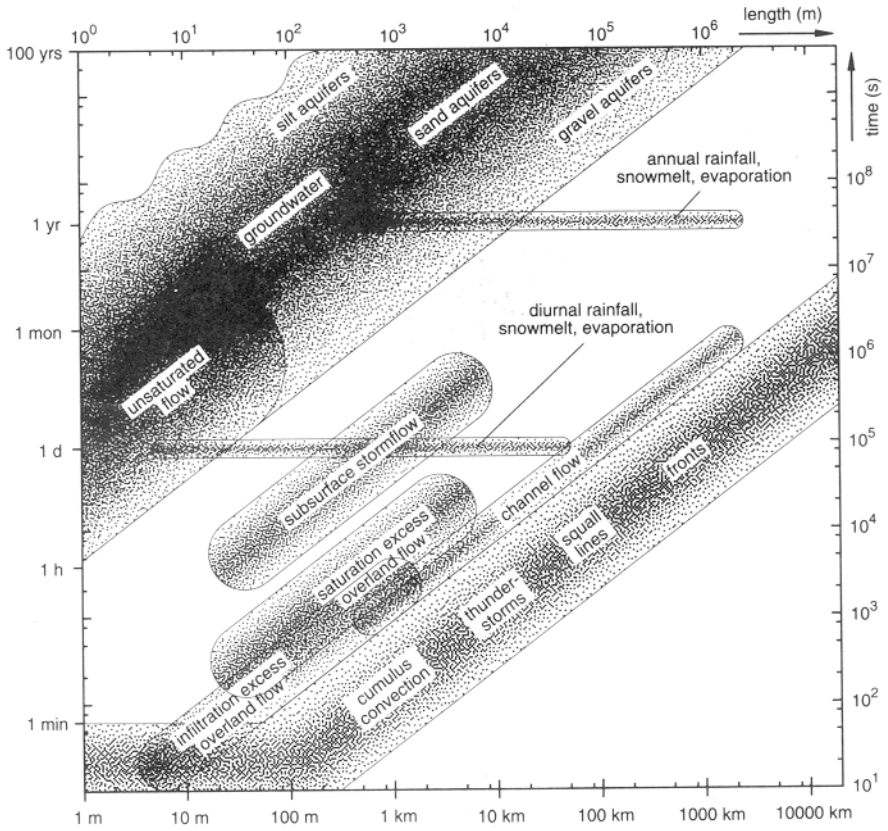

Figure 2.5 Hydrological processes at a range of characteristic space-time scales (Blöschl and Sivapalan, 1995).

Hydrological processes occur at a wide range of scales in space, from unsaturated flow in a 1 m soil profile to floods in river systems of a million square kilometres, and in time, from flash floods of several minutes duration to flow in aquifers over hundreds of years (Blöschl and Sivapalan, 1995). Hydrological processes span about eight orders of magnitude in space and time (Klemeš, 1983). Figure 2.5 shows a classification of hydrological processes according to typical space and time scales. Shaded regions show characteristic space-time combinations of hydrological variability. 'Scale' can refer to natural variability, observations or models in space and time. This process, measurement and modelling scale consists of a scale triplet involving extent, spacing and support (Blöschl and Sivapalan, 1995). 'Extent' refers to the overall coverage, 'spacing' refers to the distance between measurements or model elements and 'support' refers to the integration volume or area. All three components of the scale triplet are needed to uniquely specify the space and time dimensions of a process, measurement or model. The scale triplet is illustrated in Figure 2.6.

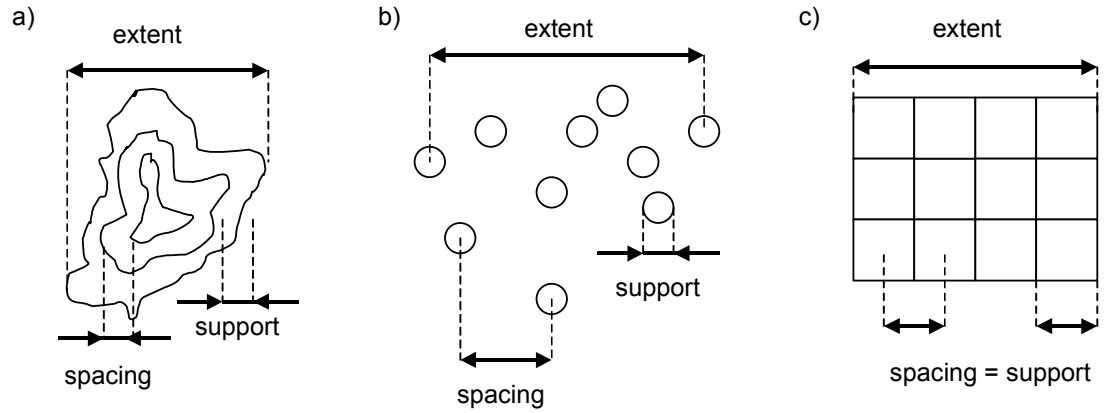

Figure 2.6 Definition of the scale triplet for natural processes (a), measurements (b) and models (c).

Ideally, processes should be measured and modelled at the scale they occur. However, this is not always necessary depending on the problem which has to be solved. It was therefore stated in section 1.3 that appropriate scales should be used in models depending on sensitivities and a right balance between uncertainties of input, model structure and model parameters. Differences between process, measurement and modelling scale will introduce differences between the true (i.e. natural) variability and the variability apparent in the data or the model (Western and Blöschl, 1999). Obviously, also differences between the variability apparent in the data and the models exist. To bridge these gaps 'scaling' is needed, which means that statistical information is transferred from a given scale to a smaller scale (downscaling) or larger scale (upscaling) (Gupta *et al*., 1986). Therefore, in this section important statistics and their dependence on scales are considered. First some definitions are introduced.

Natural, continuous process variables are approximated by means of discrete measured or modelled variables and thus are not assessed directly. For this reason, only statistics and scales with respect to measured and modelled variables are considered. A measured or modelled variable as a function of space and time $x(s,t)$ with $1 \le s \le S$ and $1 \le t \le T$ is defined, where S is the number of locations in the space domain $\mathbf{\Lambda}_d$ [here (Λ_1,Λ_2)] and T the number of time steps in the time domain Ω_d. Then the spatial scales in terms of extent L_e, spacing L_{sp} and support L_{sup} are defined as

$$(2.12) \quad L_e = \sqrt{\mathbf{\Lambda}_d} \qquad L_{sp} = \sqrt{\frac{\mathbf{\Lambda}_d}{\mathrm{S}}} \qquad L_{sup} = \sqrt{\mathbf{\Lambda}} = \Lambda$$

and the temporal scales are defined as

$$(2.13) \quad L_e = \Omega_d \qquad L_{sp} = \frac{\Omega_d}{T} \qquad L_{sup} = \Omega$$

where $\mathbf{\Lambda}$ and Ω are respectively the area and time period over which the measurements or model results are aggregated. It should be noted that in many models $L_{sp} = L_{sup}$. Unless explicitly mentioned, scale will refer to support in this section and is denoted with L (1-dimensional, specific case), Λ (1-dimensional, general case) and $\mathbf{\Lambda}$ (2-dimensional, general case).

2.3.2 Zero-order statistics and scales

Zero-order statistics considered are the probability density function (PDF) and the cumulative distribution function (CDF). These can be determined by plotting ordered values and fitting a function or by fitting a theoretical PDF or CDF with appropriate parameters. The theoretical PDF's and CDF's used in this thesis are described and an introduction to PDF's and CDF's as a function of scale is given.

The exponential PDF and CDF with scale parameter β_e are defined as

$$(2.14) \qquad f(x) = \frac{1}{\beta_e}\exp\left(-\frac{x}{\beta_e}\right) \qquad\qquad F(x) = 1 - \exp\left(-\frac{x}{\beta_e}\right)$$

with its mean and variance respectively β_e and β_e^2. The assumption of x being exponentially distributed is tested with the simple, but powerful probability plot correlation test (Filliben, 1975). This test uses the correlation between ordered values and the corresponding fitted quantiles determined by plotting positions (Probability Plot Correlation Coefficient). PPCC values near 1.0 suggest that the values could have been drawn from the fitted distribution. However, applying the PPCC test statistic to a large number of values would almost always mean a significant rejection of the hypothesis on an irrelevant basis (Albers, pers. comm.) and in that case probability plots should be used (visual inspection). The Gringorten plotting position is used for exponentially distributed values (Gringorten, 1963). Critical values are obtained from D'Agostino and Stephens (1986).

The gamma PDF with shape parameter α_g and scale parameter β_g is defined as

$$(2.15) \qquad f(x) = \left(\frac{x}{\beta_g}\right)^{\alpha_g} \frac{\exp\left(-\frac{x}{\beta_g}\right)}{\beta_g \Gamma(\alpha_g)}$$

with its mean and variance respectively $\alpha_g\beta_g$ and $\alpha_g\beta_g^2$. A closed-form expression for the CDF is not available and tables or approximations must be used. The assumption of x being gamma distributed is tested with the probability plot correlation test as well. A combination of Blom's plotting position (Blom, 1958) and Kirby's (1972) algorithm for the inverse gamma distribution is used for gamma distributed values. Critical values are obtained from Vogel and McMartin (1991, 1992).

The Gumbel PDF and CDF for extreme values with scale parameter β_G and location parameter ξ_G are defined as

$$(2.16) \qquad f(X) = \frac{1}{\beta_G}\exp\left[-\frac{X-\xi_G}{\beta_G} - \exp\left(-\frac{X-\xi_G}{\beta_G}\right)\right]$$

$$F(X) = \exp\left[-\exp\left(-\frac{X-\xi_G}{\beta_G}\right)\right]$$

with its mean and variance respectively $\xi_G+\eta\beta_G$ and $\pi^2\beta_G^2/6$ and $\eta \approx 0.5772$. The assumption of X being Gumbel distributed is again tested with the probability plot correlation test. The Gringorten plotting position is used for Gumbel distributed values. Critical values are obtained from Maidment (1993).

Aggregation generally decreases variability and therefore changes the probability distribution. More values around the mean will be found instead of values at the lower and upper tail of the distribution. This effect is qualitatively illustrated in Figure 2.7.

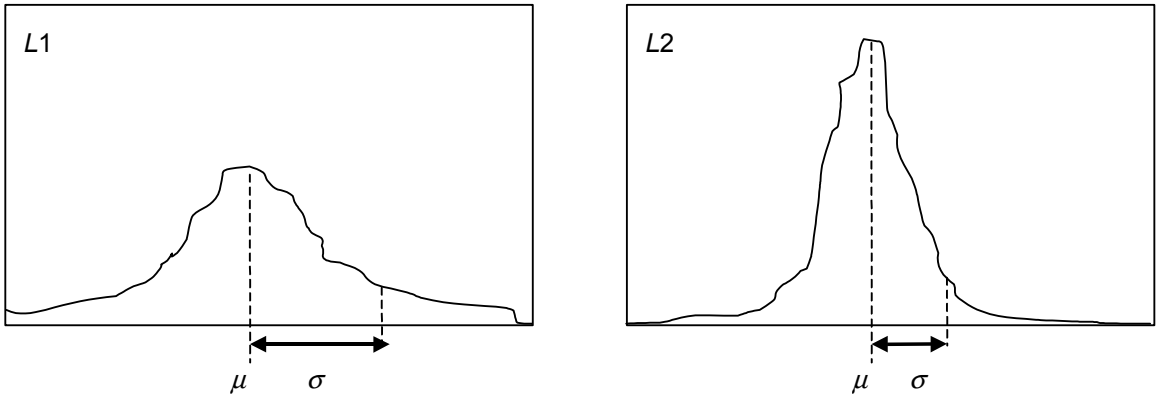

Figure 2.7 Probability density function for scale $L1$ and scale $L2 > L1$ with mean μ and standard deviation σ.

2.3.3 First-order statistics and scales

First-order statistics considered are the mean and the conditional and unconditional probabilities for different variable states. Additionally, these statistics as a function of scale will be considered.

The mean in space $\mu_{\Lambda}(t)$, time $\mu_{\Omega}(s)$ and space-time $\mu_{\Lambda\Omega}$ are estimated as

$$\mu_{\Lambda}(t)=\frac{\sum_{s=1}^{S} x(s,t)}{S} \qquad \mu_{\Omega}(s)=\frac{\sum_{t=1}^{T} x(s,t)}{T} \tag{2.17}$$

$$\mu_{\Lambda\Omega}=\frac{\sum_{t=1}^{T}\sum_{s=1}^{S} x(s,t)}{ST}$$

These definitions automatically enable comparison between different space and time scales.

A state i of $x(s,t)$ is defined in the time domain as $x_{i-1} < x(s,t) \le x_i$. Consider N different states $\{i = 1,\ldots, N\}$, then the unconditional probability $p_i(s)$ is defined as the number of states i divided by the total number of states $\{i = 1,\ldots, N\}$

$$p_i(s) = \frac{\sum_{t=1}^{T}(x_{i-1} < x(s,t) \le x_i)}{T} \tag{2.18}$$

Equation (2.18) can be applied to the average of S point time series $\mu_{\mathbf{\Lambda}}(t)$ and a spatially aggregated time series $x(\mathbf{\Lambda},t)$ to enable comparison between space scale $L1<\mathbf{\Lambda}$ and $L2=\mathbf{\Lambda}$.

When only a few point time series within area $\mathbf{\Lambda}$ are available, the average points unconditional probability $\mu_{\mathbf{\Lambda}}(t)$ can be determined for two different states in another way as well. The methodology used is described in detail by Osborn and Hulme (1997) for the comparison of station (point) and modelled (spatially averaged) precipitation. They introduced a new statistic between two point time series at distance h as the probability that both points are in state i=1 (dry) at time t given that at least one is in state i=1 at time t

$$u(s,h) = \frac{\sum_{t=1}^{T}\left(x(s,t) \le x_1 \cap x(s+h,t) \le x_1\right)}{\sum_{t=1}^{T}\left(x(s,t) \le x_1 \cup x(s+h,t) \le x_1\right)} \tag{2.19}$$

This statistic between one point and every other point is plotted against h and a decay function can be fitted to the results

$$\upsilon(s,h) = \left(\frac{1}{\upsilon_1(s)} + \frac{h}{\upsilon_2(s)}\right)^{-1} \tag{2.20}$$

The goodness-of-fit is tested by a similar correlation coefficient as used for the distribution functions, i.e. the correlation between $1/u(s,h)$ and h (PPCC*). The values of υ_1 and υ_2 in space $\mathbf{\Lambda}$ are averaged and equation (2.20) can be integrated over $\mathbf{\Lambda}$ to produce a mean statistic $\overline{\upsilon}$

$$\overline{\upsilon} = \int_0^{|\Lambda|} \upsilon(h) f(h)\, dh \tag{2.21}$$

where $|\Lambda|$ represents the maximum distance within $\mathbf{\Lambda}$ and $f(h)$ is the PDF of the random variable h representing the distance between any two points randomly chosen. Assuming a square area $\mathbf{\Lambda}$ with sides $a=\Lambda_1=\Lambda_2$ the PDF is as follows (Ghosh, 1951)

$$f(h) = \frac{4h}{a^4}\phi(h) \tag{2.22}$$

where

$$\phi(h) = \frac{1}{2}\pi a^2 - 2ah + \frac{1}{2}h^2 \qquad 0 < h < a$$

$$\phi(h) = a^2\left(\sin^{-1}\frac{a}{h} - \cos^{-1}\frac{a}{h}\right) + 2a\sqrt{h^2 - a^2} - \frac{1}{2}\left(h^2 + 2a^2\right) \qquad a < h < |\Lambda|$$

This PDF for a square will be used here for simplicity, although some model grid boxes are not completely square. Osborn and Hulme related $\overline{\upsilon}$ to $p_1(\mathbf{\Lambda})$ (spatially averaged) divided by the average $p_1(s)$ (point) through a linear function (which seems to be plausible, since for $0.3 < \overline{\upsilon} < 1.0$ the function is rather linear)

$$p_1(\mathbf{\Lambda}) = \frac{\sum_{s=1}^{S} p_1(s)}{S}\left(\beta_1 + \beta_2 \overline{\upsilon}\right) = \frac{\sum_{s=1}^{S} p_1(s)}{S} R_1 \tag{2.23}$$

in which β_1 and β_2 are two parameters dependent on S and R_1 is a reduction factor. Osborn and Hulme determined β_1 and β_2 for up to $S = 15$ precipitation stations in a grid box and used these values as an estimate of grid box means $p_1(\mathbf{\Lambda})$, because they did not expect much change in the parameters with increasing S. The parameters were determined with data from three different regions; Europe, China and Zimbabwe and can be found in Osborn and Hulme. Given the strength of the correlation found in (2.23), the similarity of the datasets and the range of precipitation regimes covered by the combined datasets ($\overline{\upsilon}$ varied from 0.25 to 0.98), the parameters derived are likely to be generally applicable. The derived state i=1-probabilities easily reveal the associated state i=2-probabilities when two states are considered. The reduction factor R_1 as a function of the dimensionless scale a/υ_2 is given in Figure 2.8 for $\upsilon_1 = 0.85$.

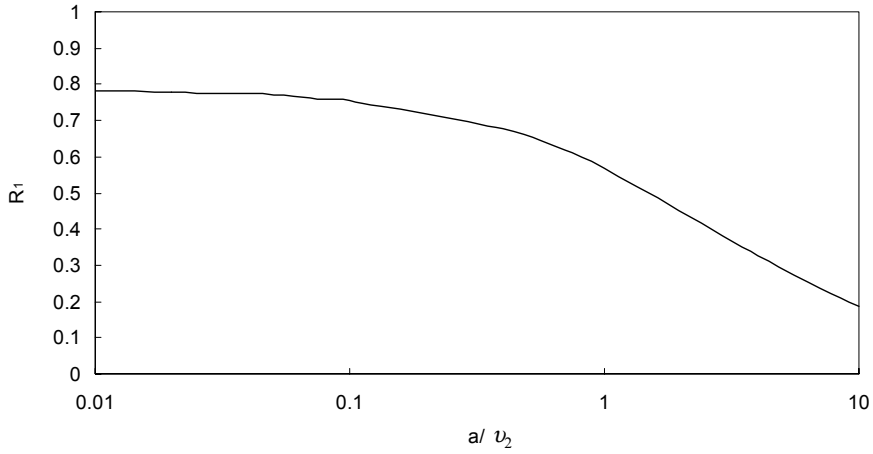

Figure 2.8 Reduction factor R_1 as a function of the dimensionless scale a/υ_2 for $\upsilon_1 = 0.85$.

Consider N different states $\{i = 1,\ldots, N\}$ at time $t = t$ and N different states $\{j = 1,\ldots, N\}$ at time $t = t$-1, then the conditional probability $p_{ij}(s)$ is estimated as

$$p_{ij}(s) = \frac{\sum_{t=1}^{T} (x_{i-1} < x(s,t) \le x_i \mid x_{j-1} < x(s,t-1) \le x_j)}{T} \tag{2.24}$$

In this way an NxN state transition matrix can be composed. As before, equation (2.24) can be applied to an average points time series $\mu_{\mathbf{\Lambda}}(t)$ and a spatially averaged time series $x(\mathbf{\Lambda},t)$ to enable comparison between space scale $L1<\mathbf{\Lambda}$ and $L2=\mathbf{\Lambda}$.

2.3.4 Second-order statistics and scales

Second-order statistics considered are the variance, the correlation and the semi-variance. Also, their relation with scales will be discussed.

The variance in space $\sigma_{\mathbf{\Lambda}}(t)$ and time $\sigma_{\Omega}(s)$ are estimated as

$$\sigma_{\Lambda}^{2}(t)=\frac{\sum_{s=1}^{S}[x(s,t)-\mu_{\Lambda}(t)]^{2}}{S-1} \qquad \sigma_{\Omega}^{2}(s)=\frac{\sum_{t=1}^{T}[x(s,t)-\mu_{\Omega}(s)]^{2}}{T-1} \tag{2.25}$$

Because more frequently used, the variance in time will be considered in the remainder of this chapter and for convenience the subscript Ω will be omitted.

Equation (2.25) can be applied to an average points time series $\mu_{\mathbf{\Lambda}}(t)$ and a spatially averaged time series $x(\mathbf{\Lambda},t)$ to enable comparison between space scale $L1<\mathbf{\Lambda}$ and $L2=\mathbf{\Lambda}$. The variance of the spatially averaged time series (apparent variance) is more directly related to the average point variance (true variance) as follows

$$\sigma^{2}(\mathbf{\Lambda})=\frac{\sum_{s=1}^{S}\sigma^{2}(s)}{S}\kappa^{2} \tag{2.26}$$

The variance reduction factor κ^2 decreases with increasing $\mathbf{\Lambda}$. The magnitude of this factor depends on the spatial correlation structure of the variable and the size and shape of the area. Rodriguez-Iturbe and Mejia (1974) showed for a stationary isotropic spatial random field that κ^2 is the expected value of the correlation coefficient ρ between any two points randomly chosen at distance h

$$\kappa^{2}=\int_{0}^{|\Lambda|}\rho(h)f(h)\,dh \tag{2.27}$$

where $|\Lambda|$ represents the maximum distance within $\mathbf{\Lambda}$ and $f(h)$ is the PDF of the random variable h from (2.22). For large S, the variance of the average points time series is approximately equal to the variance derived with (2.26) as can be shown by the following formula (after Yevjevich, 1972)

$$\sigma^{2}(\mu_{\Lambda})=\frac{\sum_{s=1}^{S}\sigma^{2}(s)}{S}\left(\frac{1+(S-1)\overline{\rho}}{S}\right) \tag{2.28}$$

where $\overline{\rho}=\kappa^2$. Using (2.27) and an exponential correlation function, κ^2 is given as a function of the dimensionless scale a/λ in Figure 2.9 (λ is the correlation length). For every point s the spatial correlation length $\lambda(s)$ can be determined by fitting the exponential correlation function to all correlation coefficients vs. distance for point s. The λ to be used in (2.27) is the average of all $\lambda(s)$'s in space $\mathbf{\Lambda}$ (Osborn and Hulme, 1997). Obviously, other correlation functions can be used as well.

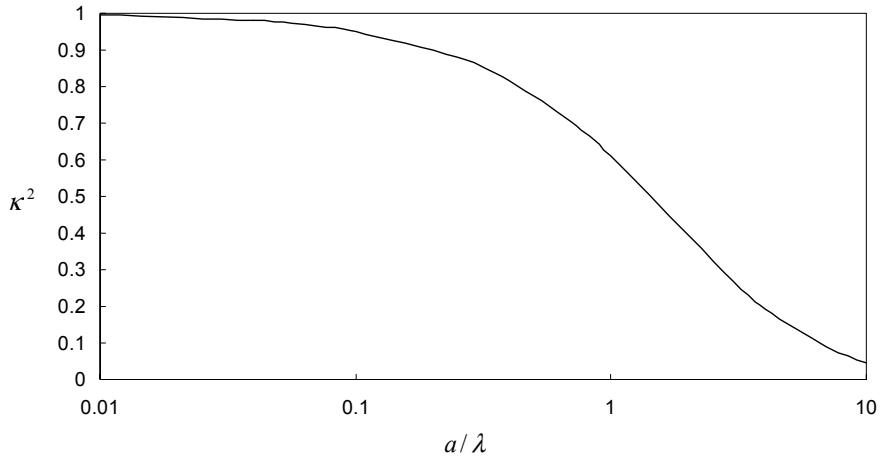

Figure 2.9 Variance reduction factor κ^2 as a function of the dimensionless scale a/λ.

In this way, the apparent variance due to aggregating over support scale $L_{sup} = \Lambda = a$ can be directly obtained from the true variance. The apparent variance due to spacing (L_{sp}) is equal to the true variance, because this variance can be interpreted as the variance of n point samples which is close to the population variance provided n is not too small (Matalas, 1967). Finally, the apparent variance of a process with the extent limited to a square of side length $L_e = a$ is the variance within the square (Western and Blöschl, 1999)

$$\sigma^2\left(L_e = a\right) = \frac{\sum_{s=1}^{S}\sigma^2(s)}{S}\left(1-\kappa^2\right) \tag{2.29}$$

The effect of support and extent on apparent variance is illustrated in Figure 2.10. It can be derived from this figure that the support scale should be sufficiently small (e.g. 20 % of the correlation length if a bias of 10 % in estimating the true variance is permitted) and the extent should be sufficiently large (more than 5 times the correlation length) when estimating the true variance.

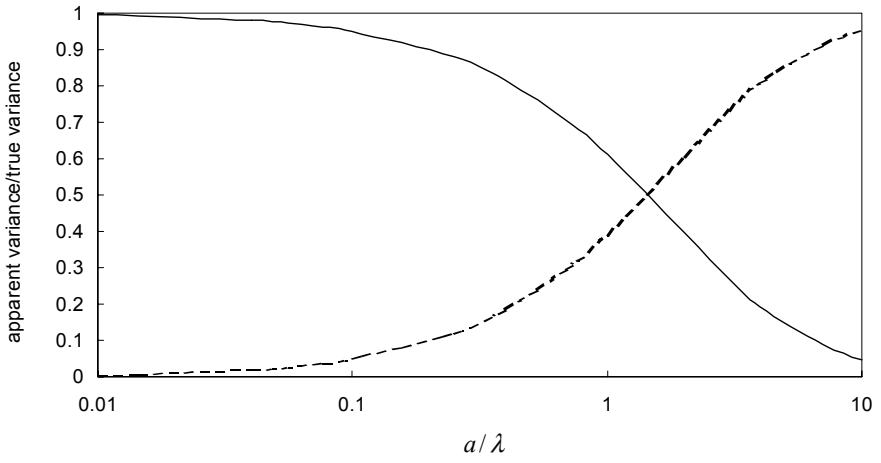

Figure 2.10 Effect of the measurement or modelling scale in terms of support (solid line) and extent (dotted line) on the apparent variance.

The lag h spatial correlation coefficient $r(h)$ and the lag k temporal correlation coefficient $r(k)$ are respectively estimated as

$$r(s,h) = \frac{\frac{1}{T}\sum_{t=1}^{T}[x(s,t)-\mu(s)][x(s+h,t)-\mu(s+h)]}{\sigma(s)\,\sigma(s+h)} \tag{2.30}$$

$$r(s,k) = \frac{\frac{1}{T}\sum_{t=1}^{T-k}[x(s,t)-\mu(s)][x(s,t+k)-\mu(s)]}{\sigma^2(s)} \tag{2.31}$$

Both coefficients are in the time domain and for convenience the subscripts have been omitted. These correlation coefficients can be approximated by exponential functions

$$\rho(s,h) = \alpha_1(s)\exp\left(-\frac{h}{\lambda(s)}\right) \tag{2.32}$$

$$\rho(s,k) = \alpha_2(s)\exp\left(-\frac{k}{\tau(s)}\right) \tag{2.33}$$

where α_1 and α_2 are constants representing the nugget effect or the microvariability at a scale smaller than the separation distance (either space or time) between the closest measurement points. Variables λ and τ are respectively the spatial and temporal correlation lengths

$$\lambda(s) = \int_0^\infty \rho(s,h)\,dh \qquad\qquad \tau(s) = \int_0^\infty \rho(s,k)\,dk \tag{2.34}$$

These lengths should not be confused with the commonly used range; i.e. the distance where ρ falls to 0.05 (see section 2.1, $L_S \approx 3\lambda$ or $T_S \approx 3\tau$). The exponential behaviour of the correlation functions (2.32) and (2.33) is tested by a similar correlation coefficient as used before; i.e. the correlation between minus the logarithm of correlation and distance PPCC*.

The spatial and temporal variability can be described by the semi-variance as well. This quantity is estimated by

$$g(s,h) = \frac{1}{2T}\sum_{t=1}^{T}[x(s,t)-x(s+h,t)]^2 \tag{2.35}$$

$$g(s,k) = \frac{1}{2T}\sum_{t=1}^{T-k}[x(s,t)-x(s,t+k)]^2 \tag{2.36}$$

These semi-variances can be approximated by exponential functions (see e.g. Kitanidis, 1997). A slightly modified version of the exponential model from geostatistical theory is

$$(2.37)\quad \gamma(s,h) = \sigma^2(s)\left[1-\rho(s,h)\right] \qquad \text{or} \qquad \gamma(s,h) = \sigma^2(s)\left[1-\alpha_1(s)\exp\left(-\frac{h}{\lambda(s)}\right)\right]$$

$$(2.38)\quad \gamma(s,k) = \sigma^2(s)\left[1-\rho(s,k)\right] \qquad \text{or} \qquad \gamma(s,k) = \sigma^2(s)\left[1-\alpha_2(s)\exp\left(-\frac{k}{\tau(s)}\right)\right]$$

The estimated semivariances can be plotted against separation distance (h or k) to obtain the experimental variogram. The parameters in (2.32) approximating (2.30) should agree with the parameters in (2.37) approximating (2.35) and so on. Actually, the variogram is a way of representing the spatial and temporal variability in another way. A variogram can give insight in the spatial and temporal ranges and the variance contributions from several sources (nugget, spatial and temporal). Their relative importance can be examined by combining the spatial and temporal variogram into a spatio-temporal one as has been done in equation (2.2)

The above mentioned statistics apply to numerical variables, but can not be used for categorical variables such as land use. These variables are time invariant in this research and therefore the spatial variability of these variables is described by defining a so-called semi-correlation r^* as

$$(2.39)\quad r^*(h,m) = \frac{\sum_{s=1}^{S}\left[\frac{x_m(s+h)}{\sum_{n=1}^{M}x_n(s+h)}\right]}{S}$$

where m is a specific category of $x(s)$ resulting in $x_m(s)$, n is an arbitrary category of $x(s)$ and M is the total number of categories. For each category m, the semi-correlation r^* can be plotted as a function of the separation distance h to obtain a semi-correlogram from which the spatial correlation length for each category can be estimated (as described for continuous variables).

Relationships for apparent correlation lengths and apparent variograms due to support, spacing and extent scale are not considered here and can be found in Western and Blöschl (1999).

2.3.5 Higher-order statistics and scales

'Higher'-order statistics considered are the T-year return values $RV(T)$. These are estimated as follows

$$(2.40)\quad RV(T) = \mu_G + K_G(T)\sigma_G$$

where μ_G and σ_G are the mean and standard deviation derived from the Gumbel parameters (see 2.3.2) and $K_G(T)$ is the frequency factor

$$(2.41)\quad K_G(T) = -\frac{\sqrt{6}}{\pi}\left[\eta + \ln\ln\left(\frac{T}{T-1}\right)\right]$$

The standard error $SE(T)$ in determining $RV(T)$ is (Shaw, 1994)

$$(2.42) \qquad SE(T) = \sqrt{\frac{{\sigma_G}^2}{N}\left(1 + 1.14\,K_G(T) + 1.1\,K_G(T)^2\right)}$$

Then, lower and upper confidence limits can be calculated for a specific $RV(T)$

$$(2.43) \qquad RV(T) \pm t_{\alpha,N-1} SE(T)$$

where $t_{\alpha, N\text{-}1}$ are values of the Student t-distribution with α the probability limit required, N the available sample of years and N-1 degrees of freedom.

Equation (2.40) can be applied to an average points time series $\mu_{\mathbf{\Lambda}}(t)$ and a spatially averaged time series $x(\mathbf{\Lambda},t)$ to enable comparison between space scale L1<$\mathbf{\Lambda}$ and L2=$\mathbf{\Lambda}$. The spatially averaged return values are more directly related to the average point return values through expressions relating the parameters of the Gumbel distribution (β_G and ξ_G) for point and spatially averaged extreme values. Sivapalan and Blöschl (1998) have derived these expressions with respect to precipitation for different durations.

The main assumption is that non-zero point values $x(s,t)$ stem from an exponential distribution, non-zero spatially averaged values $x(\mathbf{\Lambda},t)$ stem from a gamma distribution (see e.g. Sivapalan *et al.*, 1990) and point and spatially averaged extreme values (e.g. annual maxima) X stem from a Gumbel distribution. Here, the relations for different durations have been modified to obtain expressions for one duration (daily time step)

$$(2.44) \qquad \beta_G(\mathbf{\Lambda}) = \frac{\sum_{s=1}^{S} \beta_G(s)}{S} \frac{\kappa^2}{f_1(\kappa^{-2})}$$

$$(2.45) \qquad \xi_G(\mathbf{\Lambda}) = \frac{\sum_{s=1}^{S} \xi_G(s)}{S} \kappa^2 f_2(\kappa^{-2})$$

where

$$f_1(\kappa^{-2}) = 1 - 0.17 \ln\left(\kappa^{-2}\right) \qquad\qquad f_2(\kappa^{-2}) = 0.39 + 0.61\left(\kappa^{-2}\right)^{0.8}$$

In this way, generalised Gumbel parameters as a function of correlation structure and area (through κ^2) are obtained and can be compared with corresponding parameters obtained from the 'direct averaging' approach. The areally averaged return value RV_A relative to the point return value RV_p is shown as a function of the dimensionless aggregation scale a/λ in Figure 2.11.

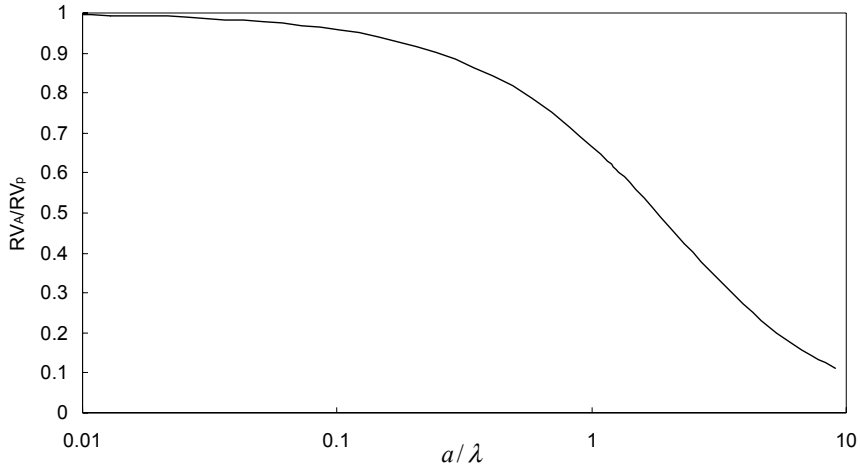

Figure 2.11 Return value reduction factor RV_A / RV_p as a function of the dimensionless scale a/λ.

Sivapalan and Blöschl (1998) used the correlation structure of complete precipitation fields in their precipitation extreme value analysis, assuming that the correlation structure of precipitation does not change with return period. However, extreme precipitation fields generally exhibit more spatial variability and consequently λ will be smaller. This results in a larger reduction of extreme precipitation values with increasing area. Therefore, λ's determined from extreme precipitation fields should be used as opposed to the approach of Sivapalan and Blöschl who used complete precipitation fields. This is achieved by analysing annual maximum precipitation fields. These fields are defined as the spatially varying precipitation fields associated with the annual maximum of precipitation averaged over the whole field. The spatial variability of an annual maximum precipitation field can be characterised by a variogram [see equation (2.37)] and λ for a specific annual maximum precipitation field can be determined. The λ averaged over the available sample of years is then used in equation (2.27) and subsequently in equations (2.44) and (2.45).

2.3.6 Statistics and appropriate scales

The statistics vs. scale relations for wet day frequency and variance have been checked by Osborn and Hulme (1997) and those for extreme values have been verified by Sivaplan and Blöschl (1998). These theoretical relations agreed reasonably with the observations at different scales. Therefore, the statistic-scale relations and an accompanying permitted bias from the true statistic can be used to determine the appropriate scale for a statistic. This is illustrated in Figure 2.12, where an example of the reduction of an arbitrary statistic as a function of dimensionless aggregation scale (a/λ) is shown. The dotted line illustrates the determination of the appropriate scale assuming a permitted bias of 10 %. Similar figures can be constructed for all reduction functions considered, although some differences exist between for example reduction functions for variance and return values (dimensionless appropriate scale respectively 0.25 and 0.21 for a 10 % bias). It depends on the variable of interest which statistic is important and thus which dimensionless appropriate scale applies.

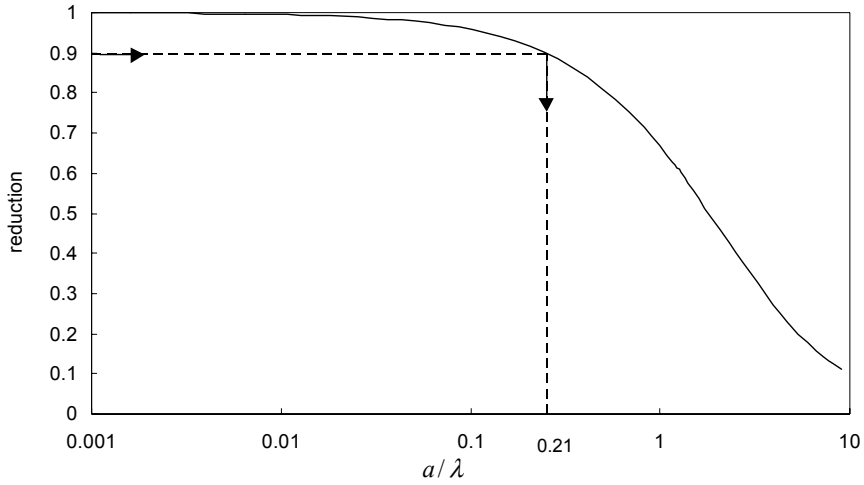

Figure 2.12 Assessment of statistic at appropriate scale by means of reduction function.

2.3.7 Integration of appropriate scales

The appropriate scales for each key variable and process should be combined to derive an appropriate river basin model scale. For variables and processes with smaller appropriate scales than this appropriate model scale, distribution functions may be used to solve the sub-grid scale variability or values and processes may be simply averaged. For variables and processes with less variability, constant values may be used over several appropriate model scales. The integration of separate appropriate variable and process scales towards an appropriate model scale will be considered by means of relations between key variable scales and the output variable. The relative importance of the separate appropriate variable and process scales is dependent on the sensitivity of the model output to changes in these scales. This sensitivity can be assessed by means of a sensitivity analysis, however when no specific model is available another method should be employed. The SCS method (see e.g. Maidment, 1993) is used for this purpose, because an approximate estimation is required and the model output of interest is the peak discharge.

The peak discharge q_p in the SCS method is derived from a triangular approximation to the hydrograph shown in Figure 2.13 resulting from a rainfall excess intensity p_e of duration T_p (and volume $P_e = p_e T_p$). The lag T_l from the centroid of rainfall excess to the peak and the time of rise T_q to the peak are illustrated as well. The base length of the hydrograph 2.67 T_q is based on the study of many unit hydrographs (Maidment, 1993) The volume of runoff under the hydrograph V_p is derived with the basic SCS relationship

$$(2.46) \qquad V_p = \frac{\left[25.4P_e - 5.08f(\mathrm{CN})\right]^2}{25.4P_e + 20.3f(\mathrm{CN})} \qquad \text{with } f(\mathrm{CN}) = \frac{1000}{\mathrm{CN}} - 10$$

where V_p and P_e are in mm and CN is the well-known curve number dependent on soil type, land use type and hydrologic condition of the land surface. CN values can be found in extensive tables (e.g. Maidment, 1993) and vary between 20 and 100. Equating

the volume V_p to the volume ½ q_p 2.67 T_q in Figure 2.13, rearranging and adjusting for units gives q_p in m^3s^{-1}

$$q_p = \frac{5.28\,AV_p}{0.5T_p + T_l} \tag{2.47}$$

where A is the catchment area in km^2, T_p is in hours and T_l is in hours as follows (Kent, 1972)

$$T_l = \frac{l^{0.8}\left[1 + f(\mathrm{CN})\right]^{0.7}}{3.42\,S_0^{\,0.5}} \tag{2.48}$$

where l is the hydraulic length of the catchment in km and S_O is the overland slope in parts per 10000.

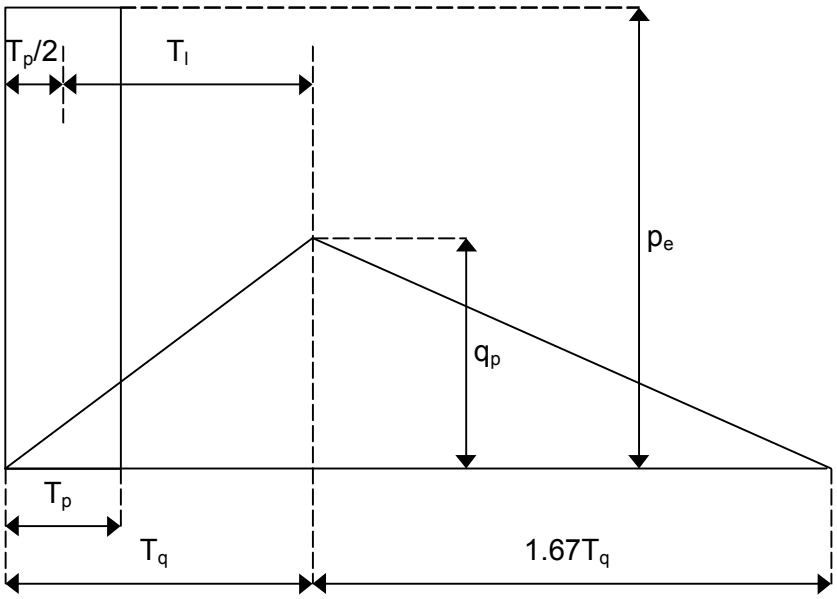

Figure 2.13 SCS triangular hydrograph.

The sensitivity of the peak discharge to changes in variable scales is assessed by introducing variable-scale relationships into equation (2.47) instead of the constant variables such as P_e, CN and S_0. For example if CN and S_0 are used as indicators for respectively soil type/ land use and topography, CN-scale/ S_0-scale relations can be incorporated into (2.47). A precipitation-scale relation can be directly implemented into equation (2.46). In this way, relationships between the key variable scale and the output variable are established. These relationships are used to assess the weights associated with an appropriate process or variable scale. The weights are multiplied with the appropriate scales to obtain the appropriate model scale. The results of this assessment will be discussed in chapter 4 and 5.

2.4 Summary and conclusions

A preliminary appropriateness framework has been described and was found to be inadequate, because of the simplified assumptions done and the necessity of selecting a model before the start of the procedure. Therefore, a more general model appropriateness framework has been introduced implying the determination of the dominant processes and variables, the appropriate scales and the associated appropriate process formulations. In this way, the characteristics of an appropriate model are determined beforehand and can be implemented in an existing or new model. So, an internally consistent model is obtained, although it depends on the criteria for the appropriateness of scales, the formulations used and the data availability whether the complete model is appropriate for the research objective. This can be revealed by comparing the output uncertainty of the appropriate model with a specific uncertainty criterion. The appropriateness framework is thus mainly based on a consistency criterion with an additional uncertainty criterion.

The key uncertainty source in climate change projections is the uncertainty in radiative forcing models. The input and parametric uncertainty are sources mainly accounted for in hydrological uncertainty analyses, although model structure uncertainty can be a considerable source as well. Several uncertainty propagation methods can be applied to climate and hydrological models. A model validation and intercomparison will be done for climate models and a simplified Monte Carlo analysis with an additional sensitivity analysis will be performed for the hydrological model.

A methodology has been described to assess the appropriate scale for a particular variable. This appropriate scale is assumed to be equal to a fraction of the correlation length of that variable. The fraction is determined on the basis of relationships between statistics and scale accepting an error in the estimation of the statistic of 10 %. This results in fractions of the correlation length between 0.20 and 0.25 for different statistics such as the standard deviation and the return value. The integration of these appropriate variable scales to an appropriate model scale is done by multiplying the appropriate variable scales with associated weights. The weights are based on SCS curve number method relationships between the peak discharge and some specific parameters. The values of these parameters are dependent on the scale of each variable and in this way, relations between the peak discharge and the variable scale are developed. Finally, the weights are determined and multiplied with the appropriate variable scale to obtain the appropriate model scale.

Chapter 3

Rainfall and basin model scale effects

3.1 Introduction

In chapter 2 the appropriateness framework was introduced. It roughly consists of three components: the assessment of dominant processes, the determination of appropriate scales and the evaluation of accompanying process descriptions. The issue of appropriate scales has been generally described in section 2.3. In this chapter, the effect of different spatial and temporal scales (resolutions) on the response of the Meuse basin will be studied. The resolutions of interest are those associated with the rainfall input and the river basin model itself.

The effect of the rainfall input resolution on catchment response has been considered in several studies, although it is difficult to separate errors associated with rainfall input from model errors (Shah *et al*., 1996a). The effect of the spatial rainfall input resolution on the response of small catchments has been investigated using either observed rainfall (e.g. Dawdy and Bergmann, 1969; Obled *et al*., 1994; Lopes, 1996) or stochastic rainfall models (e.g. Wilson *et al*., 1979; Krajewski *et al*., 1991; Shah *et al*., 1996a). The spatial rainfall variability was found to be of substantial importance. The effect of the temporal rainfall input resolution on catchment response has been found to be more important than the effect of the spatial resolution (see Krajewski *et al*., 1991), although the former is much less frequently studied. These effects are hardly examined for large basins, although the rainfall pattern is known to be potentially important in these large basins (Obled *et al*., 1994).

The effect of the spatial and temporal catchment model resolution on catchment response has been examined by comparing output from models differing in complexity (e.g. Loague and Freeze, 1985; Krajewski *et al*., 1991; Shah *et al*., 1996a). This way of examination not only assesses the effect of different model resolutions, but also considers the effect of different parameterisations and processes incorporated. This indicates a need to assess the effect of only (coupled) spatial and temporal model resolution on catchment response, in particular for large basins, with unchanged parameterisations and processes incorporated.

Therefore, in this chapter the effect of coupled spatial and temporal catchment model resolution and spatial and temporal rainfall input resolution on the response of the Meuse is assessed using data of the right order of magnitude [see also the studies of Wilson *et al*. (1979) and Krajewski *et al*. (1991)]. Obviously, the response of particular interest is the extreme river discharge. The objective is achieved by developing a simple stochastic rainfall model and using the river basin model briefly mentioned in section

---

The main part of this chapter has been published as:

Booij, M.J., 2002a. Modelling the effect of spatial and temporal rainfall and catchment model resolution on extreme river discharg *Hydrolog. Sci. J*., **47** (2).

2.1 with uniform parameters in space and spatially and temporally varying rainfall input (section 3.2). Numerical simulation is used here, because of the non-linear nature of the rainfall formulation and the future possibility to include non-linear processes in the river basin model. Models with varying resolutions are used to assess the resolution effect on extreme river discharge. The validity of the results has been examined through a sensitivity analysis with the most important parameters of the river basin model (section 3.3). The results are discussed in section 3.4. They may give some indication on the appropriate input and model resolution for a similar river basin with a similar rainfall regime. This may give some support when an appropriate model for the determination of extreme discharges of a large river basin with climate change has to be chosen.

3.2 Description and application of models

3.2.1 Stochastic rainfall model

Sophisticated stochastic rainfall models have been developed (e.g. Bras and Rodriguez-Iturbe, 1976; Waymire *et al*., 1984; Shah *et al*., 1996b). The simple stochastic rainfall model used here is a slightly modified random phase model (Cacko *et al*., 1988), because it incorporates the spatial and temporal correlation of observed precipitation to generate spatially and temporally varying rainfall series. This has been done in a similar way by for example Bras and Rodriguez-Iturbe (1976). The model assumptions are:

- The rainfall process is a stationary one, i.e. its statistics do not change with time.
- The rainfall process has a uniform character, i.e. its statistics do not vary in space.
- There is correlation in time and space between rainfall amounts.
- Time and space correlation are not independent; there is one correlation function describing both time and space characteristics.

This latter assumption makes the difference between the AR(1) model used in section 2.1 and the random phase model used here. It was considered to be necessary to incorporate this additional characteristic into this new rainfall model. However, the model is assumed to represent measured rainfall sequences and therefore does not have a coupled spatial and temporal resolution unlike the river basin model, i.e. measured rainfall can have an hourly or daily time step and can be point (gauge) or areally averaged (radar).

The starting point for the rainfall model formulation is an assumed rainfall correlation function ρ for spatial lag h_x, h_y (in hundreds of km's) and temporal lag k (in days)

$$\rho(h_x, h_y, k) = a_1 \exp\left(-b_1 h_x^{\,2} - b_2 h_y^{\,2} - b_3 k^2\right) \tag{3.1}$$

where a_1, b_1, b_2 and b_3 are parameters dependent on the observed rainfall in the area of interest. This correlation function needs to be transformed to its spectral form as a function of frequency φ, κ, and ω in order to use it in the random phase model

$$\rho(\varphi, \kappa, \omega) = \frac{1}{2\pi} \int_{-\infty}^{\infty} \int_{-\infty}^{\infty} \int_{-\infty}^{\infty} \rho(h_x, h_y, k) \exp\left(-i\varphi h_x - i\kappa h_y - i\omega k\right) dh_x\, dh_y\, dk \tag{3.2}$$

This power spectral density of the rainfall correlation function implemented in the random phase model is used to generate spatially and temporally correlated rainfall P_C [1] at location x, y on time t

$$(3.3) \qquad P_C(x,y,t) = \sqrt{2}\int_{-\infty}^{\infty}\int_{-\infty}^{\infty}\int_{-\infty}^{\infty}\left\{\rho(\varphi,\kappa,\omega)^{1/2}\cos(\varphi x+\kappa y+\omega t+\varsigma)\right\}d\varphi\, d\kappa\, d\omega$$

where ζ is a random variable uniformly distributed in the interval $\{0,2\pi\}$. The discretised form of equation (3.3) at location x, y on time t used in the simulation is

$$(3.4) \qquad P_D(x,y,t) = \sqrt{2}\sum_{i=1}^{I}\sum_{j=1}^{J}\sum_{k=1}^{K}\left\{\left[(\varphi_i,\kappa_j,\omega_k)\right]^{1/2}\cdot\Delta\varphi\cdot\Delta\kappa\cdot\Delta\omega \cos(\varphi_i' x+\kappa_j' y+\omega_k' t+\zeta_{i,j,k})\right\}$$

Here φ_i, κ_j, ω_k are representative frequencies; $\Delta\varphi$, $\Delta\kappa$, $\Delta\omega$ are respectively the equidistant intervals $|\varphi_i-\varphi_{i-1}|$, $|\kappa_j-\kappa_{j-1}|$, $|\omega_k-\omega_{k-1}|$; φ_i', κ_j', ω_k' equal $\varphi_i+\Delta\varphi_i$, $\kappa_j+\Delta\kappa_j$, $\omega_k+\Delta\omega_k$ and $\zeta_{i,j,k}$ are independent, random variables uniformly distributed in the interval $\{0,2\pi\}$. The $\Delta\varphi_i$, $\Delta\kappa_j$, $\Delta\omega_k$ are small random frequency increments uniformly distributed in the intervals $\{-\Delta\varphi/2,\ \Delta\varphi/2\}$, $\{-\Delta\kappa/2,\ \Delta\kappa/2\}$, $\{-\Delta\omega/2,\ \Delta\omega/2\}$ introduced to avoid periodicity of the simulated process. This Gaussian rainfall field sequence P_D has been modified to simulate besides a correct spatial and temporal correlation structure according to equation (3.1) also a correct mean rainfall and percentage of rainy days (when $P_D(x, y, t) > 0$). This modified (non-Gaussian) rainfall P_{XY} [L^3T^{-1}] at location x, y on time t becomes

$$(3.5) \qquad \begin{aligned} P_{XY}(x,y,t) &= \left[P_D(x,y,t)+d_1\right]d_2 && P_D(x,y,t)+d_1 > 0 \\ P_{XY}(x,y,t) &= 0 && P_D(x,y,t)+d_1 \le 0 \end{aligned}$$

where the parameters d_1 [1] and d_2 [L^3T^{-1}] are obtained using observed rainfall. The discretised form of (3.5) for cell i, j with spatial dimension Δx on time t with time step Δt is

$$(3.6) \qquad P(i,j,t) = P_{XY}(\Delta x[2i-1], \Delta x[2j-1], t)$$

The rainfall model is applied to the Meuse basin upstream of Borgharen which has a surface area A of about 21 10^3 km^2. Its parameter values have been obtained by means of available data. The values for parameters a_1, b_1 and b_2 have been obtained by approximating the spatial daily rainfall correlation function from Stol (1972), who studied the relationship between spatial correlation of rainfall and distance in the eastern part of the Netherlands. The value for b_3 has been chosen such that the lag-one-day correlation coefficient is properly simulated. A sufficient number ($I \cdot J \cdot K \approx 5000$) of representative combinations of frequencies φ_i, κ_j, ω_k on intervals $\Delta\varphi$, $\Delta\kappa$, $\Delta\omega$ have been used. The parameter values for d_1 and d_2 are based on data from Berger (1992). Parameter d_2 is based on the mean areal precipitation in the Meuse area over the three wettest months with a reference period of at least 20 years, because the focus is on extreme discharges occurring mainly during these wet months. The parameter values were taken from these studies for convenience and are assumed to be adequate taken into account the research objective. They are summarised in Table 3.1. Although these

parameter values have been determined from daily data, the rainfall model can be used at smaller time steps as well due to the continuous temporal correlation function in equation (3.1).

Table 3.1 Estimated parameter values for the rainfall model.

Parameter	Value	Parameter	Value
a_1 (-)	1.0	d_1 (-)	-3.0
b_1 (km^{-2})	4.0 10^{-1}	d_2 (m^3 s^{-1})	1.2 10^2
b_2 (km^{-2})	4.0 10^{-1}	A (km^2)	2.12 10^4
b_3 (day^{-2})	1.6		

As an example an observed (from 1994) and generated daily rainfall sequence for an arbitrary cell $P(i, j, t)$ scaled with respect to their mean values are shown in Figure 3.1. The generated sequence has realistic statistical characteristics with differences between observed and simulated mean, percentage of rainy days and spatial and temporal correlation of respectively –8 %, 11 %, -17 % and –10 %. This sequence can be used here, since the objective was not to model a particular rainfall pattern in detail, but rather to simulate an adjustable, realistic process.

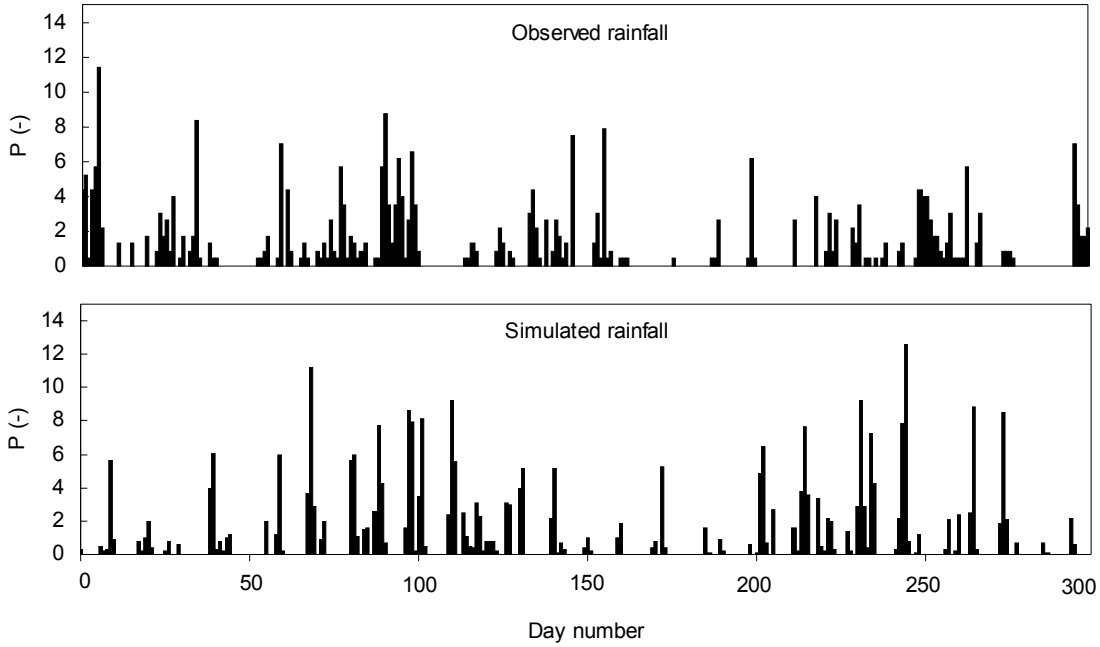

Figure 3.1 Daily observed rainfall in 1994 (NOAA, 1999) and simulated rainfall for an arbitrary cell scaled with respect to their mean values P (-) as a function of day number.

3.2.2 River basin model

Model structure and assumptions

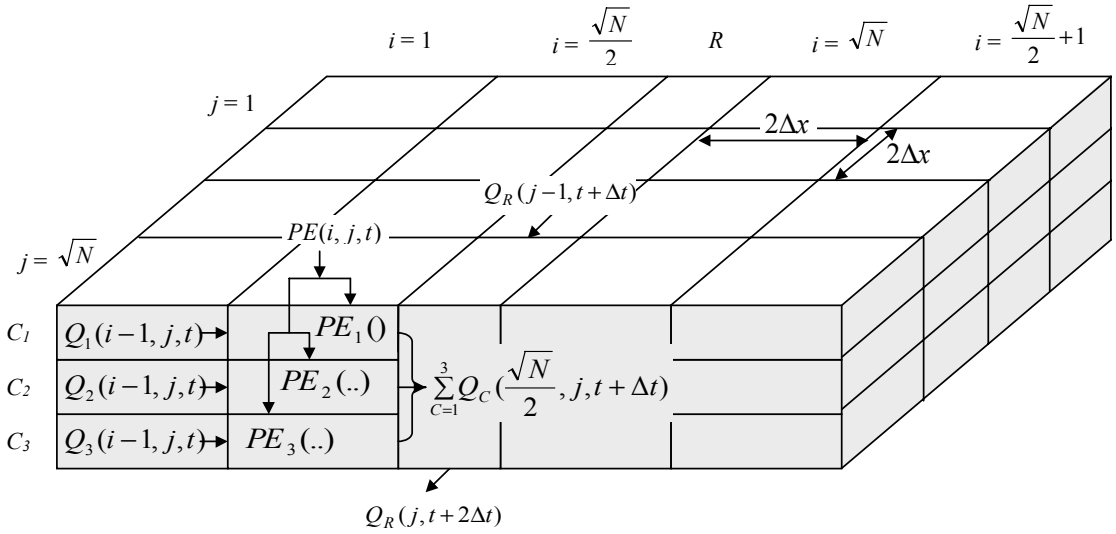

Figure 3.2 River basin model with basin cell position expressed in i and j, river cell position (R) expressed in j, cell dimensions expressed in Δx and water balance components illustrated for an arbitrary basin and river cell (extension of Figure 2.3).

The river basin model is briefly described and used in the preliminary model appropriateness procedure in section 2.1. A more comprehensive overview will be given here. The river basin model has a variable coupled spatial and temporal resolution and uniform parameterisations. The model structure for $N = 16$ catchment cells is illustrated in Figure 3.2. This structure can easily be applied to other resolutions (other N's) as well as the water balance components can be defined for other catchment and river cells than the example cells in the figure. The model structure shows that each catchment cell in strip j receives effective precipitation (PE) and discharges this precipitation to the adjacent cell in strip j in the river direction. The catchment cell that borders a river cell discharges into this river cell in strip j, from this river cell the water is transported further to the river cell in strip j+1 and finally to the outflow point; out of the river cell in strip $j = \sqrt{N}$. The water balance components in Figure 3.2 are the following

$PE(i, j, t)$ = effective rainfall for catchment cell i, j at time t [L^3T^{-1}]

$PE_{C_m}(i, j, t) = p_{C_m}(i, j, t)\, PE(i, j, t)$ = effective rainfall for reservoir C_m of catchment cell i, j at time t [L^3T^{-1}]

$p_{C_m}(i, j, t)$ = part of effective rainfall for reservoir C_m of catchment cell i, j at time t [1]

$Q_{C_m}(i, j, t)$ = discharge out of reservoir C_m of catchment cell i, j into catchment cell i+1, j at time t [L^3T^{-1}]

$Q_R(j, t)$ = discharge out of river cell j into river cell j+1 at time t [L^3T^{-1}]

Effective rainfall PE (i, j, t) is only received by catchment cells, so it is assumed that the input to the river cells is negligible. It is obtained from equation (3.6) as follows

(3.7) $$PE(i, j, t) = P(i, j, t)\, rc$$

Runoff coefficient *rc* is the ratio of observed river basin discharge $q(t)$ and observed areal rainfall $p_A(t)$. In this way a constant fraction of the rainfall is assumed to be subject to loss processes such as evapotranspiration and groundwater leakage. The discharge Q [L^3T^{-1}] at time t is defined as the output from a linear reservoir with capacity V [L^3] on time $(t-\Delta t)$ with lag constant k [T^{-1}]

$$Q(t) = k\,V(t-\Delta t) \tag{3.8}$$

The number of reservoirs of the catchment cell and the river cell has been determined through the existence of characteristic velocities associated with hydrological processes. A characteristic velocity v_c [LT^{-1}] is derived from the existence of an approximately constant ratio between length and time scale of each hydrological process (see Figure 2.5; Blöschl and Sivapalan, 1995). According to these characteristic velocities, a catchment cell can reasonably be divided into three reservoirs and a river cell can consist of only one reservoir. The three catchment cell reservoirs represent saturation and infiltration excess overland flow (m = 1), subsurface stormflow (m = 2) and groundwater flow (m = 3). Each of these reservoirs has its own characteristic velocity and reservoir capacity [compare with respectively lag constant k and reservoir capacity V in equation (3.8)].

These principles will be used to describe the water movement by means of a water balance for the catchment cells and the river cells in a dimensionless form in order to reduce the number of parameters. After that, the formulation of the initial conditions and the water distribution functions $p_{C_m}(i,j,t)$ will follow. Finally, the described model will be applied to the Meuse basin.

Mathematical formulation

The water balance expressed in water depth h [L] (= V/A) for reservoir C_m of catchment cell i,j on time t during time step Δt becomes

$$\begin{aligned} h_{C_m}(i,j,t) - h_{C_m}(i,j,t-\Delta t) = &- k_{C_m}\Delta t\; h_{C_m}(i,j,t-\Delta t) + p_{C_m}(i,j,t)\frac{PE(i,j,t)}{F_C}\Delta t \\ &+ k_{C_m} h_{C_m}(i-1,j,t-\Delta t)\,\Delta t \end{aligned} \tag{3.9}$$

where

$$F_C = [2\Delta x]^2 = \frac{A}{N} = \text{surface area of the catchment cell} \qquad [L^2]$$

The left-hand side of (3.9) represents the storage change, the first term on the right-hand side is the discharge out of the reservoir, the second term reflects the rainfall input and the third term represents input from the same reservoir of the cell upstream of the considered catchment cell. The third term does not apply to catchment cell i = 1 and/or i = $\sqrt{N}/2+1$ (see Figure 3.2). Note that $V_{(C_m)}$ from equation (3.8) is equal to $F_C h_{C_m}$. The total discharge from the adjacent catchment cells Q_C [L^3T^{-1}] into a river cell j on time t is

$$(3.10) \quad Q_C(j,t) = \sum_{m=1}^{3} \left\{ k_{C_m} F_C \left[h_{C_m}(\sqrt{N}/2, j, t-\Delta t) + h_{C_m}(\sqrt{N}, j, t-\Delta t) \right] \right\}$$

The water balance expressed in water depth h [L] for the single reservoir R of river cell j on time t during time step Δt becomes

$$(3.11) \quad \begin{aligned} h_R(j,t) - h_R(j,t-\Delta t) = -k_R \Delta t\, h_R(j,t-\Delta t) + \frac{Q_C(j,t)}{F_R} \Delta t \\ + k_R h_R(j-1,t-\Delta t)\, \Delta t \end{aligned}$$

where

$$F_R = 2\Delta x \cdot 2\Delta x \sqrt{N} = \frac{A}{\sqrt{N}} = \text{surface area of the river cell} \qquad [\mathrm{L}^2]$$

The left-hand side of (3.11) represents the storage change, the first term on the right-hand side is the discharge out of the reservoir, the second term reflects input from the adjacent catchment cells and the third term represents input from the cell upstream of the considered river cell. The third term does not apply to cell $j = 1$ (see Figure 3.2). The discharge of reservoir R Q_R [$\mathrm{L^3T^{-1}}$] in river cell $j = \sqrt{N}$ (at the outflow point) on time t can be written as

$$(3.12) \quad Q_R(\sqrt{N}, t) = k_R F_R h_R(\sqrt{N}, t-\Delta t)$$

Equations (3.9), (3.10), (3.11) and (3.12) describing the water movement in a river basin are made dimensionless by introducing the following dimensionless variables and parameters

$$\Delta x' = \frac{\Delta x}{\lambda} \qquad \Delta t' = \frac{\Delta t}{\tau}$$

$$h' = \frac{F h}{\mu \tau} \qquad k' = k \Delta t$$

$$K_m = \frac{k_{C_m}}{k_R} = \frac{k_{C_m}'}{k_R'} \qquad PE' = \frac{PE}{\mu}$$

$$Q' = \frac{Q}{\mu}$$

Here, λ and τ are respectively the spatial correlation length [L] and the temporal correlation length [T] of rainfall in the examined catchment area and μ is the mean effective rainfall averaged in space and time $\overline{PE(i,j,t)}$ [$\mathrm{L^3T^{-1}}$] equal to the mean discharge at the outflow point averaged in time $\overline{Q_R(j_{\max},t)}$ [$\mathrm{L^3T^{-1}}$]. The three dimensionless parameters K_1 K_2 and K_3 are defined with respect to reservoir R having the largest characteristic velocity $v_{c,R}$. This largest characteristic velocity and the given

spatial dimension Δx determine the temporal dimension (time step) Δt, because $\Delta t = \Delta x/v_{c,R}$ and thus Δx' and Δt' are coupled as well. The dimensionless equations become respectively

$$h_{C_m}'(i,j,t) = h_{C_m}'(i,j,t-\Delta t)\left[1-K_m'k_R'\right] + p_{C_m}(i,j,t)\,PE'(i,j,t)\Delta t' + K_m k_R' h_{C_m}'(i-1,j,t-\Delta t) \tag{3.13}$$

$$Q_C'(j,t) = \sum_{m=1}^{3}\left\{\frac{K_m k_R'}{\Delta t'}\left[h_{C_m}'(\sqrt{N}/2,j,t-\Delta t) + h_{C_m}'(\sqrt{N},j,t-\Delta t)\right]\right\} \tag{3.14}$$

$$h_R'(j,t) = h_R'(j,t-\Delta t)\left(1-k_R'\right) + Q_C'(j,t)\Delta t' + k_R' h_R'(j-1,t-\Delta t) \tag{3.15}$$

$$Q_R'(\sqrt{N},t) = \frac{k_R'}{\Delta t'} h_R'(\sqrt{N},t-\Delta t) \tag{3.16}$$

Initial conditions and water distribution functions

The initial state of the system is assumed to be the equilibrium state, implying uniform (independent of i and j) and stationary (independent of t) initial conditions. This means that on time $t = 0$ the total effective rainfall equals the total catchment discharge which in turn equals the river discharge at the outflow point

$$\sum_{i=1}^{\sqrt{N}}\sum_{j=1}^{\sqrt{N}} PE'(i,j,0) = \sum_{j=1}^{\sqrt{N}} Q_C'(j,0) = Q_R'(\sqrt{N},0) = 1$$

This leads with Figure 3.2 and equations (3.14) and (3.16) to

$$\sum_{m=1}^{3} p_{C_m}(i,j,0) = \min\left\{2\sqrt{N},N\right\}\sum_{m=1}^{3}\left\{\frac{K_m k_R'}{\Delta t'} h_{C_m}'(\sqrt{N},j,0)\right\} = \frac{k_R'}{\Delta t'} h_R'(\sqrt{N},0) = 1$$

The values of the parameters in this equation have been determined, except for the initial dimensionless water depths, so that expressions are obtained for these latter parameters. The values of the parameters $p_{Cm}(i, j, 0)$ and K_m are chosen in the calibration. The parameter $k_R' = 0.5$, because the definition of Δx prescribes that during time step Δt half of the river reservoir R, having the largest characteristic velocity $v_{c,R}$, is discharged to the reservoir R downstream. The initial dimensionless water depth of each catchment reservoir in cell $i, j = \sqrt{N}/2, j$ and cell $i, j = \sqrt{N}, j$ and of the river reservoir in cell $j = \sqrt{N}$ for a specific N (Δx' and Δt') then becomes

$$h_{C_m}'(\frac{\sqrt{N}}{2},j,0) = h_{C_m}'(\sqrt{N},j,0) = \frac{2\,p_{C_m}(i,j,0)\,\Delta t'}{\min\left\{2\sqrt{N},N\right\}K_m}$$

$$h_R'(\sqrt{N},0) = 2\Delta t'$$

The initial dimensionless water depth of each catchment reservoir in cell i, j and of the river reservoir in cell j are (see Figure 3.2)

$$h_{C_m}'(i,j,0) = W(i) h_{C_m}'(\sqrt{N},j,0) \quad W(i) = \frac{i}{\max\left\{\frac{\sqrt{N}}{2},1\right\}} \qquad 1 \le i \le \max\left\{\frac{\sqrt{N}}{2},1\right\}$$

$$W(i) = \frac{i - \frac{\sqrt{N}}{2}}{\max\left\{\frac{\sqrt{N}}{2},1\right\}} \qquad \frac{\sqrt{N}}{2} < i \le \sqrt{N} \qquad N > 1$$

$$h_R'(j,0) = \frac{j}{\sqrt{N}} h_R'(\sqrt{N},0) \qquad N > 1$$

The water distribution functions $p_{Cm}(i, j, t)$ can be defined with chosen parameters and the following assumptions:

- The more reservoir C_2 and C_3 are saturated (expressed in dimensionless water depth) the more water will flow into reservoir C_1 and C_2 respectively.
- The varying dimensionless water depth as a result of different N's and/or a different location in the catchment cascade (i) has to be scaled to its original value (on which basis the distribution functions are defined) by an appropriate scaling constant.
- The sum of $p_{C1}(i, j, t)$, $p_{C2}(i, j, t)$ and $p_{C3}(i, j, t)$ should be equal to 1.
- At $t = 0$ part $p_{Cm}(i, j, 0)$ should flow into C_m.

The distribution functions then become

$$p_{C_1}(i,j,t) = \frac{h_{C_2}'(i,j,t-\Delta t)\, k_R' K_2}{p_{C_2}(i,j,0)}\, p_{C_1}(i,j,0)\, \frac{\min\left\{2\sqrt{N},N\right\}}{\Delta t' W(i)} \tag{3.17}$$

$$p_{C_2}(i,j,t) = \frac{\left[1 - p_{C_1}(i,j,t)\right]}{\left[p_{C_2}(i,j,0) + p_{C_3}(i,j,0)\right]} \frac{h_{C_3}'(i,j,t-\Delta t)\, k_R' K_3}{p_{C_3}(i,j,0)} \\ p_{C_2}(i,j,0)\, \frac{\min\left\{2\sqrt{N},N\right\}}{\Delta t' W(i)} \tag{3.18}$$

$$p_{C_3}(i,j,t) = 1 - p_{C_1}(i,j,t) - p_{C_2}(i,j,t) \tag{3.19}$$

Application to the Meuse basin

The uniform parameter values for the river basin model have been estimated by using one extreme rainfall-runoff sequence for the Meuse basin. It is assumed that this sequence is representative for extreme sequences in the Meuse basin in general. Although extreme sequences may change due to for example climate change, this probably will not seriously influence resolution effects. The sequence used is the daily areal rainfall p_A-daily Borgharen discharge q series from 10 December 1993 through 10 January 1994 (Weijers and Vellinga, 1995) as shown in Figure 3.3. The areal rainfall has been obtained by arithmetically averaging 20 point rainfall sequences.

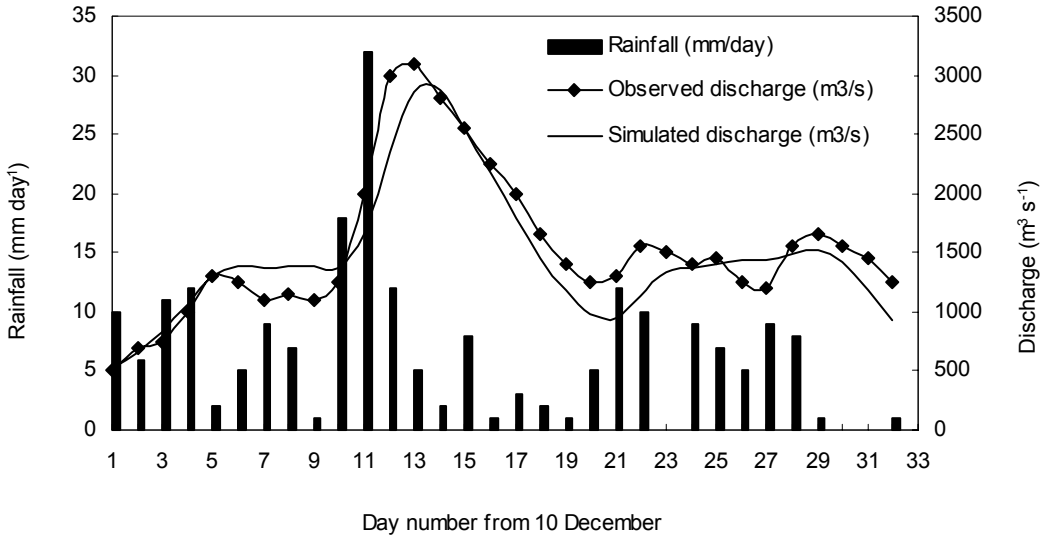

Figure 3.3 Observed daily areal rainfall (mm day^{-1}), observed daily Borgharen discharge (m^3 s^{-1}) and simulated 3-hour Borgharen discharge (m^3 s^{-1}) as a function of day number.

In order to reproduce extreme events, the constant runoff coefficient rc has been determined from this observed extreme sequence. The parameter μ is equal to the observed discharge q averaged over the December-January period. The spatial and temporal correlation lengths have been determined using the correlation function of equation (3.1) with chosen parameter values. The characteristic velocity of reservoir R (river flow) has been taken from Blöschl and Sivapalan (1995). The values of the remaining five parameters have been chosen in such a way that the observed sequence is simulated in a reasonable way and the values for K_m are in the range of values given by Blöschl and Sivapalan (1995). This parameter estimation has been done for the river basin model with the highest resolution, i.e. smallest coupled Δx' and Δt'. The simulated discharge ($Q'\mu$) using the calibrated parameter set and the observed rainfall is shown in Figure 3.3 as well. The model efficiency coefficient (Nash and Sutcliffe, 1970) for this simulation is around 0.80, which is reasonable. A value of 1 would have implied a perfect correspondence between observed and simulated discharge. The parameter values are summarised in Table 3.2.

Table 3.2 Estimated parameter values for the river basin model.

Parameter	Value	Parameter	Value
rc (-)	$9.3\ 10^{-1}$	K_1 (-)	$2.7\ 10^{-1}$
μ ($m^3\ s^{-1}$)	$7.5\ 10^{2}$	K_2 (-)	$2.5\ 10^{-2}$
λ (km)	$1.4\ 10^{2}$	K_3 (-)	$1.0\ 10^{-4}$
τ (day)	1.0	$p_1(i, j, 0)$ (-)	$5.0\ 10^{-1}$
$v_{c,R}$ ($m\ s^{-1}$)	1.0	$p_2(i, j, 0)$ (-)	$4.9\ 10^{-1}$

3.3 Assessment of resolution effect using the rainfall and river basin model

The rainfall model and the river basin model are used to assess the effect of coupled spatial and temporal river basin model resolutions and spatial and temporal rainfall input resolutions on extreme river basin discharge. This has been done by simulating the discharge with the river basin model using one year of generated rainfall as input and varying successively the river basin model and rainfall input resolutions. In the following, the spatial (Δx') and temporal (Δt') resolution for the river basin model (B) and rainfall input (R) are respectively Δx_B', Δt_B', Δx_R' and Δt_R'.

Different coupled Δx_B's and Δt_B's are created keeping in mind the magnitude of the surface area A and the method of catchment cell subdivision. Different Δx_R's are obtained by using different numbers of cells from the generated rainfall field as rainfall input as illustrated in Figure 3.4. Different Δt_R's are obtained by summing generated rainfall over different time lengths. The values used for these resolutions will be determined below.

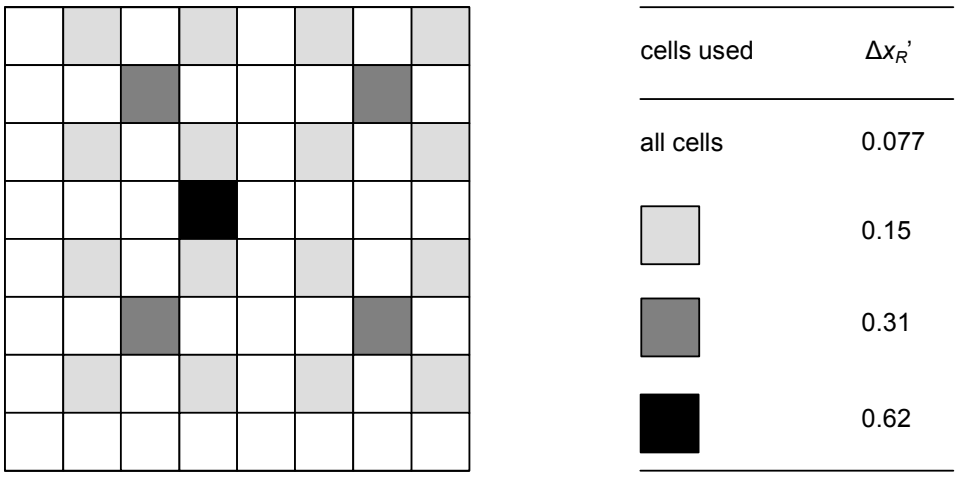

Figure 3.4 Characterisation of the spatial rainfall input resolution Δx_R' by means of the cells used from the generated rainfall field as rainfall input.

The smallest Δx_R' (resolution of generated rainfall) is the currently available spatial resolution in regional climate models (about 20 km, see for example Christensen *et al.*, 1997), because at this resolution rainfall with climate change directly is available. The smallest Δx_B' has been chosen to be equal to this smallest Δx_R'. Other combinations of

Δx_B's and coupled Δt_B's are obtained by choosing N = 1, 4, 16 and 64. These four different spatial and temporal resolutions are used for respectively Δx_R' and Δt_R' as well. The combinations of these different resolutions simulated are given in Table 3.3. Notice in this table that it is not necessary to run the model with Δt_R'<Δt_B', because different rainfall amounts within a river basin model time step are simply aggregated.

Table 3.3 Simulated combinations (X) of river basin model and rainfall input resolution. Δx_B' and Δx_R' has been scaled with λ = 140 km and Δt_B' and Δt_R' with τ = 1 day (see Table 3.2). The grid point distance is $2\Delta x_B$' or $2\Delta x_R$'.

River basin model resolution		Rainfall input resolution				
Spatial (Δx_B')	Temporal (Δt_B')	Temporal (Δt_R')	Spatial (Δx_R')			
			0.077	0.15	0.31	0.62
0.077	0.125	0.125	X	X	X	X
		0.25	X	X	X	X
		0.5	X	X	X	X
		1	X	X	X (*C*)	X
0.15	0.25	0.25	X	X	X	X
		0.5	X	X	X	X
		1	X	X	X (*B*)	X
0.31	0.5	0.5	X	X	X	X
		1	X	X	X	X
0.62	1	1	X	X	X (*A*,*C*)	X

(*A*, *B*): combinations used in sensitivity analysis
(*C*): combinations used in Figure 3.5

The validity of the results has been examined by assessing the sensitivity of the extreme discharge to the five parameters K_1, K_2, K_3, $p_{C1}(i,j,0)$, $p_{C2}(i,j,0)$ of the river basin model. This sensitivity analysis implies varying the parameter values one at a time. The most important parameters are determined by varying K_1, K_2 and K_3 with ± 50 % of their calibrated value and $p_{C1}(i,j,0)$, $p_{C2}(i,j,0)$ with about ± 20 % of their calibrated value for combination *A* in Table 3.3. The effect of these most important parameters on the discharge will be investigated in more detail for combination *B* in Table 3.3.

3.4 Results and discussion

The objectives in this chapter were to assess the effect of coupled spatial and temporal river basin model resolution and spatial and temporal rainfall input resolution on extreme river basin discharge represented by the maximum discharge and to assess the validity of the results through a sensitivity analysis. The results of these assessments will successively be considered below. First, an example of two simulated discharge sequences is treated.

These two sequences are the simulated dimensionless discharge Q' as a function of the day number for the lowest and the highest river basin model resolution as shown in Figure 3.5 (see combination *C* in Table 3.3). As expected, the differences between the hydrographs are considerable. The variability of $Q'(t)$ simulated with the smallest model resolution is much smaller than the variability of $Q'(t)$ simulated with the highest resolution (about factor 2 smaller) and the difference between corresponding maximum dimensionless discharges is considerable as well. This difference in variability is caused by the way water is distributed within the river basin (small time lag *vs*. large time lag).

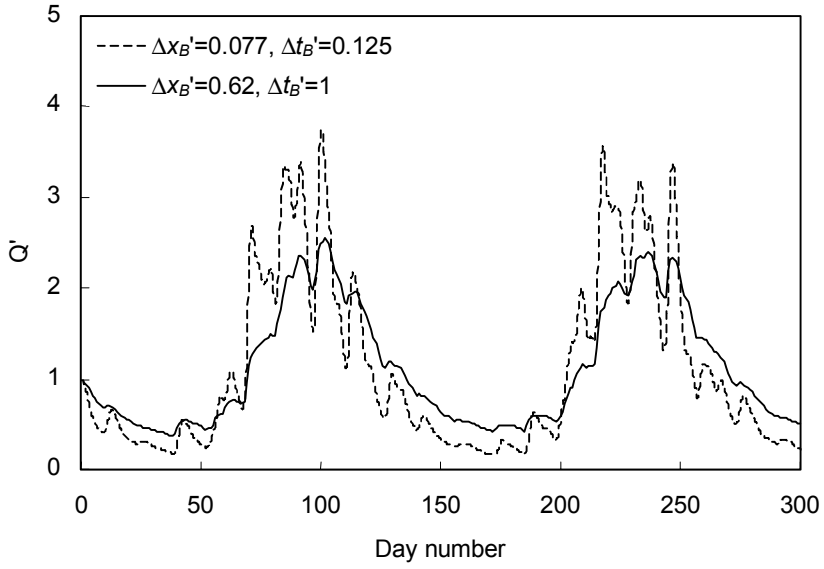

Figure 3.5 Dimensionless discharge Q' as a function of day number for lowest (Δx_B' = 0.62, Δt_B' = 1) and highest (Δx_B' = 0.077, Δt_B' = 0.125) basin model resolution (*C* in Table 3.3).

The effect of the river basin model resolution (Δx_B' and Δt_B'), spatial rainfall input resolution (Δx_R') and temporal rainfall input resolution (Δt_R') on the maximum dimensionless discharge during the simulation period $Q'_{\max}$ is shown in respectively Figure 3.6, Figure 3.7 and Figure 3.8 and will be discussed in 3.4.1, 3.4.2 and 3.4.3. The overall effect of resolutions and the sensitivity analysis is considered in 3.4.4.

3.4.1 Effect of river basin model resolution

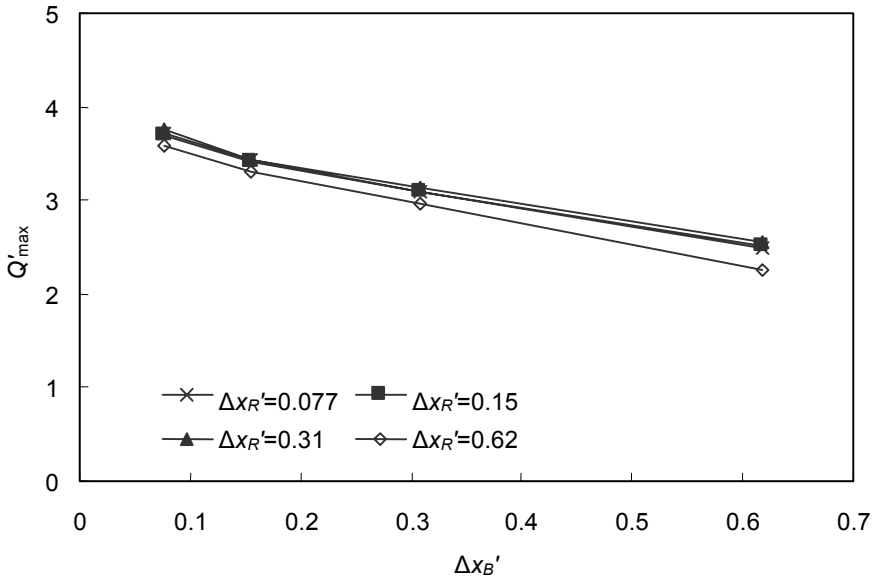

Figure 3.6 Maximum dimensionless discharge Q_{max}' as a function of river basin model resolution (expressed in Δx_B') for four different spatial rainfall input resolutions Δx_R' and constant temporal rainfall input resolution Δt_R' = 1.

In Figure 3.6, the effect of Δx_B' on Q'_{max} is considerable, but almost independent of Δx_R'. The possibility to draw straight conclusions is restricted in the absence of simulated points between Δx_B' = 0.077 (N = 64) and Δx_B' = 0.15 (N = 16). However, if it is assumed that linear convergence takes place with decreasing Δx_B' (or $N^{-½}$), the lines in Figure 3.6 can be extrapolated to the 'exact' Q'_{max} corresponding with Δx_B' = 0. This exact value is found to be close to the Q'_{max} simulated with the smallest Δx_B' independent of Δx_R' (difference is only 2-4 %).

Shah *et al*. (1996a) also found large differences when approximating SHE (Système Hydrologique Europeèn) catchment responses with a simple linear transfer model, although they studied a small catchment. Krajewski *et al*. (1991) underestimated flood peaks of a small catchment when using a lumped model instead of a distributed model. Obviously, these studies did not only compare different model resolutions, but included different model parameterisations as well. Nevertheless, they do not contradict the results obtained here.

Considering this latter finding and the convergence assumption done, the simulations performed with Δx_B' = 0.077 and coupled Δt_B' = 0.125 look reasonable and of sufficient detail for determining extreme discharges. Resolutions remain reasonable when an accuracy of 1 % is required, namely Δx_B' ≈ 0.03 or N ≈ 500 for the Meuse situation. Apart from this model resolution, of course other aspects such as the generated rainfall sequence, parameter determination and model assumptions have their effect on the results. However, the present results give some indication on the appropriate basin

model resolution for an area of similar extent using appropriate correlation lengths λ and τ and parameter values lying in the vicinity of the calibrated ones.

3.4.2 Effect of spatial rainfall input resolution

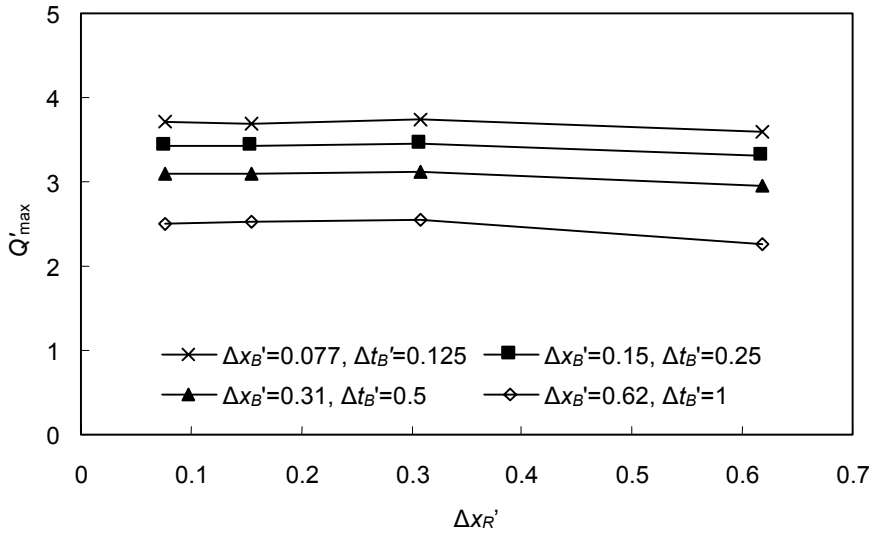

Figure 3.7 Maximum dimensionless discharge Q_{max}' as a function of spatial rainfall input resolution Δx_R' for four different river basin model resolutions Δx_B', Δt_B' and constant temporal rainfall input resolution Δt_R' = 1.

In Figure 3.7, the effect of Δx_R' on Q'_{max} is seen to be much smaller than the effect of Δx_B' on Q'_{max} (Figure 3.6). It seems that it is sufficient to use Δx_R' = 0.31 (four rainfall cells in this situation) for the simulation of extreme discharges, independent of Δx_B', Δt_B' and Δt_R' (the variation of the latter one is not shown here). This resolution is lower than would be expected, given the considerable effect of spatial rainfall resolution on catchment response found in several other studies (e.g. Wilson *et al*., 1979; Lopes, 1996). However, most of these studies have been performed on relative small catchments, where this effect can be essentially different as compared with the effect in large catchments. For a large basin in Britain comparable with the Meuse basin, Hamlin (1983) found little increase in rainfall representation error until almost 75 % of the rain gauges were removed. Assuming the same spatial correlation length of 140 km, this corresponds with $\Delta x_R \approx 0.17$ which supports the results obtained here.

The latter finding leads to the assumption that for this basin, the spatial rainfall variability is averaged out before it can influence the discharge at the outflow point. This may not be the case in large basins with a different rainfall regime and runoff concentration pattern or in relatively small basins. Another explanation for this small sensitivity to spatial rainfall input resolution might be the large spatial rainfall correlation introduced in the rainfall model.

3.4.3 Effect of temporal rainfall input resolution

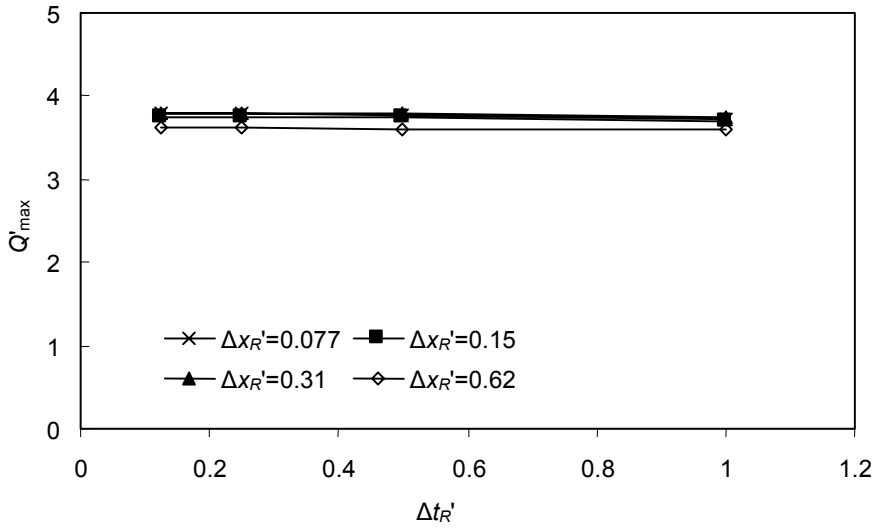

Figure 3.8 Maximum dimensionless discharge Q_{max}' as a function of temporal rainfall input resolution Δt_R' for four different spatial rainfall input resolutions Δx_R' and constant river basin model resolution Δx_B' = 0.077, Δt_B' = 0.125.

The effect of Δt_R' on Q'_{max} in Figure 3.8 is even smaller than the effect of Δx_R' on Q'_{max} (Figure 3.7). It seems that it makes almost no difference using Δt_R' = 1 or Δt_R' = 0.125 independent of Δx_R', Δx_B' and Δt_B' (the variation of the latter one is not shown here). Therefore, on the basis of these simulations, it should be sufficient to use rainfall input with Δt_R' = 1 or even larger values (not examined here). It is not plausible that smaller values than Δt_R' = 0.125 would lead to significant changes in this relation.

As mentioned earlier, Krajewski *et al*. (1991) found for a small catchment that the temporal rainfall resolution has a larger effect on catchment response than the spatial rainfall resolution. This finding is in contradiction with the results obtained here, but again the behaviour of small catchments and large basins might be very different.

The river basin model resolution effect on the maximum discharge is found to be of major importance as compared with the spatial and temporal rainfall input resolution effect. Shah *et al*. (1996a) reached similar conclusions for a small catchment when comparing the effect of model complexity and the spatial rainfall resolution on catchment response.

3.4.4 Sensitivity

The sensitivity of Q'_{max} scaled with its reference value to the three most important parameters scaled with their calibrated values can be viewed in Figure 3.9.

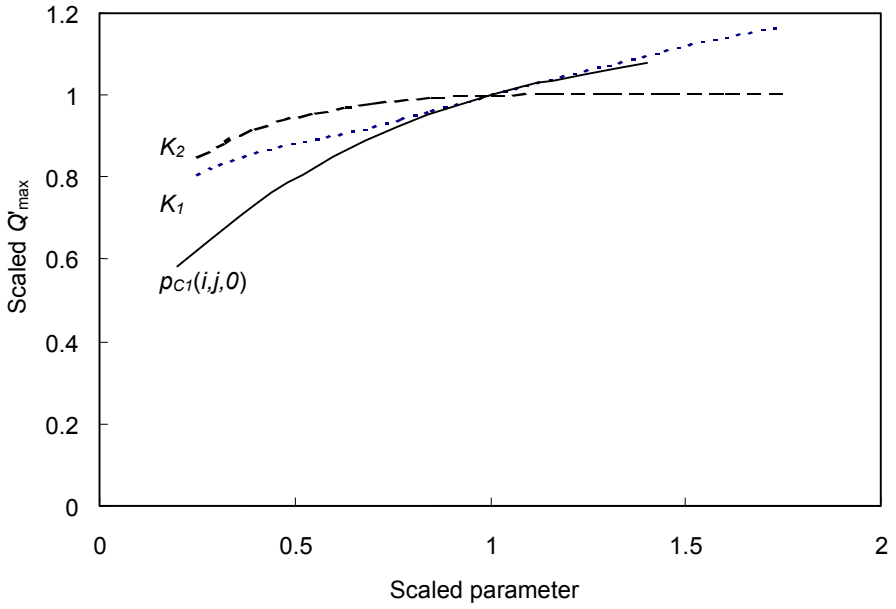

Figure 3.9 Scaled maximum dimensionless discharge Q_{max} (with respect to its median) as a function of scaled parameters K_1, K_2, $p_1(i,j,0)$ (with respect to their calibrated values).

The behaviour of Q'_{max} as a function of the parameters has found to be similar using other river basin model resolutions. Q'_{max} is most sensitive to parameters K_1 and $p_{C1}(i,j,0)$ related to the surface reservoir and somewhat less sensitive to parameter K_2 related to the subsurface flow lag constant. Q'_{max} is hardly sensitive to K_3 (not shown) since the corresponding reservoir only accounts for a marginal part of the discharge (see Table 3.2). Although it is somewhat more sensitive to $p_{C2}(i,j,0)$ (not shown), this sensitivity is not very important, maybe due to the delayed response of reservoir 2. The most important result of this sensitivity analysis is that Q'_{max} changes only gradually with the parameters and no qualitative changes occur. This could be expected from the linear nature of the river basin model.

Therefore, it can be supposed that the relations as observed in Figure 3.6 through Figure 3.8 would not change significantly using other parameter values. It has to be emphasised that the parameters have been varied only one at a time leaving the other ones at their calibrated level and that other parameter combinations not examined here may lead to qualitative changes of the obtained pictures. The error in Q'_{max} due to model resolution effects (numerical error) should preferably be much smaller than the error due to parameter estimation (data error). The results gave numerical errors of about 2-4 % and data errors up to 40 % (Figure 3.9) and therefore meet reasonably these requirements.

3.5 Summary and conclusions

In this chapter some important characteristics of an appropriate river basin model to study the effect of climate change on basin response were studied. The features examined were the spatial and temporal resolution of the rainfall input and a river basin model. The effect of these input and model resolutions on the extreme discharge of the Meuse was assessed in order to give some indication on appropriate resolutions. This was done with a simple stochastic rainfall model and a river basin model with varying resolutions, uniform parameters and multiple rainfall input.

Main conclusion is that the effect of the model resolution on extreme river discharge is of major importance as compared with the effect of the input resolution for the examined river basin and model. The highest model resolution (5-10 grid points/ spatial correlation length; 7-10 time steps/ temporal correlation length) seems to be appropriate in determining the extreme discharge for large river basins with a similar rainfall regime and runoff concentration pattern as used here. Furthermore, a relatively low spatial and temporal rainfall resolution (1-2 grid points/ spatial correlation length; at most 1 time step/ temporal correlation length) was sufficient to represent the rainfall input of a model for these large basins. These conclusions will not be significantly affected when using other parameter values in the river basin model as shown by the sensitivity analysis.

Of course these conclusions should be handled with caution, because of the simple rainfall and river basin model used and the calibration procedure followed. However, they give some indication on the appropriate input and model resolution for a similar large river basin with a similar rainfall regime and runoff concentration pattern, using appropriate correlation lengths and parameter values which are within the considered range. This gives some support when an appropriate model for the determination of extreme discharges of a large river basin with climate change has to be chosen. Moreover, a methodology has been presented to assess the effect of spatial and temporal rainfall and basin model resolutions on river basin response. For other purposes, where the extreme river discharge at the outflow point is not the only interest, other resolution requirements may be obtained.

Chapter 4

Climate data analysis

4.1 Introduction

The atmosphere controls the runoff processes in a river basin to an important extent through processes such as precipitation, wind and radiation. Precipitation plays an important role in the basin water balance and wind and radiation influence temperature and evapotranspiration. Obviously, these latter two are important for the water balance as well. Climate change will have a serious impact on these processes. It is expected that the temperature will rise, the evapotranspiration will increase and the precipitation becomes more extreme. These three variables are therefore analysed in this chapter.

Precipitation, temperature and (potential) evapotranspiration are obtained directly or indirectly from measuring stations and climate models and are inputs into the river basin model. Therefore, in particular the question of appropriate spatial and temporal scales should receive attention, because process formulations are not required for input data. These appropriate scales should be assessed for important statistics with respect to a specific variable, e.g. variability and extremes for precipitation. The statistic vs. scale relations from section 2.3 are used for this purpose. Simultaneously, the uncertainty of the dominant variables with climate change is assessed in this climate data analysis.

In section 4.2, the spatial and temporal characteristics of the observed and modelled climate data are described and an explanation of the uncertainty assessment is given. In section 4.3, the data are intercompared for the Meuse area and Western Europe for current and changed climate conditions. Furthermore, different data scales are considered (point, model and appropriate) and an uncertainty assessment for the important statistics is done. Finally, in section 4.4 the main conclusions are drawn.

4.2 Observed and modelled data

4.2.1 Spatial and temporal characteristics

Daily precipitation and temperature data from a station network, two re-analysis projects (one for temperature), three global climate models (GCMs) and two regional climate models (RCMs) are used in this analysis. Only daily potential evapotranspiration data from a station network are used. The analysis has been performed for current climate conditions (for the current 'equivalent' CO_2 concentration or 1XCO2) and changed climate conditions (twice the current 'equivalent' CO_2 concentration or 2XCO2). The changed climate conditions apply for a time period of approximately 70 years assuming an increase of 1 % 'equivalent' CO_2 per year.

Part of this chapter has been published as:

Booij, M.J., 2002b. Extreme daily precipitation in Western Europe with climate change at appropriate spatial scales. *Int. J. Climatol*., **22**, 69-85.

The precipitation, temperature and evapotranspiration station data are respectively from 39, 12 and 5 stations in the Meuse basin upstream of Borgharen (about 20 000 km^2) in Belgium and France for the period 1970-1999. The locations of the precipitation stations are shown in Figure 4.1a. The precipitation and temperature station data are compared with the accompanying model data in a so-called 'local analysis' (small bold black box in Figure 4.1a). The model data are mutually compared in the 'regional analysis' to check the consistency of the local analysis and to obtain a more representative spatial picture (large bold black box).

The re-analysis data are from the NASA-GEOS re-analysis (Schubert *et al.*, 1993) and the NCEP-NCAR re-analysis (Kalnay *et al.*, 1996). These re-analyses incorporate land surface, ship, rawinsonde, aircraft, satellite and other data. The assimilating atmospheric general circulation model is constrained at the lower boundary by the observed sea surface temperature and the derived soil moisture. The re-analyses produce a large number of variables, for example precipitation. This precipitation is not directly affected by observations, so that it is derived solely from the model fields forced by the data assimilation to remain close to the atmosphere (Kalnay *et al.*, 1996). Therefore, these data can be considered as model data as well. The NASA-GEOS1 re-analysis covers the period 1985-1993 with a spatial resolution of approximately 2.0°x2.5° (~200 km over Western Europe) and from the NCEP-NCAR re-analysis, data for the period 1970-1999 with a spatial resolution of approximately 1.9°x1.9° (~170 km) are used. The 30 NASA-GEOS and 42 NCEP-NCAR grid boxes analysed are shown in Figure 4.1a. Only precipitation data are adopted from the NASA-GEOS re-analysis.

The GCM data are from the Canadian Climate Centre, Hadley Centre and CSIRO GCMs; CGCM1, HadCM3 and CSIRO9. The atmospheric component of the CGCM1 model is a spectral model with triangular truncation at wave number 32 yielding a horizontal resolution of approximately 3.7°x3.7° (~340 km) and 10 vertical levels. The ocean component has a resolution of approximately 1.8°x1.8° (~160 km) and 29 vertical levels. The model uses heat and water flux adjustments obtained from uncoupled ocean and atmosphere model runs, followed by an adaptation procedure. A multi-century control simulation with the coupled model has been performed by Flato *et al.* (2000) using the present-day CO_2 concentration to evaluate the model performance. The transient climate change simulation uses an effective greenhouse gas forcing change corresponding to that observed from 1850 to the present and a forcing change corresponding to an increase of CO_2 at a rate of 1 % per year (compound) thereafter until 2100 (identical to the IPCC "business as usual" scenario). The direct forcing effect of aerosols is also included by increasing the surface albedo. The climate sensitivity of CGCM1 is about 3.5 °C (Boer *et al.*, 2000a, 2000b). Precipitation data from the period 1975-1995 representing current climate conditions and from the period 2080-2100 representing climate change conditions have been used in this analysis. Temperature data from 1970-1999 and 2070-2099 have been used.

The atmospheric component of HadCM3 is the HadAM3 version of the UK Meteorological Office's unified forecast and climate model with a horizontal resolution of 2.5°x3.75° (~270 km) and 19 vertical levels. Major changes over the previous version (HadAM2) are a new radiation scheme, an improvement of the convection scheme and a new land-surface scheme. The ocean component has a resolution of approximately 1.25°x1.25° (~130 km) and 20 vertical levels. The model does not

require flux adjustments to be made. A 400 year control simulation with the coupled model has been performed to evaluate the model performance. The transient climate change simulation HadCM3GGa1 was forced using the historical increase in the individual greenhouse gases from 1860-1990 and a forcing change corresponding to an increase of CO_2 at a rate of 1 % per year (compound) thereafter until 2100. The direct forcing effect of aerosols is not included (Gordon *et al.*, 2000). The climate sensitivity of HadCM3 is about 3.0 °C (IPCC, 2001). Here, precipitation and temperature data from the period 1961-1990 representing current climate conditions and from the period 2070-2099 representing climate change conditions have been used.

The atmospheric component of CSIRO9 uses a spectral R21 horizontal grid (3.2°x5.6° or ~380 km) and 9 vertical levels. The ocean model has the same horizontal resolution and 21 vertical levels. The model uses heat, salinity and wind flux adjustments obtained from uncoupled ocean and atmosphere model runs. The 185 year transient climate change simulation uses a forcing change corresponding to an increase of CO_2 at a rate of 0.5 % per year (compound) for the first 100 years and slightly faster thereafter (identical to the IPCC "central estimate" scenario). The direct forcing effect of aerosols is not included. The climate sensitivity of CSIRO9 is about 2.2 °C (Gordon and O'Farrell, 1997; Hirst *et al.*, 1997). Precipitation and temperature data from the period 1970-1999 representing current climate conditions and from the period 2070-2099 representing climate change conditions have been used. The 16 CGCM1, 20 HadCM3 and 15 CSIRO9 grid boxes are shown in Figure 4.1a.

The RCM data are from the Hadley Centre and Danish Meteorological Institute RCMs; HadRM2 and HIRHAM4. The HadRM2 is a limited area version of the Hadley Centre GCM with a horizontal resolution of 0.44°x0.44° (~50 km) and 19 vertical levels. Apart from this horizontal resolution and some details, the physical and dynamical formulations of HadRM2 are identical to those in HadAM2. In a one-way nesting technique, HadRM2 is driven at its lateral and lower sea surface boundaries by time series of data archived from integrations of HadCM2 (previous version of HadCM3). The time series used to drive HadRM2 are one 30-year and one 20-year period representing control and perturbed climate [1 % per year increase of CO_2 (compound) etc.] (Jones *et al.*, 1995; Machenhauer *et al.*, 1998). Precipitation and temperature data from the control integration representing late twentieth century conditions (1970-1999) and the perturbed integration representing the 2080-2100 climate have been used. The difference between perturbed and control climate represents the difference between pre-industrial and 2080-2100 climate (Johns *et al*., 1997).

The HIRHAM4 model combines the adiabatic part of the HIRLAM model (developed by the Nordic, Dutch and Irish meteorological services) with the ECHAM4 (atmospheric GCM from MPI, Hamburg) physical parameterisation package. It has a horizontal resolution of 0.51°x0.51° (~55 km) and 19 vertical levels. HIRHAM4 is driven at its lateral and lower sea surface boundaries by time series of data archived from integrations of ECHAM4/OPYC3, the latter being a ocean model. The time series used to drive HIRHAM4 are one approximately 9-year and one approximately 8-year period representing control and perturbed climate [1 % per year increase of CO_2 (compound) etc.] (Christensen *et al.*, 1996; Machenhauer *et al.*, 1998). Precipitation and temperature data from this 9-year and 8-year period have been used. The 404 HadRM2 and 308 HIRHAM4 grid boxes are not shown in Figure 4.1a for sake of clarity.

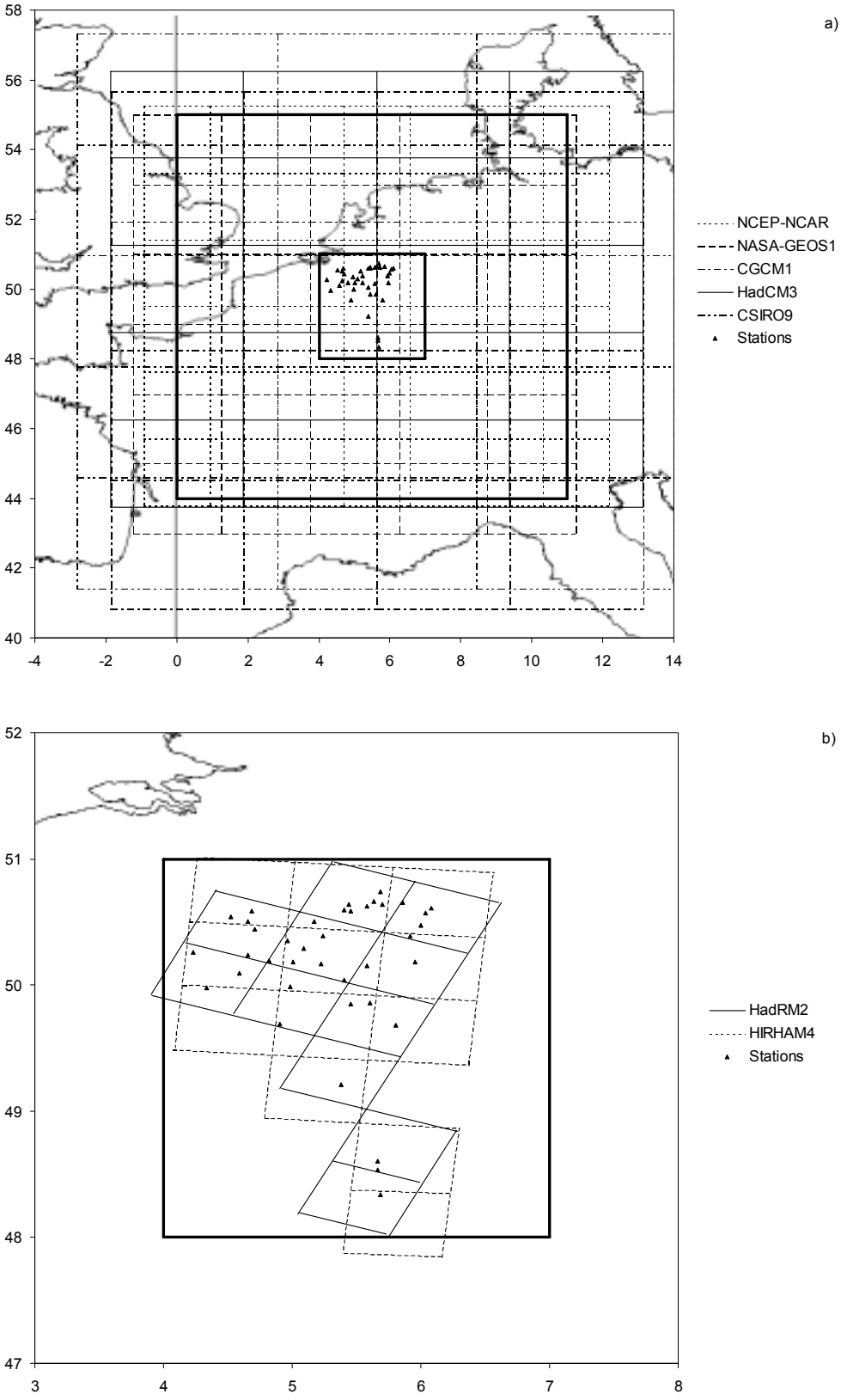

Figure 4.1 a) Spatial coverage of precipitation stations and re-analysis and GCM model grid boxes in Western and Central Europe with Meuse basin and surroundings analysed (small bold black box) and regional area analysed (large bold black box); b) spatial coverage of RCM model grid boxes in Meuse basin (bold black box is small box from a).

In the local analysis respectively 2 NASA-GEOS1, 3 NCEP-NCAR, 2 CGCM1, 3 HadCM3, 1 CSIRO9, 11 HadRM2 and 12 HIRHAM4 grid boxes are analysed. The HadRM2 and HIRHAM4 grid boxes from the local analysis are shown in Figure 4.1b. The temporal coverage of the different data sources is illustrated in Figure 4.2. Also shown is the procedure for the determination of the uncertainty in precipitation and temperature statistics at the appropriate scale with climate change to be used in 4.2.2.

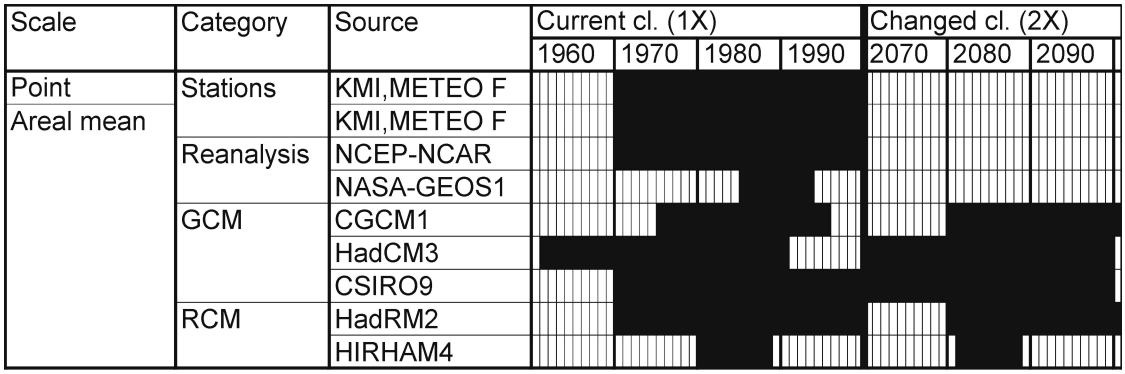

Figure 4.2 Temporal coverage of station, re-analysis, GCM and RCM data for current and changed climate and procedure for the determination of uncertainty in precipitation and temperature with climate change at the appropriate scale (1=uncertainty due to upscaling; 2=model error; 3=inter-model uncertainty; 4=climate forcing uncertainty; 5=inter-model uncertainty; 6=uncertainty due to downscaling).

4.2.2 Derivation of uncertainties

The uncertainty in precipitation and temperature statistics under climate change conditions at the appropriate scale is assessed in several steps (see Figure 4.2). The different uncertainty contributions are explained in the figure caption. All numbered steps in Figure 4.2 add uncertainty to the final uncertainty. The question is whether all partial uncertainties (probably resulting in an overestimation of the uncertainty) or part of the partial uncertainties (the most important ones) should be summed. Here, it is assumed that uncertainty 2 (model error), 3 and 5 (inter-model uncertainties) and 4 (climate forcing uncertainty) are the most important uncertainties. Furthermore, it is assumed that uncertainties 3 and 5 are comparable and are represented by one overall uncertainty equal to their mean. Only errors and uncertainties with respect to the GCMs and RCMs will be considered (see discussion at the end of 4.3.3). The uncertainty will be expressed by means of the absolute value of the Relative Error (RE) for a specific statistic X

$$RE = 100 \cdot \left| \frac{X_2 - X_1}{X_1} \right| \tag{4.1}$$

where X_1 and X_2 are statistics from different data sources.

4.3 Data intercomparison

The station data can be considered as point data and are analysed in 4.3.1. Subsequently, aggregated station data at the model scale are compared with model data in the local analysis in 4.3.2 and model data are intercompared in the regional analysis in 4.3.3. The local and regional analysis are repeated for climate change conditions in 4.3.4. The appropriate scale data are analysed in 4.3.5 and finally, the uncertainty assessments are done in 4.3.6.

4.3.1 Point statistics for local area and current climate

Precipitation

Daily point precipitation statistics defined in section 2.3 [mean μ, standard deviation σ, dry/ wet day frequency p_0/ p_1, υ_1 and υ_2 from equation (2.20), spatial and temporal correlation length λ and τ and *PPCC** values] for the 39 stations are summarised by their respective means and range (minimum and maximum) in Table 4.1. For the wet day frequency analysis, the relation between $1/u(h)$ and h for all stations is shown in Figure 4.3.

Table 4.1 Daily point precipitation statistics.

Statistics			Mean	Minimum	Maximum
μ		(mm)	2.6	2.1	3.4
σ		(mm)	5.0	4.3	6.3
p_0		(-)	0.49	0.40	0.59
p_1		(-)	0.51	0.41	0.60
υ_1		(-)	0.79	0.69	0.86
υ_2		(km)	596	435	785
*PPCC**	dry-wet	(-)	0.78	0.60	0.89
λ		(km)	314	245	387
τ		(day)	2.3	1.9	3.0
*PPCC**	spatial	(-)	0.96	0.80	0.99
*PPCC**	temporal	(-)	0.98	0.95	1.00

Differences between stations in mean precipitation can amount to more than 50 % within the relative small study area (largest separation distance between stations ~270 km). The spatial variability in dry and wet day frequencies is evident from Table 4.1 as well. The *PPCC** values indicating the goodness-of-fit of relation (2.20) in describing the relation between distance and the variable in equation (2.19) are reasonable (see Figure 4.3). Given the fact that Osborn and Hulme (1997) applied this methodology for Western Europe as well, it seems reasonable to apply the methodology here. Similar reasoning applies for the spatial and temporal behaviour of the correlograms (*PPCC** values are considerable larger). The mean spatial correlation length λ of about 300 km compares favourable with the winter and summer values of 300 km and 200 km found by Osborn and Hulme (1997). The mean temporal correlation length τ of about 2.3 days is rather large when compared with the value of about 1.5 days found by Hoosbeek (1998) for a Dutch area. This may be caused by the small number of points used in the

fitting procedure (6 points) and/ or the small number of stations used by Hoosbeek in his analysis. Differences in precipitation regimes between the two neighbouring areas are not expected to be an explanation, because temporal correlation is assumed to be associated with large scale weather patterns.

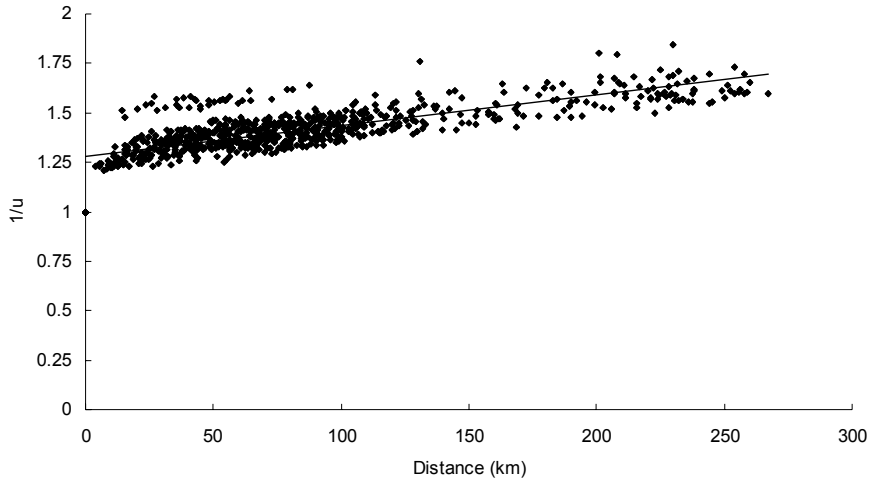

Figure 4.3 Relation 1/*u* vs. distance (= *h*) for all stations.

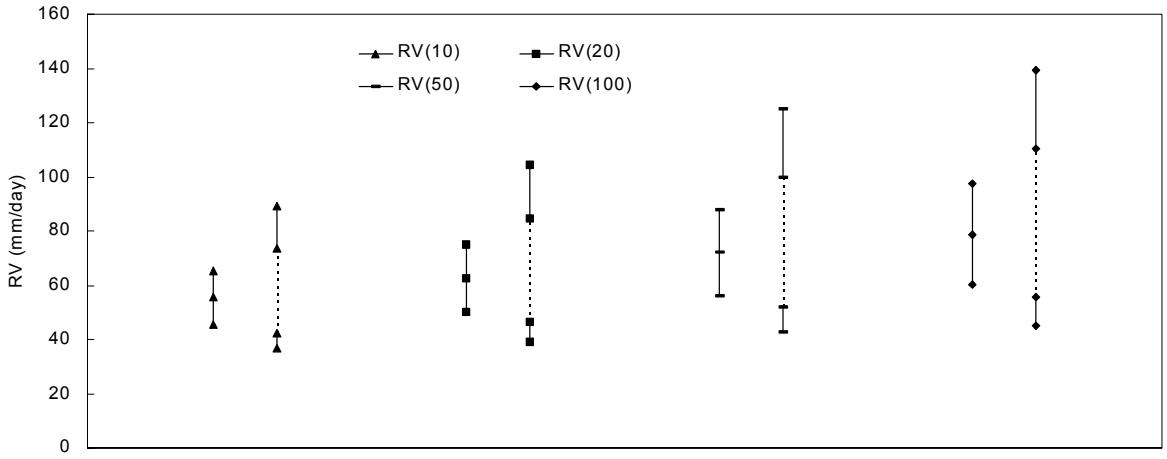

Figure 4.4 Mean (left) and minimum-maximum (dotted line, right) of precipitation return values RV in mm/day with 95%-confidence intervals derived from 39 stations.

Precipitation return values $RV(T)$ and their 95%-confidence intervals for T=10, 20 50 and 100 years for the 39 stations are summarised by their respective means and range (minimum-maximum) in Figure 4.4. The 95%-confidence intervals and the spatial variability of return values are rather large. The ratio of the maximum $RV100$ (top of dotted line in Figure 4.4) and minimum $RV100$ (bottom of dotted line) is more than 2. This large spatial variability can be largely attributed to the point quantity measured and the inherent coincidence of catching a small or large precipitation amount [sampling

problem, statistical cause] and to a lesser extent to the effect of distance to the sea (moderate correlation) and orography (weak correlation) [physical cause]. García-Ruiz *et al.* (2000) found a somewhat stronger, but still weak correlation between the maximum observed daily precipitation and the altitude for the Spanish Pyrenees for 26 stations.

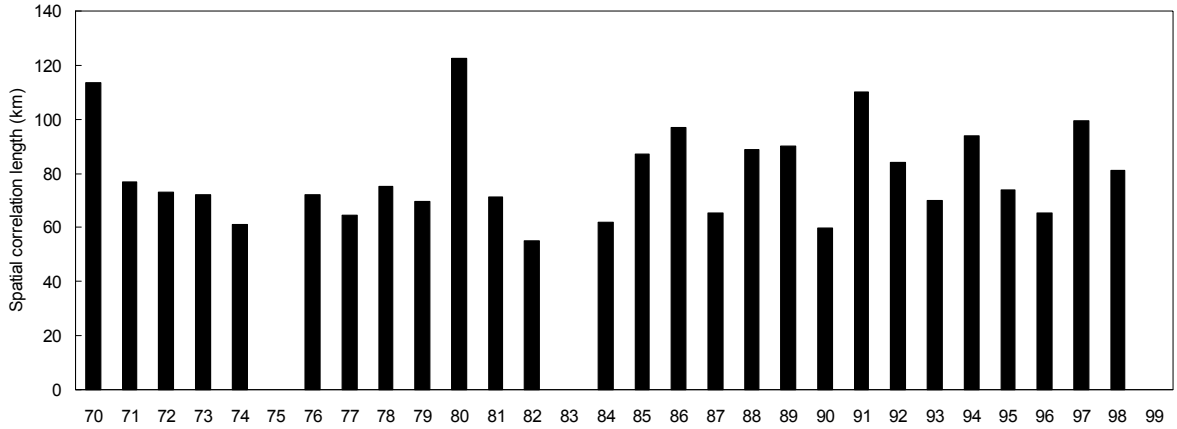

Figure 4.5 Spatial correlation length in km for each annual maximum precipitation field for 1970-1999.

The spatial correlation length λ for each annual maximum precipitation field (see 2.3.5) for 1970-1999 is shown in Figure 4.5. The λ's for 1975, 1983 and 1999 are not shown, because no reasonable variograms could be fitted to the calculated semi-variances for these particular years. The average λ is about 80 km with a standard deviation of 17 km. This value is remarkably smaller than the value derived from complete precipitation fields of about 300 km. It is therefore necessary to use correlation lengths associated with extreme precipitation fields in the reduction methodology of section 2.3.5 instead of using correlation lengths associated with complete precipitation fields as has been done by Sivapalan and Blöschl (1998).

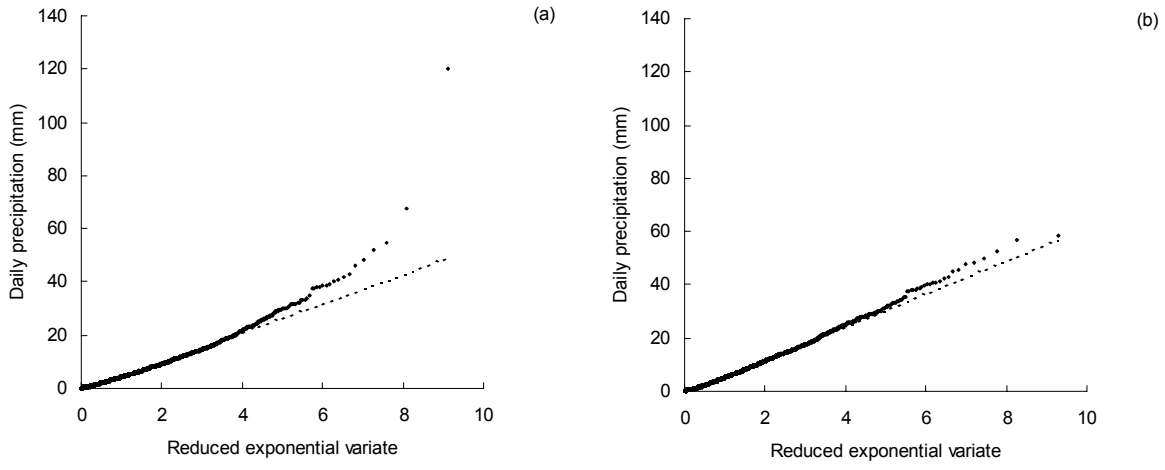

Figure 4.6 Worst (a) and best (b) goodness-of-fit for exponentially distributed point values.

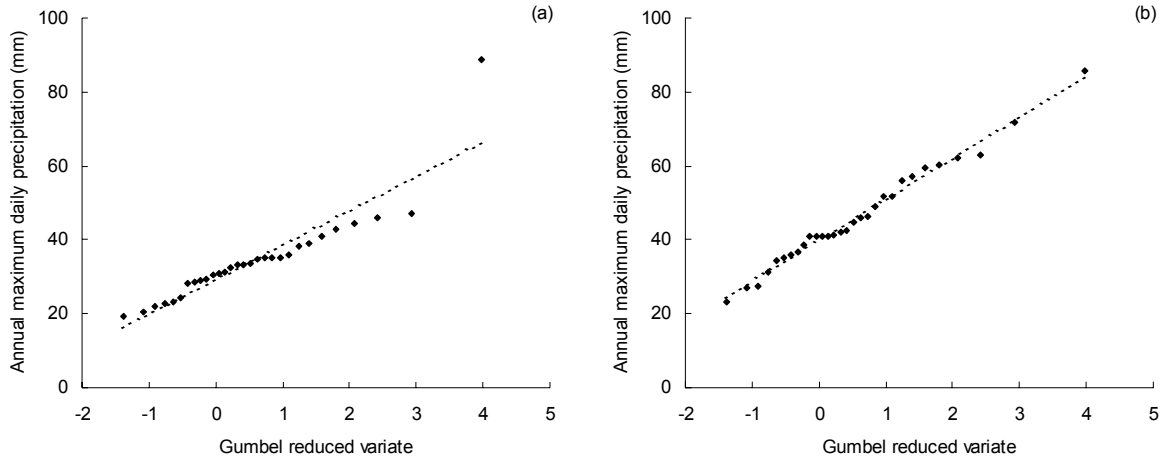

Figure 4.7 Worst (a) and best (b) goodness-of-fit for Gumbel distributed annual maximum point values.

In the same extreme value reduction methodology, it is assumed that non-zero daily point precipitation values are exponentially distributed and annual maximum daily point precipitation values are Gumbel distributed. The worst and best goodness-of-fit of non-zero daily point precipitation to the exponential distribution for two specific stations are shown in Figure 4.6. The worst and best goodness-of-fit with respect to the Gumbel distribution are shown in Figure 4.7. The PPCC test failed to reject the hypothesis of annual extremes being Gumbel distributed at a significance level of $\alpha = 0.05$ for 36 stations (or 92 %). The differences between calculated and critical PPCC values for the exponential distribution were very small. The most pronounced deviations from linearity in the probability plots in Figure 4.6 are associated with extreme values, which were fitted to the Gumbel distribution to an acceptable level (see Figure 4.7). It can therefore be concluded that non-zero and annual maximum daily point precipitation values are respectively exponentially and Gumbel distributed.

Temperature

Table 4.2 Daily point temperature statistics.

Statistics		Mean	Minimum	Maximum
μ	(°C)	8.9	7.4	10.9
σ	(°C)	6.5	6.4	6.9
λ	(km)	5272	3435	7864
τ	(day)	76.2	74.8	77.5

Daily point temperature statistics (mean μ, standard deviation σ and spatial and temporal correlation λ and τ) for 12 stations are summarised by their respective mean and range (minimum and maximum) in Table 4.2. The average spatial correlation length λ is large in comparison with the area (extent) examined and is even underestimated according to scale (extent) vs. correlation length relationships (Western and Blöschl, 1999). The large temporal correlation length τ could be expected from the annual

temperature cycle present in this area. The spatial variability of the four statistics is small, partly due to the small number of stations used and the small separation distances (up to 150 km) in relation to λ.

Evapotranspiration

Table 4.3 Daily point potential evapotranspiration statistics.

Statistics		Mean	Minimum	Maximum
μ	(mm)	1.8	1.7	1.9
σ	(mm)	1.7	1.5	1.9
λ	(km)	1051	854	1208
τ	(day)	79.9	77.1	81.3

Daily point potential evapotranspiration statistics (mean μ, standard deviation σ and spatial and temporal correlation λ and τ) for the 5 stations are summarised by their respective mean and range (minimum and maximum) in Table 4.3. The coefficient of variation CV (σ/μ) is around 1, which is smaller than the CV for point precipitation of around 2 indicating that there is more variability in the precipitation process than in the evapotranspiration process. The average spatial correlation length λ is again large (1/5 of the λ for temperature) and the temporal correlation length is comparable with the one for temperature. This latter feature could be expected, because of the strong relationship between temperature and evapotranspiration (see below). Again, the spatial variability of the statistics is small.

Precipitation, temperature and evapotranspiration

The relations between daily precipitation, temperature and evapotranspiration are briefly investigated to get some idea about their interdepencies. It may be that two of them are related in such a way, that it has to be taken into account in the climate simulation process or that one variable can be predicted by another variable (e.g. evapotranspiration under climate change conditions). Figure 4.8 gives the relations between areally average precipitation, temperature and evapotranspiration. Figures a), c) and e) give the relationships for actual values and figures b), d) and f) give the relationships for deviations with respect to daily normal values (for temperature and evapotranspiration). The daily normal values μ_i^* (i = 1,2,…,365) have been obtained by smoothing the computed average daily values μ_i (i = 1,2,…,365) using Fourier sums to filter out small fluctuations. A nice fit was already obtained using 4 periodical functions in the smoothing procedure. The deviations can give additional information because of the strong periodical structure of temperature and evapotranspiration in contrast to precipitation (for the Meuse area).

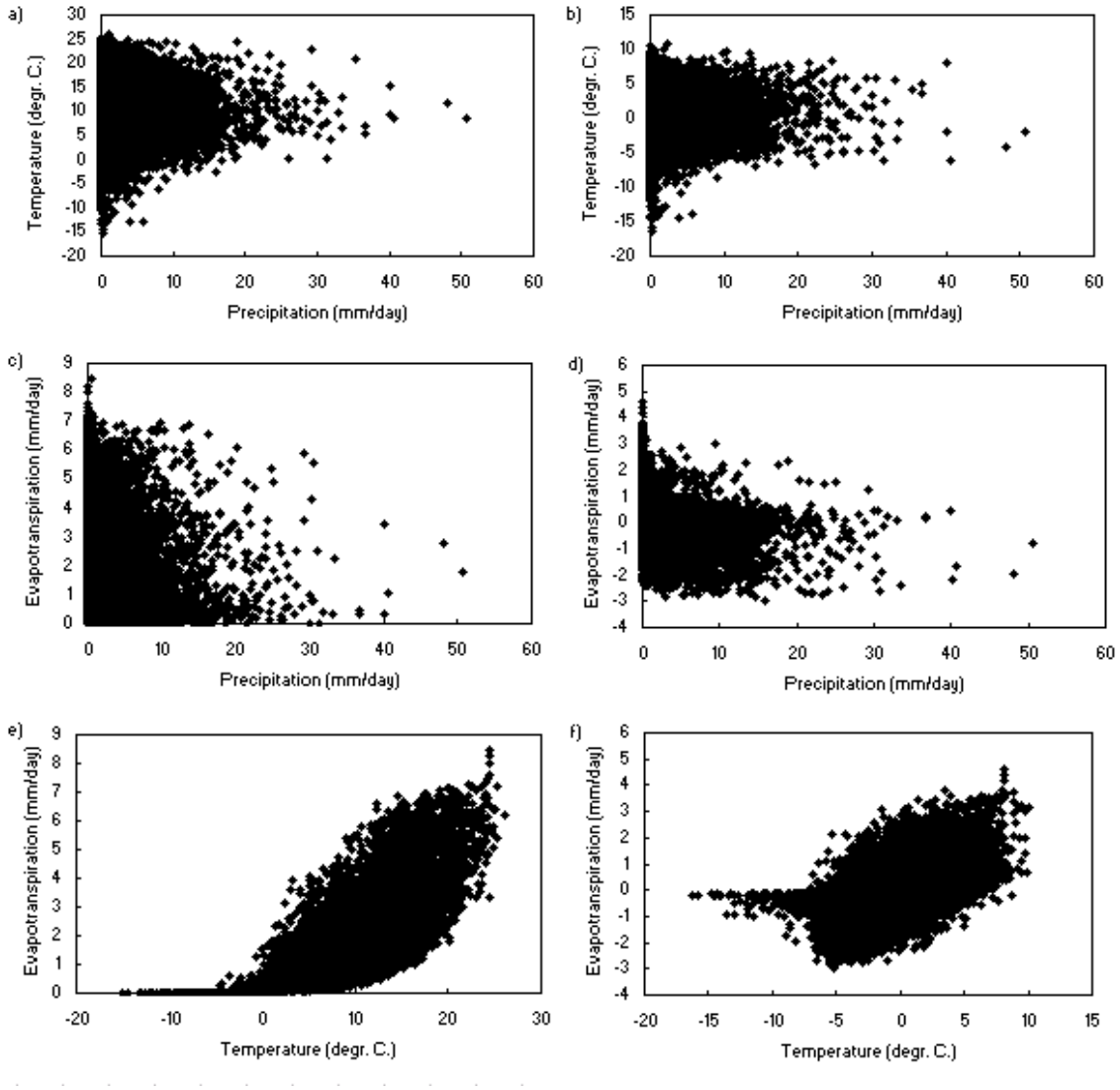

Figure 4.8 Relations between a) precipitation in mm/day and temperature in °C; b) precipitation and deviations in temperature in °C; c) precipitation and evapotranspiration in mm/day; d) precipitation and deviations in evapotranspiration in mm/day; e) temperature and evapotranspiration; f) deviations in temperature and deviations in evapotranspiration.

Figure 4.8 shows none to weak correlations for all relations with precipitation and only reveals for the temperature vs. evapotranspiration relation in e) a reasonable correlation (correlation coefficient ≈ 0.62). The precipitation vs. deviations in temperature and evapotranspiration relations do not show a significant better correlation than the corresponding 'normal' ones, the 'normal' relation for temperature vs. evapotranspiration was even better than the 'deviated' one. It can be concluded that only a relation between temperature and evapotranspiration exists and some kind of relation between these two variables can be used in the climate change simulations.

4.3.2 Model scale statistics for local area and current climate

Precipitation

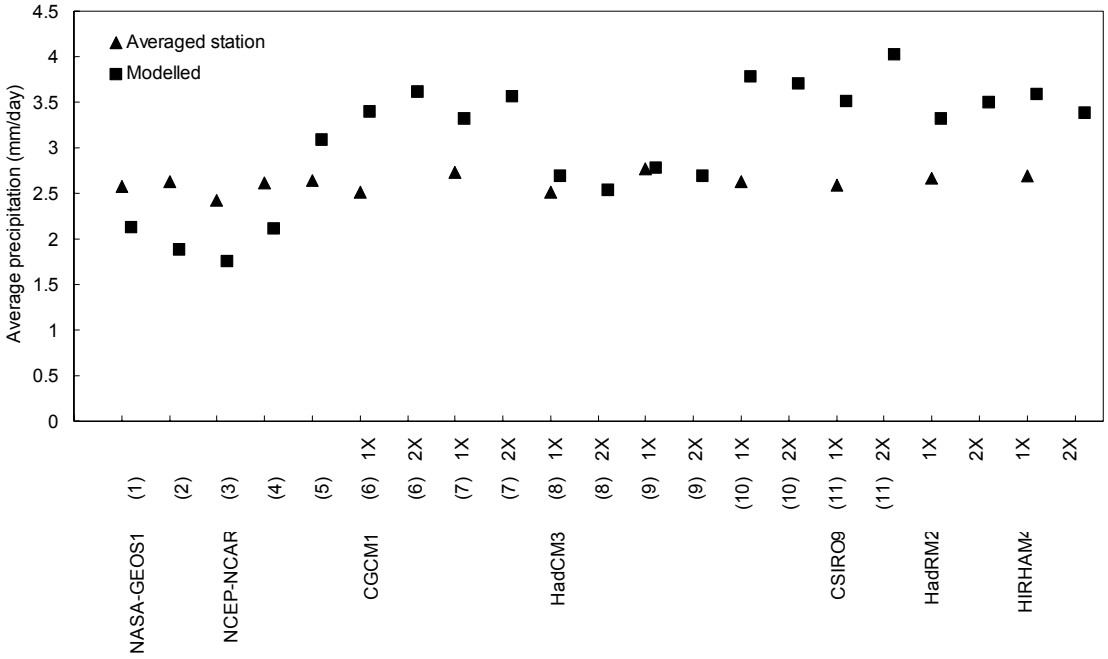

Figure 4.9 Average precipitation in mm/day for different models (1-3 grid boxes) and corresponding averaged station values. The numbers refer to the grid boxes used: (1) = 50.00N, 5.00E; (2) = 48.00N, 5.00E; (3) = 50.48N, 3.75E; (4) = 50.48N, 5.63E; (5) = 48.57N, 5.63E; (6) = 50.10N, 3.75E; (7) = 50.10N, 7.50E; (8) = 50.00N, 3.75E; (9) = 50.00N, 7.50E; (10) = 47.50N, 7.50E; (11) = 49.38N, 5.63E. For HadRM2 and HIRHAM4 average values over 11 respectively 12 grid boxes are given. Results for current (1X) and changed (2X) climate are shown.

Model scale precipitation for the station series averaged over the corresponding model grid boxes (see Figure 4.1) and modelled series for the grid boxes in the Meuse area are given in Figure 4.9. They correspond to a variable degree with each other [average RE ≈ 20 %, equation (4.1)]. Re-analyses underestimate the average precipitation, while GCMs generally overestimate the average precipitation. The overestimation by CGCM1 is in accordance with its overestimation in a study for Canada (Kharin and Zwiers, 2000). While for the re-analyses and GCMs only a few grid cells are analysed, for the RCMs 11 and 12 (HadRM2 resp. HIRHAM4) grid cells are considered. The average precipitation is overestimated by both HadRM2 (average RE ≈ 23 %) and HIRHAM4 (average RE ≈ 34 %). Differences between observed and GCM modelled average precipitation are comparable with results for Europe in Déqué and Piedelievre (1995) [30-40 % overestimation using a variable resolution GCM], Marinucci *et al*. (1995) [10-60 % underestimation with ECHAM3 GCM for Alpine region], Gregory and Mitchell (1995) [50 % underestimation to 50 % overestimation with HadCM1], Jones *et al*. (1995) [10 % underestimation with HadCM2] and Marinucci and Giorgi (1992) [5 % underestimation with NCAR CCM]. For the United States, Kalnay *et al*. (1996) found large differences between station precipitation and NCEP-NCAR re-analysed precipitation (sometimes almost 100 %). The differences between observed and RCM modelled precipitation were comparable in other studies for Europe, for example

Marinucci *et al*. (1995) [30 % underestimation – 30 % overestimation with NCAR/PSU MM4 for the Alpine region], Jones *et al*. (1995) [10-20 % underestimation with HadRM2] and Marinucci and Giorgi (1992) [30 % underestimation with NCAR/PSU MM4].

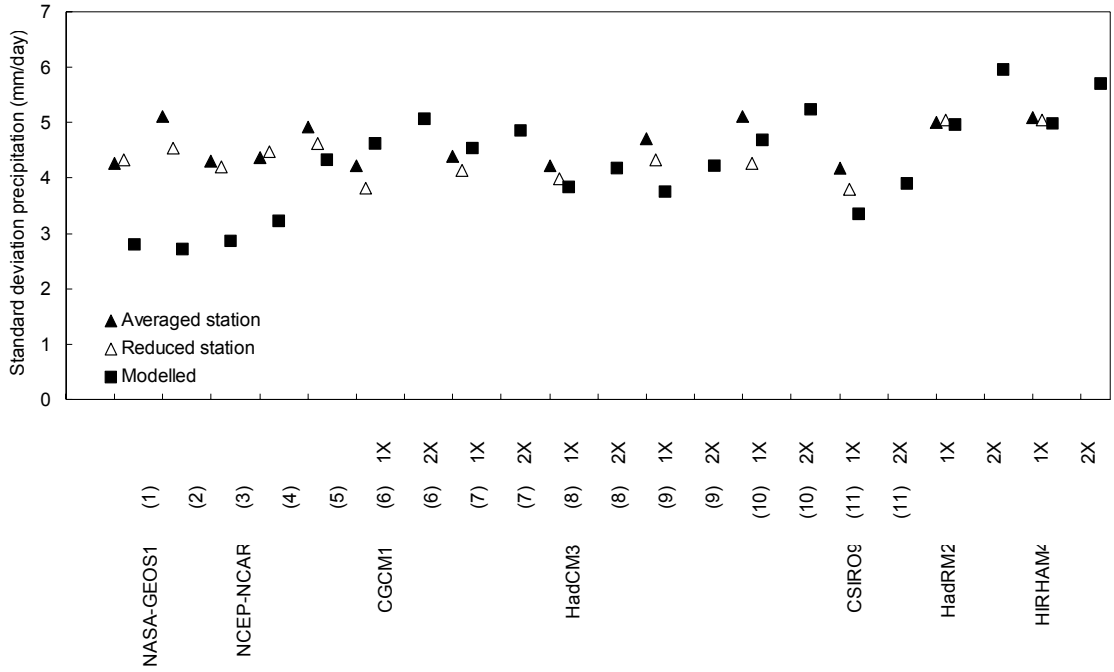

Figure 4.10 Standard deviation of precipitation in mm/day for different models (1-3 grid boxes) and corresponding averaged and reduced station values. The numbers refer to the grid boxes used and are defined in Figure 4.9. For HadRM2 and HIRHAM4 average values over 11 respectively 12 grid boxes are given. Results for current (1X) and changed (2X) climate are shown.

Figure 4.10 presents the standard deviation of precipitation for the averaged station series, for the averaged station series calculated by means of the reduction factor (reduced) and for the modelled series for the grid boxes in the Meuse area. Averaged and reduced standard deviations compare favourably, in particular if there is a large numbers of stations in a specific grid cell. It therefore seems to be reasonable to use the reduction methodology associated with the standard deviation. Observed and modelled standard deviations are comparable (average RE ≈ 25 %), although there are considerable differences in the re-analysis projects (viz. RE for CGCM1, HadCM3 and CSIRO9 respectively ~5 %, ~15 % and ~10 %; RCMs ~10 %). On the other hand, Kalnay *et al*. (1996) found for the United States that observed and NCEP-NCAR re-analysed standard deviation compare quite well. Osborn and Hulme (1998), in an intercomparison of 12 GCMs, mainly found overestimations of the daily standard deviation for Europe (RE varying between 5-60 %). They found that HadCM2 best simulated daily standard deviation. CSIRO9, CCC (variant of CGCM1) and the Australian BRMC were acceptable as well. Three, partly more recent versions, of these models have been analysed here.

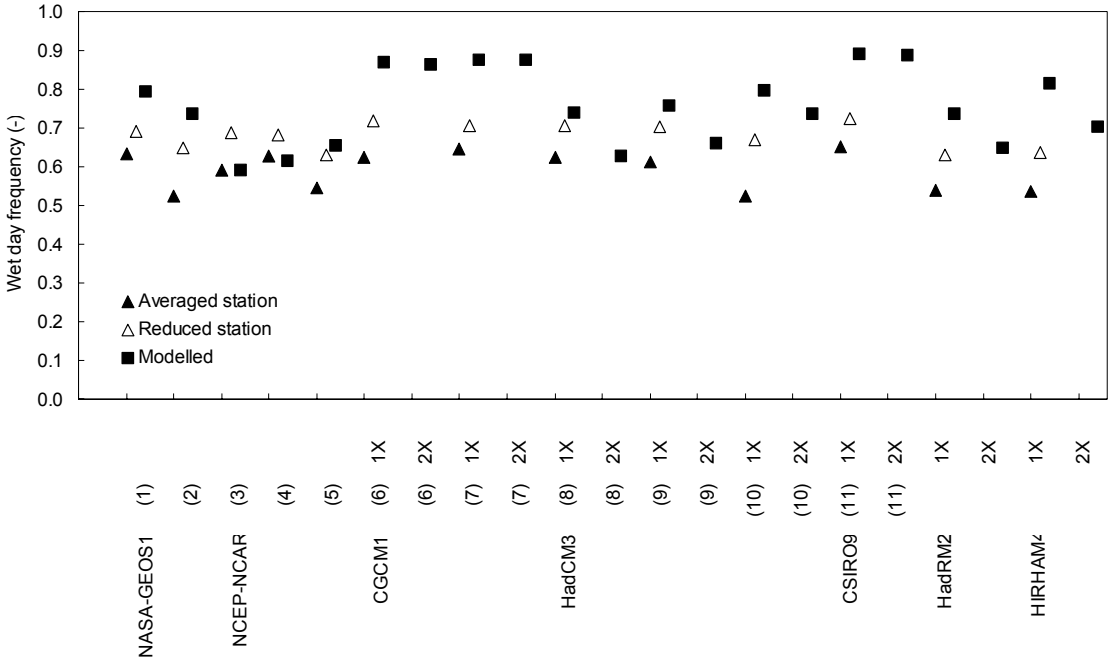

Figure 4.11 Wet day frequency for different models (1-3 grid boxes) and corresponding averaged and reduced station values. The numbers refer to the grid boxes used and are defined in Figure 4.9. For HadRM2 and HIRHAM4 average values over 11 respectively 12 grid boxes are given. Results for current (1X) and changed (2X) climate are shown.

Wet day frequencies for the averaged station series, the reduced station series and the modelled series for the grid boxes in the Meuse area are given in Figure 4.11. The reduced wet day frequencies tend to be significantly larger than the averaged ones. This is in contrast with the results from Osborn and Hulme (1997), who found good agreement between the two methodologies. Since the overall $\overline{v}$ from equation (2.20) (~0.71) agrees well with the overall $\overline{v}$ found by Osborn and Hulme, the cause may either be inaccurate determination of coefficients β_1 and β_2 (not plausible, see notes in section 2.3.3) or wrong estimation of dry and wet day frequencies by the averaging methodology. This latter reason could be explained by the fact that for large grid boxes only part of the grid box is covered by stations (Figure 4.1) and therefore averaging does not cover the complete grid box. This results in an underestimation of the wet day frequency when station values are averaged. It would therefore seem to be necessary to use the reduction methodology associated with wet day frequencies.

Dry and wet day frequencies are not modelled very well. Wet day frequencies tend to be overestimated by all models (RE ~10-25 %) except NCEP-NCAR and vice versa for dry day frequencies (RE ~30-70 %). Differences between reduced station and modelled frequencies are smaller than differences between averaged station and modelled frequencies, again suggesting that reduced values may be preferred over averaged values. For the Alpine region, Marinucci *et al*. (1995) simulated a too wet climate as well with the ECHAM3 GCM. Osborn and Hulme (1998) also found too many wet days (in particular in winter) for 12 GCMs in Europe when using their reduction methodology.

The spatial correlation behaviour is hard to evaluate, because only a few grid boxes of each model are analysed for the re-analyses and GCMs. At first sight, no striking differences appeared from the data. The RCMs somewhat overestimate spatial correlation lengths (RE ~15-20 %). The temporal correlation lengths are overestimated by all models except CGCM1 and the RCMs (average RE ≈ 35 %). Spatial and temporal correlation behaviour is further considered in the regional analysis in 4.3.3

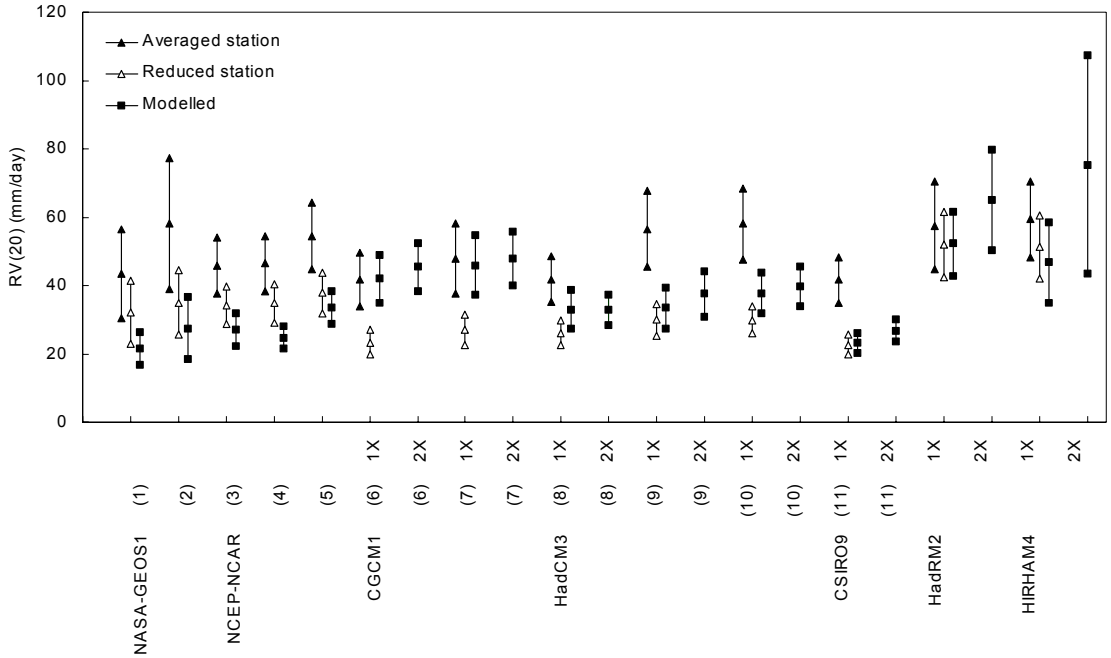

Figure 4.12 Precipitation 20-year return values RV(20) with 95%-confidence intervals in mm/day for different models (1-3 grid boxes) and corresponding averaged and reduced station values. The numbers refer to the grid boxes used and are defined in Figure 4.9. For HadRM2 and HIRHAM4 average values over 11 respectively 12 grid boxes are given. Results for current (1X) and changed (2X) climate are shown.

Precipitation 20-year return values *RV*(20) with 95%-confidence intervals for the averaged station series, the reduced station series and the modelled series for the grid boxes in the Meuse area are given in Figure 4.12. Differences between model scale return values calculated from average station series and reduced station return values are small only for the RCMs, which have the highest spatial resolution. Differences between return values calculated by the two methods seems to be larger for larger grid box areas. This can be explained by the fact that for large grid boxes only part of the box is covered by stations and therefore averaging over the complete grid box is not achieved. Here, this results in an overestimation of the extreme values by averaging station values and therefore the reduction methodology should be used.

Return values are simulated very well by HIRHAM4 (~ 10 % underestimation) and by CSIRO9 and HadRM2 (difference negligible). They are underestimated by the re-analyses (NASA-GEOS1 ~25 % and NCEP-NCAR ~20 %) and overestimated by CGCM1 (~75 %) and HadCM3 (~20%). In particular, CGCM1 performs quite poorly, which would not be concluded when looking at averaged station values alone. In that case CGCM1 would come out as the best model for simulating extreme precipitation. It

is not possible to compare the results for CGCM1 with the results of Kharin and Zwiers (2000), because of the reduced observed values used here. Kharin and Zwiers attributed the underestimation of in particular the re-analyses to the point vs. grid box effect, but this effect has been corrected for in this study. As mentioned in section 4.2.1, re-analysis precipitation values are not directly affected by observations and therefore large differences can be expected. This was observed for other statistics as well (mean, standard deviation). Katz (1999) mentioned that applications of extreme value theory to GCM output are rare with Zwiers and Kharin (1998) and Kharin and Zwiers (2000) apparently being the first to do so. Therefore, no other comparative material can be taken into consideration.

In the extreme value reduction methodology it is assumed that non-zero daily averaged precipitation values are gamma distributed and annual maximum daily averaged precipitation values are Gumbel distributed. The *PPCC* test failed to reject the hypothesis of annual extreme averaged station values being Gumbel distributed and partly failed to reject the hypothesis for the modelled values. Differences between calculated and critical (α = 0.05) *PPCC* values for the gamma distribution for the averaged station and modelled values in the Meuse area are quite small. Similar arguments as discussed in 4.3.1 for the exponential distribution applies to the gamma distributed averaged values. It may therefore be reasonable to assume this distribution and the Gumbel distribution for respectively non-zero and annual maximum daily averaged precipitation values.

Temperature

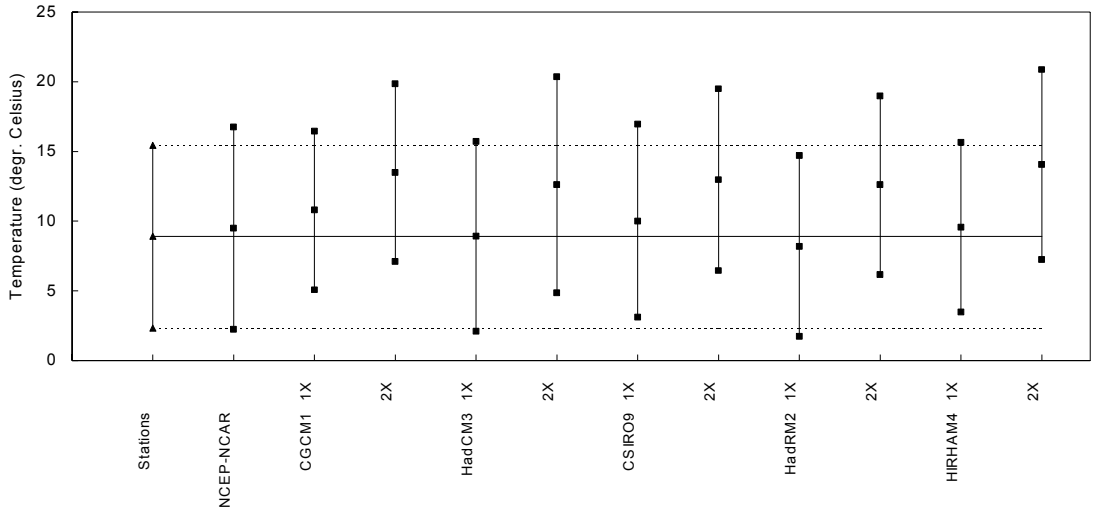

Figure 4.13 Average temperature (middle point) and standard deviation of temperature in °C for different models in the local analysis. The horizontal lines give the average and standard deviation of the station temperature. Results for current (1X) and changed (2X) climate are shown.

The average and standard deviation of the temperature for the averaged station and modelled series for grid boxes in the Meuse area are given in Figure 4.13. The average temperature is well simulated by HadCM3 (difference = dT < 0.1 °C), moderately by

NCEP-NCAR, HadRM2 and HIRHAM 4 (0.1 °C < dT < 1 °C) and poorly by CGCM1 and CSIRO9 (dT > 1 °C). These differences are small compared with GCM results for Europe in Marinucci *et al*. (1995) [1.3 °C overestimation with ECHAM3 GCM for Alpine region], Jones *et al*. (1995) [1.3 °C underestimation with HadCM2], Marinucci and Giorgi (1992) [1.2 °C underestimation with NCAR CCM], Kittel *et al*. (1998) [0.5-6 °C biases with nine different GCMs for Northern Europe] and Giorgi and Francisco (2000) [about 1 °C bias for different experiments with HadCM2 for Northern Europe]. RCM results for Europe are similar to these GCM results [e.g. 1.4 °C underestimation in Marinucci *et al*. (1995) with NCAR/PSU MM4 for Alpine region].

The temperature variability is well simulated by HadRM2 (dT in daily standard deviation < 0.1 °C), moderately by HadCM3, CSIRO9 and HIRHAM 4 (0.1 °C < dT < 0.5 °C) and poorly by NCEP-NCAR and CGCM1 (dT > 0.5 °C). Mearns *et al*. (1995) mainly found underestimations of daily temperature variability when simulating with the RegCM RCM over the United States. Giorgi and Francisco (2000) found large biases (0.5 °C < dT < 1 °C) in the interannual standard deviation for different experiments with HadCM2 for Northern Europe. Bell *et al*. (2000) generally found overestimations of the interannual standard deviation when comparing results from 16 GCMs over land. Overall, it was found from the comparison presented here that HadCM3 and the regional models simulate daily temperature behaviour quite well and in particular CGCM1 poorly reproduces this behaviour. The spatial and temporal correlation behaviour is discussed in the regional analysis.

4.3.3 Model scale statistics for regional area and current climate

Precipitation

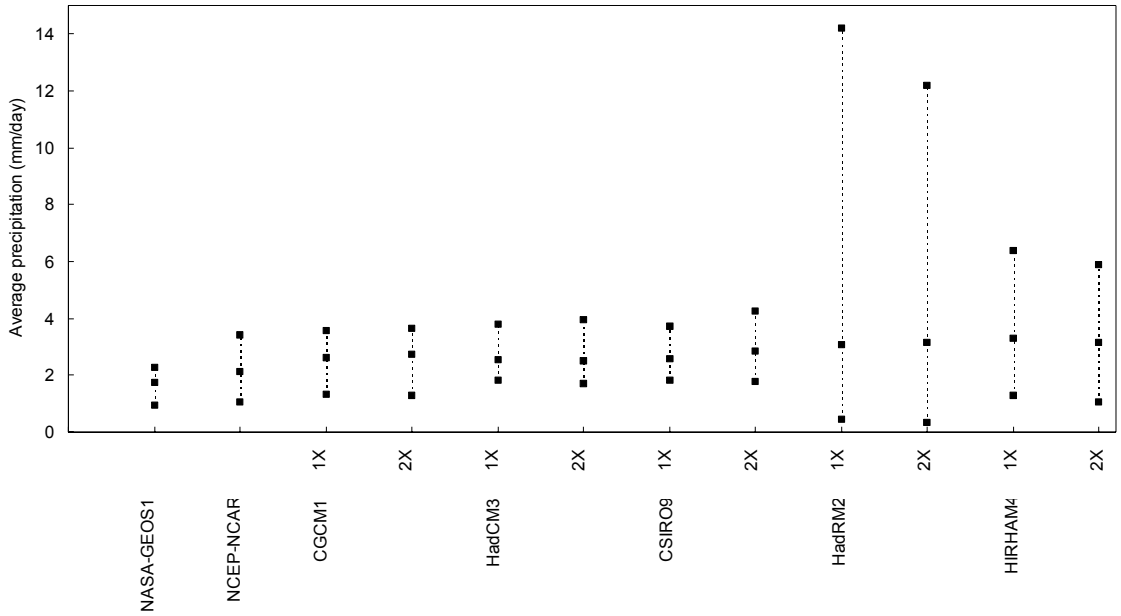

Figure 4.14 Average precipitation in mm/day in the regional analysis for NASA-GEOS1 (30 grid boxes), NCEP-NCAR (42), CGCM1 (16), HadCM3 (20), CSIRO9 (15), HadRM2 (404) and HIRHAM4 (308). Mean (middle point), minimum and maximum of the grid boxes are given. Results for current (1X) and changed (2X) climate are shown.

Average precipitation for the two re-analysis projects, three GCMs and two RCMs is summarised in Figure 4.14 by the mean, minimum and maximum of the grid boxes (in the large black box in Figure 4.1). The two re-analysis projects underestimate average precipitation compared to the GCMs (~0.5-1.0 mm/day or RE ~20-40 %), while the RCMs overestimate average precipitation (RE ~20-30 %) compared to the GCMs. Furthermore, when including the results from the local analysis (sub-section 4.3.2) and assuming that the station values are representative for the regional area, the conclusion seems to be justified that the GCMs and RCMs simulate average precipitation in a more acceptable way than the re-analysis projects. However, we should keep in mind the differences found in 4.3.2. The spatial variability of average precipitation is somewhat higher than that for stations, which is not surprising in view of the much larger area studied. Jones *et al*. (1995) found with the HadCM2 GCM for Europe a mean pattern correlation coefficient between observations and simulations of 0.85 implying reasonable simulation of the spatial variability (with monthly values).

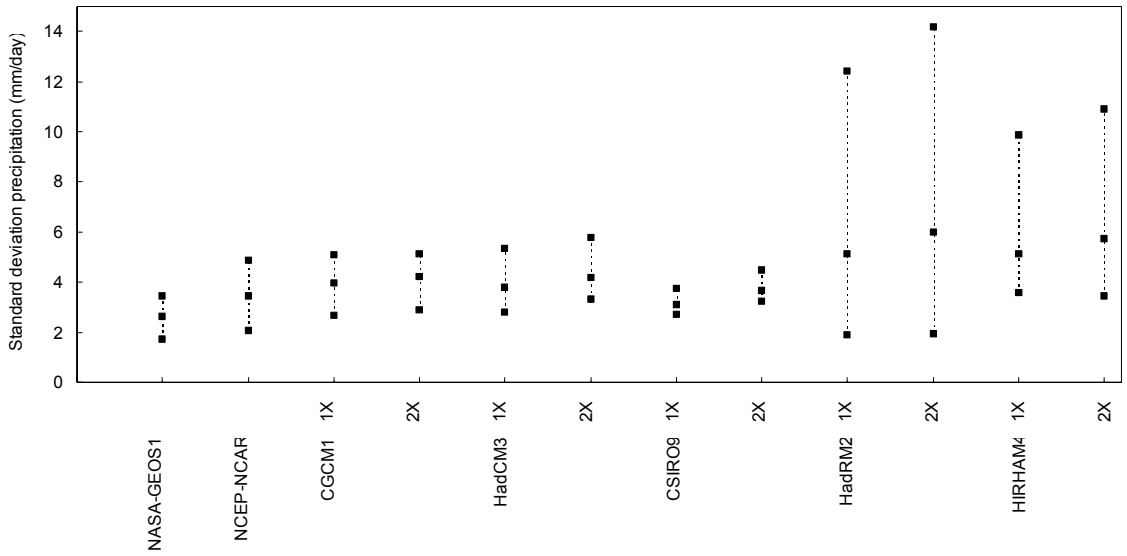

Figure 4.15 Standard deviation of precipitation in mm/day in the regional analysis for NASA-GEOS1, NCEP-NCAR, CGCM1, HadCM3, CSIRO9, HadRM2 and HIRHAM4. Mean (middle point), minimum and maximum of the grid boxes are given. Results for current (1X) and changed (2X) climate are shown.

The standard deviation of precipitation for the two re-analysis projects, three GCMs and two RCMs is summarised in Figure 4.15 by the mean, minimum and maximum of the grid boxes. Similar results as for the average have been obtained for the standard deviation of precipitation. The regional comparison largely confirmed the results from the local analysis. In particular, NASA-GEOS-1 underestimates the standard deviation. The differences between models can amount up to RE = 50 %, which is in the same range as the differences found by Osborn and Hulme (1998) for a slightly larger European region.

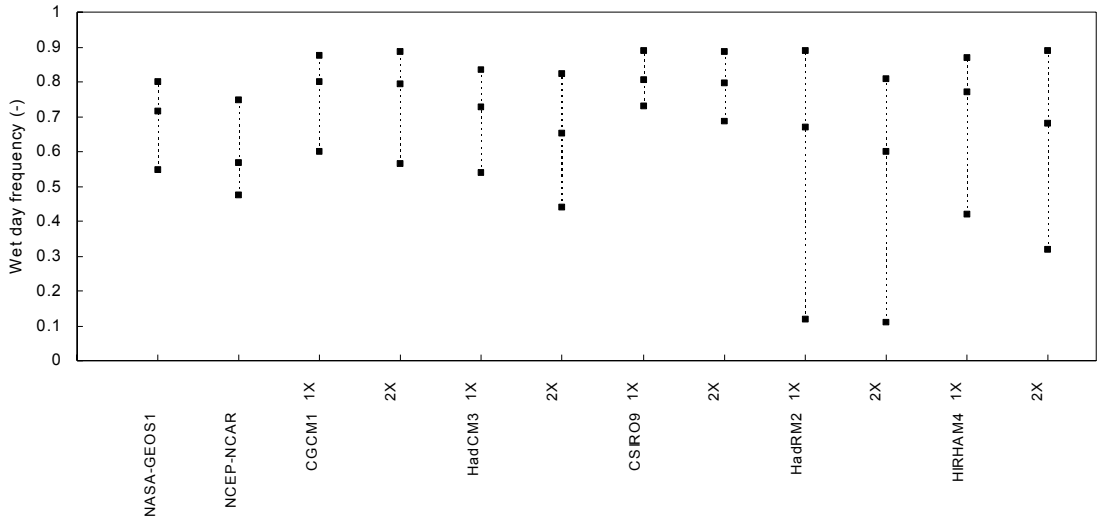

Figure 4.16 Wet day frequency in the regional analysis for NASA-GEOS1, NCEP-NCAR, CGCM1, HadCM3, CSIRO9, HadRM2 and HIRHAM4. Mean (middle point), minimum and maximum of the grid boxes are given. Results for current (1X) and changed (2X) climate are shown.

The wet day frequency for the two re-analysis projects, three GCMs and two RCMs is summarised in Figure 4.16 by the mean, minimum and maximum of the grid boxes. As in the local analysis, it seems that all models except NCEP-NCAR estimate a too wet climate (drizzly climate). Wet day frequencies tend to be overestimated and vice versa for dry day frequencies. However, this drizzling effect often is exaggerated, because of the direct comparison of station and GCM values.

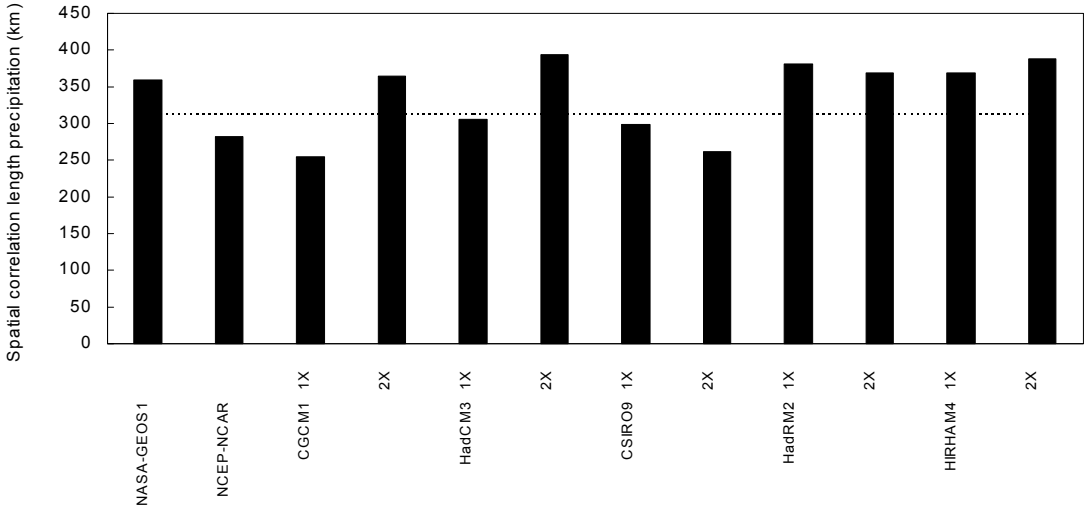

Figure 4.17 Spatial correlation length in km in the regional analysis for NASA-GEOS1, NCEP-NCAR, CGCM1, HadCM3, CSIRO9, HadRM2 and HIRHAM4. The dotted line gives the average station spatial correlation length. Results for current (1X) and changed (2X) climate are shown.

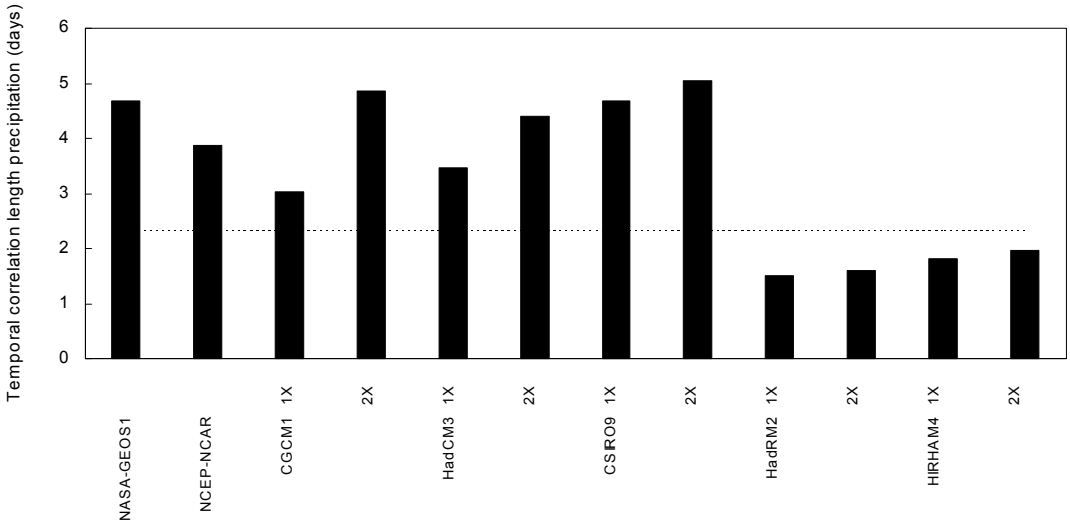

Figure 4.18 Temporal correlation length in days in the regional analysis for NASA-GEOS1, NCEP-NCAR, CGCM1, HadCM3, CSIRO9, HadRM2 and HIRHAM4. The dotted line gives the average station temporal correlation length. Results for current (1X) and changed (2X) climate are shown.

The spatial and temporal correlation length for precipitation for the two re-analysis projects, three GCMs and two RCMs are summarised by their means in Figure 4.17 and Figure 4.18. Differences between mean correlation lengths can be substantial. These can amount up to more than 100 km for the spatial correlation length and almost 2 days for the temporal correlation length. Remarkably, the modelled spatial correlation lengths compare favourable with the observed ones as opposed to the differences found for the temporal correlation lengths. The temporal correlation lengths estimated from the RCMs compare favourable with the value found by Hoosbeek (1998), but are less than those observed for the Meuse area. They deviate considerably from the temporal correlation lengths estimated by the other models, which can be partly explained by the larger variability in the RCMs (30-100 %) due to scale differences.

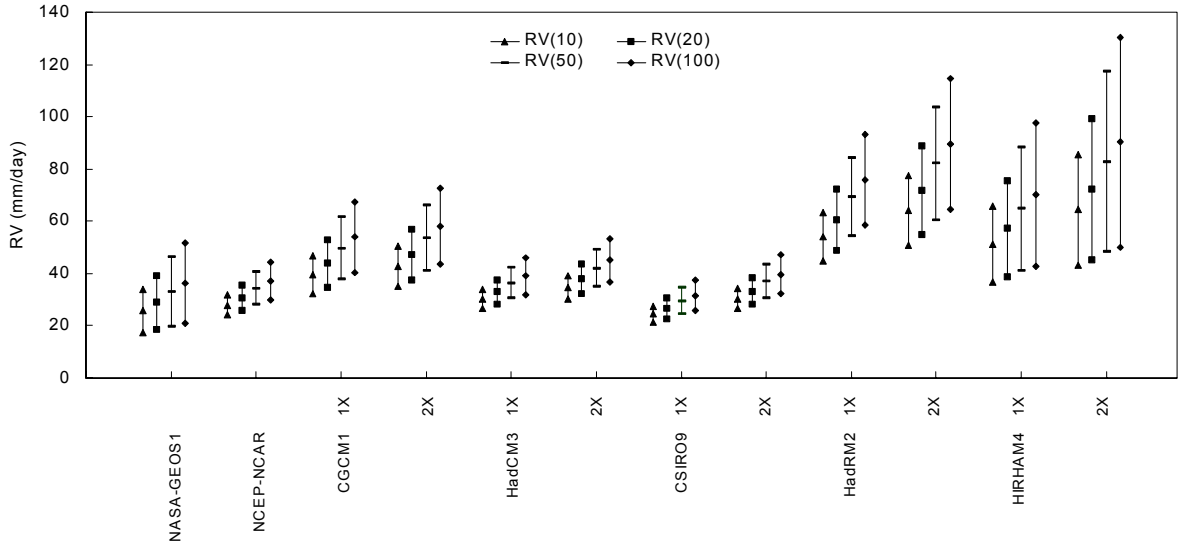

Figure 4.19 Mean of precipitation return values RV with 95%-confidence intervals in mm/day in the regional analysis for NASA-GEOS1, NCEP-NCAR, CGCM1, HadCM3, CSIRO9, HadRM2 and HIRHAM4. Results for current (1X) and changed (2X) climate are shown.

Precipitation return values $RV(T)$ for T=10, 20 50 and 100 years with 95%-confidence intervals for the two re-analysis projects, three GCMs and two RCMs are summarised by their means in Figure 4.19. Similar conclusions as in section 4.3.2 apply to this regional comparison assuming station values are representative. The return values of NASA-GEOS1, NCEP-NCAR, HadCM3 and CSIRO9 are comparable and those of CGCM1 and the RCMs are about 40-60 % higher. The 95%-confidence intervals of these former four models fall completely or almost completely outside the 95%-confidence intervals of the latter three models. It should be kept in mind that spatial resolutions of the RCMs are much higher and therefore RCM extreme values 'upscaled' to re-analysis and GCM scale are more comparable to re-analysis and GCM extreme values, as has been found in the local analysis. Kharin and Zwiers (2000) found a global average $RV(20)$ for CGCM1 which was 15 mm/day higher than the corresponding value in the ECMWF re-analysis (Gibson *et al.*, 1997). This difference is comparable to the difference found here.

Overall, it seems that the re-analysis data are not well suited to validate GCM and RCM model precipitation given the differences with average station data for this particular area. Only with respect to the dry-wet day frequencies one re-analysis project (NCEP-NCAR) performed significantly better than the GCMs and RCMs. Re-analysis precipitation is solely derived from model fields and in fact is a modelled value as well. Insufficient spin-up in the re-analyses and the role of soil moisture are responsible for these shortcomings (Van den Dool, pers. comm.). Soil moisture determines evaporation and thus air humidity and precipitation. On the other hand, precipitation is an important parameter in determining soil moisture and thus if precipitation is wrong, soil moisture is wrong, precipitation is wrong etc. The necessity of re-analysis data is therefore questioned and for the time being, without contrasting data or literature, use of re-analysis precipitation data is not recommended (note that for areas for which station data availability is scarce one has to use re-analysis data).

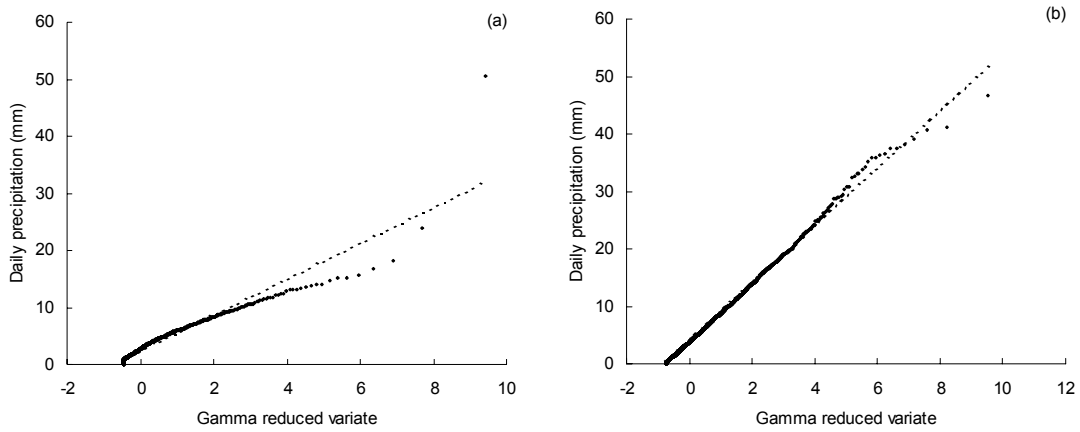

Figure 4.20 Worst (a) and best (b) goodness-of-fit for gamma distributed areally mean values.

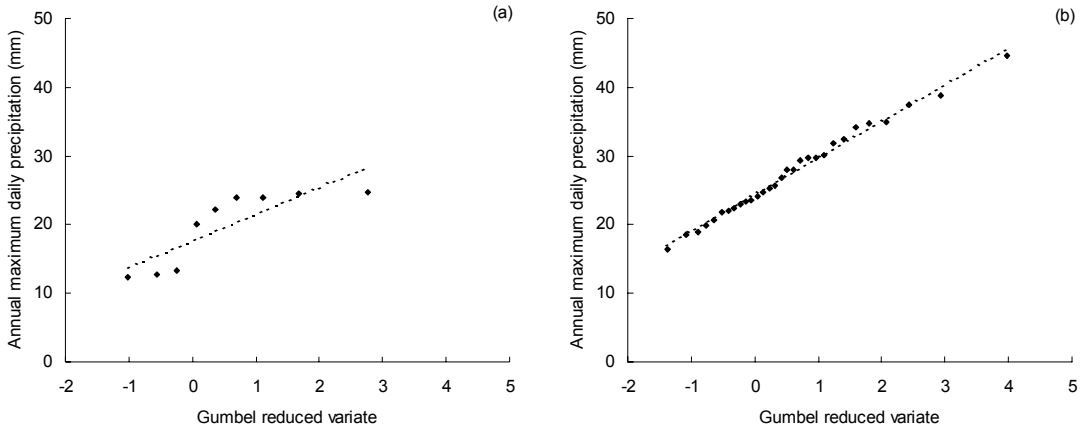

Figure 4.21 Worst (a) and best (b) goodness-of-fit for Gumbel distributed annual maximum areally mean values.

Again, differences between calculated and critical (α = 0.05) *PPCC* values for the gamma distribution are very small. The failure rates with respect to rejection for the annual extreme values being Gumbel distributed varied for the different models and re-analysis projects between 81 % and 100 %. The worst and best goodness-of-fit for the gamma and Gumbel distribution are shown in respectively Figure 4.20 and Figure 4.21. With similar reasoning as in 4.3.1 and 4.3.2, it is assumed that non-zero and annual maximum daily averaged precipitation values are respectively gamma and Gumbel distributed.

Temperature

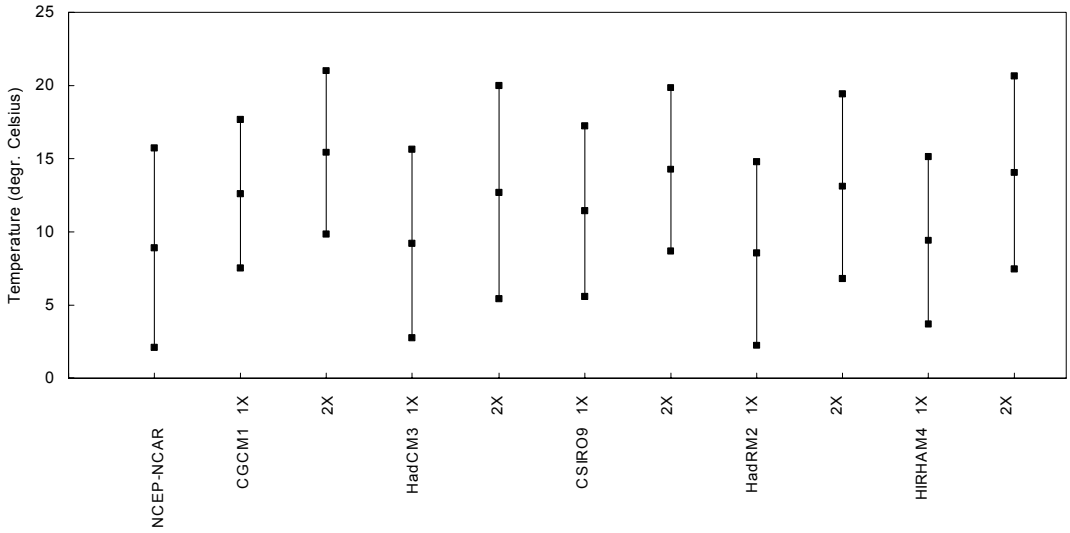

Figure 4.22 Average temperature (middle point) and standard deviation of temperature in °C for NCEP-NCAR, CGCM1, HadCM3, CSIRO9, HadRM2 and HIRHAM4 in regional analysis. Results for current (1X) and changed (2X) climate are shown.

The average and standard deviation of the temperature for the modelled series for the regional analysis are given in Figure 4.22. There is a considerable difference between the average temperature simulated by CGCM1 and CSIRO9 and the other models (2-4 °C), as already observed in the local analysis. The underestimation of the temperature variability by CGCM1 in the local analysis is confirmed in the regional analysis. Furthermore, it seems that CSIRO9 and HIRHAM4 underestimate temperature variability as well.

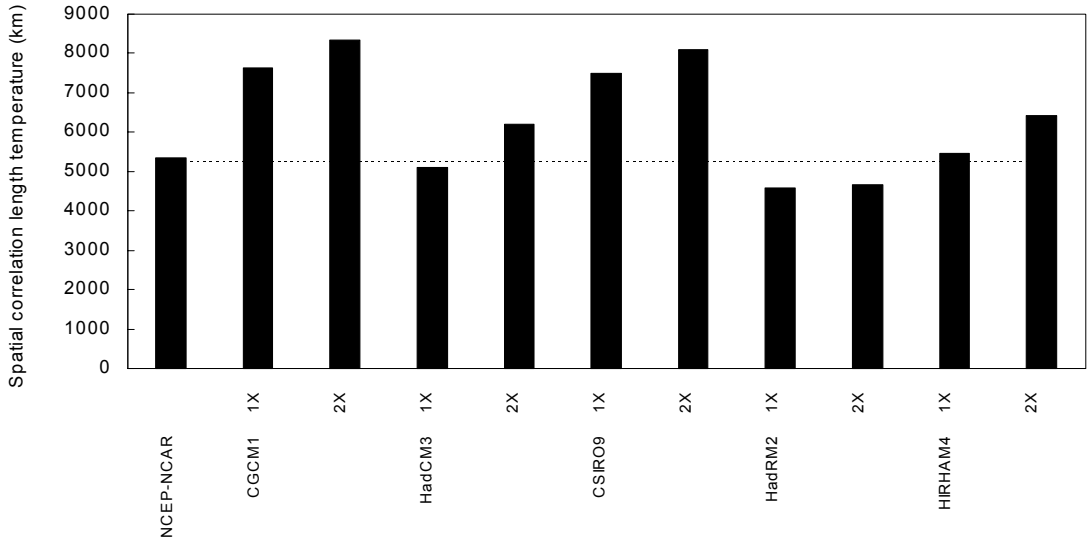

Figure 4.23 Spatial correlation length in km in the regional analysis for NCEP-NCAR, CGCM1, HadCM3, CSIRO9, HadRM2 and HIRHAM4. The dotted line gives the average station spatial correlation length. Results for current (1X) and changed (2X) climate are shown.

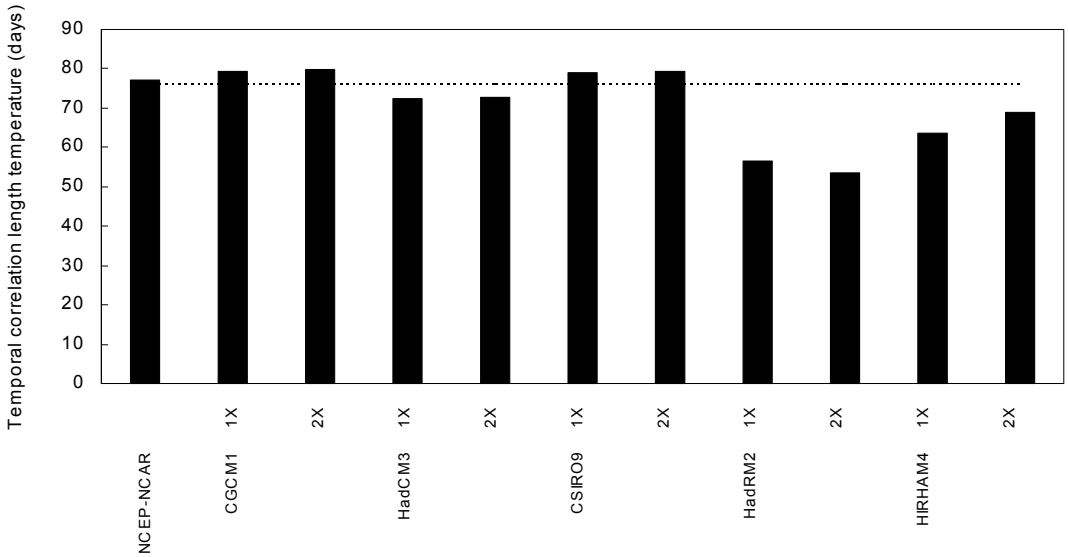

Figure 4.24 Temporal correlation length in days in the regional analysis for NCEP-NCAR, CGCM1, HadCM3, CSIRO9, HadRM2 and HIRHAM4. The dotted line gives the average station temporal correlation length. Results for current (1X) and changed (2X) climate are shown.

The spatial and temporal correlation length for temperature for the re-analysis project, three GCMs and two RCMs are summarised by their means in Figure 4.23 and Figure 4.24. The spatial correlation lengths are somewhat underestimated by NCEP-NCAR, CGCM1 and CSIRO9 and considerably underestimated by the other three models (> 20 %) in the local analysis (not shown here). Results from the regional analysis in Figure 4.23 suggest that CGCM1 and CSIRO9 overestimate spatial correlation lengths (more than 40 %) and the other models perform quite well (< 20 %) assuming the station values are representative for the regional area. Combining the results from these two analyses, it seems that NCEP-NCAR simulates spatial temperature behaviour most acceptable. The temporal correlation lengths are well simulated by the re-analysis and GCMs and rather underestimated (15-30 %) by the RCMs in the local and regional analysis. This underestimation by the RCMs would not be expected given the reasonable simulation of the daily temperature variability. Probably, the variability on larger time scales (weekly, monthly) is overestimated by the RCMs and therefore temporal correlation lengths are underestimated.

4.3.4 Model scale statistics for changed climate

Precipitation and temperature statistics of the three GCMs and two RCMs for the local analysis and climate change conditions are given in the figures in 4.3.2. Statistics for the regional analysis and climate change conditions are given in 4.3.3. Most striking features will be successively discussed for the local and regional analysis for precipitation and temperature.

Precipitation

Average precipitation values do not show significant changes in Figure 4.9 (~5 %), while Whetton *et al*. (1993) and Jones *et al*. (1997) showed respectively with the CSIRO9 GCM for the globe and HadCM2 for Europe average increases of about 10 % and Giorgi *et al*. (1992) simulated with NCAR CCM for Western Europe increases of about 15 %. The standard deviation of precipitation for grid boxes in the Meuse area increases in all models under climate change conditions by about 10-20 % in Figure 4.10. Return values increase for 5 out of 6 GCM grid boxes in the Meuse area by 5-15 % (Figure 4.12). The RCMs simulated an average increase in return values of 25 % (HadRM2) and even 60 % (HIRHAM4). Kharin and Zwiers (2000) obtained with CGCM1 a global mean increase in return values of about 15 %, but found for the European region an increase less than 10 %. The models gave different results with respect to the dry and wet day frequencies (Figure 4.11). These frequencies remain more or less unchanged in CGCM1 and CSIRO9, while the results show a trend towards more dryness (30-40 % more dry days) in HadCM3 and the RCMs. Temporal correlation lengths increase for HadCM3 and CGCM1, in one grid box of CGCM1 with more than 80 %. The spatial variability of the average and the standard deviation remains unchanged, while it slightly decreases for return values (2-10 %) and slightly increases for dry and wet day frequencies and temporal correlation lengths. Although the increased correlation lengths suggest less spatial variability, this may not hold for the spatial variability of summary statistics like the average and the standard deviation. Return values are more directly related to the underlying daily values and therefore show some decrease in spatial variability.

In the regional analysis, the results from the local analysis are confirmed to a large extent, although increases of return values for in particular HIRHAM4 are less extreme (Figure 4.19). There is a difference in mean increase of return values between CGCM1 (~8 %), HadCM3 (~15 %), CSIRO9 (~25 %), HadRM2 (~19 %) and HIRHAM4 (~27 %). This means an average increase in extreme precipitation with climate change of about 18 %, which could have considerable consequences. The correspondence between the results from Kharin and Zwiers (2000) and the results of CGCM1 presented here is obvious, because both results are at the same spatial scale. Spatial and temporal correlation lengths show a considerable increase (30-40 %) for the GCMs, implying more correlation and less variability.

Temperature

The models agree on the fact that the temperature is going to rise with a doubling of CO_2. There is some difference between the GCMs (CGCM1 +2.7 °C, HadCM3 +3.7 °C CSIRO9 +2.9 °C) and RCMs (HadRM2 + 4.4°C and HIRHAM4 + 4.5°C) in the local analysis in Figure 4.13 as well as in the regional analysis in Figure 4.22 (changes respectively +2.8, +3.5, +2.9, +4.6, +4.7 °C). The average predicted temperature change in the local and regional analysis is thus about 3.7 °C. This change is comparable with the results from GCMs of 4.4 and 3.5 °C temperature increase in respectively HadCM2 (Jones *et al*., 1997) and NCAR CCM (Giorgi *et al*., 1992) and results from RCMs of 3.6, 4.0 and 2.8 °C temperature increase in respectively NCAR/PSU MM4 (Giorgi *et al*., 1992), HadRM2 (Jones *et al*. 1997) and again NCAR/PSU MM4 (Rotach *et al*., 1997).

The models differ with respect to the change in temperature variability in Figure 4.13 and Figure 4.22. CGCM1, HadCM3 and HIRHAM4 predict an increase in temperature variability (0.5-1 °C for the standard deviation), whereas HadRM2 does not simulate significant changes in variability and CSIRO9 even predicts a decrease in variability. Gregory and Mitchell (1995) also predicted a decrease in variability in European winter with HadCM1. Mearns *et al*. (1995) found substantial changes in temperature variability when simulating with the RegCM RCM over the United States. They observed large decreases in variance throughout winter and early spring and sharp increases in variance in late spring and early summer. Only HadCM3 and HIRHAM4 predict a significant increase in the spatial correlation length of temperature according to Figure 4.23 (> 20 %). The models do not simulate significant changes in temporal correlation behaviour (Figure 4.24).

Major changes in climate due to a doubling of carbon dioxide are an increase in precipitation variability (10-20 %) and extreme precipitation (15-25 %) and an increase in average temperature of about 3.7 °C. In general, this implies an intensification of the hydrological cycle. Minor changes include a slight increase in average precipitation, more dry days and an increase in temporal and spatial correlation lengths for precipitation.

4.3.5 Appropriate scale statistics for local area

The appropriate spatial scales can be assessed and the statistics from the preceding sections can be translated to these appropriate scales as described in section 2.3 (e.g. Figure 2.12). Suppose the permitted bias in the estimation of the statistics is set at 10 %. Then, the appropriate scale for the standard deviation of precipitation and the wet day frequency is estimated at 21 % of the average spatial correlation length (see Figure 2.9) and is 60 km. The appropriate scale for extreme precipitation is estimated at 25 % of the spatial correlation length associated with extreme precipitation (Figure 2.11) and is 20 km. This 20 km scale will be used as the appropriate scale for all precipitation statistics, because extreme precipitation is of major importance for river flooding. The appropriate scale becomes 10 km and 30 km, if the permitted bias is set at respectively 5 % or 15 %. Thus, the permitted bias influences seriously the appropriate scale and should therefore be solidly founded. It is assumed that the parameters from the reduction methodologies remain unchanged with changed climate (λ, υ_1, υ_2, β_1, β_2) and considerable reduced scale (β_1, β_2).

Assuming the same criteria for temperature statistics results in an appropriate scale of approximately 1000 km, which is much more than the extent of the Meuse area and the climate model resolutions. Therefore, modelled temperature data can directly be used and consequently it is not necessary to translate temperature statistics to statistics at appropriate scales.

Precipitation

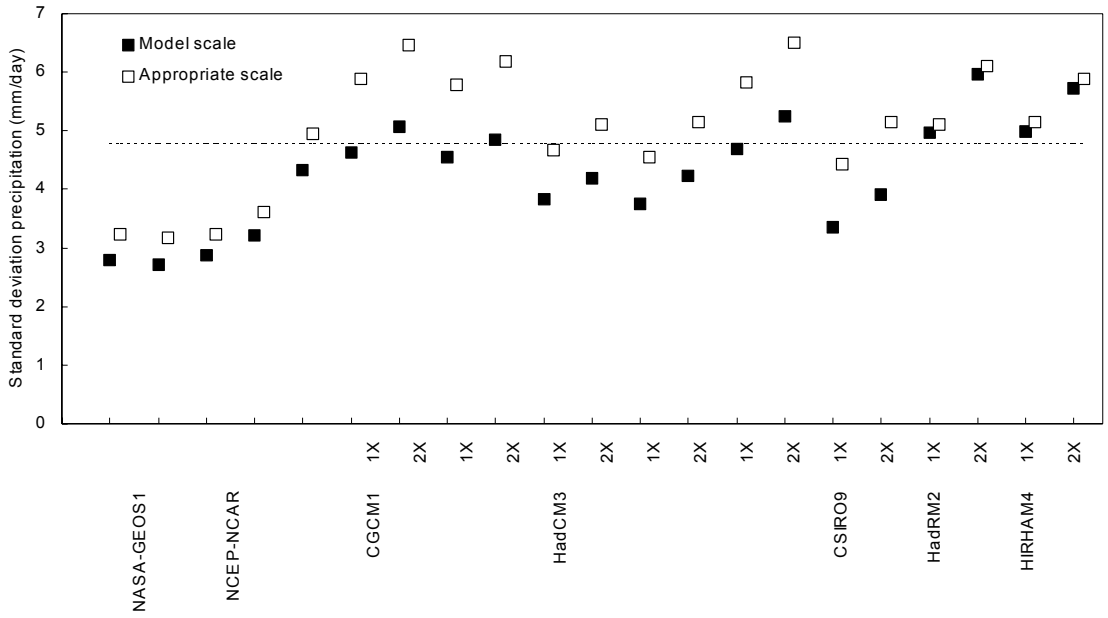

Figure 4.25 Model scale and appropriate scale (20 km) standard deviation of precipitation in mm/day for NASA-GEOS1, NCEP-NCAR, CGCM1, HadCM3, CSIRO9, HadRM2 and HIRHAM4. The dotted line gives the average scaled station standard deviation. Results for current (1X) and changed (2X) climate are given.

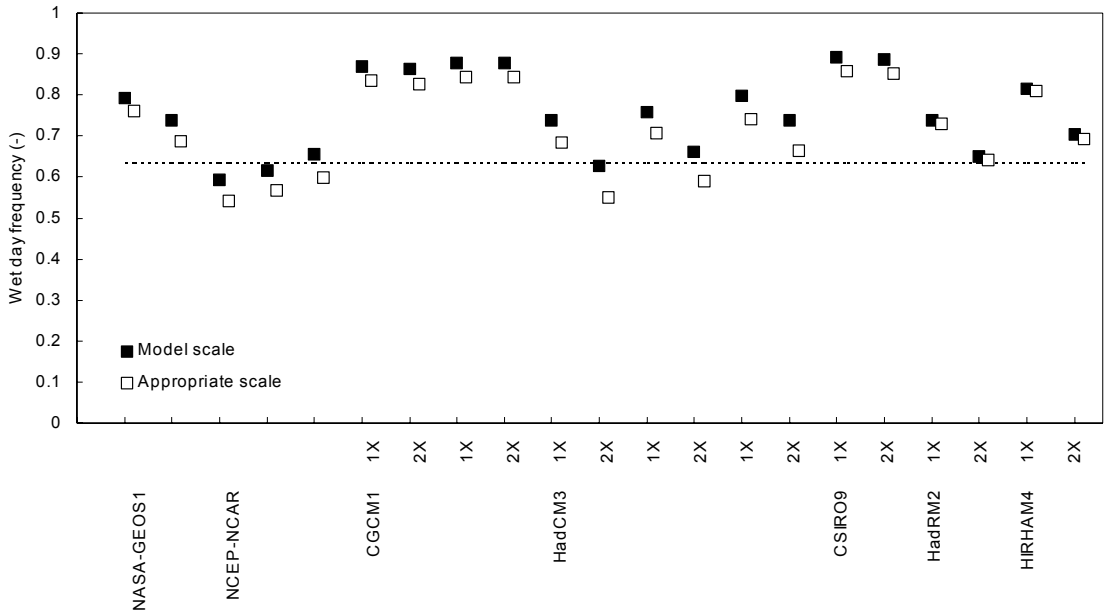

Figure 4.26 Model scale and appropriate scale (20 km) wet day frequencies for NASA-GEOS1, NCEP-NCAR, CGCM1, HadCM3, CSIRO9, HadRM2 and HIRHAM4. The dotted line gives the average scaled station wet day frequency. Results for current (1X) and changed (2X) climate are given.

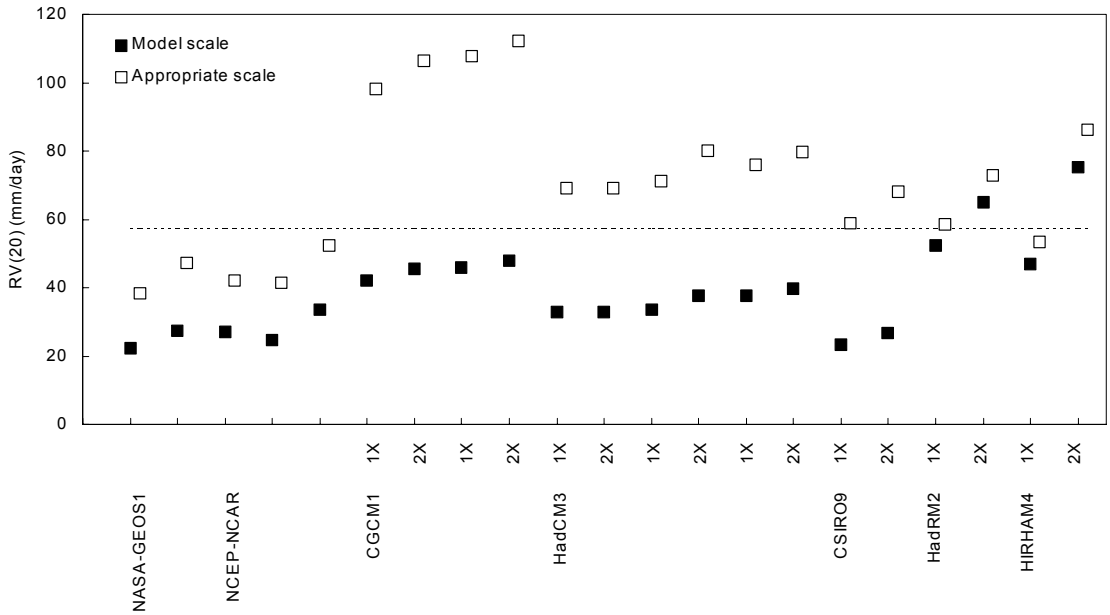

Figure 4.27 Model scale and appropriate scale (20 km) precipitation 20-year return values RV(20) in mm/day for NASA-GEOS1, NCEP-NCAR, CGCM1, HadCM3, CSIRO9, HadRM2 and HIRHAM4. The dotted line gives the average scaled station RV(20). Results for current (1X) and changed (2X) climate are given.

The results for the standard deviation, wet day frequency and 20-year return values for the two re-analyses, three GCMs and two RCMs for the appropriate and model scale are given in Figure 4.25, Figure 4.26 and Figure 4.27. These statistics can now also be compared at identical scales.

The results in Figure 4.25 and Figure 4.26 show considerable differences between re-analysis/ GCM scale and appropriate scale standard deviation and wet day frequency (RE up to 40 %, about 20 % on average). The results in Figure 4.27 show even larger differences between re-analysis scale and appropriate scale return values (50-70 %) and GCM scale and appropriate scale return values (> 100 %). It is obvious that for these models statistics at appropriate scales should be used instead of at the original scales. Differences between appropriate and original scale RCM statistics are small (<10 %), because of the higher resolution of the RCMs. RCM precipitation data therefore may be directly used as input in the river basin model. The results presented here confirm the results from sub-sections 4.3.2 and 4.3.3, e.g. the good agreement of CSIRO9 and RCM simulated extreme precipitation and station extreme precipitation and the overestimation of extreme precipitation by CGCM1. The appropriate scale statistics are approximately the point statistics implied for each model, because the reduction factors κ^2, R_1 and R_2 are close to 1 for the appropriate scales.

It was assumed that the parameters necessary to calculate the reduction factors remain unchanged with changed climate and geographic scale. It has not been attempted to verify this, but a first insight can be gained when the modelled spatial correlation lengths for the current and changed climate are compared. It was found that λ increases considerably with changed climate for all models (30-40 %). Osborn (1997) considers the possibility of changes in spatial scales of precipitation events as well. A larger λ results in an increase of the appropriate scale to 25-30 km. This will give less reduction and thus slightly smaller differences between model and appropriate scale return values (2-3 %). Similar or opposite results might be obtained for the other parameters. However, these differences are considered of minor importance with respect to the already found differences between model and appropriate scale statistics.

4.3.6 Uncertainties for local area

A first assessment of the total uncertainties can now be made by means of the procedure outlined in 4.2.2. The uncertainty will be assessed for the standard deviation and return values of daily precipitation with climate change simulated by the GCMs and RCMs at the appropriate scale and for the average and standard deviation of daily temperature with climate change simulated by the GCMs and RCMs.

Precipitation

Standard deviation. The model error (uncertainty 2) and intermodel uncertainties (mean of 3 and 5) for the GCMs expressed as RE are respectively about 12 % and 20 % (both uncertainty 3 and 5 are 20 %). The climate forcing uncertainty can not be extracted from the available data, but will be at least comparable with uncertainties 2 and 3/5. This uncertainty can be assessed by including more radiative forcing scenarios and ensembles (see Hulme and Carter, 1999). The uncertainties in Figure 4.2 have a rather stochastic nature, although the less important uncertainties 1 and 6 may have a more systematic nature. The uncertainties should therefore be summed in a quadratic rather than a linear way. This amounts up to 30-40 % if the main uncertainties are summed in this way (without sensitivity weighting factors). The uncertainties 2 and 3/5 for the RCMs are estimated as 10 % and 5 % (5/5). This amounts up to 15-20 % (including uncertainty 4). Important to mention is the fact that the intermodel uncertainties under current and changed conditions are almost equal, suggesting they are comparable and

even have similar origins. The calculated GCM uncertainty in the standard deviation of precipitation under climate change (noise ~30-40 %) is significantly larger than the simulated change (signal ~10 %). However, this uncertainty is not supposed to completely overshadow the simulated change, because some uncertainties seemed to be similar under current and changed climate conditions and there are no signs of abrupt changes in climate behaviour. The calculated RCM noise (15-20 %) and signal (12-17 %) are more comparable.

Return values. The model error and intermodel uncertainties are respectively about 23 % and 28 % (uncertainty 3 is 33 % and uncertainty 5 is 23 %). The total uncertainty amounts up to 50 % of the mean return value. It is only about 20 % when the CGCM1 results are not included in the calculation. However, it can be expected that results of other GCMs and RCMs not considered here may give similar over- or underestimations. Therefore, the uncertainty in mean return values with climate change is assumed to be about 50 %. It is important to note that the uncertainties due to extrapolation from annual maximum values to *T*-year return values is not included in this total uncertainty (the 95%-confidence intervals). The noise (~50 %) is again significantly larger than the signal (18 %).

Temperature

Average. The model error and intermodel uncertainties are respectively about 0.8 °C and 1.7 °C (uncertainty 3 is 2.1 °C and uncertainty 5 is 1.3 °C). The total uncertainty amounts up to 2-3 °C, which is comparable with the signal (3.7 °C).

Standard deviation. The model error and intermodel uncertainties are respectively about 0.5 °C and 0.8 °C (uncertainty 3 is 0.7 °C and uncertainty 5 is 0.9 °C). The total uncertainty is then about 1.3 °C, which is much more than the simulated change of about 0.4 °C.

A summary of the average changes predicted by the GCMs and RCMs and associated uncertainties (signal and noise) with respect to the precipitation and temperature statistics considered is given in Figure 4.28.

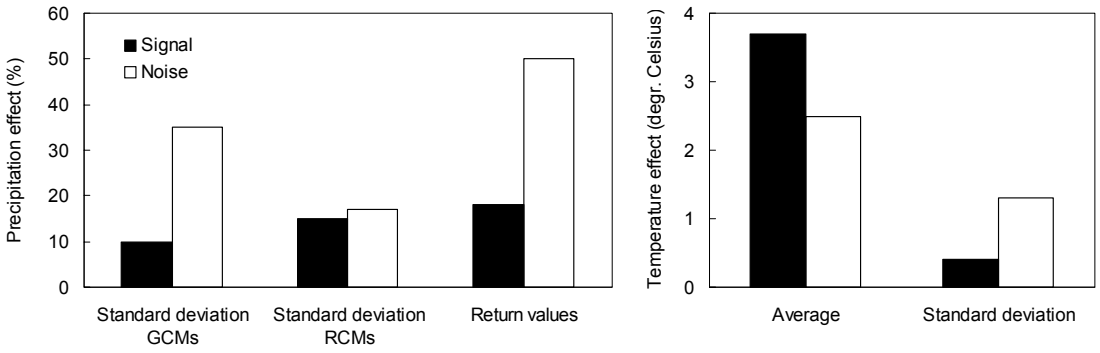

Figure 4.28 Average predicted changes and uncertainties (signal and noise) with respect to precipitation and temperature statistics.

4.4 Summary and conclusions

The average spatial correlation length of 300 km for daily station precipitation compares well with values found in literature, while the mean temporal correlation length could not be confirmed by earlier obtained results. The 95% confidence intervals and spatial variability of the precipitation station return values are large, which has rather a statistical than a physical cause. The average spatial correlation length for daily station temperature is large in comparison with the extent examined and is even underestimated according to extent vs. correlation length relationships.

The regional comparison for the current climate largely confirmed the results from the local analysis. Overall, it seems that the re-analysis data are not well suited to validate GCM and RCM precipitation data given the differences found with the station data for this particular geographic region. The re-analyses underestimated the mean and standard deviation and performed only moderately for the wet and dry day frequencies. CGCM1 simulated precipitation variability quite well (difference about 5 %), but tended to overestimate mean precipitation and wet day frequency. The goodness-of-fit of precipitation behaviour simulated by HadCM3, CSIRO9 and the RCMs (HadRM2 and HIRHAM4) fell in between CGCM1 and the re-analyses. Although differences between observations and model results were substantial, they were not unusual given the differences found in some other studies. Return values are simulated quite well by the RCMs and CSIRO9. They are underestimated by the re-analyses and overestimated by CGCM1 and HadCM3.

The model intercomparison with respect to return values would look quite different when only station averaged values were used. In that case CGCM1 would come out as the best model in simulating extreme precipitation. These results were found in the small domain 'local' analysis as well as in the medium domain 'regional' analysis.

Overall, it was found in the local analysis that HadCM3 and the regional models simulate daily temperature behaviour quite well, but in particular CGCM1 poorly reproduces this behaviour. In the regional analysis, the difference between average temperature simulated by CGCM1 and CSIRO9 and the other models is even larger (2-4 °C). The underestimation of the temperature variability by CGCM1 in the local analysis is confirmed in the regional analysis. Combining the results from both analyses, it seems that NCEP-NCAR simulates spatial temperature behaviour most acceptably. Temporal correlation lengths are well simulated by the re-analysis and GCMs and rather underestimated (15-30 %) by the RCMs in the local and regional analysis.

Average precipitation values do not show significant changes with climate change, while standard deviations increase by about 10 %. Return values increase for 5 out of 6 GCM grid boxes with climate change in the local analysis. In the regional analysis results from the local analysis are confirmed to a large extent. There is a difference in mean increase of return values between CGCM1 (~8 %), HadCM3 (~15 %), CSIRO9 (~25 %), HadRM2 (~19 %) and HIRHAM4 (~27 %). This means an average increase in extreme precipitation with climate change of about 18 %, which could have serious implications for society. The latter is in accordance with the few results found in literature. Spatial and temporal correlation lengths show a considerable increase (30-40 %), implying more correlation and less variability.

The models agree on the fact that the temperature is going to rise with a doubling of CO_2. The average predicted temperature change in the local and regional analysis is about 3.7 °C (2.9-4.7 °C). The models differ with respect to the change in temperature variability and only HadCM3 and HIRHAM4 predict a significant increase in the spatial correlation length of temperature (> 20 %).

The uncertainties associated with precipitation under climate change were assumed to have a stochastic rather than a systematic character. The uncertainty in the standard deviation of GCM modelled precipitation under climate change amounted up to 30-40 % if the main uncertainties are included (model error, inter-model uncertainties, climate forcing uncertainties and uncertainties due to up- and downscaling). This uncertainty is significantly larger than the simulated change of about 10 %. However, it is not supposed to completely cancel out the simulated change, because some uncertainties seemed to be similar under current and changed climate conditions and there are no signs of abrupt qualitative changes in climate behaviour in the near future. For the RCMs, noise (15-20 %) and signal (12-17 %) are more comparable. The calculated uncertainty in the precipitation return values under climate change of about 50 % is again significantly larger than the simulated change of about 18 %. The uncertainty in average temperature with climate change amounts up to 2-3 °C, which is comparable with the simulated change of about 3.7 °C. The uncertainty in the standard deviation of temperature with climate change is about 1.3 °C, which is much more than the simulated change of about 0.4 °C.

The reduction methodologies associated with the standard deviation, wet day frequencies and return values of precipitation can be used to compare point and areally mean values, but caution should be taken with respect to their use for the determination of wet day frequencies. Areally mean return values calculated by averaging station values and using the reduction methodology compare favourably only for the RCMs, which have the highest spatial resolution. The observed extreme values are overestimated when averaging over large areas partially covered by stations and it is therefore necessary to use the extreme value reduction methodology. It is recommended to use in this reduction methodology correlation lengths associated with extreme precipitation fields instead of average correlation lengths as has been done for standard deviations. Annual extreme precipitation fields are assumed to be appropriate in this case. It can reasonably be assumed that non-zero and annual maximum daily station precipitation values are respectively exponentially and Gumbel distributed and that non-zero and annual maximum areally mean precipitation are respectively gamma and Gumbel distributed. These assumptions have been supported by statistical significance tests and probability plots and have been used in the extreme value reduction methodology.

The appropriate scale for the standard deviation of precipitation and the wet day frequency was estimated at 21 % of the spatial correlation length or 60 km, when the permitted bias in the estimation of these statistics is set at 10 %. The appropriate scale for extreme precipitation was estimated at 25 % of the spatial correlation length or 20 km. This 20 km scale has been used as the appropriate scale for all precipitation statistics, because extreme precipitation is of major importance for river flooding. The results show considerable differences between model scale and appropriate scale standard deviation and wet day frequency (differences up to 40 %, about 20 % on

average). Differences for return values are even larger, for re-analysis scale and appropriate scale 50-70 % and GCM scale and appropriate scale more than 100 %. It is obvious that for these models statistics at appropriate scales instead of at their original scales should be used. Differences between appropriate and original scale RCM statistics are small (<10 %), because of the higher resolution of the RCMs. RCM precipitation data may therefore be directly used as input in for example a rainfall-runoff model. Assuming the same criteria for temperature statistics gives an appropriate scale of approximately 1000 km, which is much more than the extent of the Meuse area and the climate model resolutions. Therefore, modelled temperature data can directly be used and consequently it is not necessary to translate temperature statistics to statistics at appropriate scales.

Chapter 5

River basin analysis

5.1 Introduction

The occurrence of extreme discharges is controlled by atmospheric input and runoff processes in the river basin. The atmospheric input has been considered in chapter 4. Runoff processes such as overland flow and subsurface flow will be considered in this chapter. Main features related to these processes are the relative importance of flood generating processes, the appropriate spatial and temporal scales of these processes and the corresponding appropriate process formulations. These features together constitute the essential components of an appropriate river basin model for the simulation of river flooding.

In section 5.2, the processes and the related variables are discussed, in section 5.3 the appropriate scales of the most important variables are determined and integrated and in section 5.4 process formulations are considered. Finally, in section 4.4 the major findings are summarised.

5.2 Processes and variables

5.2.1 Processes in the river basin

The hydrological cycle is the most fundamental principle of hydrology. Water evaporates from the oceans and the land surface and is transpirated by vegetation. It is then transported over the earth in the atmospheric circulation as water vapour and precipitates again as rain or snow. In the land phase of the hydrological cycle, water is intercepted by vegetation, provides runoff on the land surface, infiltrates into soils, recharges groundwater and discharges into streams. Ultimately, it flows out into the oceans from which it will eventually evaporate once again. Every process in the hydrological cycle influences the amount of water flowing through a river. The dominant process is precipitation which is the key input into a river basin. The hydrological processes in the land phase mainly determine the fraction of precipitation available for river flow and the distribution in time of river flow. In this thesis, in particular the flood generating processes are of importance. These and other processes have been, and still are, extensively studied in so-called research catchments. These field studies have provided useful information on the occurrence and relative importance of flood generating processes under a variety of climatological and geographical conditions. The integrated river basin response as a result of the complex interactions between hydrological processes is predicted by rainfall-runoff models (see chapter 1).

5.2.2 Flood generating processes

Three processes are being recognised as being responsible for the relatively fast transport of precipitation to the stream network during flood events (Maidment, 1993):

- infiltration excess overland flow (Horton overland flow)
- saturation excess overland flow (Dunne overland flow)
- subsurface storm flow (interflow)

Infiltration excess overland flow is surface runoff produced at the ground surface when the rainfall intensity exceeds the infiltration capacity. It is named after Horton, who in the 1930's claimed that runoff peaks are generated by this mechanism only (Hall, 1987). Saturation excess overland flow occurs when, on part of the drainage basin, the surface horizon of the soil becomes saturated as a result of either the build up of a saturated zone above a soil horizon of lower hydraulic conductivity or the rise of a shallow water table to the surface (Maidment, 1993). Anderson and Burt (1990) recognise three locations where soil saturation relatively often occurs: near-stream areas at the base of a hillslope, hill slope hollows and locations where a low-conductivity subsurface layer is positioned close to the ground surface. Infiltration excess and saturation excess water flows through micro channels, rills and gullies to first-order streams and can thus be considered as extended stream systems. Subsurface storm flow is water that infiltrates into the soil and percolates rapidly, largely through macropores such as cracks and root and animal holes, and then moves laterally in a temporarily saturated zone. It reaches the stream channel quickly and differs from other subsurface flow by the rapidity of its response and its relatively large magnitude (Maidment, 1993).

The relative contributions of these three flood generating processes to a specific flood vary heavily between different watersheds and different precipitation events. Therefore, there is no uniformly valid concept of the relative importance of flood generating processes. However, field experiments have provided information on the influence of catchment characteristics on the relative contributions of flood generating processes. Diermanse (2001) summarised a number of catchment characteristics known to enhance a specific process:

- infiltration excess overland flow: impermeable soils, no vegetation and high rainfall intensities
- saturation excess overland flow: shallow, moderately permeable soils, concave-shaped hills and wide valley bottoms
- subsurface storm flow: steep straight slopes, deep permeable soils, forests and narrow valley bottoms

The majority of the river basins consists of a combination of these characteristics and therefore floods will be generated by a combination of the three processes. In particular in a large basin such as the Meuse, all kinds of combinations of catchment characteristics can be found. However, it is widely recognised that in vegetated basins with a humid climate (e.g. the Meuse basin) a large proportion of the flood runoff originates from a small saturated part of the basin (variable source area), mainly to be found adjacent to the stream (Diermanse, 2001). These areas are often saturated due to the relatively large upslope area and complete saturation is the requirement for saturation overland flow and the best condition for subsurface storm flow to occur. Furthermore, flow paths to the streams are relatively short.

A major consequence of the dominating role of saturated areas in generating floods is that soil moisture conditions at the beginning of a flood are of importance and should be accurately determined. These initial conditions are mainly influenced by the preceding precipitation, evapotranspiration and subsurface flow in the soil matrix. Additionally, the river flow itself contributes to the occurrence and magnitude of floods.

The next step is to link the important processes for flood generation to variables to be able to assess the appropriate scales for the different processes through the variables. The variables to be considered are meteorological variables and catchment characteristics. The most important variables for the flood generating processes and the processes important for the initial conditions will determined in the next sub-section.

5.2.3 From processes towards variables

Table 5.1 shows the most important variables influencing the different flood generating processes. These relations are based on several studies (e.g. Mauser and Schädlich, 1998; Veihe and Quinton, 2000) and general literature (e.g. Maidment, 1993; Shaw, 1994). Meteorological processes (precipitation, potential evapotranspiration) are treated as variables, because they are inputs into the river basin and thus are not explicitly modelled. It is obvious that precipitation influences all important processes, as already observed in sub-section 5.2.2. Other important variables in the flood generation process are elevation, land use and soil properties such as texture and parent material. Temperature is the most important variable determining potential evapotranspiration and the soil moisture content (texture, parent material) plays a significant role in the realisation of the actual evapotranspiration. The meteorological variables precipitation, temperature and potential evapotranspiration have been analysed in chapter 4. The catchment variables (elevation, soil, land use) and their related processes will be considered in the remainder of this chapter.

Table 5.1 Variables influencing the identified dominant processes.

Variables	Processes						
	Precipitation	Actual evapotranspiration	Infiltration excess overland flow	Saturation excess overland flow	Subsurface storm flow	Subsurface flow	River flow
Precipitation	■	■	■	■	■	■	■
Temperature	■						
Potential evapotranspiration		■					
Elevation	■	■		■	■		■
Land use		■	■	■	■		■
Soil texture		■	■	■	■	■	■
Macropores					■		
Soil parent material			■			■	

5.3 Spatial and temporal scales

5.3.1 Introduction

The spatial and temporal scales of elevation, soil and land use will be discussed in this section. The emphasis will be on the spatial scales, because the variables are relatively time-invariant. The variables elevation, soil and land use are taken to be independent of time on the temporal domain considered here (< 100 years). Although land use may show a seasonal dependence, in particular for agricultural areas and forests, and long term trends, it is assumed to be a time-invariant variable in this thesis. First, some examples of scale related studies with respect to elevation, soil and land use are given in Table 5.2 to identify possible generalities.

Table 5.2 Scale related studies with respect to elevation, soil and land use (appr. means appropriate).

Reference	Variable	Application area	Extent km^2	Support scale m	Method	Appr. scale m
Bruneau *et al*., 1995	elevation	Southern France	12	20-100	hydrological	<50
Brasington and Richards, 1998	elevation	Nepal	4.5	20-500	entropy	100-200
Wolock and McCabe, 2000	elevation	US	50 x 7000	100-1000	hydrological	2-2500
Farajalla and Vieux, 1995	soil property	Washita, US	610	30-2500	entropy	1200
Western *et al*, 1998	soil moisture	Australia	0.1	15	geostatistical	35-60
Cosh and Brutsaert, 1999	soil moisture	Washita, US	450	200	geostatistical	1000
Moody and Woodcock, 1995	land use	California, US	~2500	30-1020	statistical	250-500
Walsh *et al*, 2001	land use	Northern Thailand	1300	30-1050	statistical	~100
Kok *et al*., 2001	land use	Costa Rica, Honduras	$\sim 10^5$	15000-~300000	sensitivity	
Kok and Veldkamp, 2001	land use	central America	$\sim 10^5$	15000-75000	statistical	

In general, it can be concluded from the studies in Table 5.2 and other studies not shown here, that appropriate scales for elevation, soil type and land use type vary considerably dependent on geographical area (climate, vegetation), extent of the area and support scale of the data. For example, it is found that the scales determined by Farajalla and Vieux (1995) and Cosh and Brutsaert (1999) compare favourably, in contrast to the ones estimated by Western *et al*. (1998). This may be due to incorrect, large sampling distances in the former studies resulting in an overestimation of the 'true' appropriate scale. It should be mentioned that the spatial scales of land use have been mainly assessed in relation to land use change, implications of spatial scales of land use for hydrological modelling are rarely investigated. The extent and support scale are the basics of the scale triplet defined in chapter 2 and can have a substantial effect on the estimation of the correlation length and related appropriate scales (see Western and

Blöschl, 1999). Therefore, in the remaining part of this section the appropriate scales for the key variables will be determined and integrated taking into account the influences of these scale features.

5.3.2 Observed data

Elevation, land use and soil data have been used in this river basin scale analysis. The data sources and spatial characteristics (spacing, extent) of the data will be described below.

Elevation

Elevation data are from a global Digital Elevation Model (DEM) GTOPO30 (U.S. Geological Survey, 1996) and a continental United States digital elevation model US7.5MIN (U.S. Geological Survey, 1995). These data are distributed by the EROS Data Center Distributed Active Archive Center (EDC DAAC), located at the U.S. Geological Survey's EROS Data Center in Sioux Falls, South Dakota. Two data sources are used here to compare variable-scale relationships (see section 2.3.7) derived from high resolution data (US7.5MIN, only available for the United States) with lower resolution data (GTOPO30). The geographical region chosen for this comparison is a region in the Northeast of the United States (69°W-68°W and 46°N-47°N) with a similar elevation pattern and elevation distribution as the Meuse basin.

GTOPO30 is a global data set covering the full extent of latitude and longitude with elevation values ranging from –407 to 8752 m. The horizontal grid spacing is 30-arc seconds (1/120 degree or approximately 1 km) and the vertical unit is meter above mean sea level. The source for the European GTOPO30 data is the Digital Terrain Elevation Data (DTED) set. DTED is a raster topographic data base with a horizontal grid spacing of 3-arc seconds (approximately 90 m). The source for United States GTOPO30 data are USGS 1-degree DEMs with a horizontal grid spacing of 3-arc seconds. The 30-arc second data were obtained from the 3-arc second data by selecting one representative elevation value to represent the area covered by 100 full resolution cells (10x10). The absolute vertical accuracy of GTOPO30 for Europe and the United States is +/- 30 m linear error at the 90%-confidence level (U.S. Geological Survey, 1993)

US7.5MIN is a data set for the continental United States. The horizontal grid spacing is 30 m and the vertical unit is meter above mean sea level. The data sources are digitised cartographic map contour overlays and scanned National Aerial Photography Program (NAPP) photographs. The absolute vertical accuracy of US7.5MIN derived from photographs is 7 m or better (90 %) and 8-15 m (10 %) (U.S. Geological Survey, 1995). Figure 5.1 shows the elevation maps for the Meuse basin (upstream of Borgharen) from GTOPO30, the US region from GTOPO30 and two arbitrary sub-regions (of about 150 km^2) within the US region from US7.5MIN.

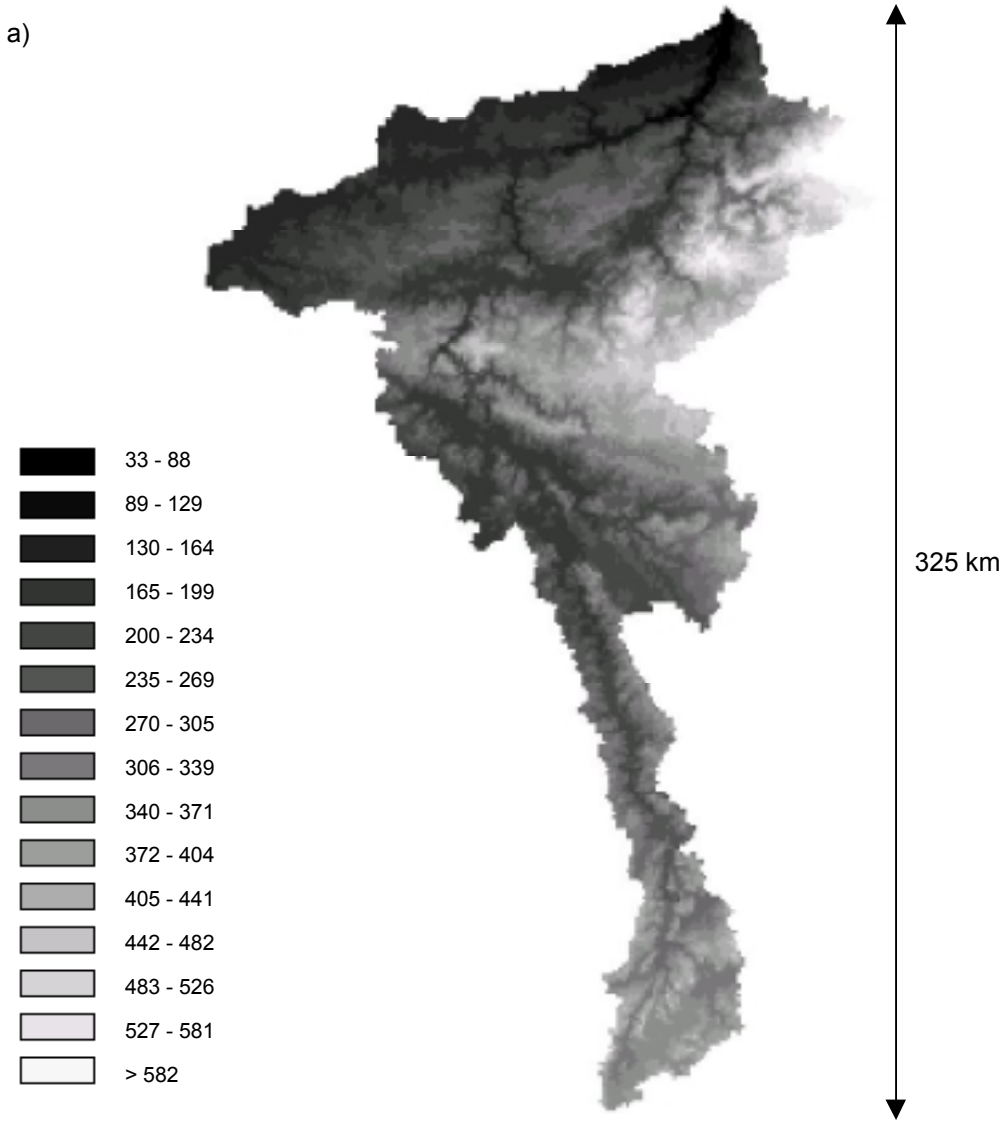
a)
33 - 88
89 - 129
130 - 164
165 - 199
200 - 234
235 - 269
270 - 305
306 - 339
340 - 371
372 - 404
405 - 441
442 - 482
483 - 526
527 - 581
> 582
325 km

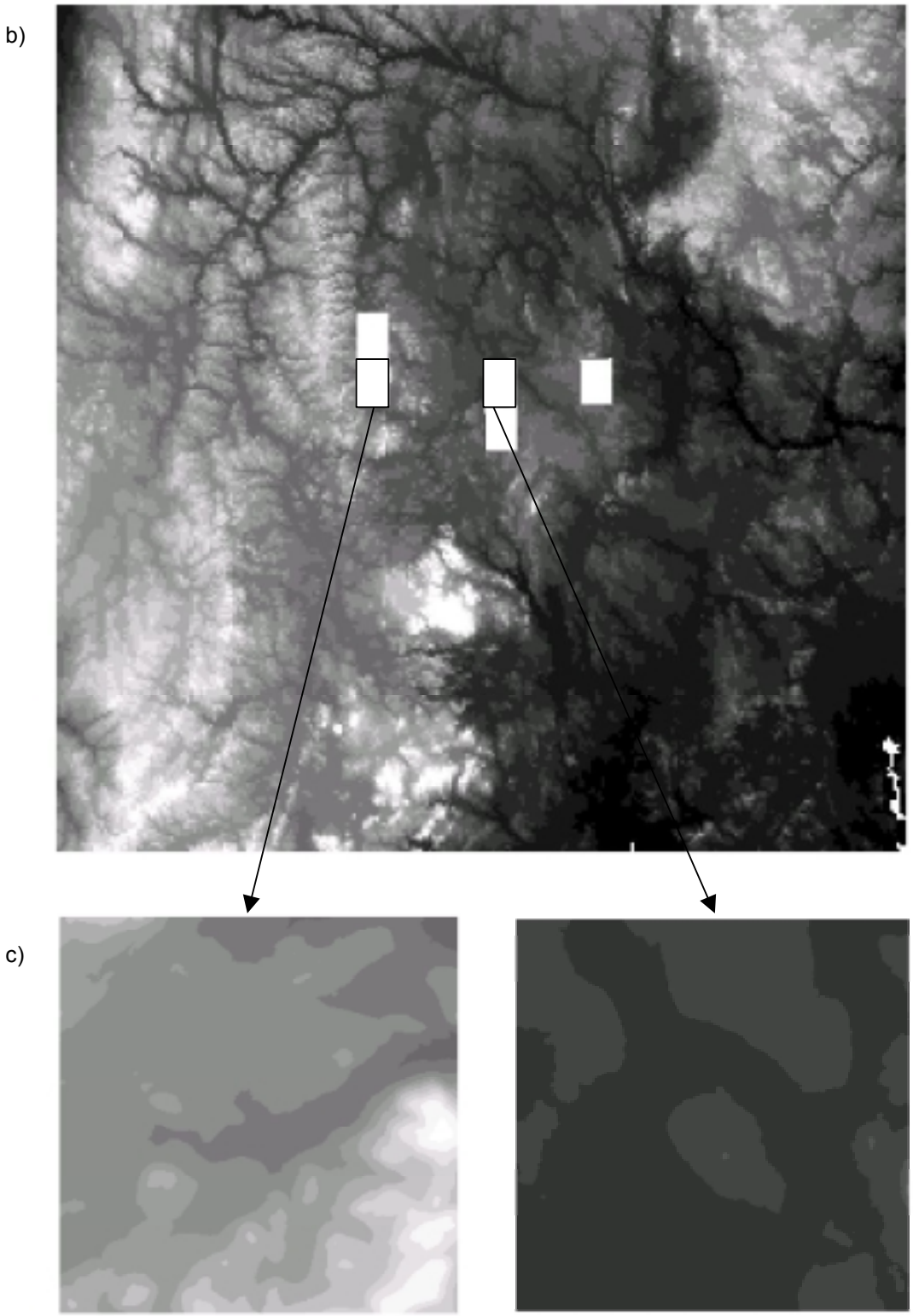

Figure 5.1 Elevation in m for a) Meuse basin upstream of Borgharen from GTOPO30; b) US region from GTOPO30 (extent = 256 km x 256 km) with five sub-regions studied; c) two arbitrary sub-regions within the US region from US7.5MIN (extent = 11 km x 14 km).

Soil

Soil data are from the European Soil Database. The data are distributed by the European Soil Bureau located at the Joint Research Centre's Space Applications Institute in Ispra, Italy. Only data from the Soil Geographical Data Base (King *et al*., 1994), part of the European Soil Database, are used. The horizontal scale is 1:1,000,000 similar to a horizontal grid spacing of approximately 2.5 km, because the positional accuracy is estimated at 0.5-5 km (0.5-5 mm at scale 1:1,000,000). Two attributes from this database have been used, namely Dominant Parent Material (MAT1) and Dominant Surface Textural Class (TEXT1). Figure 5.2 gives the spatial distribution of MAT1 and TEXT1 for the Meuse basin.

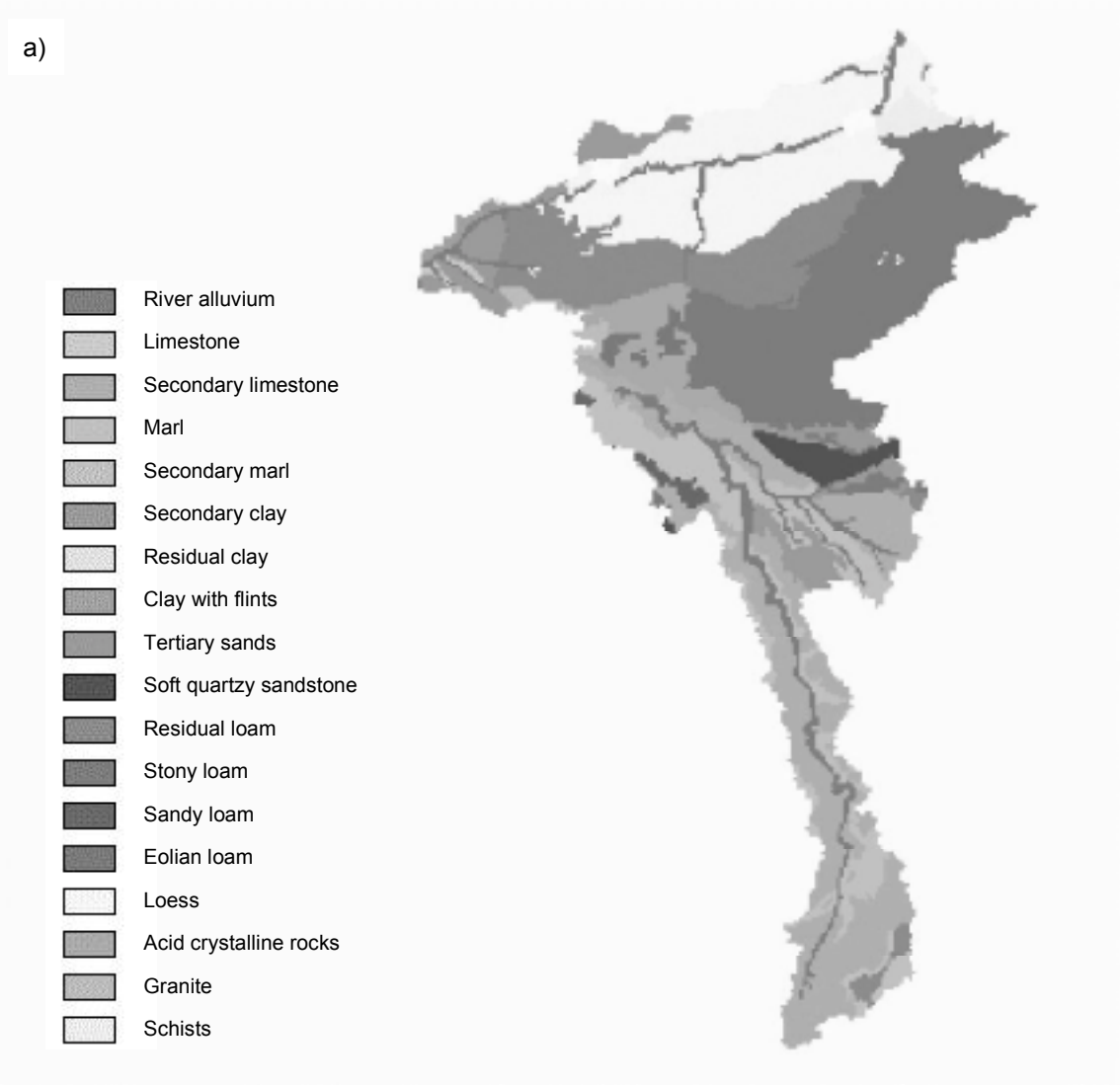

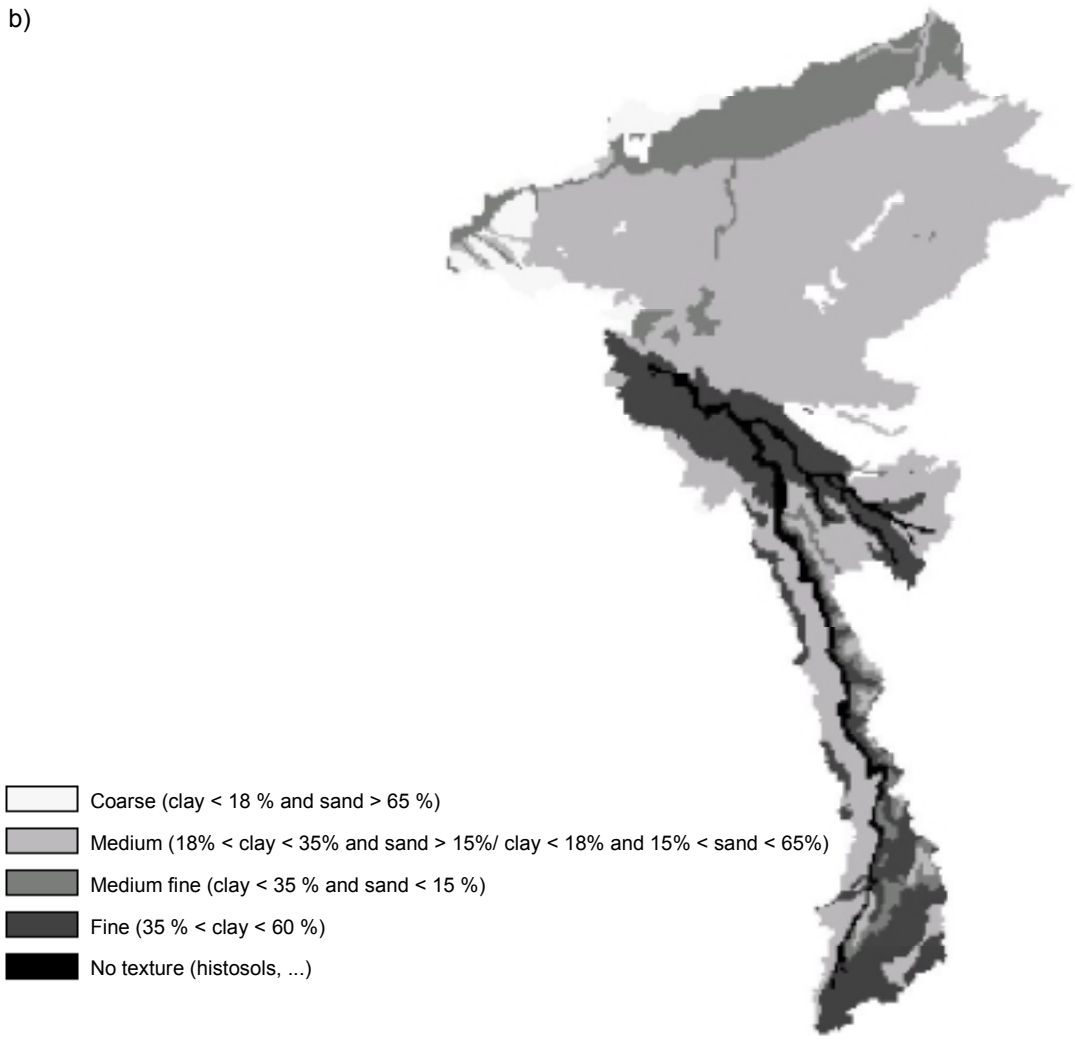

Figure 5.2 Spatial distribution of a) Dominant Parent Material (MAT1) and b) Dominant Surface Textural Class (TEXT1) in the Meuse basin.

Land use

Land use data are from the European Environmental Agency (EEA) NATLAN Database. The data are distributed by the European Environmental Agency in Copenhagen, Denmark. Only data from the CORINE Land Cover Data Base (Bossard *et al*., 2000), part of the EEA NATLAN database, are used. The horizontal grid spacing is 250 m. The CORINE database has 44 classes and is derived from Landsat and SPOT satellite images. Figure 5.3 gives the spatial distribution of land use types for the Meuse basin.

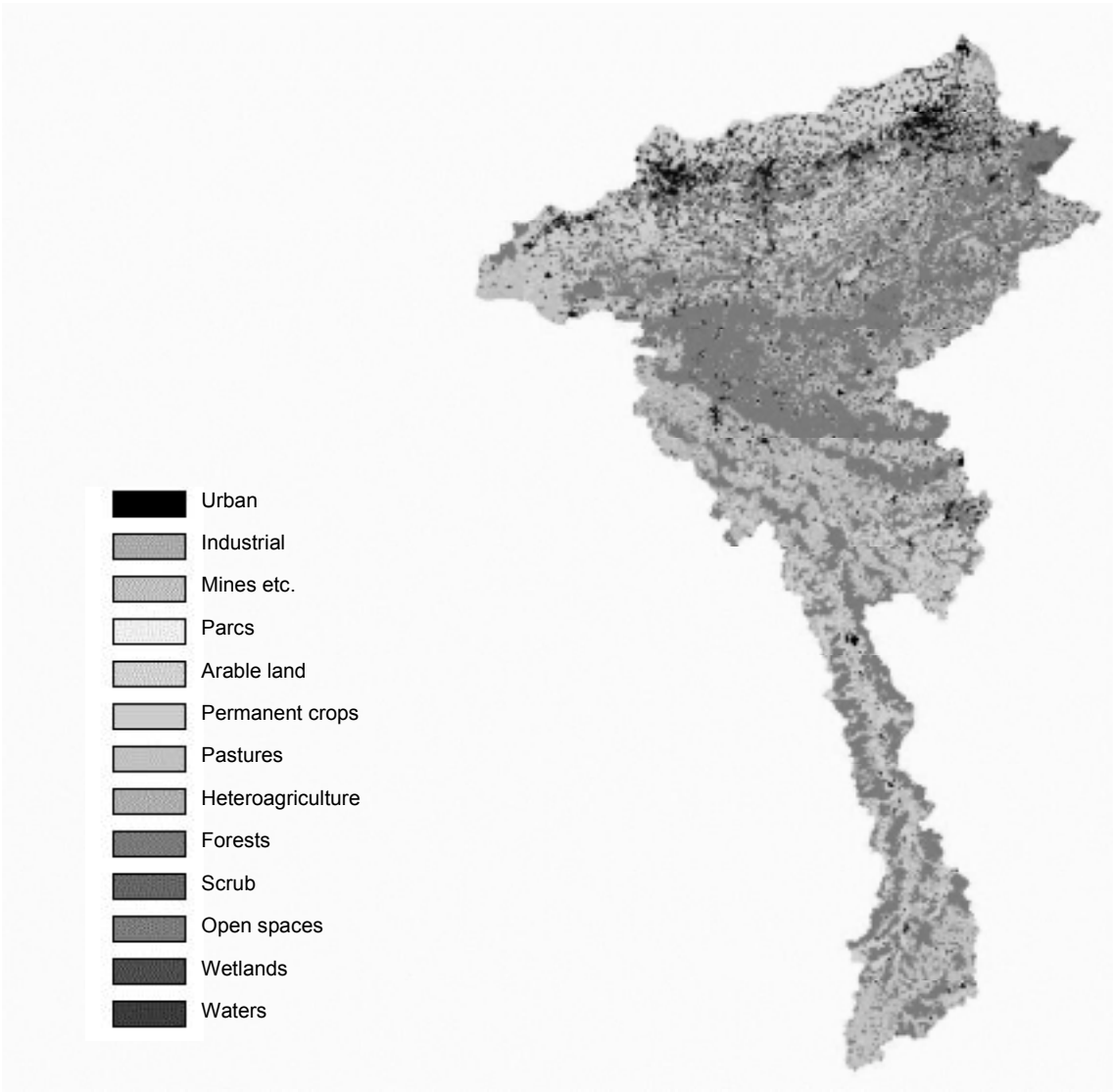

Figure 5.3 Spatial distribution of land use types in the Meuse basin.

5.3.3 Data statistics and scales

Elevation

Figure 5.4 shows the cumulative frequency distribution of elevations from US7.5MIN (US 30m DEM) for five selected sub-regions of about 150 km^2, GTOPO30 for the whole region (US 1000m DEM), GTOPO30 for the 15 main sub-catchments of the Meuse basin (Tributary 100m DEM) and GTOPO30 for the Meuse basin (Meuse 1000m DEM). The cumulative frequency distributions for the US region and the Meuse basin are similar indicating that the US region has a similar elevation pattern and elevation distribution as the Meuse basin. The cumulative frequency distributions for elevations derived from the US 30m DEM are steeper than those derived from the Tributary 1000m DEM and thus in the latter DEMs larger elevation differences can be found. This can be explained by the fact that the Tributary 1000m DEMs have been derived for larger areas (350-3200 km^2) than the US 30m DEMs (150 km^2). A similar effect as for the extent has been observed for the support scale, i.e. the smaller the support scale for a specific area, the larger elevation differences. Large elevation differences are particularly found for the sub-catchments in the eastern part of the Meuse basin (e.g. the Amblève). The mean, minimum and maximum elevation in the Meuse 1000m DEM are respectively 284, 43 and 676 m.

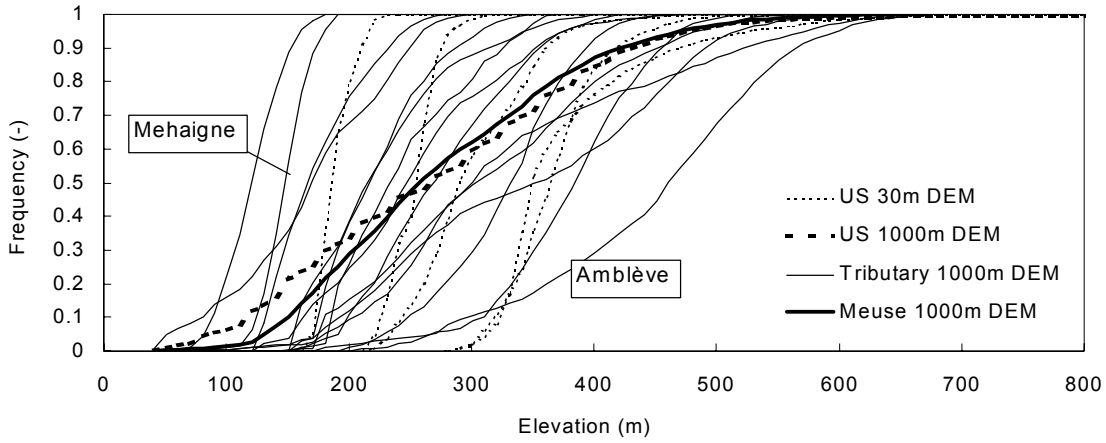

Figure 5.4 Cumulative frequency distribution of elevation for US 30m DEM, US 1000m DEM, Meuse tributary 1000m DEM and Meuse 1000m DEM.

Figure 5.5 shows the semi-variance as a function of separation distance for the US 1000m DEM, the Meuse 1000m DEM and the US 30m DEM. For the US 30m DEM, the semi-variance has been derived for the five sub-regions from Figure 5.1 for very small separation distances up to 2 km. Nine grid points were selected in each sub-region and for each grid-point average semi-variances were calculated for a specific separation distance (radius). The average semi-variance as a function of separation distance over 45 (5×9) grid points is shown in Figure 5.5b. Similar approaches were used for the US 1000m DEM and Meuse 1000m DEM, but then for nine grid points in the whole region and separation distances up to 20 km. The variograms in Figure 5.5a are similar, although the one for the US region shows less spatial variability. Therefore, it is assumed that the US region is representative for the Meuse basin with respect to elevation patterns and consequently, the variogram for the US 30m DEM in Figure 5.5b is representative for the Meuse basin as well.

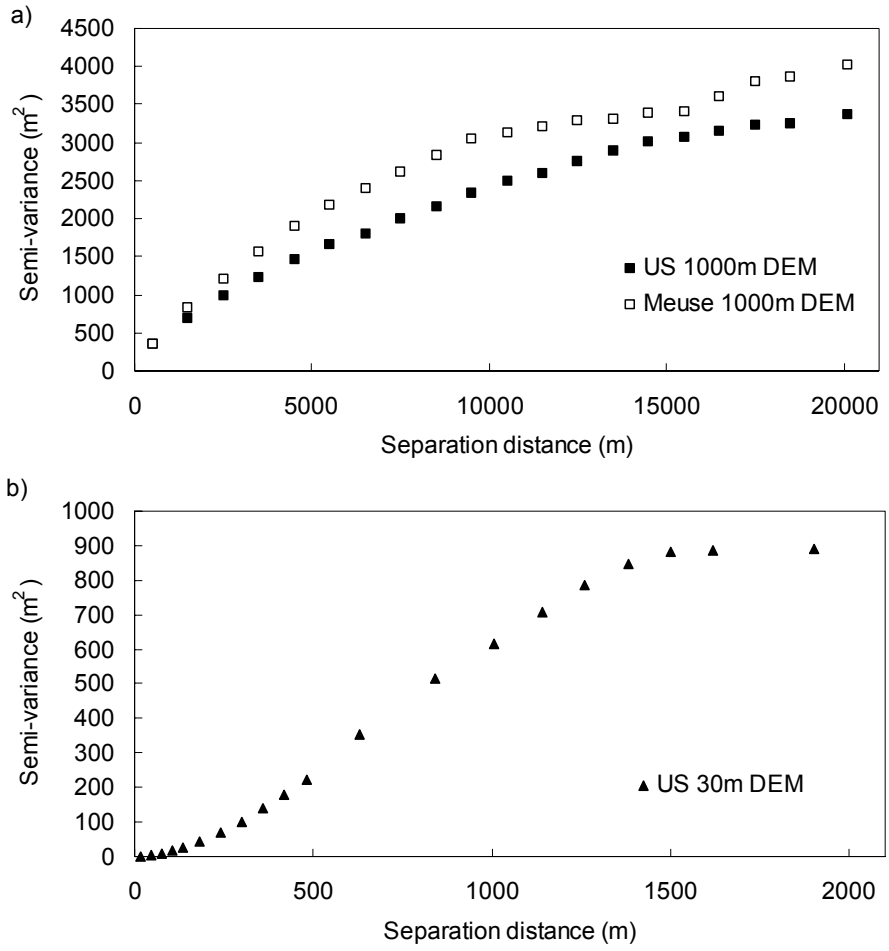

Figure 5.5 Semi-variance in m^2 as a function of separation distance in m for a) US 1000m DEM and Meuse 1000m DEM and b) US 30m DEM.

The spatial correlation length should be determined from the 30m DEM, because the resolution of the 1000m DEMs is too coarse in relation to the expected or 'true' correlation length. Western and Blöschl (1999) presented directives on spacing, support and extent when estimating the correlation length. They gave for spacing (equal to support in this case) a maximum value of 20 % of the true correlation length. Assuming true correlation lengths of about 100-1000 m corresponding to realistic hill slope lengths, it is obvious that 1000m DEMs cannot be used for this purpose. The mean, minimum and maximum correlation length determined from the US 30m variograms are respectively 527, 272 and 1401 m. It can be seen that even for the minimum correlation length the resolution of the US 30m DEM is sufficient. The mean correlation lengths computed from the US 1000m DEM and the Meuse 1000m DEM were respectively 4138 and 4220 m. This overestimation of the correlation lengths could be expected from the relations between spacing and apparent correlation described in Western and Blöschl (1999). The appropriate scale for elevation can be determined with the criterion for appropriate scales with respect to variability from section 2.3.6. There, it was found that the appropriate scale for an appropriate description of the variability is about 20 % of the correlation length. The appropriate scale for elevation in the Meuse basin is therefore 110 m. This scale is in the same range as the scales recommended for DEMs in other studies (e.g. Brasington and Richards, 1998).

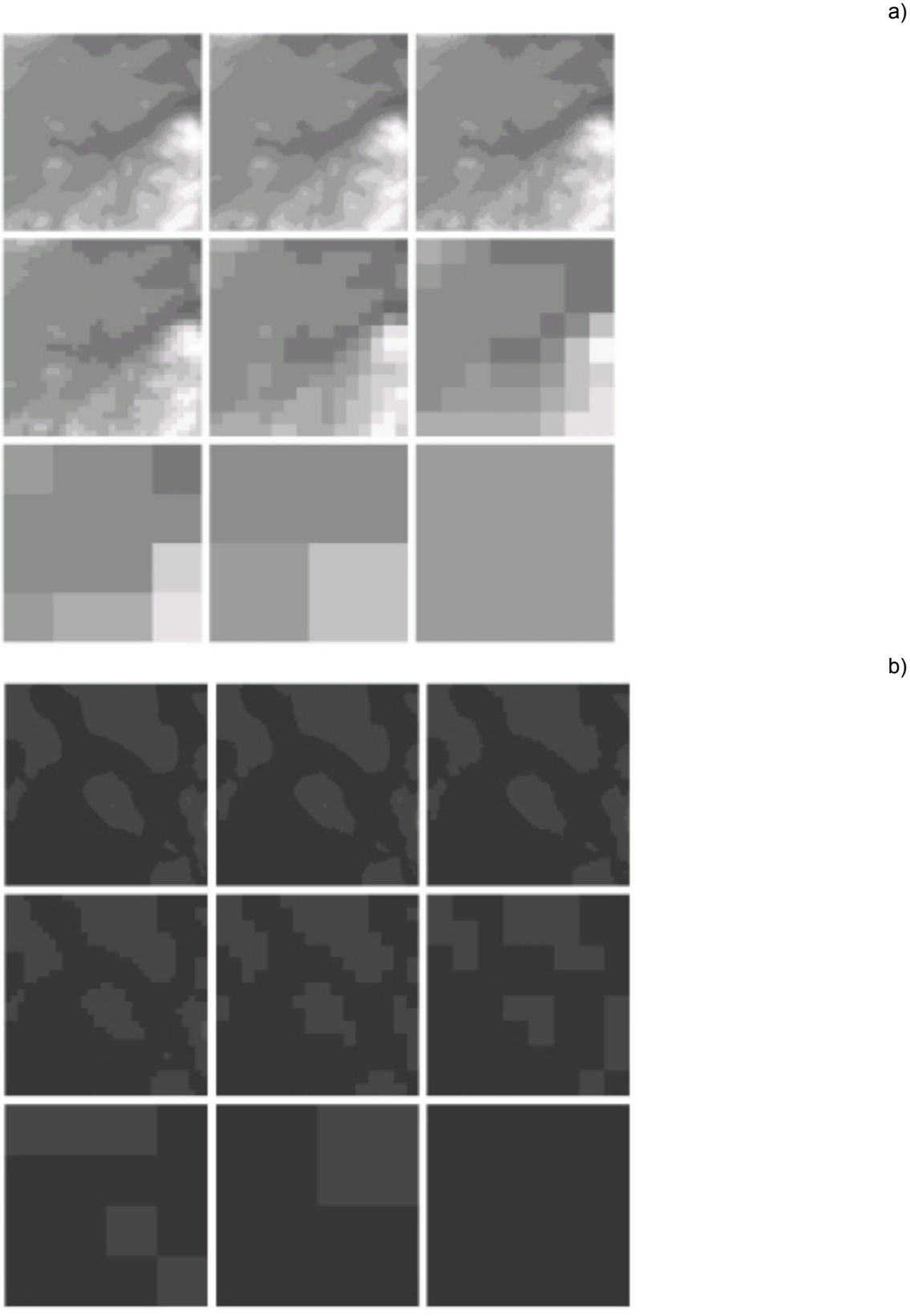

Figure 5.6 Elevation map for US 30m DEM and aggregated versions: 60m, 120m, 240m, 480m, 960m, 1920m, 3840m and 7680m for 2 sub-regions of Figure 5.1c (a and b). See Figure 5.1 for the legend.

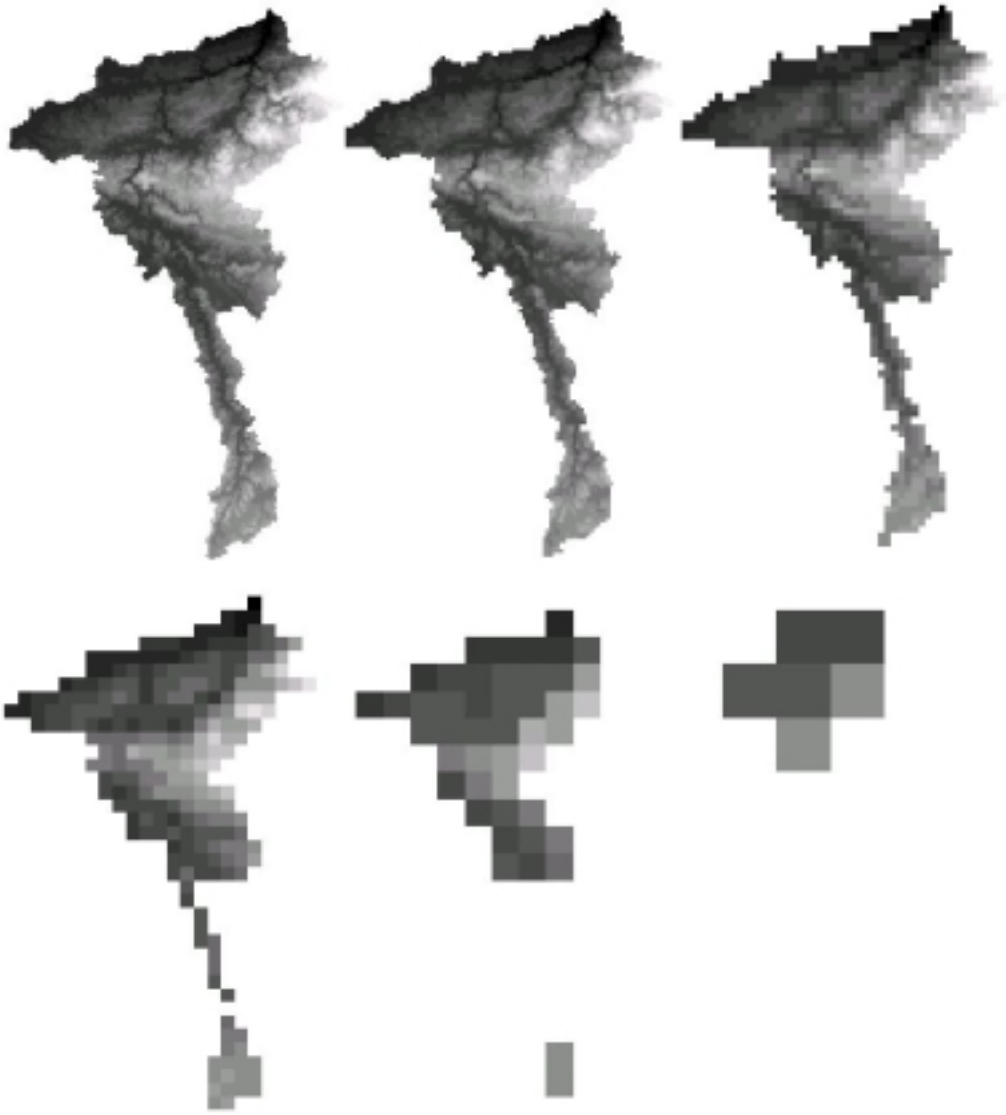

Figure 5.7 Elevation map for Meuse 1000m DEM and aggregated versions: 2000m, 4000m, 8000m, 16000m and 32000m. See Figure 5.1 for the legend.

The methodology for the integration of scales requires relationships between key variable scales and the output variable of interest (section 2.3.7). The key variable elevation is represented in equation (2.48) by the slope. Therefore, the average slope should be derived from elevation maps with different resolutions. These different resolutions are assumed to represent different data availability levels (e.g. at 1 km or 8 km resolution). The elevation maps for the US 30m DEMs from Figure 5.1c are given in Figure 5.6 together with aggregated versions of these maps up to a version with one average elevation. Figure 5.7 gives the elevation map for the Meuse 1000m DEM from Figure 5.1a together with its aggregated versions.

Soil

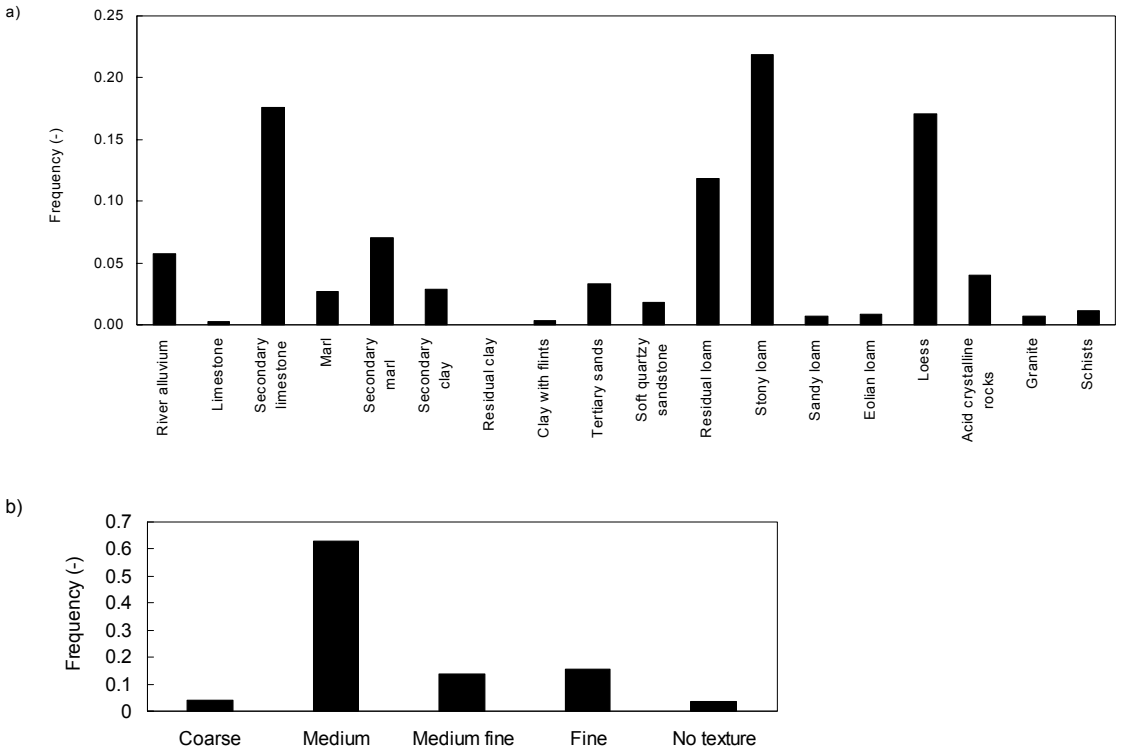

Figure 5.8 Frequencies of a) Dominant Parent Materials (MAT1) and b) Dominant Surface Textural Classes (TEXT1) in the Meuse basin.

Figure 5.8 shows the frequency distribution of Dominant Parent Materials (MAT1) and Dominant Surface Textural Classes (TEXT1) in the Meuse basin. Major dominant parent materials are secondary limestone (18 %, particularly in the southern part of the basin), residual and stony loam (34 %, in the Ardennes and central part) and loess (17 %, in the northern part). Besides these dominant materials other, minor materials can be found as well in these areas. The major surface textural class is medium, which means 18% < clay < 35% and sand > 15% or clay < 18% and 15% < sand < 65% (see Figure 5.2).

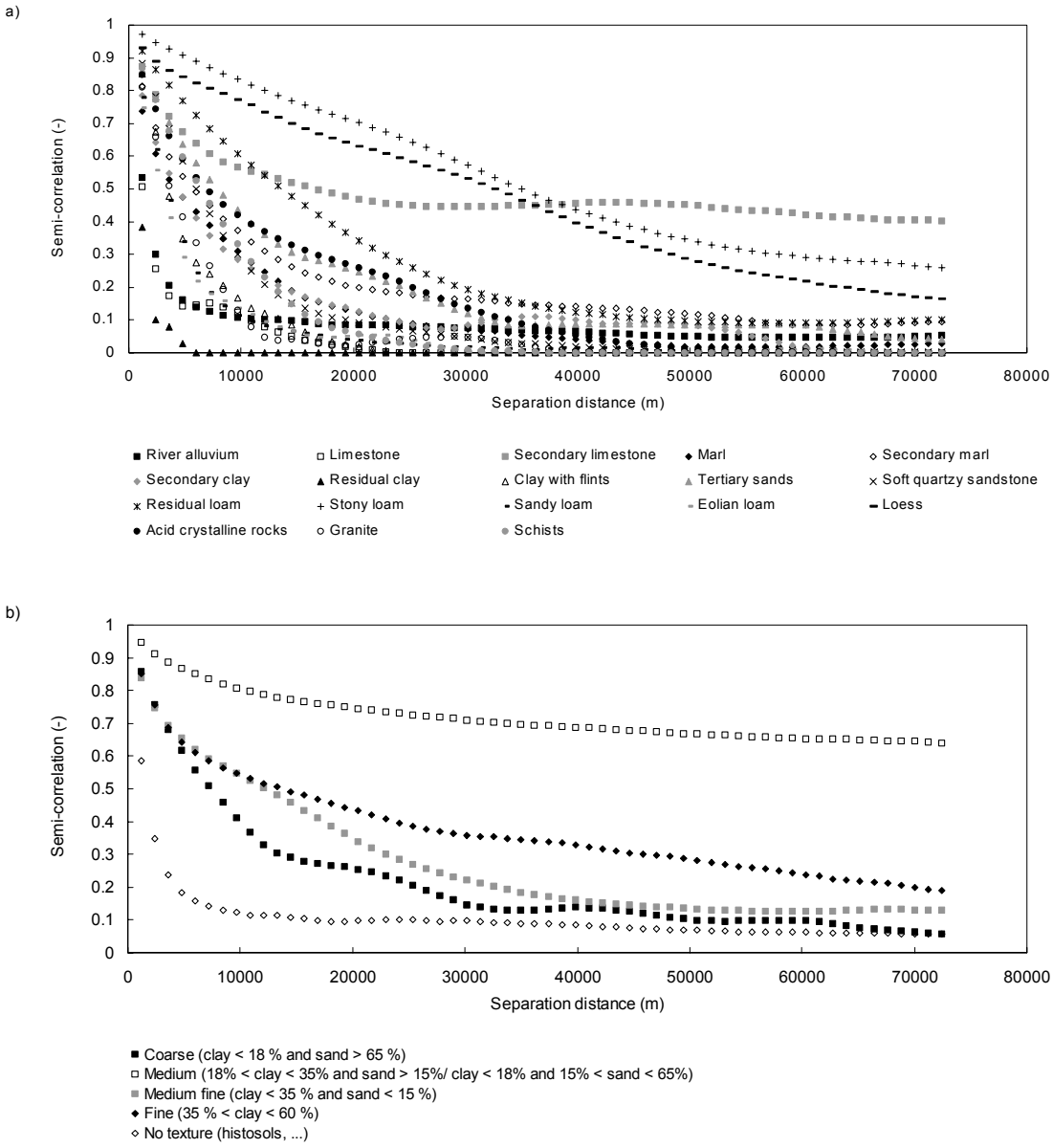

Figure 5.9 Semi-correlation as a function of separation distance in m for a) Dominant Parent Materials (MAT1) and b) Dominant Surface Textural Classes (TEXT1).

Variograms for the different soil types can not be constructed, because soil data are categorical data and thus semi-variances can not be computed. Therefore, a so-called semi-correlation is calculated (see section 2.3 4). These semi-correlations are plotted vs. separation distance in a semi-correlogram. The semi-correlogram can be used to derive the correlation lengths for the different soil types. Figure 5.9 shows the semi-correlogram for the different classes of MAT1 and TEXT1. Obviously, the general trend is a decreased semi-correlation with increased separation distance. This trend is approximately exponential as confirmed by the high weighted mean (taking into account the frequencies) *PPCC** values (see section 2.3) of 0.93 for MAT1 and 0.98 for TEXT1. The semi-correlogram for secondary limestone in Figure 5.9a shows a slightly increasing semi-correlation with increasing distance between 30 and 45 km. This may be attributed to large scale spatial patterns of secondary limestone. The semi-correlation

decreases towards its 'background' frequency from Figure 5.8 at a distance larger than the corresponding correlation length. The semi-correlograms can be used to derive spatial correlation lengths.

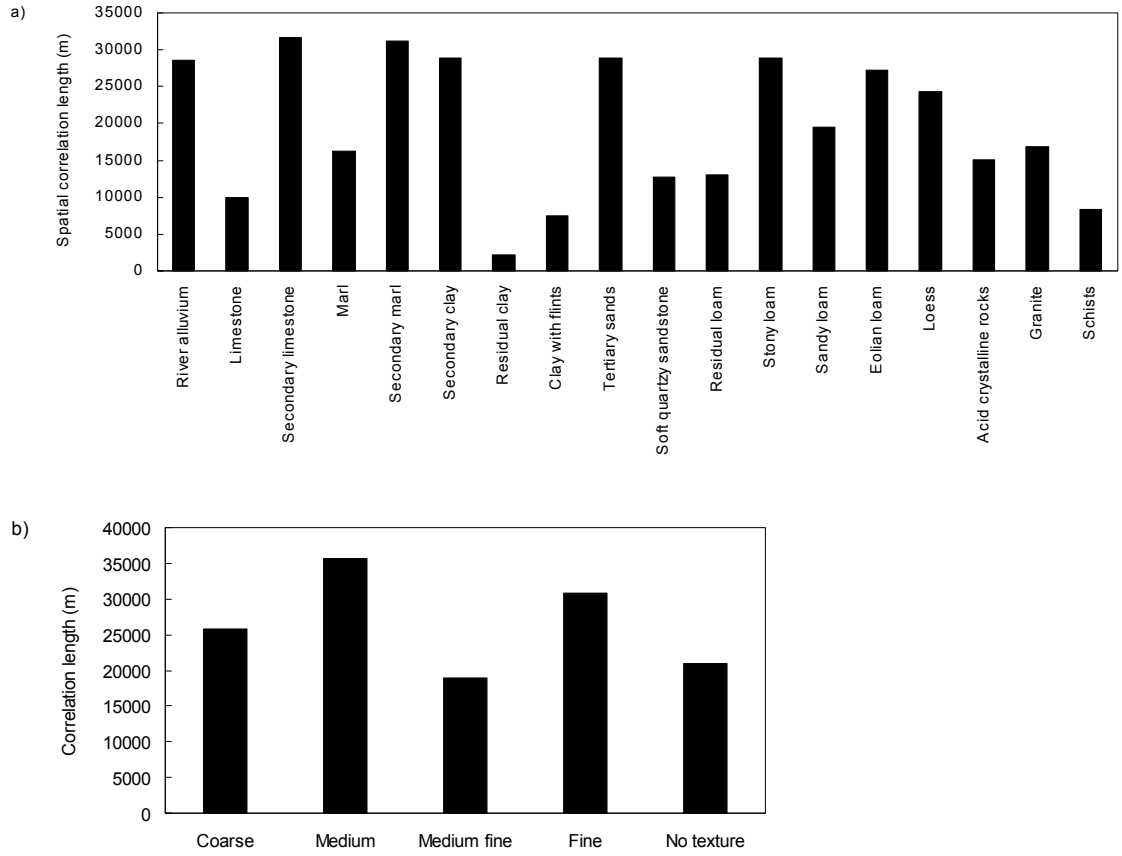

Figure 5.10 Spatial correlation length in m for a) different Dominant Parent Materials (MAT1) and b) different Dominant Surface Textural Classes (TEXT1).

Figure 5.10 shows the spatial correlation lengths for the different classes of MAT1 and TEXT1. The correlation lengths for MAT1 vary between 1-10 km for residual clay, clay with flints and schists to more than 30 km for secondary limestone and secondary marl. The correlation lengths for TEXT1 vary between 15-35 km. The horizontal grid spacing of the soil data is sufficient for most of the soil types, because their correlation lengths are more than five times the grid spacing The grid spacing is insufficient for the above mentioned three MAT1 classes with small correlation lengths and limestone. However, these MAT1 classes occupy less than 5 % of the Meuse basin and therefore possible errors in estimated correlation lengths due to grid spacing can be neglected. The weighted mean spatial correlation length for dominant parent material is about 25.1 km. Then, the appropriate scale for a good description of the parent material variability is about 20 % of this correlation length or 5.3 km. These figures are for the dominant surface textural class respectively 31.5 km and 6.6 km. The appropriate scale with respect to the parent material has been chosen to be representative for the soil data, because it is the smallest one and it is supposed to be more suitable in the methodology for the integration of appropriate scales. The correlation lengths for parent material and dominant surface textural class are much larger than the correlation lengths for soil

moisture found in the literature (see 5.3.1; 50-1200 m). These differences can be attributed to the additional variability for soil moisture introduced by for example topography and vegetation on top of the variability of the parent material and soil texture itself.

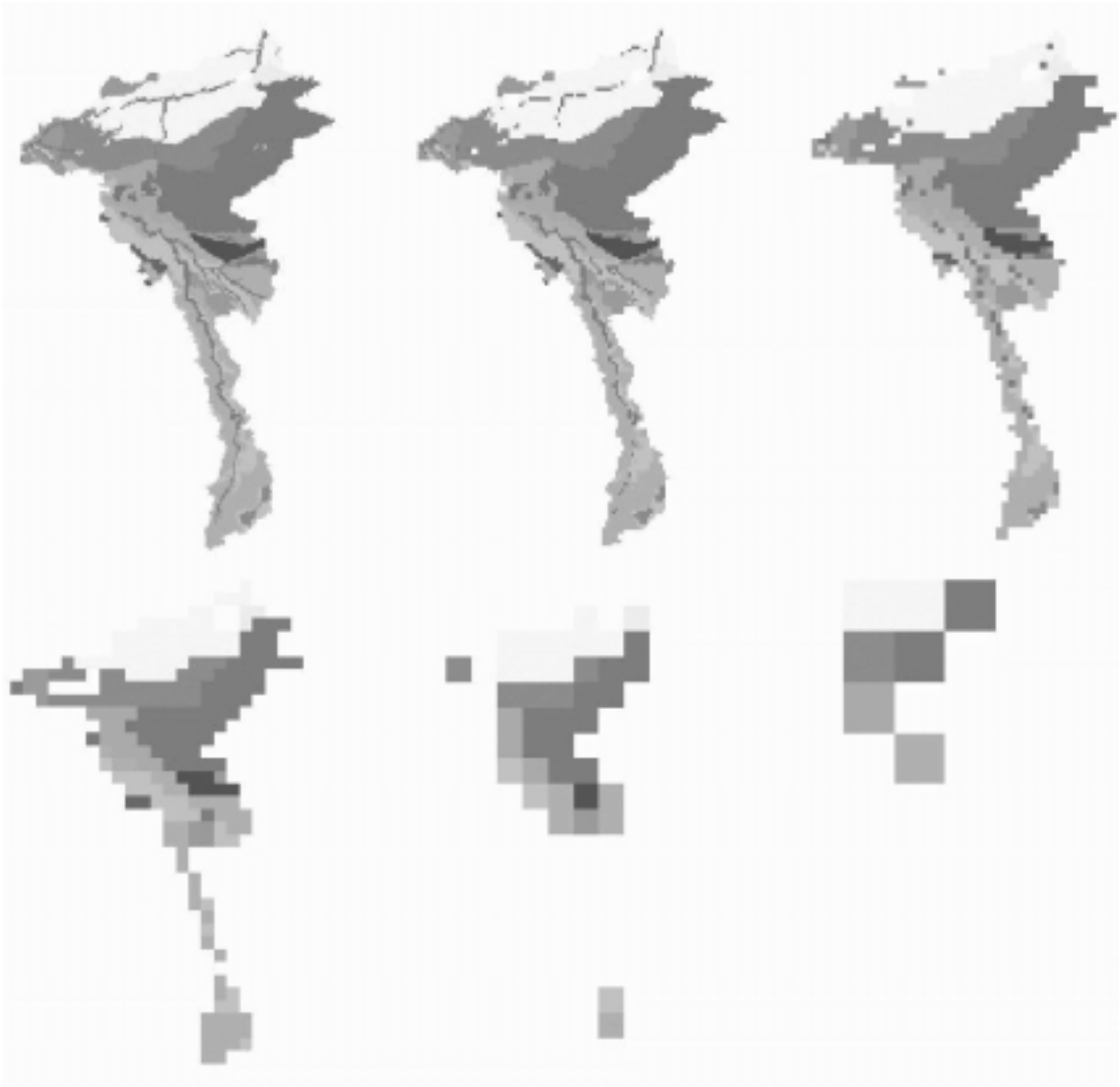

Figure 5.11 Spatial distribution of Dominant Parent Material (MAT1) for Meuse basin (1000 m) and aggregated versions: 2000m, 4000m, 8000m, 16000m and 32000m. See Figure 5.2 for legend.

The key variable soil is represented in equations (2.46)-(2.48) by the curve number CN. The average CN will be derived from soil (MAT1) maps with different resolutions. The MAT1 map for the Meuse basin from Figure 5.2a is given in Figure 5.11 together with its aggregated versions.

Land use

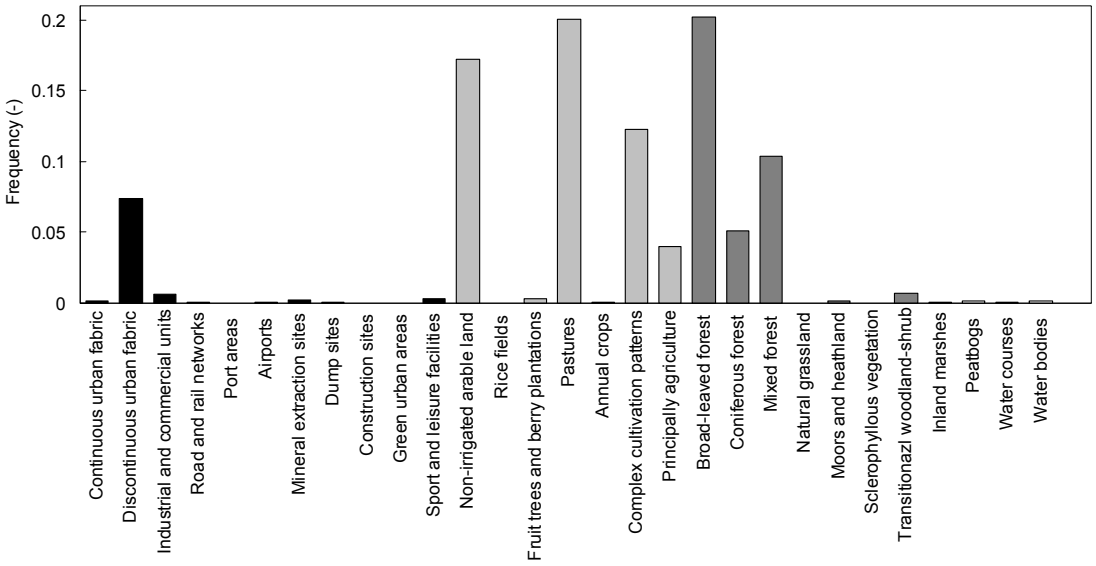

Figure 5.12 Frequencies of land use types in the Meuse basin.

Figure 5.12 shows the frequency distribution of land use types in the Meuse basin. The land use types are described in Bossard *et al*. (2000). In the Meuse basin, 29 of the 44 land use types in the CORINE data base are present. Urban, industrial and mining areas occupy about 9 % of the space, agricultural areas 54 %, forests and scrubs about 36 % and water related areas about 1 %. The Meuse north sub-catchment has the largest fraction of urban, industrial and mining areas (29 %, not shown here), the North-western Jeker and Mehaigne sub-catchments have the largest fraction agricultural areas (80 %) and the Viroin sub-catchment has the largest fraction forests and scrubs (57 %).

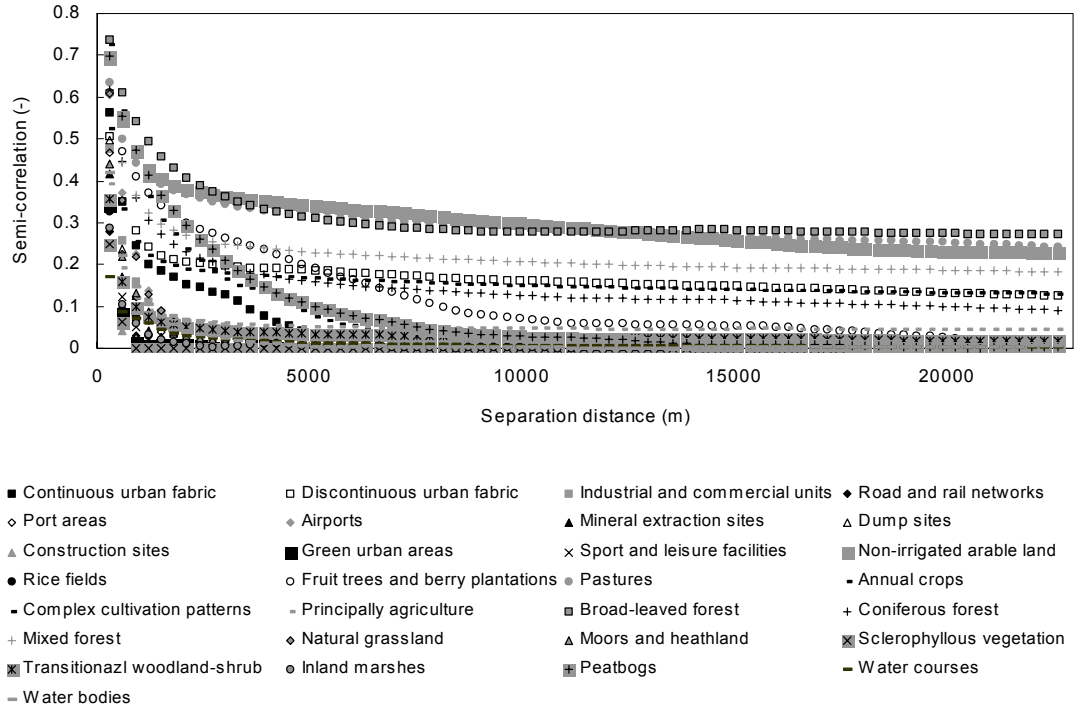

Figure 5.13 Semi-correlation as a function of separation distance in m for different land use types.

Land use data are categorical data as well and therefore semi-correlograms are computed for the different land use types as shown in Figure 5.13. The correlograms can be approximated by exponential functions as confirmed by the reasonable weighted mean *PPCC** value of 0.89. Figure 5.13 shows expected features such as the slow decrease of the semi-correlation with separation distance for broad-leaved forest and the fast decrease of the semi-correlation with separation distance for continuous urban fabric. The 'background' frequency from Figure 5.12 is reached at a large distance compared to the correlation length as shown for some land use types with small correlation lengths (<< 20 km).

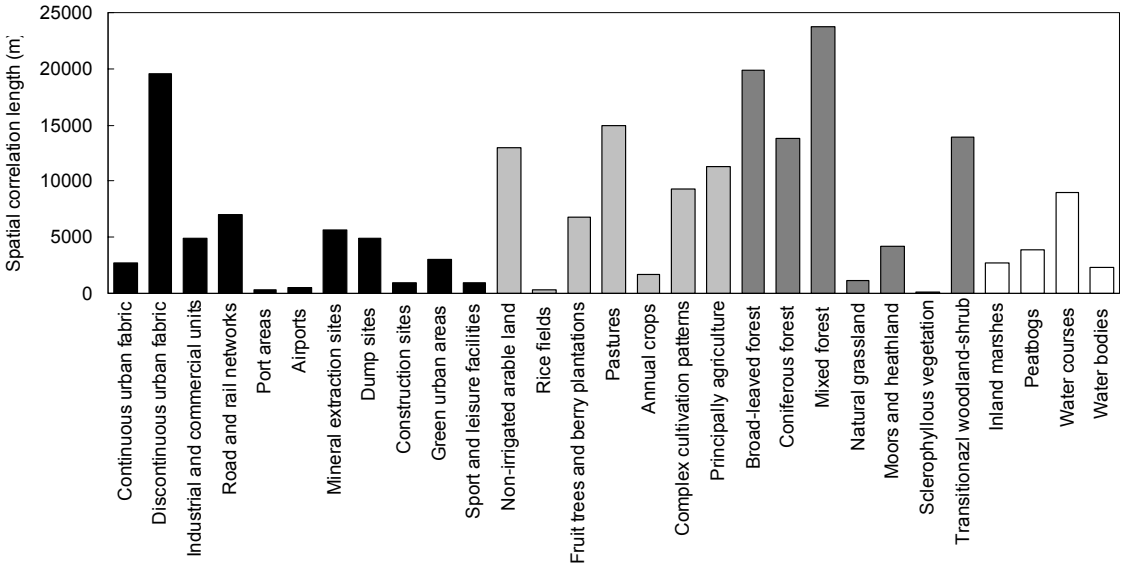

Figure 5.14 Spatial correlation length in m for land use types in the Meuse basin.

Figure 5.14 shows the spatial correlation lengths for the different land use types in the Meuse basin. The correlation lengths vary between 100-500 m for port areas, airports, rice fields and sclerophyllous vegetation to about 20 km for discontinuous urban fabric, broad-leaved forest and mixed forest. The horizontal grid spacing of the CORINE land use data is sufficient for most of the land use types, except for the above mentioned four land use types with small correlation lengths and construction sites, sport and leisure facilities and natural grassland. However, these seven land use types occupy less than 1 % of the Meuse basin and therefore possible errors in estimated correlation lengths due to grid spacing can be neglected. The weighted mean spatial correlation length for land use is 15.7 km which gives an appropriate scale for a good description of the land use variability of about 3.3 km. This appropriate scale is in the middle of the range of spatial scales recommended for land use mapping and used in land use models (see 5.3.1).

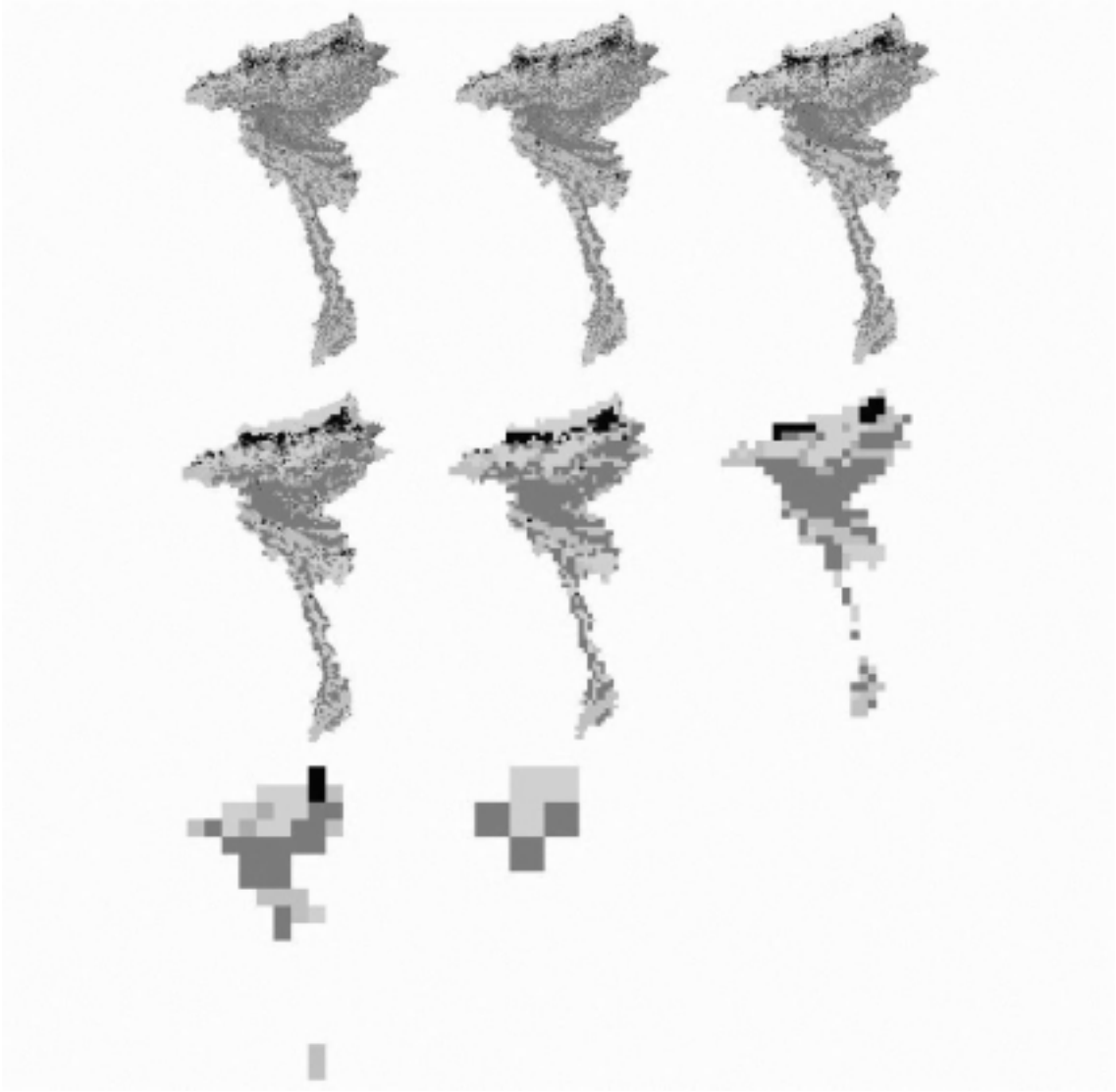

Figure 5.15 Land use map for Meuse basin (250 m) and aggregated versions: 500m, 1000m, 2000m, 4000m, 8000m, 16000m and 32000m. See Figure 5.3 for the legend.

The key variable land use is represented in equation (2.46)-(2.48) by the curve number CN as well. The average CN will be derived from land use maps with different resolutions. The land use map from Figure 5.3 is given in Figure 5.15 together with its aggregated versions.

5.3.4 Integration of appropriate scales

Here, the appropriate scales for precipitation (4.3.5), elevation (5.3.3), soil (5.3.3) and land use (5.3.3) are integrated to one appropriate model scale. This is achieved by applying the methodology described in 2.3.7. First, the relationships between the variables from equations (2.46)-(2.48) (the key variables) and spatial scales are considered. Second, these relationships are integrated into equations (2.46)-(2.48) to obtain relations between the output and spatial scales for the different key variables. The output of interest is the peak discharge with a return period of 20 years $RV(20)$.

Precipitation

The key variable precipitation in equation (2.46) P_e should be the extreme precipitation with a return period of 20 years, because of the return period of 20 years assumed for the discharge. The relation between precipitation return values and scales has been theoretically considered in chapter 2 [see equations (2.44) and (2.45) and Figure 2.11] and has been applied in chapter 4. This relation can directly be used in equation (2.46) to obtain a relationship between the output and spatial scales of extreme precipitation.

Elevation

The key variable elevation is represented in equation (2.48) by the slope S_0. The average slopes derived from the maps in Figure 5.6 and Figure 5.7 for the US 30m DEM and Meuse 1000m DEM as a function of scale are given in Figure 5.16. Also given are the average slopes derived from the US 1000m DEM map and their aggregated versions as a function of scale. Main features are the similarity of the US 1000m DEM and Meuse 1000m DEM slope vs. scale relationships and the apparent continuity of the relationships over a broad range of scales (from 30 m to more than 30 km). The combination of these two aspects leads to the assumption that the slope vs. scale relationships from the US 30m DEM can also be used for the Meuse basin and thus the appropriate scale for elevation (represented by slope) of about 100 m (see 5.3.3) is covered by these relationships. This coverage is necessary for the methodology for the integration of appropriate scales. Namely, the scale-variable relation should at least cover the range between the appropriate variable scale and the appropriate model scale or vice versa. This requirement has been checked after the determination of the appropriate model scale. Another interesting feature in Figure 5.16 is the clear distinction between relations for flat US regions (lower curves for US 30m DEM) and hilly US regions (upper).

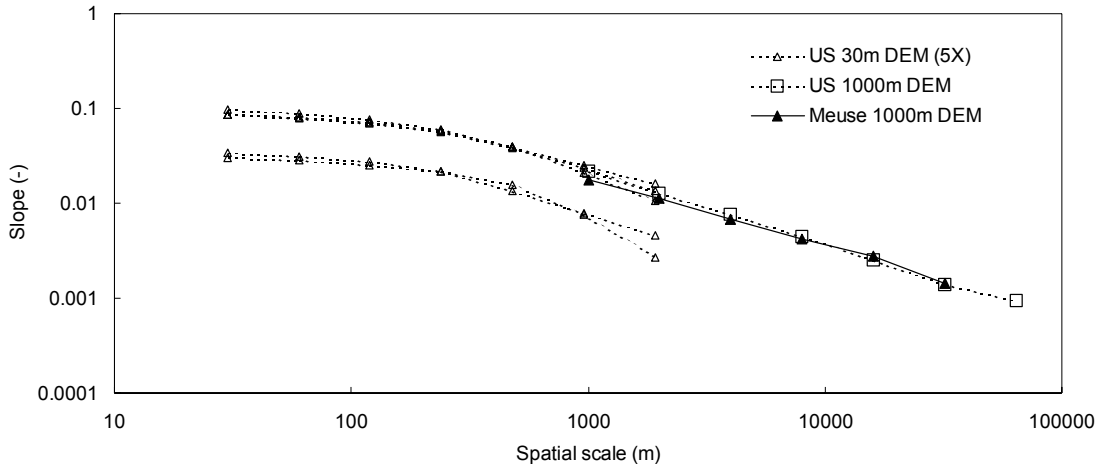

Figure 5.16 Average slope as a function of scale in m for US 30m DEM, US 1000m DEM and Meuse 1000m DEM.

Soil and land use

Table 5.3 Values for variables/ parameters in equations (2.46)-(2.48).

Variable/ parameter	Unit	Value
P_e	mm	44.6
q_p	m^3/s	2390
A	km^2	21 10^3
T_p	hour	24
$l = \sqrt{A}$	km	145
S_0	parts/10000	176
CN	-	77.1

The key variables soil and land use are represented in equations (2.46)-(2.48) by the curve number CN. The average, overall curve number for the Meuse basin has been derived with equations (2.46)-(2.48) and the variables and parameters in Table 5.3. The values for P_e and q_p have been derived keeping in mind the 20-year return period and the scale (for P_e) and the value for S_0 is estimated from the elevation field with the highest resolution (1000 m). This results in an average CN of 77.1 (see Table 5.3) for the soil and land use map with the highest resolution. This average CN and standard tables (Maidment, 1993) have been used to estimate curve numbers for the different soil and land use types in the maps from Figure 5.11 and Figure 5.15. Finally, the average curve numbers as a function of map resolution for soil parent material and land use derived from these maps could be determined. These relations are given in Figure 5.17 and Figure 5.18. There is only a slight change of average CN with soil and land use scale, respectively an increase of about 1.0 and a decrease of about 1.2 (at 16 km).

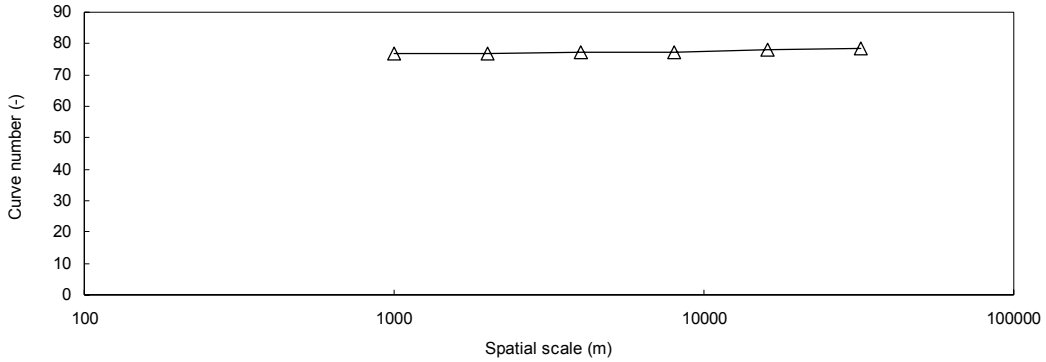

Figure 5.17 Average curve number as a function of scale in m for soil (Dominant Parent Material).

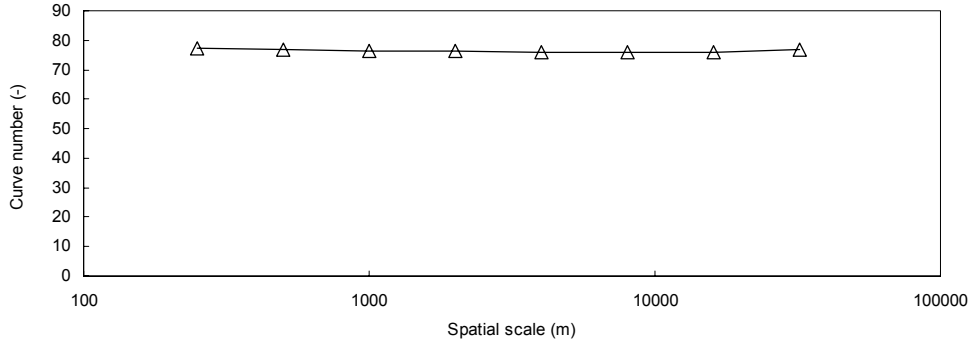

Figure 5.18 Average CN as a function of scale in m for land use.

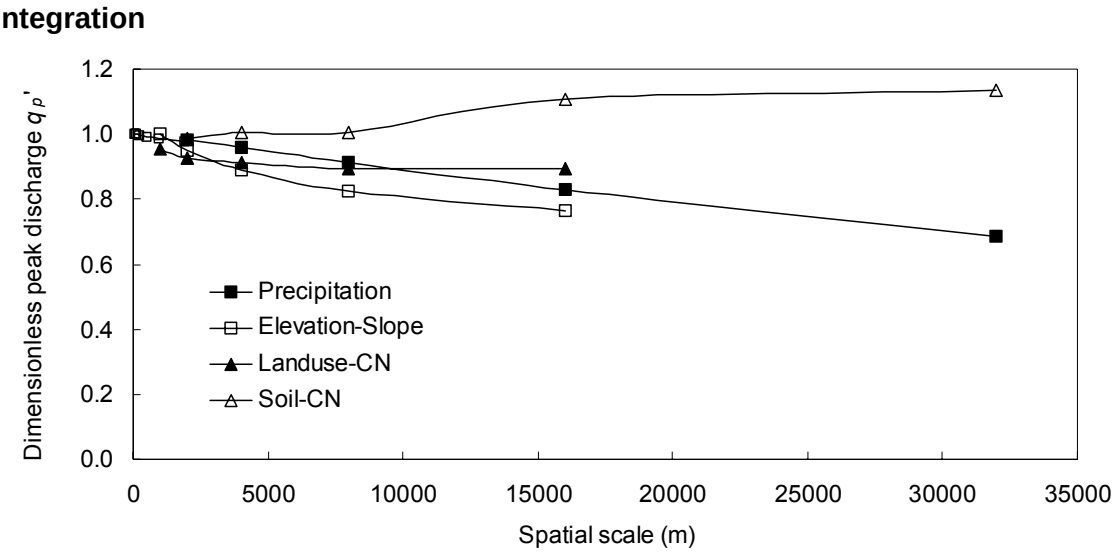

Figure 5.19 Dimensionless peak discharge q_p' as a function of key variable spatial scale in m.

The derived scale relationships for extreme precipitation, slope and curve number can be implemented in equations (2.46)-(2.48) to obtain relationships between the output and key variable scales. Figure 5.19 gives the dimensionless peak discharge [q_p(spatial scale)/q_p(smallest spatial scale)] as a function of key variable spatial scale. The peak discharge increases slightly with scale for soils in contrast to the other key variables, which may be due to the spatial distribution of soil types. This distribution results in a particular distribution of the curve numbers at different scales and finally the relations in this figure. Figure 5.19 has been used to assess the weights associated with an appropriate variable scale by comparing the slopes of the different relationships. The larger the slope, the larger the weight which should be attributed to a specific appropriate variable scale. The sum of the four weights (precipitation, elevation, soil type and land use) is obviously equal to 1. The slope has been determined for at least the range between the appropriate variable scale and the appropriate model scale (checked a posteriori). The appropriate variable scales, the associated weights and the resulting appropriate model scale are summarised in Table 5.4. The appropriate model scale of about 10 km will result in 225-250 model cells or sub-basins when modelling the Meuse basin.

Table 5.4 Appropriate variable scales, associated weights and appropriate model scale.

Variable	Appropriate variable scale (km)	Weight (-)
Precipitation	19.9	0.39
Elevation	0.1	0.26
Soil	5.3	0.21
Land use	3.3	0.14
Integrated	9.5	1.00

5.4 Process formulations

Given the dominant processes at the appropriate scales described in section 5.2 and 5.3, the appropriate formulations have to be determined. For each process, the most important formulations available will be considered and their appropriateness for the current research objective will be assessed, mainly on the basis of literature.

Actual evapotranspiration

The spatial and temporal variability of potential evapotranspiration has been considered in chapter 4. This potential evapotranspiration has been derived by the Royal Meteorological Institute of Belgium with the Penman-Monteith equation which combines energy and diffusion features (Maidment, 1993)

$$(5.1) \qquad ET_p = \frac{\Delta_E}{\Delta_E + \gamma_E}\left(R_n + A_h\right) + \frac{\gamma_E}{\Delta_E + \gamma_E}\frac{6.43\left(1 + 0.536U_2\right)D_E}{\lambda_E}$$

where Δ_E is the gradient of the relation between saturated vapour pressure and temperature (kPa °C^{-1}), γ_E is the psychrometric constant dependent on air temperature (kPa °C^{-1}), R_n is the net radiation exchange for the free water surface (mm day^{-1}), A_h is the energy advected to the water body (mm day^{-1}), U_2 is the wind speed measured at 2 m (m s^{-1}), D_E is the vapour pressure deficit (kPa) and λ_E is the latent heat of vaporisation (MJ kg^{-1}). This equation requires measurement of various variables and therefore simplifications have been proposed. These include radiation-based equations which neglect the second term of equation (5.1) (e.g. Turc, 1961; Priestley and Taylor, 1972; Doorenbos and Pruitt, 1977) and temperature-based methods (e.g. Blaney and Criddle, 1950; Hargreaves *et al*., 1985).

Potential evapotranspiration is reduced to actual evapotranspiration by differences in land use compared to potential conditions and soil moisture restrictions. The former restriction is often incorporated through multiplication of the reference crop evapotranspiration [a slightly modified version of equation (5.1)] with a crop coefficient dependent on the crop and its development and the average climate. The soil moisture restriction is usually modelled by multiplying potential evapotranspiration with a factor dependent on the volumetric soil moisture content θ (e.g. for daily values Baier and Robertson, 1966; Minhas *et al*.,1974).

Kite and Droogers (2000) compared eight different methods to estimate actual evaporation and transpiration based on field data (FAO-24, FAO-56 and scintillometer), hydrological models (SWAP for the field scale and SLURP for the basin scale) and satellite data [feedback mechanisms (LANDSAT, NOAA AVHRR), biophysical model and energy balance equations]. The SLURP model uses the Penman-Monteith equation (5.1) to calculate potential evapotranspiration and was the only one able to estimate evapotranspiration for the full spatial and temporal ranges (crop to basin, day to long-term annual average).

Although it is difficult to give a general rule for evapotranspiration modelling, it can be concluded that the Penman-Monteith equation is most probably adequate in describing evapotranspiration at a large range of spatial and temporal scales. Radiation-based methods may be used in case of data restrictions, but methods solely based on temperature should generally be avoided (Maidment, 1993).

Surface flow

Surface flow consist of infiltration and saturation excess overland flow and channel flow. Overland flow is the flow of water over the land surface and channel flow is the flow of water through streams and rivers. Overland flow occurs through micro-channels, rills and gullies and can be considered as a small scale version of stream flow (Freeze and Harlan, 1969). Overland and channel flow can be modelled by the Saint-Venant equations of continuity and momentum for one-dimensional, unsteady flow (Saint-Venant, 1871)

$$\underset{\text{(I)}}{\frac{\partial h}{\partial t}} + \underset{\text{(II)}}{h\frac{\partial v}{\partial x}} + \underset{\text{(III)}}{v\frac{\partial h}{\partial x}} = S_s \tag{5.2}$$

$$\underset{\text{(IV)}}{\frac{\partial v}{\partial t}} + \underset{\text{(V)}}{v\frac{\partial v}{\partial x}} + \underset{\text{(VI)}}{g\frac{\partial h}{\partial x}} + \underset{\text{(VII)}}{g\left(S_f - S_0\right)} = -\frac{v}{h}S_s \tag{5.3}$$

where h is the flow depth [L], t is time [T], x is the longitudinal dimension [L], v is the flow velocity [LT^{-1}], S_s is a sink/source term representing interactions with external processes like precipitation, evapotranspiration and infiltration [LT^{-1}], g is the acceleration due to gravity [LT^{-2}], S_f is the slope of the energy line [1] and S_0 is the river bed slope [1]. The basic assumptions used to derive this system are a one-dimensional flow, a hydrostatic pressure distribution and a flow direction towards the lowest elevated neighbouring cell (Chow, 1959). The Saint-Venant equations cannot be solved analytically and should be approximated numerically. Simplifications can be made with respect to the momentum equation (5.3), the three terms of equation (5.2) are generally of the same order of magnitude and can not be omitted (Moussa and Bocquillon, 1996a). In equation (5.3), term (IV) represents the local inertia term, term (V) represents the convective inertia term, term (VI) represents the pressure differential term and term (VII) accounts for the friction and bed slopes. Various wave models can be constructed depending on which of these four terms are used (Grijsen and Vreugdenhil, 1976; Vreugdenhil, 1989):

- kinematic wave (VII)
- diffusion wave (VI and VII)
- steady dynamic wave (V, VI and VII)
- gravity wave (IV, V and VI)
- dynamical wave (IV, V, VI and VII)

A kinematic wave model for overland and channel flow can be obtained by means of storage routing. This method has been used in chapter 3 to model overland and channel flow [equation (3.8)]. A more general form of this equation is

$$Q = k V^m \tag{5.4}$$

where Q [L^3T^{-1}] is defined as the output from a reservoir with capacity V [L^3] and lag constant k [T^{-1}] and m is a dimensionless parameter. If m = 1, the system is linear [see equation (3.8)]. Storage routing can be done in a lumped way (1 reservoir) or in a distributed way (a number of reservoirs).

The mathematical description of channel flow in river basin models usually implies a formulation for flood routing. Flood routing is defined as a mathematical procedure for predicting the changing magnitude, speed and shape of a flood wave as a function of time at one or more points along a river or stream. The river discharges water from sub-basins with an extent of at least the appropriate model scale to sub-basins downstream or directly to the basin outlet. Flood routing in rivers is a classical subject for which many methods of different levels of complexity are available. Besides the one-dimensional formulations mentioned, more complex developments include multibranch models (e.g. Estrela and Quintas, 1994) and detailed 2D models (e.g. Vreugdenhil and Wijbenga, 1982). Flood routing can be classified as either lumped or distributed. The Muskingum method (McCarthy, 1938) is an example of a lumped, kinematic wave-type routing method. The Muskingum-Cunge method (Cunge, 1969) is an example of a distributed, diffusion wave-type method. The first method describes only the displacement of a flood wave, while the second method comprises attenuation as well.

Moussa and Bocquillon (1996a) have developed a quantitative method to identify the appropriate flood routing method for a specific river (stretch) with its own characteristics. Their method defines for a specific threshold (e.g. 5 %) different river wave type zones (e.g. kinematic, diffusion) as a function of two dimensionless numbers: the Froude number F_0^2 that characterises the unperturbed flow regime and T_+ that characterises the wave period in relation to wave damping time

$$(5.5) \qquad F_0^{\,2} = \frac{v_0^{\,2}}{g\,h_0} \qquad T_+ = \frac{\omega_0\, v_0\, S_{f0}}{h_0}$$

where ω_0 [T] is the wave period and the subscript 0 indicates equilibrium conditions. The values for the variables in equation (5.5) and the corresponding dimensionless numbers for the main river stretch and a representative tributary in the Meuse basin are given in Table 5.5. The combinations of these dimensionless numbers and the river wave type zones assuming a threshold of 5 % are shown in Figure 5.20.

Table 5.5 Variables and dimensionless numbers for main river stretch and tributary in Meuse basin.

Variable/ number	Unit	Main river	Tributary
v_0	m/s	0.5	0.5
g	m/s^2	10	10
h_0	m	2	0.5
ω_0	day	10	5
S_{f0}	-	0.0004	0.002
T_+	-	86.4	864
F_0^2	-	0.0125	0.05

Both for the main river and the tributary, the kinematic wave model can be used, although this finding is not convincing for the main river stretch. Other studies (Todini, 1991; Moussa and Bocquillon, 1996a) came to similar conclusions, namely that in most practical applications the inertia terms in equation (5.3) (IV and V) can be neglected and the diffusion wave or kinematic wave equation can be applied. This result is dependent on scale, because the variables of equation (5.5) depend partly on scale (e.g. ω_0).

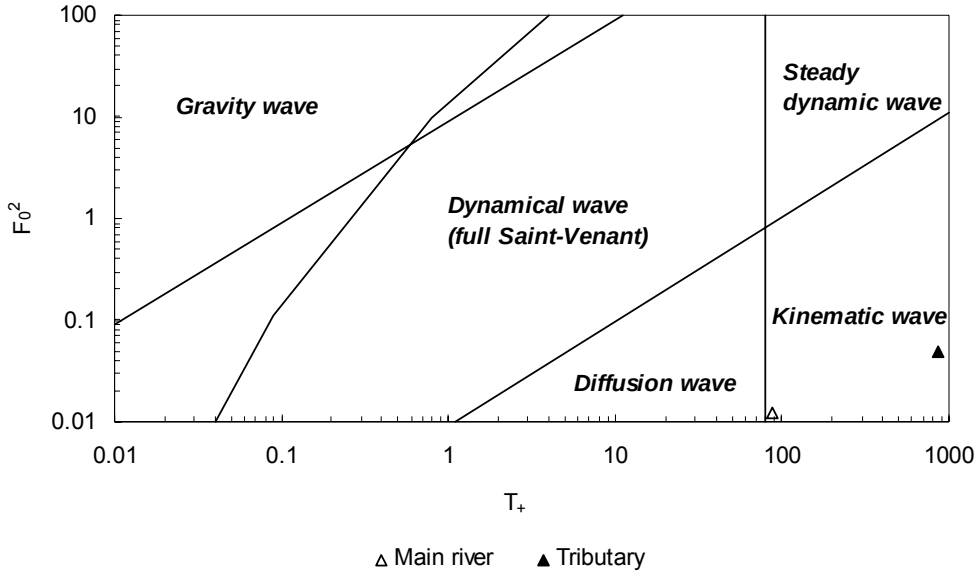

Figure 5.20 River wave type dependent on T_+ and F_0^2 assuming a threshold of 5 %. The cases for the main river and a representative tributary are illustrated.

Subsurface storm flow (macropore flow)

There are only a few hydrological response models which contain a separate macropore flow component (Diermanse, 2001). Germann and Beven (1986) proposed to use the kinematic wave approximation for one-dimensional, unsteady, vertical macropore flow. The continuity equation and the Germann-Beven relation are as follows

$$\frac{\partial \theta_m}{\partial t} + \frac{\partial q_m}{\partial z} = S_m \tag{5.6}$$

$$q_m = a_m \theta_m^{\,b_m} \tag{5.7}$$

where θ_m is the volumetric macropore water content [1], q_m is the specific macropore discharge [LT^{-1}], z is the vertical dimension, S_m is a sink/source term representing interactions with the soil matrix system [T^{-1}] and a_m [LT^{-1}] and b_m [1] are empirically derived constants. Because of the unfamiliarity with macropore flow in general and the difficulty to determine parameters a_m and b_m for the specific case of equation (5.7), subsurface storm flow is often not explicitly modelled or equations (5.6) and (5.7) are approximated (e.g. by the storage routing method).

Subsurface flow

Subsurface flow of water through porous media is modelled as laminar flow and can be described by the continuity equation and the Buckingham-Darcy equation (Buckingham, 1907) for one-dimensional, unsteady, vertical flow

$$\frac{\partial \theta}{\partial t} + \frac{\partial q}{\partial z} = S_{sub} \tag{5.8}$$

$$q = -K_H(\theta)\left[\frac{\partial \psi(\theta)}{\partial z} - 1\right] \tag{5.9}$$

where θ is the volumetric water content [1], q is the specific discharge [LT^{-1}], S_{sub} is a sink/source term representing interactions with external processes like precipitation, evapotranspiration and discharge [T^{-1}], K_H is the hydraulic conductivity [LT^{-1}] and ψ is the pressure head for saturated flow ($\psi \geq 0$) and the tension head for unsaturated flow ($\psi < 0$). It should be mentioned that the hydraulic head is defined as $H = z + \psi$. The combination of equation (5.8) and (5.9) in a general three-dimensional form is called the Richards equation (Richards, 1931). For saturated flow, the value of ψ equals the distance to the groundwater table assuming that the pressure distribution is hydrostatic. For unsaturated flow, the value of ψ depends on θ and thus on the type of soil. The models most frequently used to describe the relationship between ψ and θ for different kinds of soils are the empirical power function relations proposed by Brooks and Corey (1964), Campbell (1974) and Van Genuchten (1980). They have developed power function relationships for $K_H(\theta)$ as well. Equation (5.8) and (5.9) should be solved through application of numerical solution techniques, which requires large amounts of data and computational power. Therefore, often simplified equations are employed such as the Dupuit equations for unconfined, steady state saturated subsurface flow and the storage routing equation (3.8) for saturated and unsaturated subsurface flow.

The infiltration of water into the soil determines the fraction of water subject to infiltration or saturation excess overland flow on the one hand and the fraction subject to subsurface flow on the other hand. Infiltration can also be described by equation (5.8) and (5.9) given S_{sub} and the initial conditions. Because of the complexity of these equations, simplified empirical and approximate models have been developed. Additionally, rainfall excess models which lump all losses (infiltration, depression storage, interception) are used. Empirical infiltration models generally relate infiltration rate to elapsed time modified by certain soil properties. The three most common empirical equations have been developed by Kostiakov (1932), Horton (1940) and Holtan (1961). Approximate theory-based models include those from Green-Ampt (1911) and Philip (1957). Rainfall excess models include index models (e.g. constant loss rate) and the SCS method from equation (2.46).

Several infiltration model comparisons have been conducted in the past. Chen *et al*. (1994a; b) compared the results of the spatially horizontally averaged Richards equation (SHARE) and the averaged Green-Ampt model with the results from a three-dimensional finite difference model of Richards equation for unsaturated flow. They found a very good agreement between the averaged Green-Ampt model and the three-dimensional model, while the SHARE model provided results applicable only when fluctuations in soil parameters are small with respect to their mean values. Mbagwu (1995) compared the results of the Kostiakov, two modified Kostiakov, the Philip and two modified Philip infiltration models with experimental data for highly permeable sandy soils in Southeast Nigeria. He found that the modified Kostiakov models and one modified Philip model agreed very well with observed data. Although these comparisons have been done for small scales, they identified the attractiveness of relatively simple empirical and approximate theory-based infiltration models. Chen *et al*. (1994b) advocated the use of simple formulations like Green-Ampt in large-scale models, such as atmospheric meso-scale models (10-60 km). Obviously, the findings

from these comparisons can not be extrapolated to all geographical areas, objectives and scales, but at least the comparisons did not contradict the application of more simple models to describe infiltration and subsurface flow.

5.5 Summary and conclusions

The dominant processes in flood generation have been derived from literature and can be divided in primary and secondary flood generating processes. Primary processes are, besides precipitation, infiltration excess overland flow, saturation excess overland flow and subsurface storm flow. Secondary processes are processes important for the initial conditions preceding a flooding event and are evapotranspiration and subsurface flow in the soil matrix. The key variables related to these dominant processes have been derived on a qualitative basis and consist of climate and river basin variables. Dominant climate variables are precipitation, temperature and evapotranspiration and dominant river basin variables are elevation, soil type (texture, parent material) and land use type.

Scale features of climate variables have been discussed in chapter 4. The spatial scales of the river basin variables have been dealt with in this chapter; it has been assumed that the variables are time-independent. The appropriate spatial scale of each key variable is assumed to be equal to a fraction of the spatial correlation length of each variable. The fraction was determined on the basis of relationships between statistics and scale and an accepted error in the estimation of the statistic of 10 %. This procedure has been described in chapter 2 and applied to the climate variables in chapter 4 and resulted in an appropriate spatial scale for precipitation of about 20 km. The application to the river basin variables revealed appropriate spatial scales for elevation, soil and land use of respectively 0.1, 5.3 and 3.3 km. The appropriate model scale is determined by multiplying the appropriate variable scales with their associated weights. The weights are based on SCS curve number method relationships between the peak discharge and some specific parameters like slope and curve number. The values of these parameters are dependent on the scale of each key variable. The resulting appropriate model scale is about 10 km, implying 225-250 model cells in an appropriate model of the Meuse basin meant to assess the impact of climate change on river flooding.

Appropriate formulations related to these appropriate scales have been derived from literature and some rough estimations. Formulations of importance were those related to evapotranspiration, surface flow and subsurface (storm) flow. The Penman-Monteith formulation for potential evapotranspiration is able to estimate evaporation and transpiration for the full spatial and temporal ranges (crop to basin, day to long-term annual average), however this formulation requires measurement of various variables among which the radiation balance and wind speed. If these data are not available, simplifications such as the Priestley-Taylor relation are recommended. The appropriate surface flow (overland and river flow) formulation have been determined on the basis of two dimensionless numbers. The kinematic wave model for one-dimensional surface flow can be used for the Meuse and its tributaries. Models for subsurface flow and infiltration have been evaluated and compared in literature, where it was found that simple formulations like Green-Ampt can be appropriately implemented in large-scale models (10-60 km).

Chapter 6

Impact of climate change on river flooding

6.1 Introduction

The importance of assessments of climate change impacts on river flooding has been illustrated in chapter 1. These assessments should be preferably done with appropriate models incorporating the key processes described with appropriate formulations at appropriate scales. The appropriate model components have been determined in chapter 4 and 5 and will be implemented in an existing modelling framework to assess impacts of climate change on river flooding. Additionally, two other model complexities will be used to see the effect of model complexity on the model results. The climate and river basin data to be used in the impact assessment were described in chapter 4 and 5, however the climatic input with climate change requires additional actions and is extensively considered here.

Temperature and evapotranspiration under current and changed climate conditions are considered in section 6.2. Precipitation under current and changed climate conditions modelled with a rainfall model is dealt with in section 6.3. The modelling framework and the implementation of appropriate model components is described in section 6.4. The results of the assessment of climate change impacts on river flooding are discussed in section 6.5 and finally the main results are summarised in section 6.6.

6.2 Temperature and evapotranspiration

6.2.1 Current and changed temperature

Temperature is particularly important for evapotranspiration, but significantly affects snow melt and refreezing of liquid water as well. The appropriate spatial scale for temperature (~1000 km) was found to be much larger than the spatial scale of the Meuse basin (~150 km) (see chapter 4). Therefore, one temperature series can be used as input into a river basin model and consequently General Circulation Model (GCM) simulated temperature can directly be employed (spatial scale of about 300 km). The temperature should only be corrected for elevation differences, because it can decrease considerably with elevation (more than 5 °C/ km).

The temperature data were described in chapter 4. Observed temperature from 12 stations for the period 1967-1996 is used to obtain areally averaged (over the Meuse basin) temperature for the current climate. Modelled temperature from the HadCM3 GCM for the current (1961-1990) and changed (2070-2099) climate is used to estimate average daily changes in temperature with climate change. This is illustrated in Figure 6.1, where the smoothed annual cycle of the daily observed temperature, the HadCM3

simulated temperature for current and changed climate and the difference between HadCM3 simulated temperature for changed and current climate is given. The observed annual temperature cycle is very well simulated by the HadCM3 model, while the other GCMs and Regional Climate Models (RCMs) did this considerably worse. The annual cycle of daily differences between current and changed temperature has been added to the observed temperature series to obtain a 30-year temperature series with climate change. The HadCM3 simulated temperature with climate change has not been directly used, because of the relation between observed temperature and evapotranspiration utilised to derive evapotranspiration with climate change.

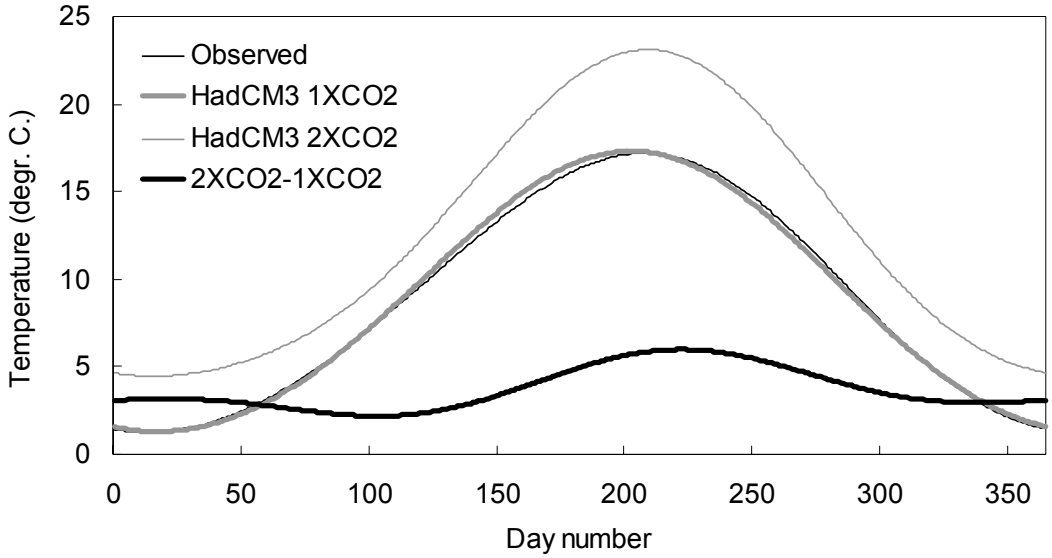

Figure 6.1 Smoothed annual cycle of daily observed temperature, HadCM3 simulated temperature for current (1XCO2) and changed (2XCO2) climate and difference between HadCM3 simulated temperature for changed and current climate (2XCO2-1XCO2).

6.2.2 Current and changed evapotranspiration

The appropriate spatial scale for potential evapotranspiration (~200 km) has about the same magnitude as the spatial scale of the Meuse basin (see chapter 4). Therefore, one evapotranspiration series can be used as input into a river basin model. The evapotranspiration data were described in chapter 4. Observed potential evapotranspiration from 5 stations for the period 1967-1996 is used to obtain areally averaged evapotranspiration for the current climate. The change in potential evapotranspiration is obtained as a function of the day-dependent temperature change from 6.2.1. For that, a relation of Brandsma (1995) is used describing the relative change in monthly evapotranspiration for different temperature changes. The relative change in monthly evapotranspiration for a temperature increase of 3 °C is given in Figure 6.2. Also shown is a fitted curve of the relative daily evapotranspiration change for a temperature increase of 3 °C. This curve has been used to estimate for a given temperature change the average daily evapotranspiration changes by simple scaling (e.g. a temperature increase of 4.5 °C for a day in February gives approximately a 22.5 % change in evapotranspiration instead of 15 % with a 3 °C temperature increase). Finally,

these relative changes in evapotranspiration have been multiplied with the observed series to obtain a 30-year evapotranspiration series with climate change. The obtained 30-year temperature and evapotranspiration series with climate change are both based on observed series and thus are correlated in a similar way as observed in chapter 4.

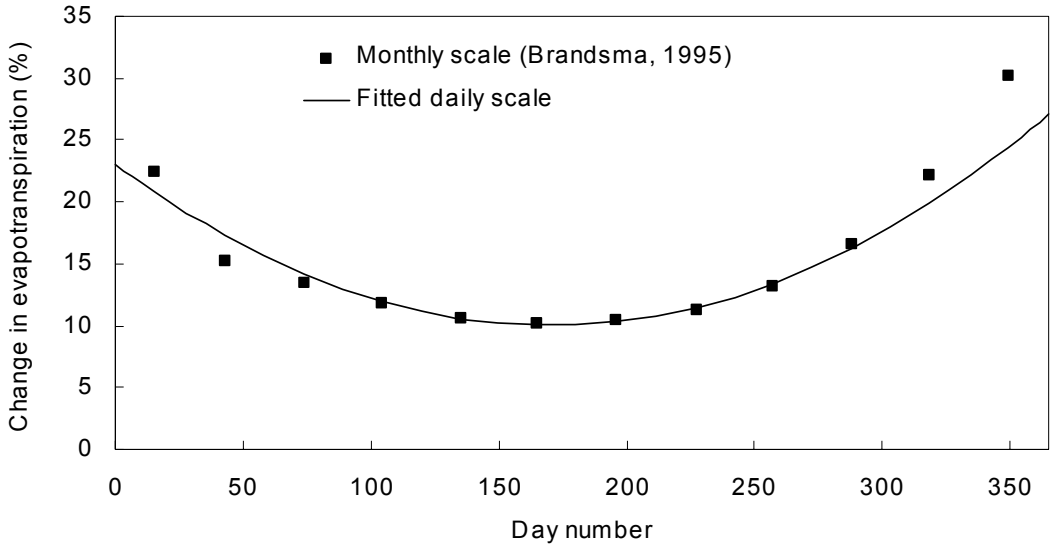

Figure 6.2 Monthly scale and fitted daily scale change in evapotranspiration in % for a temperature increase of 3 °C.

6.3 Rainfall: space-time random cascade model

6.3.1 Introduction

The generation of rainfall for the current and changed climate, to be used as input into a river basin model, is less straightforward than the generation of temperature and evapotranspiration, because the appropriate spatial scale of precipitation is much smaller (~20 km) than for temperature and evapotranspiration. GCMs and RCMs have a spatial resolution of about 300 km and 50 km respectively and therefore they are not able to provide rainfall input at an appropriate spatial scale. Moreover, RCM time series generally have an insufficient length in the context of flood frequency analysis. Therefore, other, more statistical downscaling approaches are needed as mentioned in chapter 1. The main approaches were factor, regression, classification, re-sampling and conditional methods. Comparisons between these different methods do not agree about which method to choose (e.g. Wilby and Wigley, 1997; Kidson and Thompson, 1998; Murphy, 1999) as discussed in chapter 1. Factor methods are seriously deficient in physical consistency and can not represent changes in spatial and temporal correlation. Re-sampling methods are able to reproduce current climate well, but are not preferable in climate change issues, in particular with respect to extreme events which have never been observed. A similar reasoning applies to regression methods, for which the regression equations have not been proven to be valid for the climate change situation. Here, classification and conditional methods are supposed to be most suitable for downscaling the GCM and RCM generated climate to the appropriate spatial scale. A

conditional method (stochastic rainfall model) will be used here, because of its ability to generate multiple realisations that characterise the stochastic behaviour of rainfall.

The stochastic rainfall model should at least be able to reproduce the following statistics at the appropriate scale (20 km):

- mean and variability
- occurrence of dry and wet days
- transition probabilities between different rainfall states
- spatial and temporal correlation behaviour
- extreme values

These spatial and temporal requirements automatically exclude application of temporal rainfall models such as Markov chains and truncated negative binomial distributions (Chapman, 1997) or the generalised Pareto distribution model and the random pulse Bartlett-Lewis gamma model (Cameron *et al*., 2000). Space-time stochastic rainfall models are required instead.

Two general approaches are available for modelling space-time rainfall. The first approach focuses on the mathematical theory of cluster point processes to reproduce the hierarchical spatial and temporal organisations exhibited by observations (e.g. Waymire *et al*., 1984; Kavvas *et al*.., 1987). The main difficulties with this approach are the parameter estimation and the inability to fully describe the statistical structure of rainfall over a large range of scales. These two difficulties can be avoided by using the second approach of space-time rainfall modelling. This involves the use of certain scale invariant features seen in measured rainfall fields. Most of the modelling efforts in this respect are based on the theory of multiplicative random cascades (Lovejoy and Schertzer, 1990; Gupta and Waymire, 1993). These cascades have their conceptual basis in turbulence theory, where a cascade of turbulent eddies is seen as transferring kinetic energy from a large energy scale progressively to smaller dissipation scales. In rainfall, the analogous situation is to disaggregate the total mass of rainfall in a hierarchical manner, such that an area of higher intensity is embedded in larger areas of lower intensity, which are, in turn, part of even larger structures of even lower rainfall intensity (Jothityangkoon *et al*., 2000). Continuous and discrete random cascade models have been developed. Here, the discrete form of Over and Gupta (1996) has been used for two reasons. First, a discrete form is able to represent non-rainy areas and second, it can be appropriately adapted in rainfall-runoff modelling where a discrete partitioning of sub-basins exists.

6.3.2 Space-time rainfall model

The random cascade model consists of a temporal rainfall model for the whole region and a spatial model for the disaggregation of this rainfall to the appropriate scale. The two models are described below.

Temporal rainfall model

The temporal rainfall model consists of a first-order discrete Markov chain determining rainfall occurrence and a truncated two-parameter gamma distribution describing rainfall amount. Markov chains have been frequently used in the past to model daily rainfall occurrence (Gabriel and Neumann, 1962; Moon *et al.*, 1994; Jimoh and Webster, 1996). Compared to more traditional time-series models [autoregressive

moving average (ARMA) models] they have the advantage that they can handle zero-rainfall. The first-order discrete Markov chain is a stochastic process which describes the occurrence of daily rainfall as belonging to a number of discrete states; the zero-rainfall state and a number of states defined on the basis of the rainfall amount. The probability of the rainfall on any given day belonging to a specified state is conditional on the rainfall state of the previous day. Therefore, the first-order Markov chain can be characterised by a NxN state transition matrix with elements p_{ij} as described by equation (2.24). This first-order, N-state Markov chain can be used to generate a sequence of daily rainfall states.

The rainfall amount belonging to one of the non-zero rainfall states is generated from a truncated form of the two-parameter gamma distribution [see equation (2.15)], which has proven to be appropriate for the description of non-zero, spatially averaged daily rainfall (see chapter 4). The parameters of this distribution can be estimated from spatially averaged rainfall data and they can possibly vary throughout the year. Truncated gamma distributions are constructed for each of the non-zero rainfall states. Knowing the lower and upper limits of the rainfall amounts for each state, the probability weight between these limits can be estimated. The truncated gamma distribution for each state is then obtained by dividing the full gamma distribution by the corresponding estimated probability weight (Jothityangkoon *et al.*, 2000).

Spatial rainfall model

The spatial disaggregation of the daily temporal rainfall series is achieved using the discrete random cascade approach as proposed by Over and Gupta (1996). A summary of their approach, also given by Jothityangkoon *et al*. (2000), follows here.

The construction of a discrete random cascade begins with a rainfall volume over a two-dimensional (d = 2) area that was simulated with the temporal rainfall model. This volume is successively divided into b equal parts ($b = 2^d$) at each step, and during each subdivision the volume obtained at the previous disaggregation step is distributed into the b subdivisions by multiplication by a set of 'cascade generators' W, as shown for two arbitrary steps in Figure 6.3. At the first step, the volume for the total area is subdivided into b = 4 subareas denoted by Δ^i_1, i = 1, …, 4. At the second step, each of the above subareas is further subdivided into b = 4 further subareas (Δ^i_2, i = 1, …, 16). This subdivision is continued down the scale, leading to b^n subareas (Δ^i_n, i = 1, …, b^n) at the nth step. If the initial intensity is P_0 and L_0 is the scale of the total area, then with Figure 6.3, the volume $V_n(\Delta^i_n)$ in the subareas at the nth step of subdivision is given by

$$V_n\left(\Delta^i_n\right) = P_0 L_0{}^d b^{-n} \prod_{j=1}^{n} W_j^i \qquad (6.1)$$

where each j, i represents the subarea along the path to the nth step subarea. The multipliers W are random cascade generators with the constraints that they are nonnegative and their average is 1, as follows from the mass conservation law. The generated precipitation fields are isotropic, i.e. its correlation lengths do not depend on wind direction.

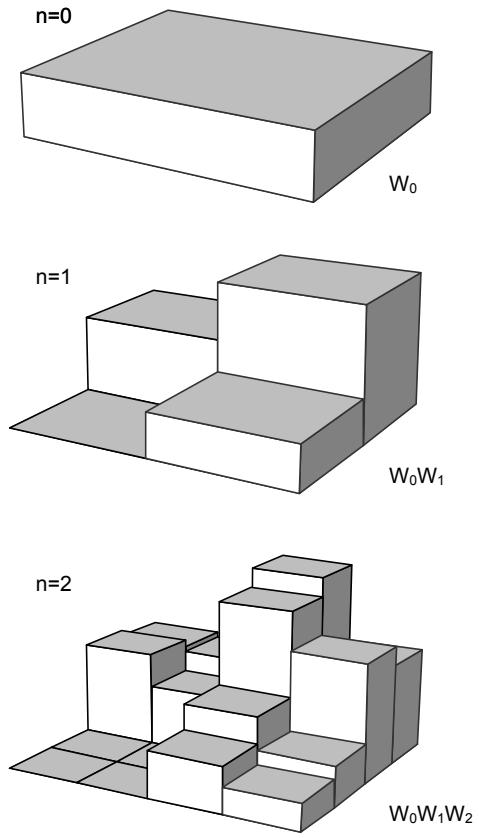

Figure 6.3 Illustration of two steps (n = 2) of rainfall volume subdivision in the random cascade model with cascade generators W_0, W_1, W_2.

Over and Gupta (1994; 1996) proposed the so-called beta-lognormal model for the generation of the cascade generators. This model considers W as a composite generator $W = BY$, where B is drawn from the beta model and Y is drawn from the lognormal model. The beta model partitions the region into sets with and without rain and the lognormal model assigns rainfall amounts for each subdivision. The probability distribution of $W = BY$ for an arbitrary subarea and step of subdivision is as follows

$$\begin{aligned} &P(W=0)=1-b^{-\beta} \\ &P(W=BY=b^{\beta}Y=b^{\beta-\ln(b)\sigma^2/2+\sigma X})=b^{-\beta} \end{aligned} \tag{6.2}$$

where X is the standard normal random variate and β and σ are parameters. Over and Gupta (1994; 1996) proposed that these parameters can be estimated by using the so-called Mandelbrot-Kahane-Peyriere (MKP) function, named after Mandelbrot (1974) and Kahane and Peyriere (1976). The MKP function, denoted by $\chi(q)$, is defined as the slope of the scaling relationship of the qth ensemble moment of the random

precipitation field with respect to the level of subdivision n. The qth ensemble moment for scale ratio $\lambda_n = L_0/L_n$ (= 2^n in this two-dimensional case) $M(\lambda_n, q)$ is as follows

$$M(\lambda_n, q) = \sum_{i=1}^{b^n} \left[V_n\left(\Delta^i{}_n\right)\right]^q \tag{6.3}$$

The scaling behaviour of $M(\lambda_n, q)$ with λ_n can be investigated with the following relationship

$$M(\lambda_n, q) = [\lambda_n]^{\tau(q)} \tag{6.4}$$

where $\tau(q)$ is the slope of the log-log relationship between $M(\lambda_n, q)$ and λ_n for a specific exponent q. The estimator of the MKP function $\chi(q)$ is then equal to $\tau(q)/d$, also if λ_n is not a multiple of 2 and thus n is a noninteger (Jothityangkoon *et al*., 2000). Over and Gupta (1996) theoretically derived an expression for $\chi(q)$ for the beta-lognormal model

$$\chi_n(q) = (\beta - 1)(q - 1) + \left[\sigma^2 \ln(b)/2\right](q^2 - q) \tag{6.5}$$

Next, equation (6.5) can be matched with the estimated $\tau(q)/d$ to derive β and σ^2. Therefore, Over and Gupta (1996) used the first and second derivatives of $\tau(q)$ with respect to q to obtain

$$\tau^{(1)}(q) = d\left[\beta - 1 + \left(\sigma^2 \frac{\ln(b)}{2}\right)(2q - 1)\right] \tag{6.6}$$

$$\tau^{(2)}(q) = d\sigma^2 \ln(b) \tag{6.7}$$

Both $\tau^{(1)}(q)$ and $\tau^{(2)}(q)$ can be derived from the empirical plots of $\tau(q)$ vs. q, usually at q = 1, however Jothityangkoon *et al*. (2000) have used q = 2 with good results. Finally, equations (6.6) and (6.7) are combined to express the cascade parameters β and σ^2 in terms of $\tau^{(1)}(q)$ and $\tau^{(2)}(q)$

$$\sigma^2 = \frac{\tau^{(2)}(q)}{d \ln(b)} \tag{6.8}$$

$$\beta = 1 + \frac{\tau^{(1)}(q)}{d} - \frac{\sigma^2 \ln(b)}{2}(2q - 1) \tag{6.9}$$

6.3.3 Parameter estimation and generation of synthetic fields

The rainfall data were described in chapter 4. Observed rainfall from 39 stations for the period 1970-1999 is used to estimate the parameters of the temporal and spatial rainfall model for the current climate. Modelled rainfall from 3 GCMs and 2 RCMs for various periods is used to estimate changes in the parameters of the temporal model with climate change and the 2 RCMs are used to estimate changes in the parameters of the spatial model with climate change.

Parameter estimation for temporal model

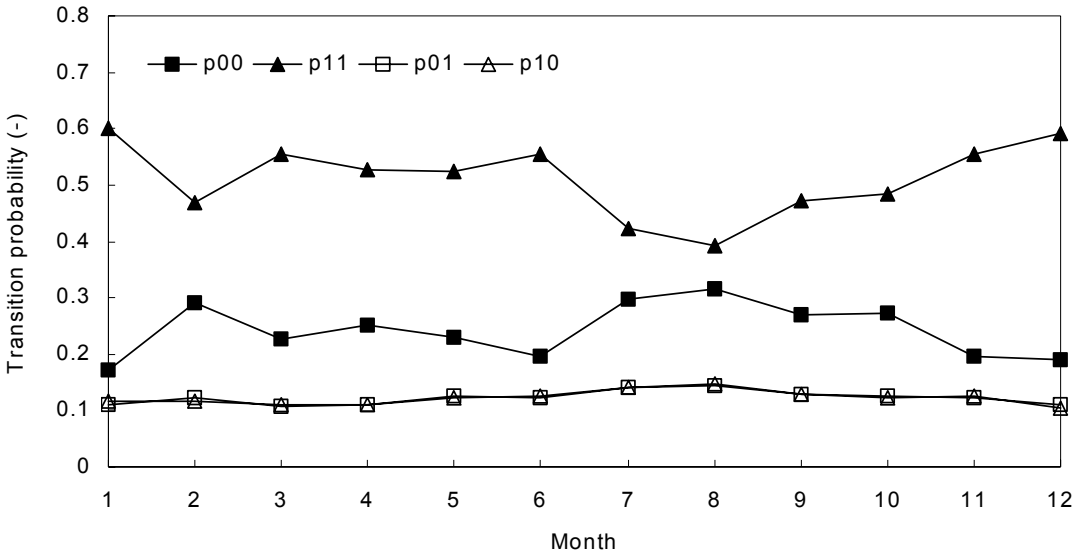

Figure 6.4 Transition probabilities (p00, p11, p01 and p10) of areally averaged observed precipitation as a function of month.

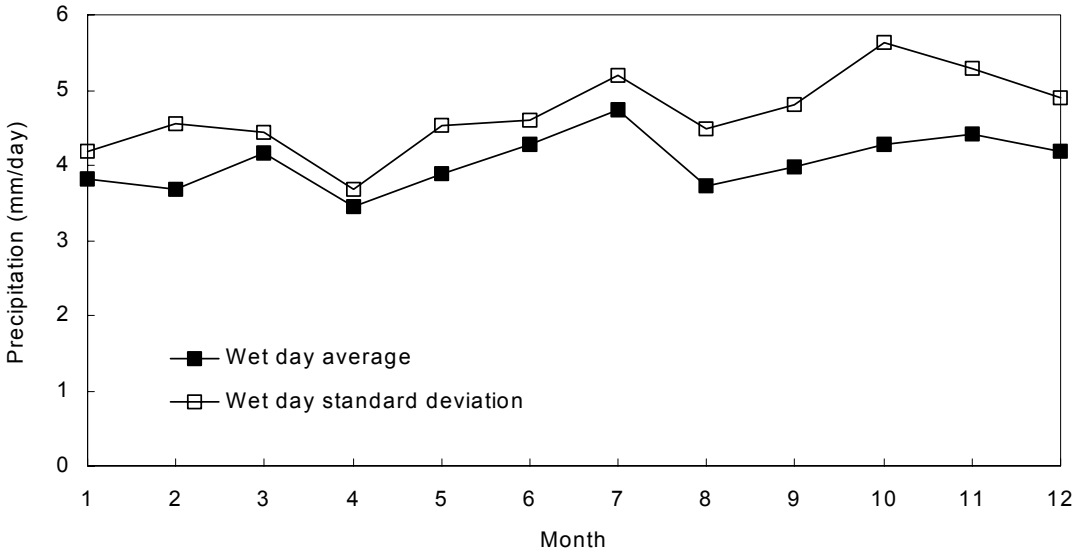

Figure 6.5 Wet day average and standard deviation of areally averaged observed precipitation as a function of month.

Four rainfall states are considered ($N = 4$): $P \leq 0.1$ mm/day (p_1), $0.1 < P \leq 1$ mm/day (p_2), $1 < P \leq 4$ mm/day (p_3) and $P > 4$ mm/day (p_4). These limits have been determined on the basis of approximately equal probabilities (0.25) that rainfall on an arbitrary day belongs to one of these states. The transition probabilities of the first-order, four-state discrete Markov chain p_{ij} are estimated from the areally averaged observed rainfall

series for the current climate and changes in these probabilities with climate change are estimated from the 3 GCMs and 2 RCMs. The transition probabilities are assumed to be time-invariant as supported by Figure 6.4, where the transition probabilities for two states ($P \leq 0.1$ mm/day and $P > 0.1$ mm/day) for each month are given.

The wet day ($P > 0.1$ mm/day) rainfall amounts are used to estimate the parameters (α_g and β_g) of the gamma-distribution [see equation (2.15)] for the current and changed climate. These parameters are also assumed to be constant throughout the year as supported by Figure 6.5, where the wet day average and standard deviation for each month are given. The parameters of the temporal rainfall model are summarised in Table 6.1.

Table 6.1 Parameters of the temporal rainfall model for current and changed climate.

	Current climate	Changed climate
α_g	0.59	0.59
β_g	5.10	6.65
p_{11}	0.18	0.25
p_{21}	0.04	0.05
p_{31}	0.02	0.02
p_{41}	0.01	0.01
p_{12}	0.05	0.06
p_{22}	0.09	0.08
p_{32}	0.05	0.04
p_{42}	0.03	0.03
p_{13}	0.03	0.03
p_{23}	0.05	0.04
p_{33}	0.16	0.12
p_{43}	0.05	0.04
p_{14}	0.01	0.01
p_{24}	0.02	0.02
p_{34}	0.05	0.04
p_{44}	0.16	0.15

Parameter estimation for spatial model

The parameter estimation for the spatial model involves three steps: the estimation of the qth ensemble moments $M(\lambda_n, q)$ as a function of scale ratio λ_n, the estimation of the slope $\tau(q)$ of the log-log relationship between $M(\lambda_n, q)$ and λ_n for a specific exponent q and the estimation of the cascade parameters β and σ^2. These steps are described below.

Figure 6.6 shows an example of the qth statistical moments $M(\lambda_n, q)$ as a function of scale ratio λ_n for q in the range 0-4.0 (also noninteger values) for a given observed day. Therefore, all rainfall data for that day were used and aggregated in different manners (e.g. 1, 4, 9, 16, 36, 64 cells). This was done for all days of the 1970-1999 period. Next, for each exponent q and day of the estimation period straight-line regressions were fitted with log-log scales and the slope $\tau(q)$ could be estimated. Figure 6.7 shows examples of the estimated slopes $\tau(q)$ as a function of q for 12 arbitrary days for observed winter, observed summer, HadRM2 simulated current climate and HIRHAM4 simulated current climate.

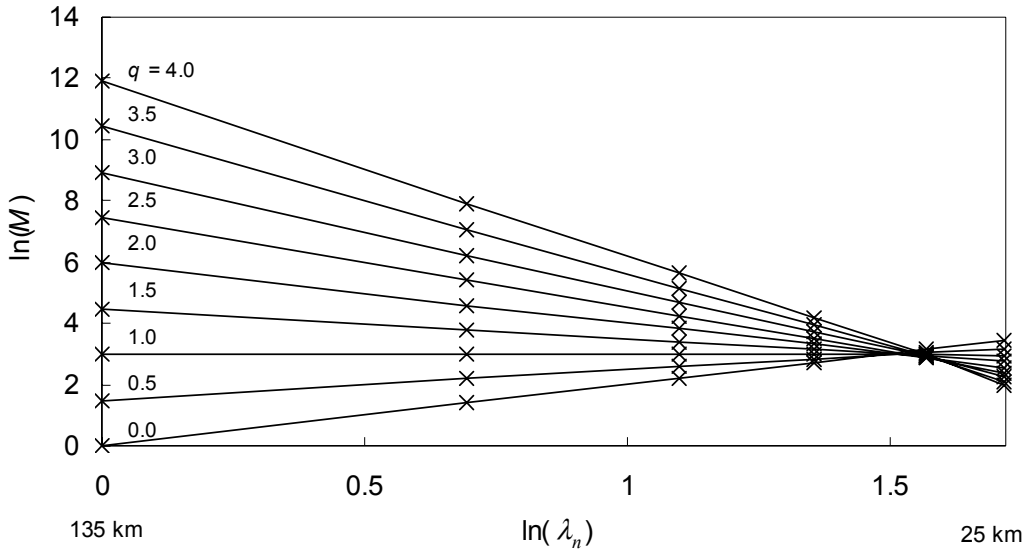

Figure 6.6 Estimated qth statistical moments $M(\lambda_n, q)$ as a function of scale ratio λ_n for a given observed day.

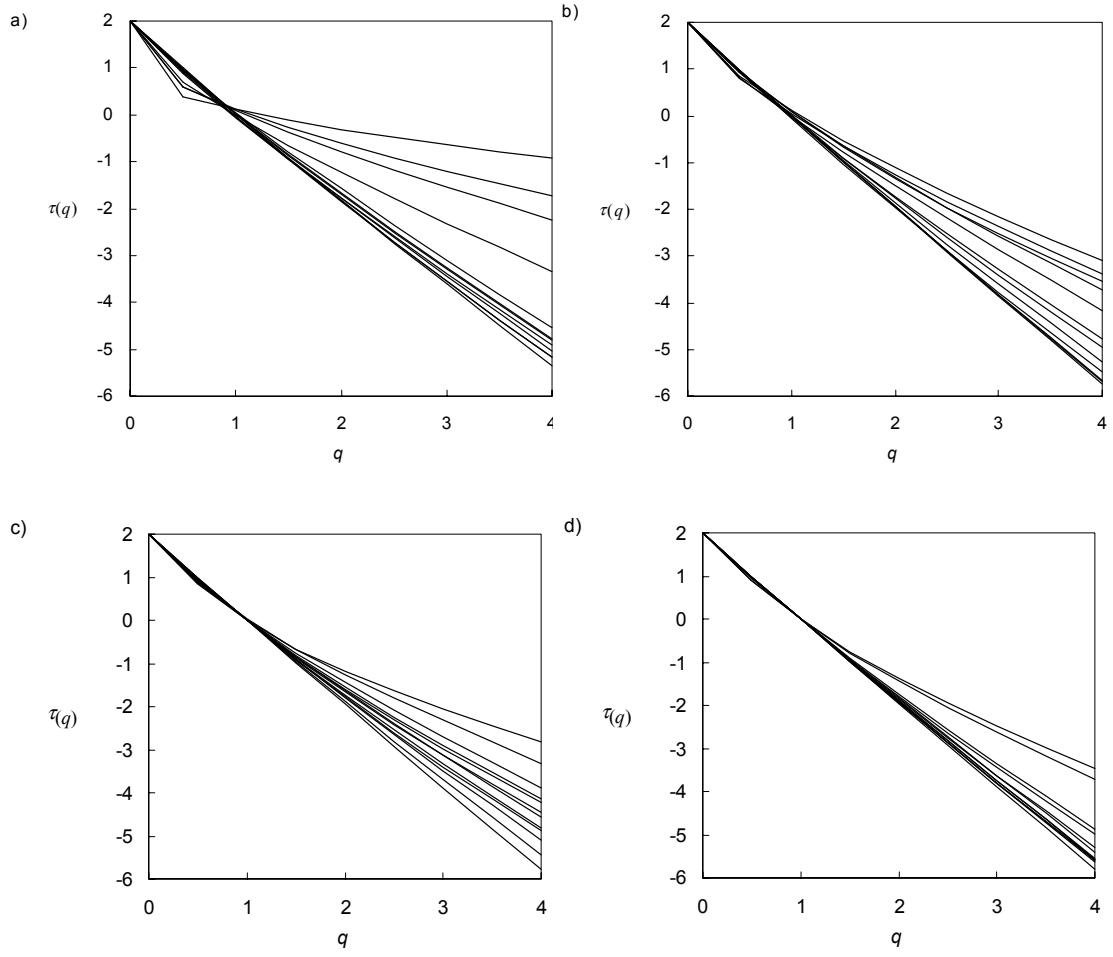

Figure 6.7 Estimated slopes $\tau(q)$ as a function of q for a) 12 (arbitrary) observed winter days, b) 12 observed summer days, c) 12 days in HadRM2 for current climate, d) 12 days in HIRHAM4 for current climate.

Finally, the cascade parameters β and σ^2 were estimated for each day using the first and second derivative of $\tau(q)$ at q = 2. The use of q = 2 can be questioned, but Jothityangkoon *et al*. (2000) came to the conclusion that this value can be favoured over q = 1 used by others (e.g. Over and Gupta, 1996). The cascade parameters β and σ^2 as a function of areally averaged rainfall intensity P_0 (over the whole region) are given in Figure 6.8 and Figure 6.9 for observed rainfall and HadRM2 and HIRHAM4 simulated rainfall for current and changed climate for all considered days. These figures show a dependence of the cascade parameters on average rainfall intensity, in particular for observed (point) rainfall. This feature has been found by Jothityangkoon *et al*. (2000) as well, in contrast to Over and Gupta (1996). The relations between the cascade parameters and average rainfall intensity have been analytically expressed by empirical functions

$$\beta = f_1^{P^{f_2}} \tag{6.10}$$

$$\sigma^2 = \exp\left[f_3 (\ln P_0)^2 + f_4 (\ln P_0) + f_5\right] \tag{6.11}$$

where f_1, f_2, f_3, f_4 and f_5 are constants which have been obtained by least square optimisation [analogous to Jothityangkoon *et al*. (2000)]. The cascade parameters were assumed to be homogeneous over the Meuse basin and stationary in time following Jothityangkoon *et al*. (2000). They found for a larger and much more variable region relatively space and time invariant cascade parameters as well. The constants from equations (6.10) and (6.11) are given in Table 6.2 for the current climate (from observed rainfall) and for the changed climate. The constants for changed climate conditions have been derived by using the relative differences between the HadRM2 and HIRHAM4 simulated constants for the current and changed climate and the observed constants.

Table 6.2 Parameters of the spatial rainfall model for current and changed climate.

	Current climate	Changed climate
f_1	0.18	0.20
f_2	0.42	0.41
f_3	-0.074	-0.071
f_4	-0.12	-0.11
f_5	-2.50	-2.56

If observed rainfall exhibits strong spatial gradients in average rainfall, a deterministic multiplier can be added to W [equation (6.2)] to account for these gradients (see Jothityangkoon *et al*., 2000). However, Figure 6.10 shows no clear spatial patterns in average rainfall and therefore no deterministic generator has been used.

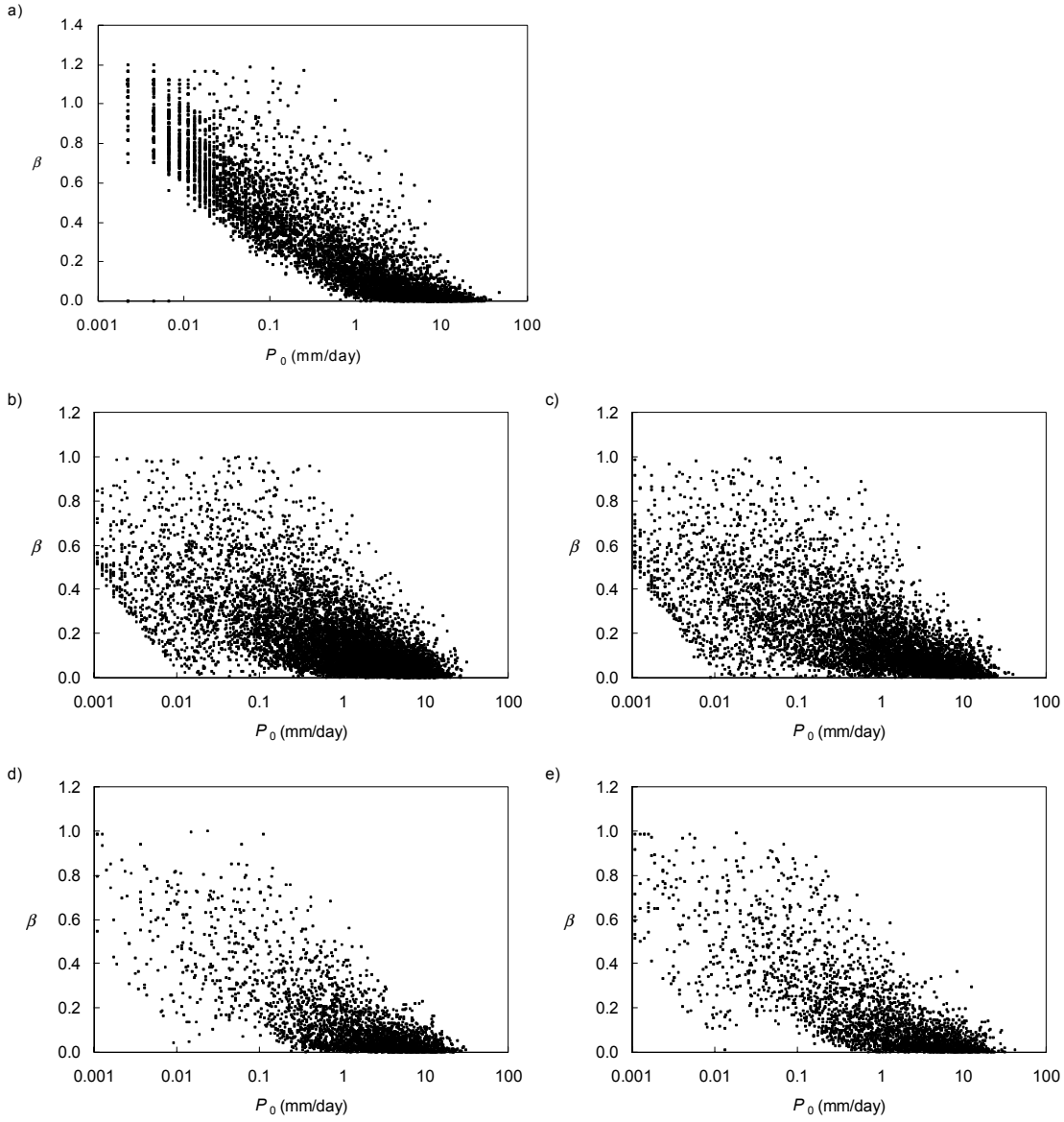

Figure 6.8 Cascade parameter β as a function of areally averaged rainfall in mm/day for a) observed rainfall, b) HadRM2 for current climate, c) HadRM2 for changed climate, d) HIRHAM4 for current climate, e) HIRHAM4 for changed climate.

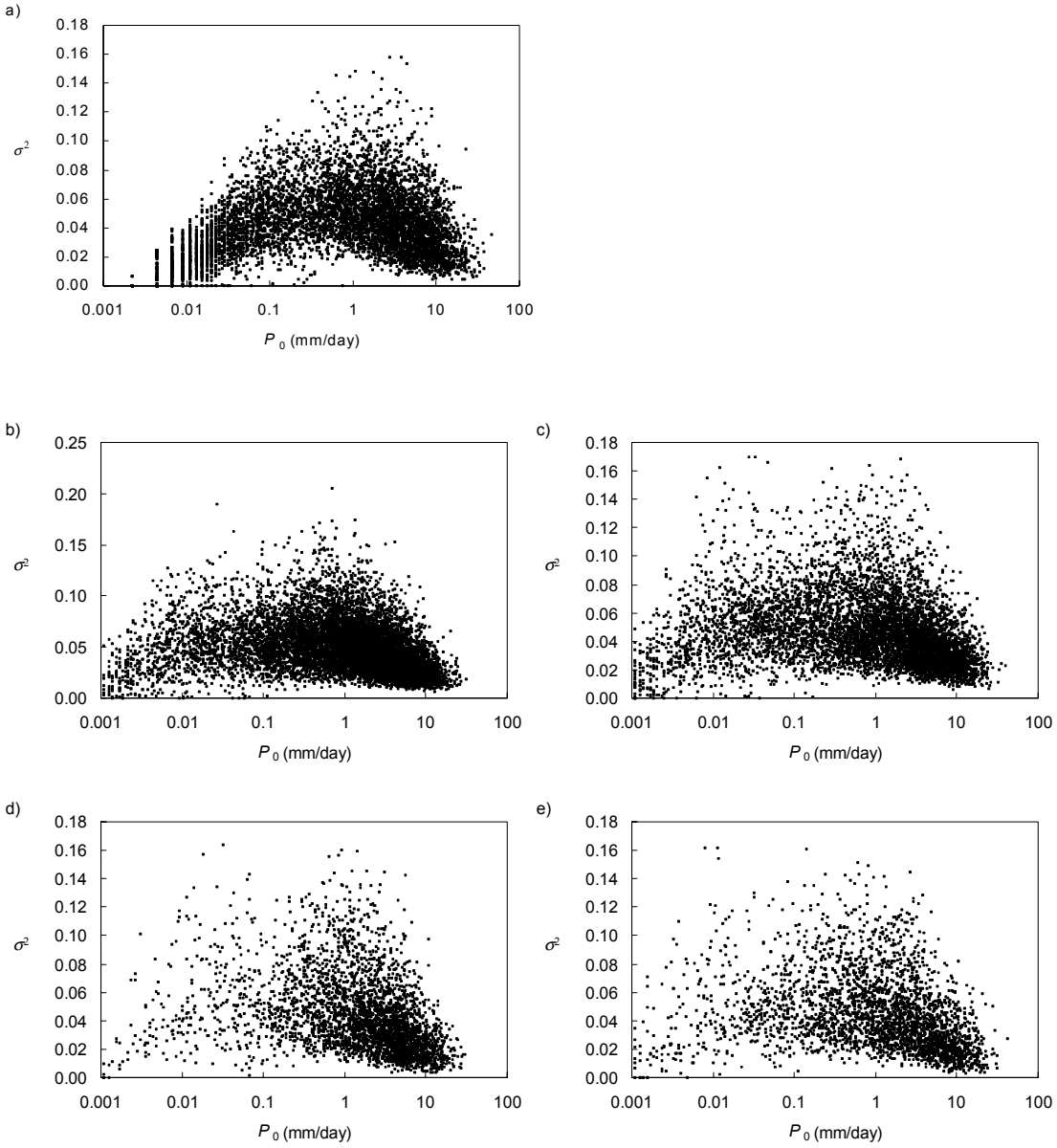

Figure 6.9 Cascade parameter σ^2 as a function of areally averaged rainfall in mm/day for a) observed rainfall, b) HadRM2 for current climate, c) HadRM2 for changed climate, d) HIRHAM4 for current climate, e) HIRHAM4 for changed climate.

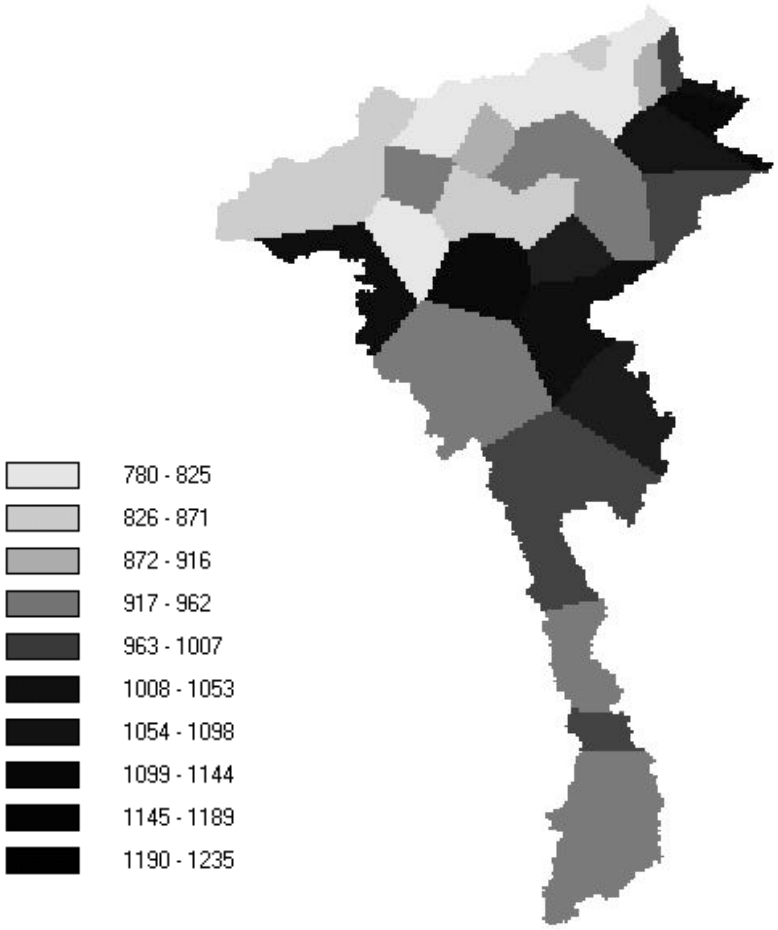

Figure 6.10 Average rainfall in mm year^{-1} for Thiessen polygons in the Meuse area. A Thiessen polygon is based on the assumption that for any point in the river basin, rainfall is equal to the observed rainfall at the closest rain gauge.

Generation of synthetic rainfall fields

The generation of synthetic rainfall fields consists of two main steps. First, the generation of a regionally averaged rainfall time series using the first-order four-state Markov chain and the two-parameter truncated gamma distribution. Second, for each day of the time series, the disaggregation of the daily averaged rainfall using the stochastic random cascade model.

The temporal rainfall simulation is straightforward. Depending on the starting state, the subsequent state is generated on the basis of the appropriate transition probabilities. Then, depending on the generated state, the truncated gamma distribution is used to generate the rainfall amount. These steps are repeated for each time step in the simulation period.

The random cascade model works by progressively subdividing a 320 km × 320 km region over four successive levels down to the appropriate scale of 20 km and, at each level, multiplying the rainfall volume estimated at the previous level by the stochastic cascade generator $W = BY$. In this way, 16 × 16 = 256 rainfall cells would be obtained. However, the majority of these cell lies outside the Meuse basin, because this basin does

not have a square shape, but rather an elongated shape. Therefore, rainfall is only generated for cells entirely or partly lying in the Meuse basin (at the 20 km scale) and for all cells at other disaggregation levels necessary to obtain the 20 km scale rainfall in the 'Meuse basin cells'. The resulting 76 cells in the Meuse basin are illustrated in Figure 6.11.

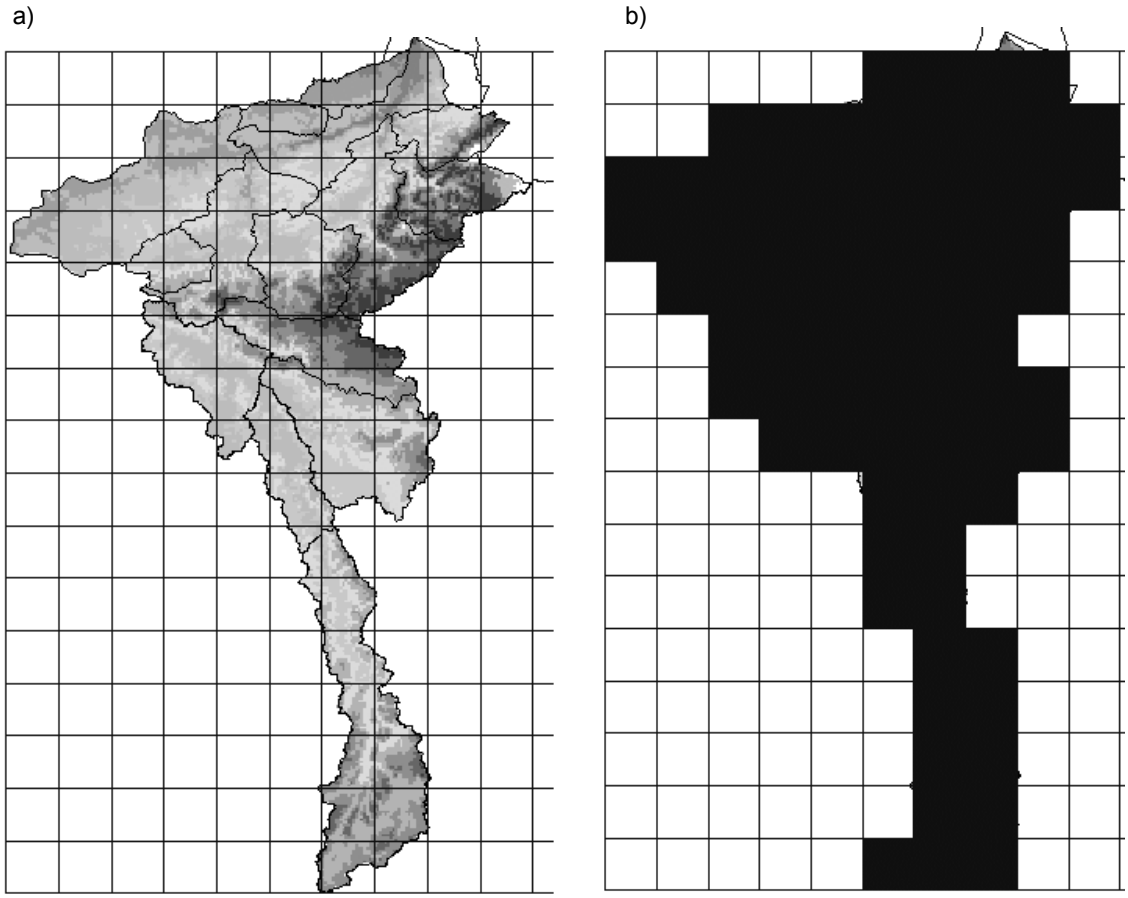

Figure 6.11 Cell grid of random cascade model for the Meuse basin with a) projected on the Meuse basin with 15 sub-basins, b) resulting 76 model cells representing the Meuse basin.

The random cascade model parameters β and σ^2 are continuously updated on the basis of the P_0 value at each level of disaggregation. This methodology of continuously updating was found to be better than using cascade parameters β and σ^2 as a function of the (same) regionally averaged P_0 value at each level of disaggregation, in particular in simulating rainfall variability and extreme rainfall (Jothityangkoon *et al*., 2000).

6.3.4 Synthetic rainfall for current and changed climate

The adequacy of the random cascade rainfall model is tested by comparing relevant statistics as mentioned in 6.3.1 of observed and simulated space-time rainfall series for current climate conditions. Subsequently, the relevant statistics of simulated and GCM/RCM simulated changed climate can be compared to assess the ability of the random cascade model to simulate precipitation with climate change at the appropriate scale. The influence of the stochasticity of the precipitation process is investigated by

performing for both current and changed climate conditions 5 realisations with the random cascade model keeping the parameters at a constant level. The influence of the outcomes of the 5 individual climate models is considered by performing 5 simulations for changed climate conditions with parameters in each simulation according to the individual climate models.

Current climate

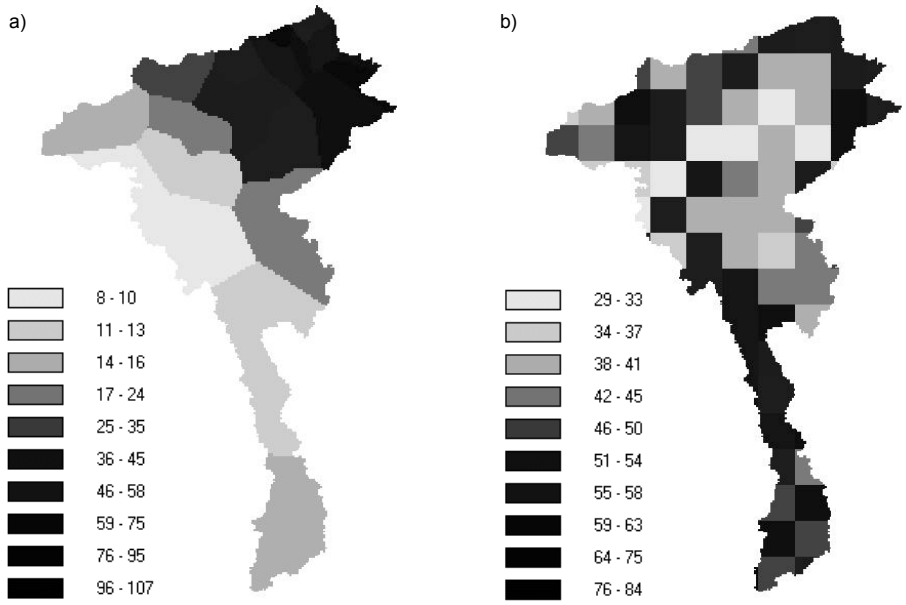

Figure 6.12 Precipitation fields associated with the 30-year maximum of daily precipitation averaged over the whole field in mm day^{-1} for the Meuse area obtained from a) point measurements shown through Thiessen polygons and b) the random cascade model for current climate.

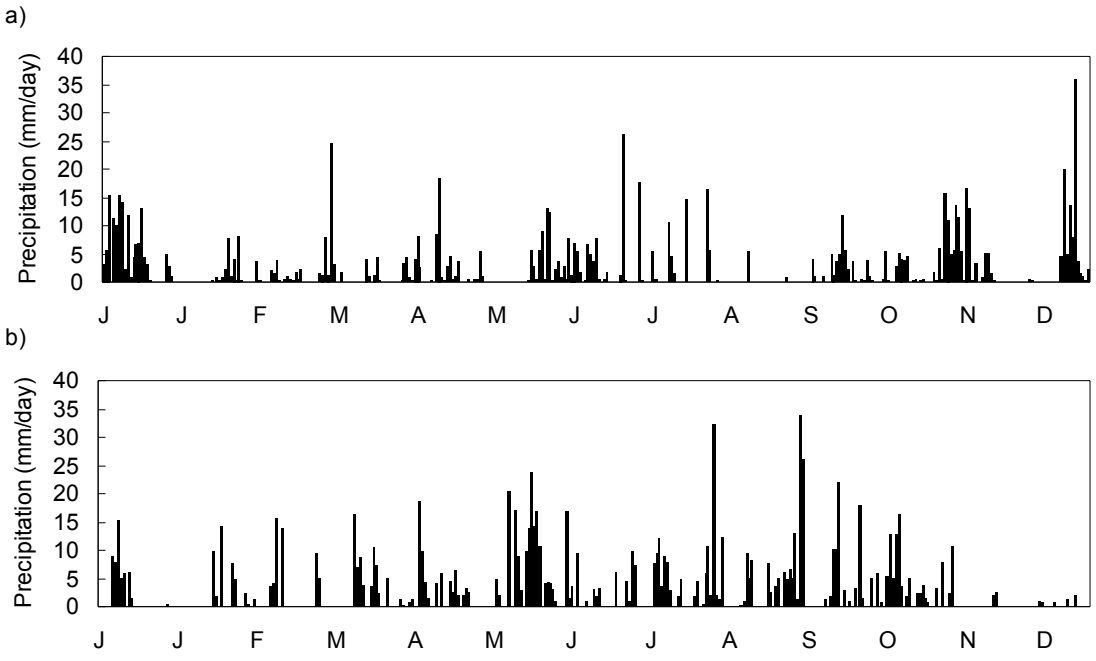

Figure 6.13 Daily precipitation at the 20 km scale in mm day^{-1} during an arbitrary year (J = January,..,D = December) for a) an averaged observed series and b) a random cascade modelled series.

Figure 6.12 and Figure 6.13 give some idea of the ability of the model to simulate spatial and temporal rainfall patterns. In Figure 6.12, the precipitation fields associated with the 30-year maximum of daily precipitation averaged over the whole field are given. The pattern in Figure 6.12a represents point values, whereas the pattern in Figure 6.12b represents areally mean values at the 20 km scale. The spatial patterns exhibit a similar variability, although general conclusions can not been drawn on the basis of just one, arbitrary extreme day. The temporal patterns in Figure 6.13 are at the same scale. These patterns do not show striking differences in behaviour, however a more thorough statistical analysis of the results should further assess the quality of the rainfall model.

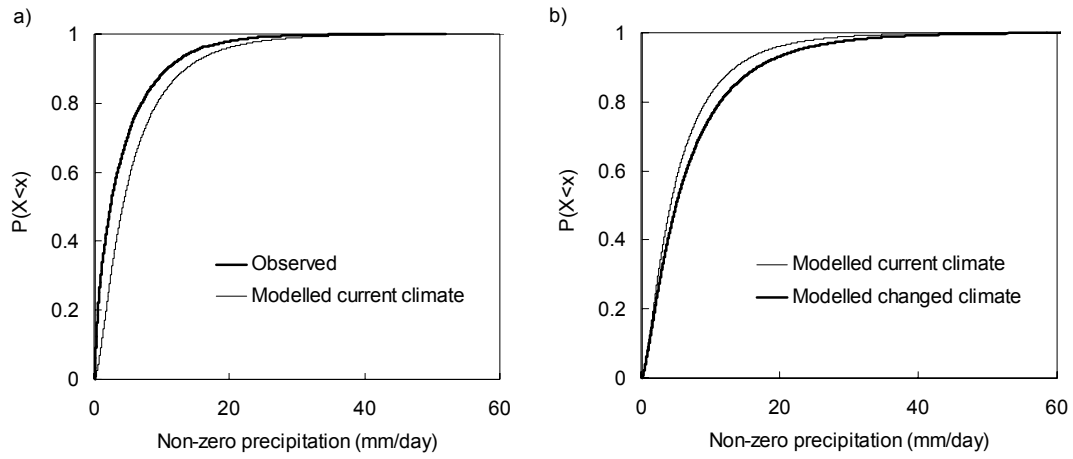

Figure 6.14 Cumulative frequency distribution for non-zero precipitation (> 0.1 mm/day) at the 20 km scale for a) observed station series and modelled series for current climate and b) modelled series for current and changed climate.

Therefore, Figure 6.14 shows the cumulative frequency distribution of non-zero daily precipitation for observed and modelled current and changed climate (one realisation). The observed precipitation is a little overestimated by the model in Figure 6.14a, but the distributions have a similar shape. Figure 6.14b shows a slight increase of precipitation with climate change, a feature simulated by the GCMs and RCMs as well. Figure 6.15 gives the extreme value distributions of annual maximum daily precipitation at the appropriate scale (20 km) for observed ordered values (reduced from point to 20 km scale) and the minimum and maximum of 5 realisations of ordered modelled values. The observed annual maxima are even overestimated by the minima of the realisations for small return values (left-hand side of the figure), but are well simulated for larger return values which are in particular important with respect to river flooding.

The relevant statistics for the observed and modelled climate by means of 5 realisations are summarised in Table 6.3. Besides the daily return values, also the 5-day, 8-day and 10-day return values are given as they may be important for river flooding (see e.g. Diermanse, 2001). The results show that all statistics except the wet day frequency are well simulated. The underestimation of the wet day frequency by the model originates from the spatial disaggregation. Namely, the wet day frequency of the temporal areally averaged precipitation series is well simulated by the precipitation model, but during the disaggregation, the model gradually simulates too many dry days. This may be an artefact of the model and can be investigated in future, also because the reduction of the variability and return values is quite well simulated by the random cascade model.

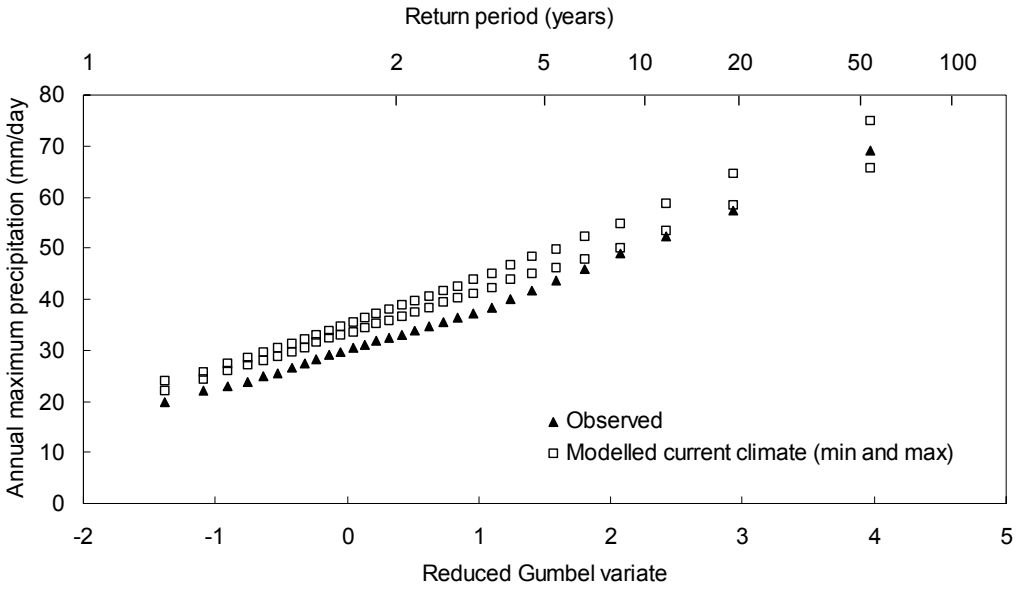

Figure 6.15 Annual maximum precipitation in mm day^{-1} at the 20 km scale as a function of the reduced Gumbel variate and return period in years for reduced ordered station values (averaged over 39 points) and the minimum and maximum of 5 realisations of ordered modelled values (averaged over 76 cells).

Table 6.3 Daily precipitation statistics at the 20 km scale for observed and random cascade modelled current climate and GCM/ RCM modelled and random cascade modelled changed climate.

Appropriate scale statistics (20 km)		Current climate			Changed climate		
		Observed	Modelled	Diff. (%) [A]	GCMs/ RCMs	Modelled	Diff. (%) [B]
Average	mm	2.6	(2.7-2.9)	+4/+12	2.9	(2.7-3.1)	-7/+7
Standard deviation	mm	5.0	(5.1-5.3)	+2/+6	5.9	(5.7-6.1)	-3/+3
Wet day frequency	-	0.63	(0.45-0.46)	-29/-27	0.49	(0.38-0.40)	-22/-18
Spatial correlation length	km	324	(332-349)	+2/+8	389	(382-404)	-2/+4
Temporal correlation cf. lag-1	-	0.26	(0.23-0.25)	-12/-4	0.23	(0.24-0.26)	+4/+13
20-year return value	mm	57.5	(57.3-63.2)	0/+10	68.8	(67.8-77.6)	-1/+13
100-year return value	mm	72.1	(70.6-78.7)	-2/+9	84.8	(83.1-98.4)	-2/+16
5-day 100-year return value	mm	130	(122-134)	-6/+3	142	(138-157)	-3/+11
8-day 100-year return value	mm	158	(152-161)	-4/+2	172	(166-184)	-3/+7
10-day 100-year return value	mm	174	(165-173)	-5/-1	190	(182-206)	-4/+8

[A] difference in % between modelled and observed statistic.
[B] difference in % between modelled and GCM/RCM predicted statistic.

Changed climate

The increase in extreme precipitation with climate change is illustrated is Figure 6.16, where the precipitation fields associated with the 30-year maximum of daily precipitation averaged over the whole field for current and changed climate conditions are given. This increase has also been considered in chapter 4 and is reasonably simulated by the random cascade model. A more complete picture of the behaviour of extreme values gives Figure 6.17, where the extreme value distributions of annual maximum daily precipitation at the appropriate scale for the minimum and maximum of 5 realisations of ordered modelled values for current and changed climate are shown. The increase of extreme precipitation values with climate change is obvious. The

relevant statistics for the modelled changed climate by means of 5 realisations are summarised in Table 6.3 as well, together with the changes from observed as predicted by the GCMs and RCMs. The general trend, of a slight increase of average precipitation, and a considerable increase of variability and extreme values with climate change, is well reproduced by the random cascade model, although the increase of extreme values is somewhat exaggerated.

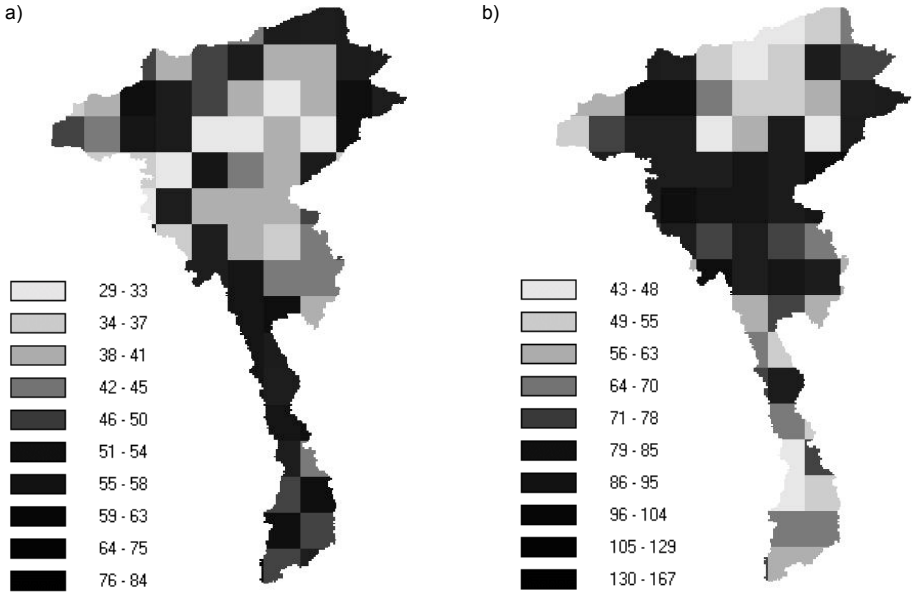

Figure 6.16 Precipitation fields associated with the 30-year maximum of daily precipitation averaged over the whole field in mm day^{-1} obtained from a) the random cascade model for current climate and b) the random cascade model for changed climate.

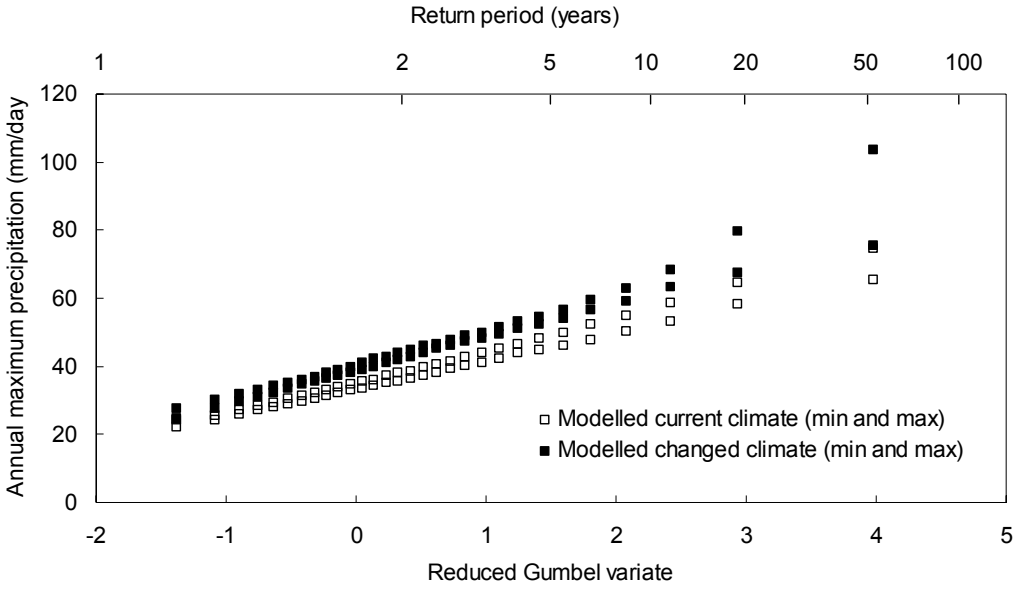

Figure 6.17 Annual maximum precipitation in mm day^{-1} at the 20 km scale as a function of the reduced Gumbel variate and return period in years for the minimum and maximum of 5 realisations of ordered modelled values (averaged over 76 cells) for current and changed climate.

6.4 River basin modelling: HBV model

6.4.1 Introduction

The appropriate model components, namely the appropriate processes, scales and formulations have been derived in chapter 5. The most important processes in the context of climate change impacts on river flooding were found to be precipitation, evapotranspiration, infiltration excess overland flow, saturation excess overland flow, subsurface storm flow, subsurface flow and river flow. The appropriate spatial model scale has been assessed at about 10 km with a corresponding temporal scale of 1 day. Surface flow can be appropriately modelled with diffusion or kinematic wave based methods, whereas subsurface flow at a 10-60 km scale can be simulated using simplified equations such as Green-Ampt. Potential evapotranspiration should be preferably calculated using the Penman-Monteith equation or the Priestley-Taylor formulation if not all the data are available.

This brief summary of the components of an appropriate model already gives some directives about which kind of model can be used for implementation of these appropriate components. Three main categories of hydrological models have been considered in chapter 1, namely empirical, conceptual and physically-based models. Empirical models are based on mathematical equations which do not take into account the underlying physical processes and therefore are not useful for implementation of the appropriate model components. Physically-based models like SHE (Abbot *et al*., 1986) and IHDM (Beven *et al*., 1987), on the other hand, incorporate physical laws based on the conservation of mass, momentum and energy. The governing equations include a lot of parameters and must be solved numerically. The high amount of parameters may result in different parameter combinations giving equally good output performances, which is usually labelled as overparameterisation. Examples are given by Beven (1993) and Uhlenbrook *et al*. (1999), who got very good model performances for different parameter sets. The main solution is to use more data, either through direct measurements of parameters in the field or through measurement of intern state variables like soil moisture contents. Besides this overparameterisation effect, physically-based models generally incorporate too many processes and too complex formulations at a too detailed scale in the context of climate change and river flooding as revealed by the appropriate components found. Therefore, the so-called conceptual models seem to be an attractive alternative. These models are usually able to capture the dominating hydrological processes at the appropriate scale with accompanying formulations. The conceptual models can therefore be considered as a nice compromise between the need for simplicity on the one hand and the need for a firm physical basis on the other hand. A disadvantage may be that it is generally impossible to derive the model parameters directly from field measurements and therefore calibration techniques must be used (Refsgaard, 1996). Well-known conceptual models are the Stanford watershed model (Crawford and Linsley, 1966), the HBV model (Bergström and Forsman, 1973) and the Precipitation Runoff Modelling System – PRMS (Leavesley *et al*., 1983).

The next step is to choose one of the available conceptual models for the implementation of the appropriate model concepts. Therefore, conceptual model intercomparisons may be used like the ones performed by Franchini and Pacciani (1991) for the STANFORD, SACRAMENTO, TANK, APIC, SSARR, XINANJIANG and

ARNO model and Ye *et al*. (1997) for the GSFB, IHACRES and LASCAM model. However, these intercomparisons do not encompass all important conceptual models and therefore the model intercomparison of Passchier (1996) has been used as primary directive for the choice of a model. He selected 5 'event' (single runoff event) models and 10 continuous hydrological models out of 31 models for comparison on the basis of 7 criteria (e.g. state of the art, application areas, level of complexity and detail). His research objective was to select models for rainfall-runoff modelling of the Rhine and Meuse basin with emphasis on 4 specific aims, namely land use impact modelling, climate change impact modelling, real-time flood forecasting and physically based flood frequency analysis. Besides these 4 aims, 10 evaluation criteria (e.g. reliability, scientific basis, scale, availability) have been used for all of the 31 models. Four continuous models (PRMS, SACRAMENTO, HBV and SWMM) and one event model (HEC-1) were evaluated as the best ones. These results and the results for the four specific research aims were used to select a few appropriate models for each of the four research aims. The HEC-1 and HBV model were found to be most appropriate for flood frequency analysis, the HBV and SLURP model for assessments of climate change impacts on peak discharges and the PRMS and SACRAMENTO model for assessments of climate change impacts on discharge regimes. It should be mentioned that HBV only performed poorly on the criterion availability, which means there are restrictions on its use and it is not available online.

On the basis of this intercomparison and the fact that the model could be easily obtained, the HBV model of the Swedish Hydrological and Meteorological Institute has been chosen for implementation of the appropriate model concepts and for subsequently assessing the impact of climate change on river flooding. The dominating processes precipitation, evapotranspiration, infiltration excess overland flow, saturation excess overland flow, subsurface storm flow (the latter three summarised by a fast flow component), subsurface flow and river flow are represented in the model, several sub-basins can be created to obtain the appropriate spatial scale and simulations can be done with different time steps. Moreover, the process formulations have approximately the same level of complexity as revealed being appropriate from the literature analysis. For example surface flow is simulated by storage routing (overland flow) and a modified version of Muskingum's equations (river flow) implying a kinematic or diffusion wave type approach as recommended in section 5.4. An additional advantage of the HBV model is the large number of applications found world-wide. It has been applied in more than 30 countries including many countries in Europe and its applications cover basins in different climatological and geographical regions, ranging in size from less than 1 to more than 40 000 km^2 (Bergström, 1995).

6.4.2 Description of HBV model

The HBV model is a conceptual model of river basin hydrology which simulates river discharge using precipitation, temperature and evapotranspiration as input. The model consists of a precipitation routine representing rainfall, snow accumulation and snow melt, a soil moisture routine determining actual evapotranspiration and overland and subsurface flow, a fast flow routine representing storm flow, a slow flow routine representing subsurface flow, a transformation routine for flow delay and attenuation and a routing routine for river flow. The model version used is the HBV96 model

(version 4.4) described in detail by SMHI (1999). The six model routines and their interactions are illustrated in Figure 6.18 for one sub-basin and are described below.

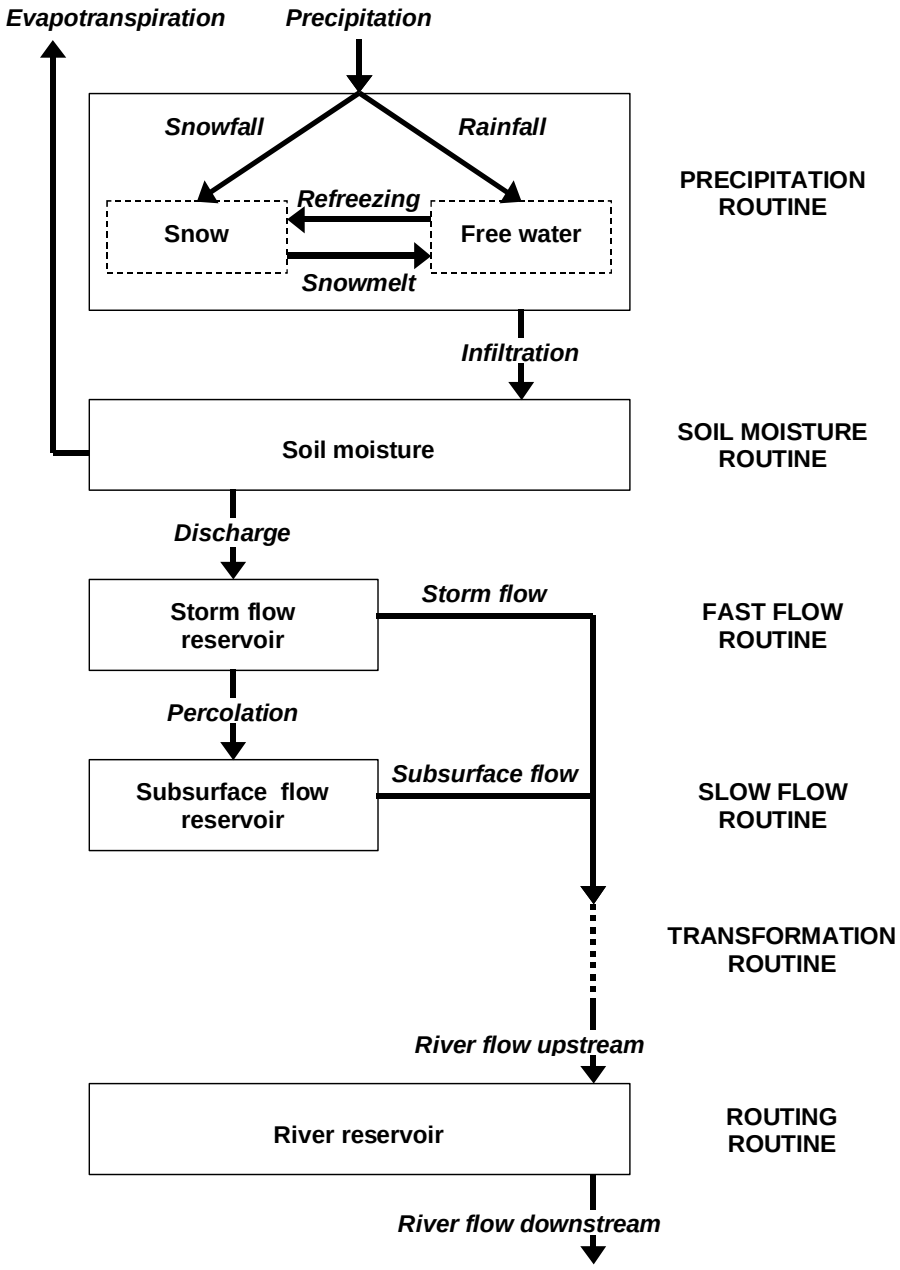

Figure 6.18 Schematisation of HBV model with six routines for one sub-basin.

Precipitation routine

Precipitation occurs as snowfall if the air temperature T_a [θ] is below a defined threshold temperature T_b [θ] and occurs as rainfall if $T_a > T_b$. Snowfall is added to the dry snow reservoir (within the snow pack) and rainfall is added to the free water reservoir, which represents the liquid water content of the snow pack. Interactions between these two components take place through snow melt Q_m [LT^{-1}] and refreezing Q_r [LT^{-1}]

$$Q_m = C_m\left(T_a - T_b\right) \qquad T_a > T_b \tag{6.12}$$

$$Q_r = C_m C_r\left(T_b - T_a\right) \qquad T_a < T_b \tag{6.13}$$

where C_m [$LT^{-1}\theta^{-1}$] is the melting factor and C_r [1] is the refreezing factor. The free water reservoir content is at most equal to a specified fraction (0-1) of the water equivalent of the dry snow content. If this fraction is exceeded through rainfall or snow melt, the water becomes available for the soil moisture routine.

Soil moisture routine

The water from the precipitation routine Q_p [LT^{-1}] is divided into direct discharge, indirect discharge and evapotranspiration. The direct discharge Q_d [LT^{-1}] over land is determined by

$$\begin{aligned} Q_d &= 0 && Q_p + \frac{S_{sm}}{\Delta t} < \frac{FC}{\Delta t} \\ Q_d &= Q_p + \frac{S_{sm} - FC}{\Delta t} && Q_p + \frac{S_{sm}}{\Delta t} > \frac{FC}{\Delta t} \end{aligned} \tag{6.14}$$

where S_{sm} [L] is the soil moisture depth, FC [L] is the capacity of the soil to hold water and Δt [T] is the time step. The indirect discharge Q_{in} [LT^{-1}] through the soil layer is determined by the amount of infiltrated water (Q_p-Q_d) and the soil moisture content S_{sm} through a power relationship with parameter *BHETA*

$$Q_{in} = \left(\frac{S_{sm}}{FC}\right)^{BHETA}\left(Q_p - Q_d\right) \tag{6.15}$$

The amount of water that does not run off is added to the soil moisture. The actual evapotranspiration ET_a [LT^{-1}] is defined as follows

$$\begin{aligned} ET_a &= \frac{S_{sm}}{LP \times FC} ET_p && S_{sm} < LP \times FC \\ ET_a &= ET_p && S_{sm} > LP \times FC \end{aligned} \tag{6.16}$$

where LP [1] is a fraction between 0 and 1 and ET_p is the potential evapotranspiration. The actual evapotranspiration is thus equal to the potential evapotranspiration when the actual soil moisture is above a specified threshold.

Fast flow routine

The direct and indirect discharge (Q_d and Q_{in}) are available for the fast and slow flow routines, where runoff delay is simulated through the use of two reservoirs. One reservoir represents storm flow (overland flow and interflow) and the other one represents subsurface flow (groundwater flow). The direct and indirect discharge percolate into the subsurface reservoir until the subsurface gets saturated and a specific threshold Q_{perc} (LT^{-1}) is exceeded, the redundant water flows into the storm flow

reservoir. The storm flow out of this (fast) reservoir Q_f [LT^{-1}] into the river network is defined as follows

(6.17) $$Q_f = k_f h_f^{(1+\alpha)}$$

where k_f [T^{-1}] is a recession coefficient, h_f [L] is the reservoir water depth and α [1] is a measure of non-linearity. The recession coefficient k_f is determined by using α and two additional parameters k_H and Q_H, representing respectively a recession coefficient and a high flow rate at a corresponding reservoir water depth h_H

(6.18) $$Q_H = k_H h_H$$

The high flow rate Q_H can be directly derived from observed average flow rate Q_{avg} and average annual maximum flow rate Q_{max} (both in mm day^{-1})

(6.19) $$Q_H = \sqrt{Q_{avg}\, Q_{\max}}$$

The combination of equations (6.17), (6.18) and (6.19) with chosen α and k_H finally gives recession coefficient k_f.

Slow flow routine

The subsurface flow out of the slow reservoir Q_s [LT^{-1}] into the river network is given by the outflow of a linear reservoir

(6.20) $$Q_s = k_s h_s$$

where k_s [T^{-1}] is again a recession coefficient and h_s [L] is the reservoir water depth.

Transformation routine

The total discharge $Q_t = Q_f + Q_s$ can be further transformed to get a proper shape of the hydrograph by using a transformation function. This transformation function is a simple filter technique with a triangular distribution of weights over a period *MAXBAS* [T].

Routing routine

The resulting hydrograph $Q_t(t)$ serves as input into the river network. In the river, the water is routed downstream with a modified version of Muskingum's equations (see section 5.4). The river is subdivided into a number of segments and each segment corresponds to a delay given by a parameter L_r [T]. The discharge downstream $Q_{td}(t)$ of a segment depends on the discharge upstream of that segment at the same time step $Q_{tu}(t)$ and the discharge upstream and downstream at the preceding time step $Q_{tu}(t\text{-}\Delta t)$ and $Q_{td}(t\text{-}\Delta t)$ as follows

(6.21) $$Q_{td}(t) = C_1 Q_{tu}(t) + C_1 Q_{td}(t-\Delta t) + C_2 Q_{tu}(t-\Delta t)$$

where

$$C_1 = \frac{D_r}{1+D_r} \qquad C_2 = \frac{1-D_r}{1+D_r}$$

and D_r [1] is a coefficient for wave attenuation. If $D_r = 0$, the shape of the hydrograph will not be changed and only a delay of the hydrograph will occur.

Additional parameters and zones

In addition to the parameters mentioned for the six model routines, several other parameters can be used such as lapse rate parameters for temperature, precipitation and evapotranspiration, forest dependent parameters and snow, lake and glacier parameters. Furthermore, sub-basins can contain different elevation zones with for each elevation zone different land use types (the most important are field and forest). Finally, simplifications such as long-term mean values for evapotranspiration corrected by the actual temperature can be used instead of measured evapotranspiration.

6.4.3 Different model complexities: HBV-1, HBV-15 and HBV-118

Different model complexities will be used to see the effect of model complexity on the model results. In this way, a verification of the appropriate model complexity found in chapter 4 and 5 can be made. The appropriate model requires 225-250 sub-basins as revealed in section 5.3. The realisation of the schematisation for the appropriate model (described below) finally resulted in 118 sub-basins (HBV-118). This number of sub-basins is of the same order of magnitude as the one revealed in 5.3 and assumed to be sufficient for checking the appropriateness requirements of chapter 5. The HBV-118 model is compared with a model consisting of only 1 sub-basin (HBV-1) and a model with 15 sub-basins (HBV-15) following a commonly used division into the main sub-basins (RIZA, 2000). The three different schematisations are given in Figure 6.19. The realisation of the schematisation for HBV-118 is described below.

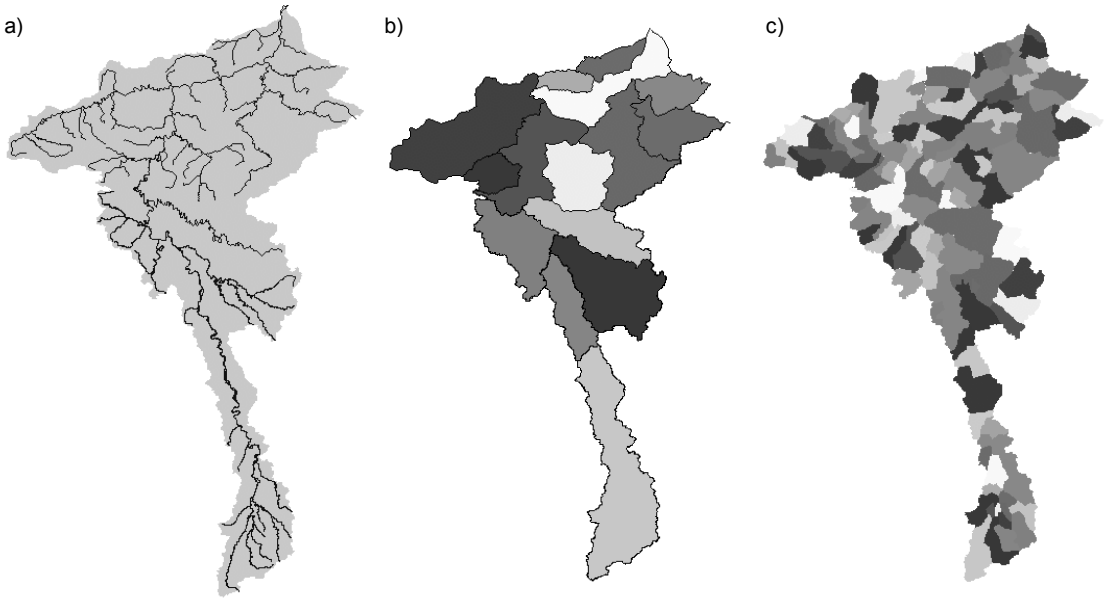

Figure 6.19 Schematisations of the Meuse basin in a) HBV-1, b) HBV-15 and c) HBV-118.

The Meuse 1000m DEM described in 5.3.2 has been used to derive the 118 sub-basins employing the following procedure:

1. Merging of the river network as depicted in Figure 6.19a and the Meuse 1000m DEM to obtain a DEM without unnatural pits due to the coarse resolution used
2. Derivation of the flow direction for each DEM cell. The flow is assumed to be directed towards the lowest elevated neighbouring cell.
3. Fixing of the outflow point for each of the 118 sub-basins assuring approximately equal sub-basin surface areas. The points should lie as much as possible at the confluence of two rivers or streams. The automatic generation of sub-basins causes an uncheckable number of sub-basins and can not be used.
4. Use of the results of point 2. and 3. to generate 118 sub-basins.
5. Adaptation of the sub-basin boundaries by hand to agree with the sub-basin boundaries of HBV-15 (as far as necessary).

6.4.4 Parameter estimation and model experiments

The HBV model has been frequently used in many countries for river basins of various sizes as mentioned in 6.4.1. In these studies, much experience in parameter estimation has been gained and this can be used here to derive the most important parameters and to identify reasonable ranges of parameter values. The studies used are summarised in Table 6.4, where some important features of each study are given. The parameter estimation consists of three steps:

1. determination of key parameters for calibration
2. sensitivity analysis with key parameters to obtain optimal parameter set for HBV-1 and some sub-basins of HBV-15
3. 'regionalisation' of these parameters to derive parameters for each sub-basin in HBV-15 and HBV-118.

The three parameter estimation steps are described below. This sub-section ends with a description of the model experiments performed with HBV-1, HBV-15 and HBV-118.

Table 6.4 HBV modelling studies. Surface area indicates area of the sub-basins in the case of distributed HBV versions (no. sub-basins > 1).

Reference	Application area (no. basins)	No sub basins	Surface area km^2	Calibration period	Validation period	No. of simulations
Bergström, 1990	Sweden (1)	41	(0.3-35) 10^3	1981-1986	1987-1991	
Diermanse, 2001	Mosel, Germany(1)	1 [A]	27030	flood events		~10^2-SA [B]
Harlin and Kung, 1992	Sweden (2)	1	1370-4483	18-20 years		~10^3-MC[C]
Krysanova *et al*., 1999	Elbe, Germany (1)	1-44	(1-81) 10^3	1981-1983	1984-1989	
Lindström *et al*., 1997	Sweden (7-10)	1	174-5975	10 years	10 years	
Seibert, 1999	Sweden (11)	1	7-950	1981-1990		~10^5-MC
Uhlenbrook *et al*., 1999	Brugga, Ger. (1)	1	40	1975-1984		~10^5-MC
Velner, 2000	Ourthe, Belgium(1)	1	1597	1986-1996	1968-1986	~10^2-SA

[A] one parameter (*FC*) was 'fully distributed' into 27 10^3 different values (1 km^2 scale), rainfall gauge density and rainfall averaging effect was assessed.

[B] SA = sensitivity or similar analysis.

[C] MC = Monte Carlo analysis.

Key parameters

The most important and uncertain parameters occur in the soil moisture and the fast flow routine. The precipitation routine mainly contains snow parameters and therefore, because the Meuse is a rainfed river, default values can be used. This has also been concluded by Velner (2000), who calibrated a HBV model for a tributary of the Meuse river (the Ourthe, see Table 6.4). The slow flow routine will only contribute a small amount to flood volumes and values from e.g. Velner (2000) can be used. Parameter values (*MAXBAS* and L_r) for the transformation and routing routines can be easily derived from (hydrometric) data, if wave attenuation is assumed to be negligible (see chapter 5, parameter $D_r = 0$). The main parameters are *FC*, *LP* and *BHETA* in the soil moisture routine and α, k_H and Q_H in the fast flow routine. Values and ranges of these parameters used in the studies from Table 6.4 and two additional studies are given in Table 6.5. For convenience, the most important parameters from the slow flow routine (Q_{perc} and k_s) are given in Table 6.5 as well.

Table 6.5 Parameter values and ranges from the studies in Table 6.4, Killingtveit and Sælthun (1995), SMHI (1999) and HBV-1, HBV-15 and HBV-118.

Reference	*FC*	*LP*	*BHETA*	α [D]	k_H [D]	Q_H [D],[E]	Q_{perc}	k_s
	mm	-	-	-	day^{-1}	mm day^{-1}	mm day^{-1}	day^{-1}
Bergström, 1990	100-300	0.50-1.0	1.0-4.0					
Diermanse, 2001	0-580	0.80	3.0				0.6	0.01
Harlin and Kung, 1992	50-274	0.73-1.0	1.0-5.9				0.6-2.1	0.0008-0.05
Killingtveit and S., 1995	75-300	0.70-1.0	1.0-4.0				0.5-1.0	0.0005-0.002
Krysanova *et al*., 1999	220-391	0.70	2.0				1.0	0.005
Seibert, 1999	50-500	0.30-1.0	1.0-6.0				0.0-3.0	0.001-0.15
SMHI, 1999 [F]	200	0.9	2.0	1.0	0.17	3.0		
Uhlenbrook *et al*., 1999	100-550	0.30-1.0	1.0-5.0				0.0-4.0	0.00005-0.1
Velner, 2000	180	0.66	1.8	1.1	0.10	3.4	0.4	0.023
HBV-1 (SA)	200-500	0.2-0.8	1.0-3.0	0.1-1.1	0.06-0.11			
HBV-15 (SA)	100-400	0.2-0.8	1.0-3.0	0.8-1.1	0.08-0.15			
HBV-1 (optimal values)	340	0.34	1.0	0.7	0.074	2.22	0.4	0.02
HBV-15 Lesse	253	0.65	1.5	1.1	0.095	3.02	0.4	0.02
HBV-15 Ourthe	180	0.71	1.5	1.1	0.12	3.27	0.4	0.02
HBV-15 Amblève	202	0.68	1.9	1.1	0.11	4.15	0.4	0.02
HBV-15 Vesdre	350	0.68	1.3	1.1	0.14	3.79	0.4	0.02
(optimal values)								
HBV-15 (regionalisation)	180-384	0.28-0.71	1.0-2.3	0.2-1.1	0.01-0.14	1.69-4.30	0.4	0.02
HBV-118 (regionalisation)	185-660	0.28-0.71	1.2-2.1	0.1-1.9	0.07-0.17	1.69-4.30	0.4-0.8	0.02

[D] In the fast flow routine of HBV96 α, k_H and Q_H are used, while in older versions of HBV one or more recession coefficients k_i were directly used (without α). Therefore, comparisons between the fast flow routine parameters in both versions can not be made.

[E] Q_H can be directly determined from measured discharges [equation (6.19)] and has not been calibrated.

[F] Default values for HBV96.

Sensitivity analyses

A sensitivity analysis is performed to assess the influence of individual (univariate) or multiple (multivariate) parameters on the output of the model (see 2.2.3). This can be used to determine the parameter set that generates optimal model results. Univariate sensitivity analysis involves varying the value of one parameter while the other parameters remain constant (at a default value). Multivariate sensitivity analysis should be used if a strong interdependence between key parameters exists. This involves varying two (bivariate) or more parameters keeping the other parameters at their default level. Obviously, it depends on the interrelations between the five key parameters *FC*, *LP*, *BHETA*, α and k_H (Q_H is derived from measured data and is not calibrated), which kind of sensitivity analysis should be used.

The HBV model equations from 6.4.2 can give information about possible interdependencies between the key parameters. From equations (6.14), (6.15) and (6.16) of the soil moisture routine and (6.17), (6.18) and (6.19) of the fast flow routine, it is clear that respectively parameters *FC*, *LP* and *BHETA* and α and k_H are interdependent. Therefore, multiple sensitivity analyses for the parameters in the soil moisture and fast flow routine should be performed. Possible interdependencies between parameters of these routines should be checked. Table 6.5 has been used to determine the parameter ranges for the multiple sensitivity analyses (SA) for HBV-1. Additional univariate sensitivity analyses were done for four sub-basins of HBV-15 (Lesse, Ourthe, Amblève and Vesdre) with overall parameter ranges and values given in Table 6.5 as well.

The optimality of the model output (discharge) is assessed in different ways, namely by applying the Nash-Sutcliffe efficiency coefficient R^2 (Nash and Sutcliffe, 1970), the relative volume error *RVE* and the relative extreme value error *REVE*

$$R^2 = 1 - \frac{\sum_{i=1}^{N}\left[Q_m(i) - Q_o(i)\right]^2}{\sum_{i=1}^{N}\left[Q_o(i) - \overline{Q_o}\right]^2} \tag{6.22}$$

$$RVE = 100 \cdot \frac{\sum_{i=1}^{N}\left[Q_m(i) - Q_o(i)\right]}{\sum_{i=1}^{N} Q_o(i)} \tag{6.23}$$

$$REVE = 100 \cdot \frac{RV_m(T) - RV_o(T)}{RV_o(T)} \tag{6.24}$$

where i is the time step, N is the total number of time steps, Q is the discharge, subscripts o and m means observed and modelled and $RV(T)$ is the T-year return value. Furthermore, visual inspections of the observed and simulated hydrographs should always accompany model experiments. Since the soil moisture routine parameters particularly influence the discharge volume, the criteria for the multiple sensitivity analysis with *FC*, *LP* and *BHETA* are *RVE* and R^2. On the other hand, the fast flow routine parameters particularly affect the shape of the hydrograph and extreme discharges and therefore R^2 and *REVE* are used as criteria in the bivariate sensitivity analysis with α and k_H.

Regionalisation

The HBV-15 and HBV-118 models can not be calibrated in the same way as the HBV-1 model, because additional observed discharges are available for four sub-basins and thus sensitivity analyses can only be done for these four sub-basins as described above. It is therefore necessary to determine the key parameters of the other sub-basins in an alternative way. The concept of 'regionalisation' is used for this purpose. This involves the use of relationships between key parameters and river basin characteristics (e.g. land use, soil type) to assess the parameter values for the remaining sub-basins. These relationships can be established by employing the calibrated parameters from the sensitivity analyses and the corresponding basin characteristics or using relationships from literature. Separate relationships for each key variable or for example Hydrological Response Units (HRUs) representing hydrologically similar areas (e.g. Kite and Kouwen, 1992) can be used for this purpose. The separate relationships for the five key parameters in HBV-15 are described in a general way below and applied in sub-section 6.5.1. The regionalisation for seven key variables (additionally Q_H and Q_{perc}) in HBV-118 is described by Van der Wal (2001). He used one indicator based on the slope, the soil texture and the parent material (see chapter 5) of the sub-basin representing the reaction behaviour of the sub-basin to distribute the seven key parameters among the 118 sub-basins. The resulting parameter ranges are given in Table 6.5.

The soil moisture routine parameters *FC*, *LP* and *BHETA* are relatively scale independent (Bergström and Graham, 1998) and can be used at all covered scales (~100-20000 km^2). This is in the same range as the scales in Bergström (1990). Parameter *FC* is the maximum capacity of the soil to hold water and is related to soil properties as the soil moisture content at field capacity and wilting point and the soil depth. Here, the *FC* from HBV-1 is distributed taking into account the calibrated *FC* values from the four sub-basins in HBV-15 using the volumetric soil moisture content at wilting point θ_w and the soil porosity ϕ

$$FC \sim \phi - \theta_w \tag{6.25}$$

Parameter *LP* is the fraction of *FC* above which potential evapotranspiration occurs [equation (6.16)]. It is assumed to be dependent on the volumetric soil moisture content at wilting point θ_w and field capacity θ_f analogous to Baier and Roberston (1966) and on the soil porosity ϕ to account for the dependency of *LP* on *FC*

$$LP \sim \frac{\phi - \theta_w}{\theta_f - \theta_w} \tag{6.26}$$

Parameter *BHETA* describes how the runoff coefficient increases as the maximum soil moisture content *FC* is approached. This parameter can be regarded more as an index of heterogeneity than a measure of soil properties (Bergström and Graham, 1998). This is because for low values runoff is gradually generated indicating heterogeneous conditions whereas for high values runoff is simultaneously generated implying homogeneous conditions. In general, this means for large sub-basins with much heterogeneity smaller values for *BHETA* than for small sub-basins with relatively little variability. Seibert (1999), on the other hand, found an increase of *BHETA* values with sub-basin area *A*, although his relation was weak. The former explanation (increasing *BHETA* values with decreasing area) will serve as a basis for a *BHETA*-area

relationship, because it is physically more plausible and has been formulated by the developer of the HBV model

$$BHETA \sim \frac{1}{A} \quad (6.27)$$

Parameter α is a measure of the non-linearity of the fast flow process. Small sub-basins with steep hills and low permeable soils will generally result in more non-linearity in the fast flow mechanisms than large sub-basins with flat terrains and high permeable soils. The calibrated α values were found to be most dependent on slope S_0 rather than on surface area or soil type

$$\alpha \sim S_0 \quad (6.28)$$

Parameter k_H is a recession coefficient at high flow rate Q_H and can be approximated by estimating the recession coefficient from an observed hydrograph at flow rate Q_H (SMHI, 1999). This parameter is influenced by similar factors as α and calibrated k_H values were found to be most dependent on slope S_0 as well

$$k_H \sim S_0 \quad (6.29)$$

Model experiments

The impact of climate change on river flooding is assessed with HBV-1, HBV-15 and HBV-118 in four steps. These four steps are the calibration described above, the validation, the simulation under current climate conditions with the random cascade model and the simulation under changed climate conditions with the random cascade model. The climatic input for the four steps is summarised in Table 6.6 (see also section 6.2 and 6.3). Information about the model experiments with HBV-1, HBV-15 and HBV-118 is given in Table 6.7.

Table 6.6 Climatic input for model experiments.

	Precipitation	Temperature	Evapotranspiration
Calibration	Stations (39 stations) 1970-1984	Stations (12) 1970-1984	Stations (8) 1970-1984
Validation	Stations (39) 1985-1996	Stations (12) 1985-1996	Stations (8) 1985-1996
Current climate	Random Cascade Model (76) 30 years 5 realisations [A]	Stations (12) 1967-1996	Stations (8) 1967-1996
Changed climate	Random Cascade Model (76) 30 years 10 realisations [B]	Stations+change (12) 1967-1996	Stations+change (8) 1967-1996

[A] 5 realisations using the same parameters from Table 6.1 and Table 6.2 for HBV-1 and HBV-15, 1 realisation for HBV-118.

[B] 5 realisations using the same parameters from Table 6.1 and Table 6.2 and 5 realisations using parameters derived from each model separately (3 GCMs and 2 RCMs) for HBV-1 and HBV-15, 1 realisation for HBV-118.

Table 6.7 Model experiments with HBV-1, HBV-15 and HBV-118.

	HBV-1	HBV-15	HBV-118
Calibration	Discharge (1)	Discharge (5)	Discharge (5)
		Regionalisation	Regionalisation
	1970-1984	1970-1984	1970-1984
Validation	Discharge (1)	Discharge (5)	Discharge (5)
	1985-1996	1985-1996	1985-1996
Current climate	Discharge (1)	Discharge (5/15)	Discharge (5/118)
	30 years	30 years	30 years
	5 realisations	5 realisations	1 realisation
Changed climate	Discharge (1)	Discharge (5/15)	Discharge (5/118)
	30 years	30 years	30 years
	5 realisations	10 realisations	1 realisation

The temperature and evapotranspiration data are averaged to obtain one temperature and one evapotranspiration series (see section 6.2). The point precipitation series from stations are interpolated using Thiessen polygons. These areally averaged precipitation series are combined with the HBV-1, HBV-15 and HBV-118 schematisations from Figure 6.19 to obtain areally averaged precipitation series for respectively 1, 15 and 118 sub-basins. The areally averaged random cascade precipitation series are combined with the HBV-1, HBV-15 and HBV-118 schematisations in the same way.

6.5 Climate change impact on river flooding in the Meuse basin

6.5.1 Calibration

The results of the multiple sensitivity analyses with HBV-1 for parameters *FC*, *LP* and *BHETA* of the soil moisture routine are given in Figure 6.20 and for parameters α and k_H of the fast flow routine are given in Figure 6.21. The combination of the pictures at the left-hand and right-hand side in Figure 6.20 gives the optimal values for the soil moisture routine parameters by requiring that *RVE* should be less than 1 % and R^2 should be as high as possible. The optimum values are poorly defined and are given in Table 6.5. A similar approach has been conducted for the fast flow routine parameters by combining R^2 as a function of α (and associated optimal k_H from Figure 6.21a) and *REVE* as a function of $\alpha(k_H)$ in Figure 6.21b. Here, the requirements are that *REVE* should be less than 10 % and R^2 should be as high as possible. The resulting α and k_H values are given in Table 6.5 as well. During these sensitivity analyses, the values of the other (less important) parameters were kept at pre-determined values based on univariate sensitivity analyses and the studies mentioned in Table 6.4. The calibrated parameter values are generally within the ranges from other studies and seems to be realistic. The value for the parameter *LP* is low, which means that potential evapotranspiration occurs already under relatively dry conditions. Although this could yield an overestimation of the total evapotranspiration, observed and simulated water balances compared favourably.

Similar sensitivities of the three criteria [equations (6.22)-(6.24)] with respect to the different parameters were found for the 4 sub-basins (Lesse, Ourthe, Amblève and Vesdre) and are not shown here. The optimal values of the soil moisture and fast flow routine parameters derived from the univariate sensitivity analyses for these sub-basins are summarised in Table 6.5.

The optimal parameter values for HBV-1 and the 4 sub-basins of HBV-15 together with θ_w, θ_f and ϕ-values based on soil texture (Maidment, 1993), S_0 values based on elevation data and A values have been used to quantify the regionalisation relationships from equations (6.25)-(6.29). Finally, these equations have been used to determine the parameters values for the remaining 11 sub-basins. The ranges of these resulting parameter values are given in Table 6.5 as well.

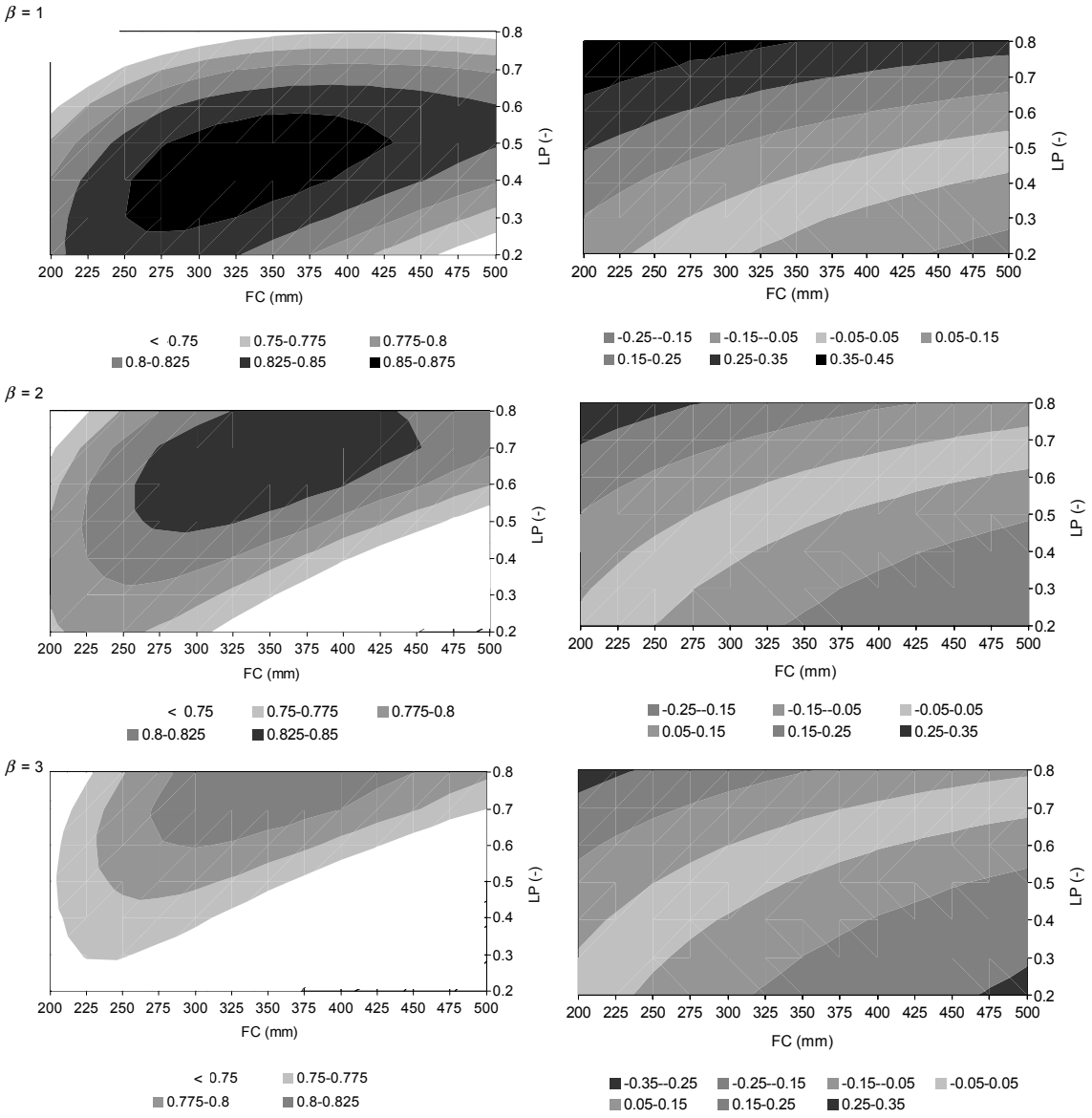

Figure 6.20 Sensitivity analyses with *FC* and *LP* for *BHETA* (β) = 1, 2 and 3 for HBV-1. The left-hand side shows R^2 as a function of *FC*, *LP* and *BHETA* (β) and the right hand side shows *RVE* as a function of *FC*, *LP* and *BHETA* (β).

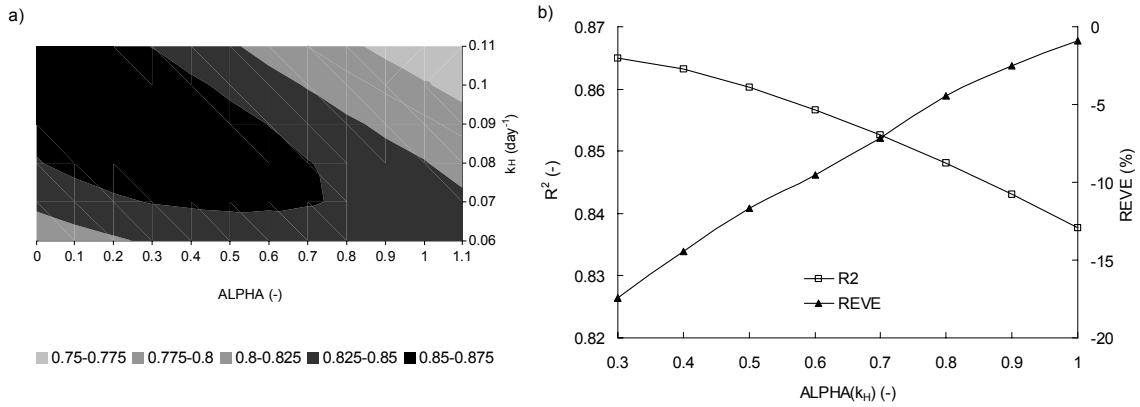

Figure 6.21 Sensitivity analysis with α and k_H for HBV-1 with a) R^2 as a function of α and k_H and b) R^2 as a function of $\alpha(k_H)$ and *REVE* as a function of $\alpha(k_H)$.

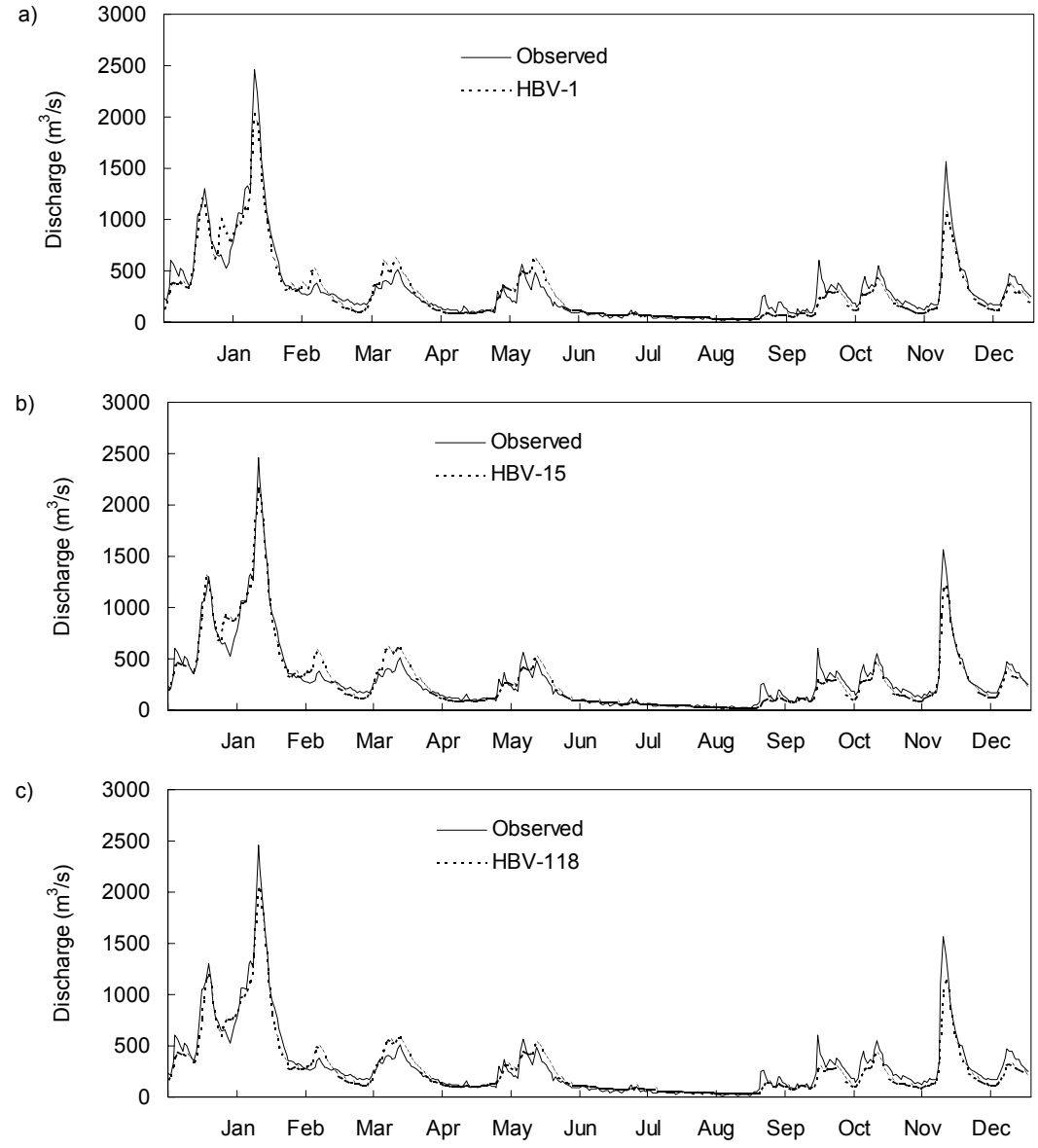

Figure 6.22 Observed and simulated discharge at Borgharen in m^3s^{-1} for 1984 for a) HBV-1, b) HBV-15 and c) HBV-118.

Next, the results obtained with the chosen parameter values for HBV-1, HBV-15 and HBV-118 can be compared. Therefore, Figure 6.22 shows the daily discharge at Borgharen for one arbitrary year with a considerable peak for the observed and HBV-1, HBV-15 and HBV-118 simulated situation. The observed hydrograph is simulated realistically by all three models, although the performance becomes somewhat better with an increasing number of sub-basins. Figure 6.23 and Figure 6.24 give respectively the cumulative frequency distribution of daily discharges and the extreme value distribution of annual extremes for the observed and simulated series. Most striking feature is the good simulation of the extreme value distribution by HBV-15 and HBV-118, but also by HBV-1. The resulting criteria R^2, *RVE* [by means of average] and *REVE* [by means of *RV*(100)] together with the standard deviation of daily discharges are summarised in Table 6.8. This table mainly confirms the findings from the visual inspection; the good simulation of average discharge behaviour illustrated by high R^2 values and the good simulation of extremes (difference is negligible for HBV-15 and HBV-118).

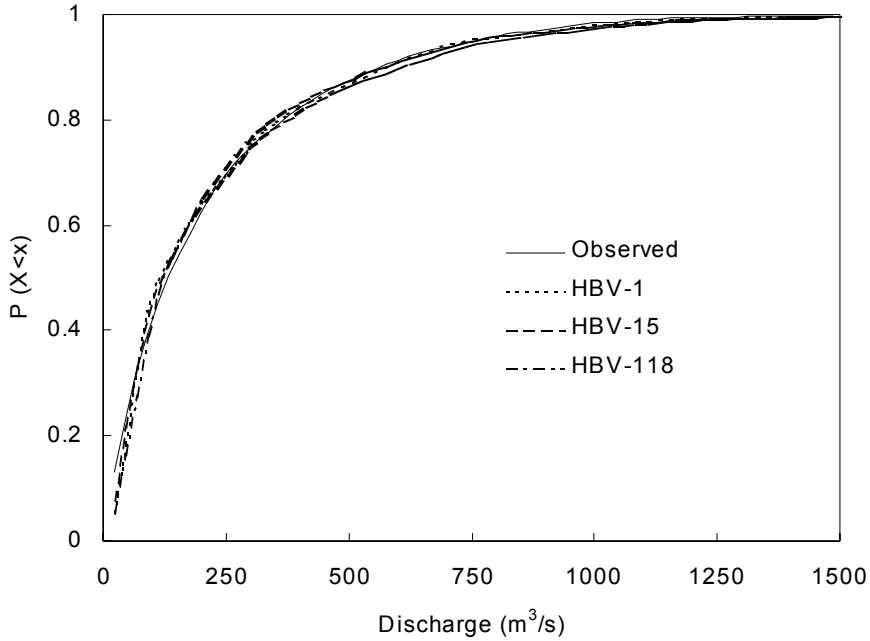

Figure 6.23 Cumulative frequency distribution $P(X<x)$ for daily discharges up to 1500 m^3s^{-1} for observed and HBV-1, HBV-15 and HBV-118 simulated series for 1970-1984.

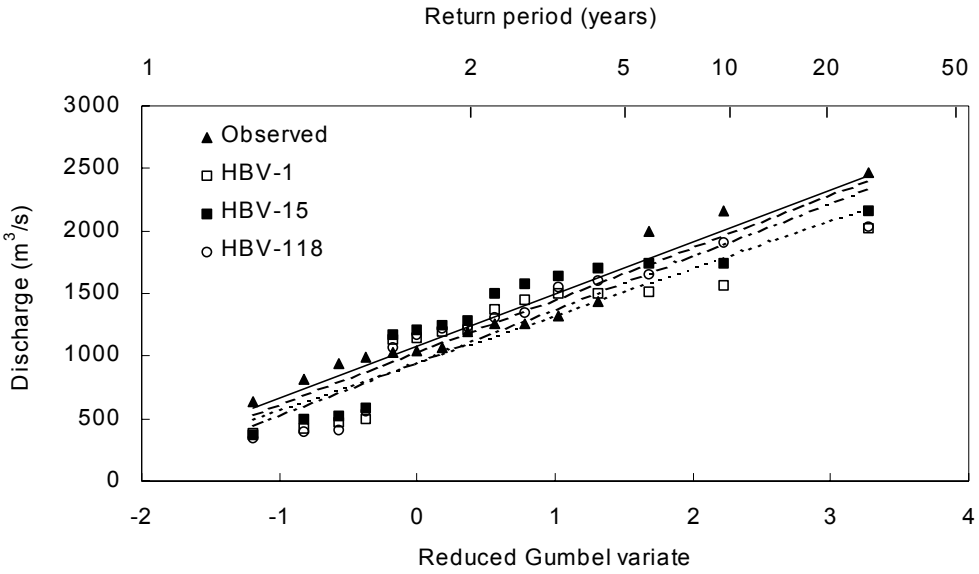

Figure 6.24 Gumbel plot for annual maximum discharges in m^3s^{-1} for the period 1970-1984 as observed and simulated with HBV-1, HBV-15 and HBV-118. Regression lines for observed (solid), HBV-1 simulated (dotted), HBV-15 simulated (dashed) and HBV-118 simulated (dashed-dotted) are shown as well.

Table 6.8 Results from calibration, validation and simulations with rainfall model for current and changed climate.

		R^2	Average		Standard deviation		RV(100)	
		-	Value m^3s^{-1}	Diff. [A] %	Value m^3s^{-1}	Diff. [A] %	Value m^3s^{-1}	Diff. [A] %
Calibration	Observed		222		252		2929	
	HBV-1	0.85	222	0	251	0	2719	-7
	HBV-15	0.87	231	+4	270	+7	2977	+2
	HBV-118	0.88	224	+1	255	+1	2896	-1
Validation	Observed		235		300		3703	
	HBV-1	0.91	238	+1	307	+2	3817	+3
	HBV-15	0.92	244	+4	324	+8	4008	+8
	HBV-118	0.93	239	+2	303	+1	3772	+2
Synthetic	Observed		229		275		3292	
current	HBV-1		(232-266)	+1/+16	(265-296)	-4/+8	(2553-3236)	-22/-2
climate	HBV-15		(237-271)	+3/+18	(275-306)	0/+11	(2621-3226)	-20/-2
	HBV-118		244	+6	264	-4	2958	-10
Synthetic	HBV-1		(204-264)	-12/-1	(253-334)	-5/+13	(2426-3565)	-5/+10
changed	HBV-15		(207-266)	-13/-2	(260-344)	-5/+12	(2591-3661)	-1/+13
climate	HBV-118		258	+6	314	+19	3354	+13
Uncertainty	HBV-15		(208-244)	-12/-10	(270-299)	-2/-2	(2551-3530)	-3/+9

[A] diff. means difference in % with respect to the corresponding observed (calibration, validation, synthetic current climate) or simulated (synthetic changed climate) value.

6.5.2 Validation

In the validation, the parameter values are kept the same as in the calibration, but the simulations are repeated with another, independent precipitation, temperature, evapotranspiration and discharge series (see Table 6.6 and Table 6.7). The results are shown in Figure 6.25, Figure 6.26, Figure 6.27, Figure 6.28 and Table 6.8. Figure 6.25 shows the daily discharge at Borgharen for 16 months with two considerable peaks for the observed and HBV-15 and HBV-118 simulated situation. The observed hydrograph is simulated realistically by the two models, even better than in the calibration. Figure 6.26 shows the daily discharge at Martinrive (Amblève) and Tabreux (Vesdre) for the same 16 months for HBV-15 to illustrate also the good performance for sub-basins. Figure 6.27 and Figure 6.28 give respectively the cumulative frequency distribution of daily discharges and the extreme value distribution of annual extremes for the observed and simulated series. Again the extreme value distribution is well simulated by all models. The resulting criteria R^2, *RVE* and *REVE* and the standard deviation of daily discharges at Borgharen are summarised in Table 6.8. Additionally, Table 6.9 gives R^2, *RVE* and *REVE* for the calibration and validation of HBV-15 and HBV-118 for the four sub-basins. The differences between average discharge behaviour of the sub-basins modelled by HBV-15 and HBV-118 are small. Extreme discharges are generally better simulated by HBV-118 in the calibration, where in the validation HBV-15 is somewhat better.

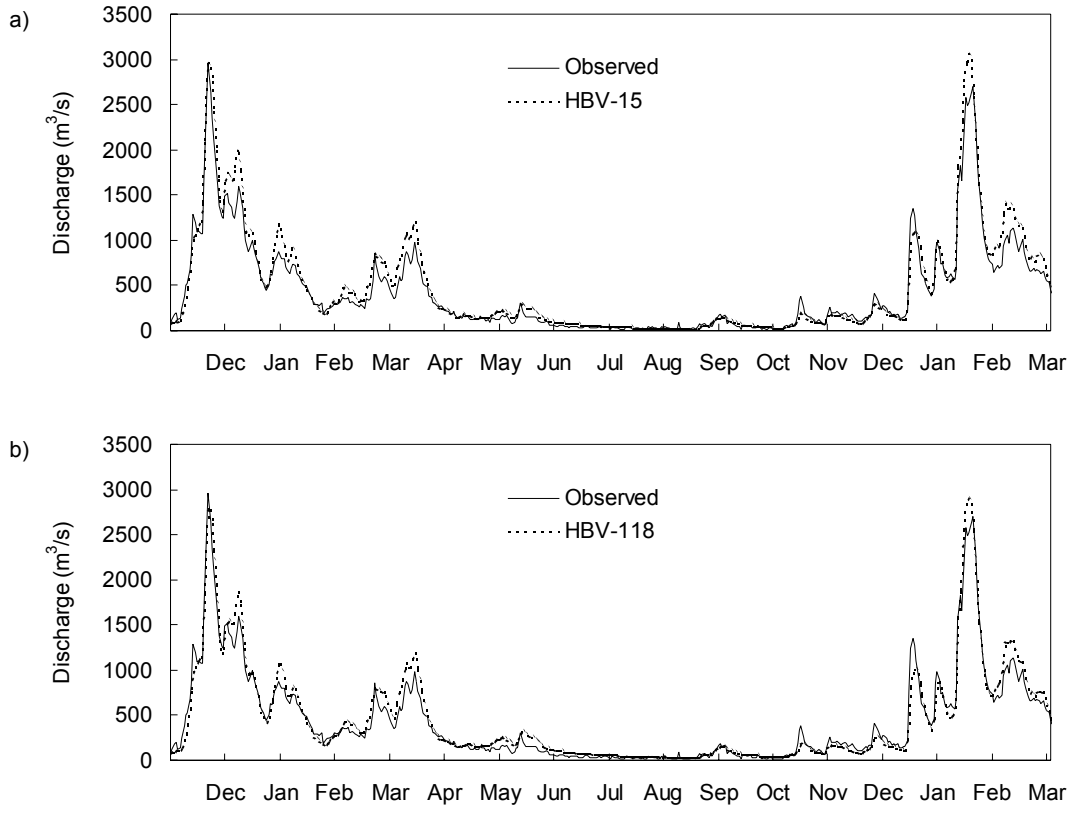

Figure 6.25 Observed and simulated discharge at Borgharen in m^3s^{-1} for December 1993-March 1995 for a) HBV-15 and b) HBV-118.

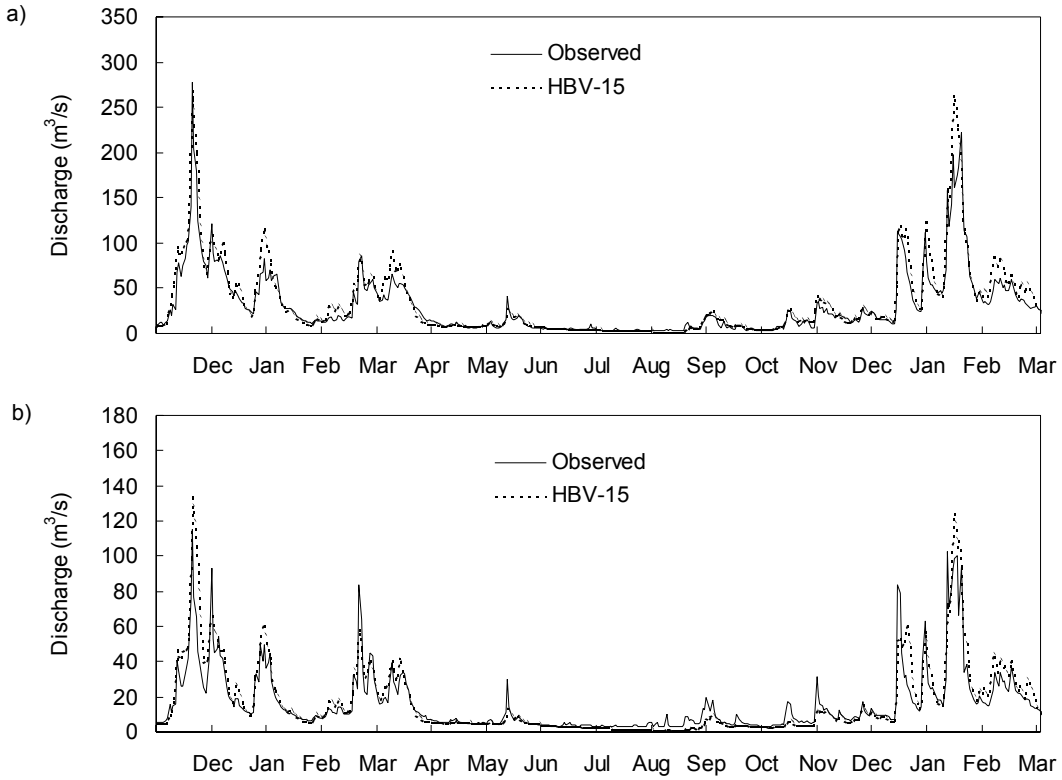

Figure 6.26 Observed and HBV-15 simulated discharge in m^3s^{-1} for December 1993-March 1995 for a) Amblève ($R^2 = 0.87$) and b) Vesdre ($R^2 = 0.76$).

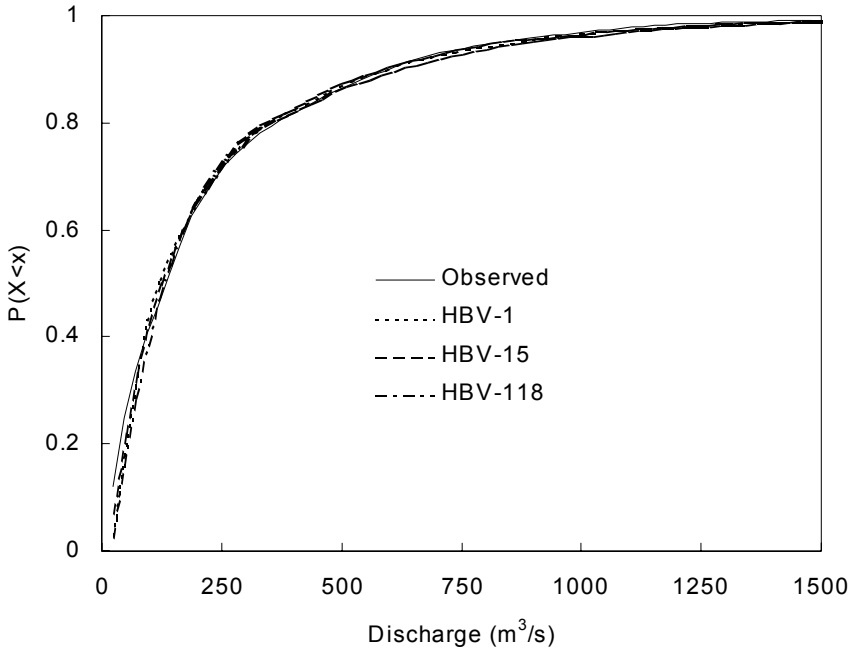

Figure 6.27 Cumulative frequency distribution $P(X<x)$ for daily discharges up to 1500 m^3s^{-1} for observed and HBV-1, HBV-15 and HBV-118 simulated series for 1985-1996.

Table 6.9 Results for tributaries from calibration and validation of HBV-15 and HBV-118.

			R^2	Average		RV(100)	
			-	Value m^3s^{-1}	Diff. [A] %	Value m^3s^{-1}	Diff. [A] %
Calibration	Lesse	Observed		17.3		250	
		HBV-15	0.88	17.3	0	225	-10
		HBV-118	0.88	17.6	+1	254	+2
	Ourthe	Observed		22.1		393	
		HBV-15	0.80	22.3	+1	354	-10
		HBV-118	0.87	22.4	+1	378	-4
	Amblève	Observed		18.7		351	
		HBV-15	0.80	18.8	+1	311	-12
		HBV-118	0.78	19.2	+3	343	-2
	Vesdre	Observed		10.1		244	
		HBV-15	0.80	10.0	0	148	-39
		HBV-118	0.77	10.3	+2	187	-23
Validation	Lesse	Observed		18.1		467	
		HBV-15	0.89	19.3	+7	358	-23
		HBV-118	0.91	19.7	+9	368	-21
	Ourthe	Observed		22.4		486	
		HBV-15	0.86	23.3	+4	472	-3
		HBV-118	0.92	23.3	+4	505	+4
	Amblève	Observed		18.6		439	
		HBV-15	0.87	19.5	+5	430	-2
		HBV-118	0.84	19.9	+7	468	+7
	Vesdre	Observed		10.5		202	
		HBV-15	0.76	10.1	-4	204	+1
		HBV-118	0.76	10.5	0	238	+18

[A] diff. means difference in % with respect to the corresponding observed value.

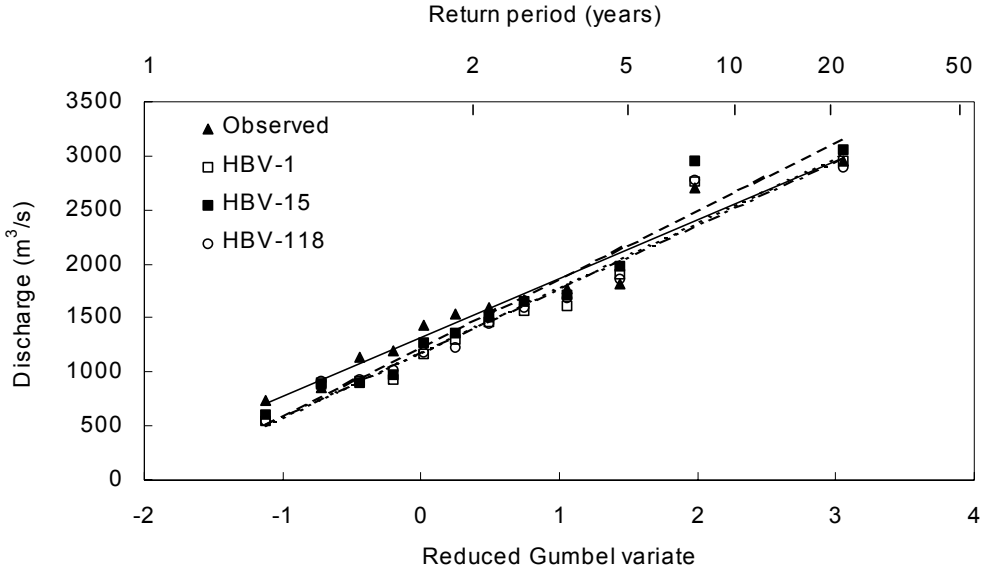

Figure 6.28 Gumbel plot for annual maximum discharges in m^3s^{-1} for the period 1985-1996 as observed and simulated with HBV-1, HBV-15 and HBV-118. Regression lines for observed (solid), HBV-1 simulated (dotted), HBV-15 simulated (dashed) and HBV-118 simulated (dashed-dotted) are shown as well.

6.5.3 Synthetic current climate

The results of the random cascade model for the current climate are used as input in HBV-1, HBV-15 and HBV-118 to simulate daily discharge series for the current climate (see Table 6.7). Figure 6.29 shows the cumulative frequency distribution of daily discharges for the observed series and 5 realisations with HBV-1 and HBV-15 and 1 realisation with HBV-118 for current climate. The only realisation with HBV-118 is the maximum one in terms of HBV-15 extreme discharges. Figure 6.30 gives the extreme value distribution of annual extremes for the observed and simulated series. The 5 realisations are quantified in Table 6.8 by means of the average and standard deviation of daily discharges and the 100-year return value *RV*(100).

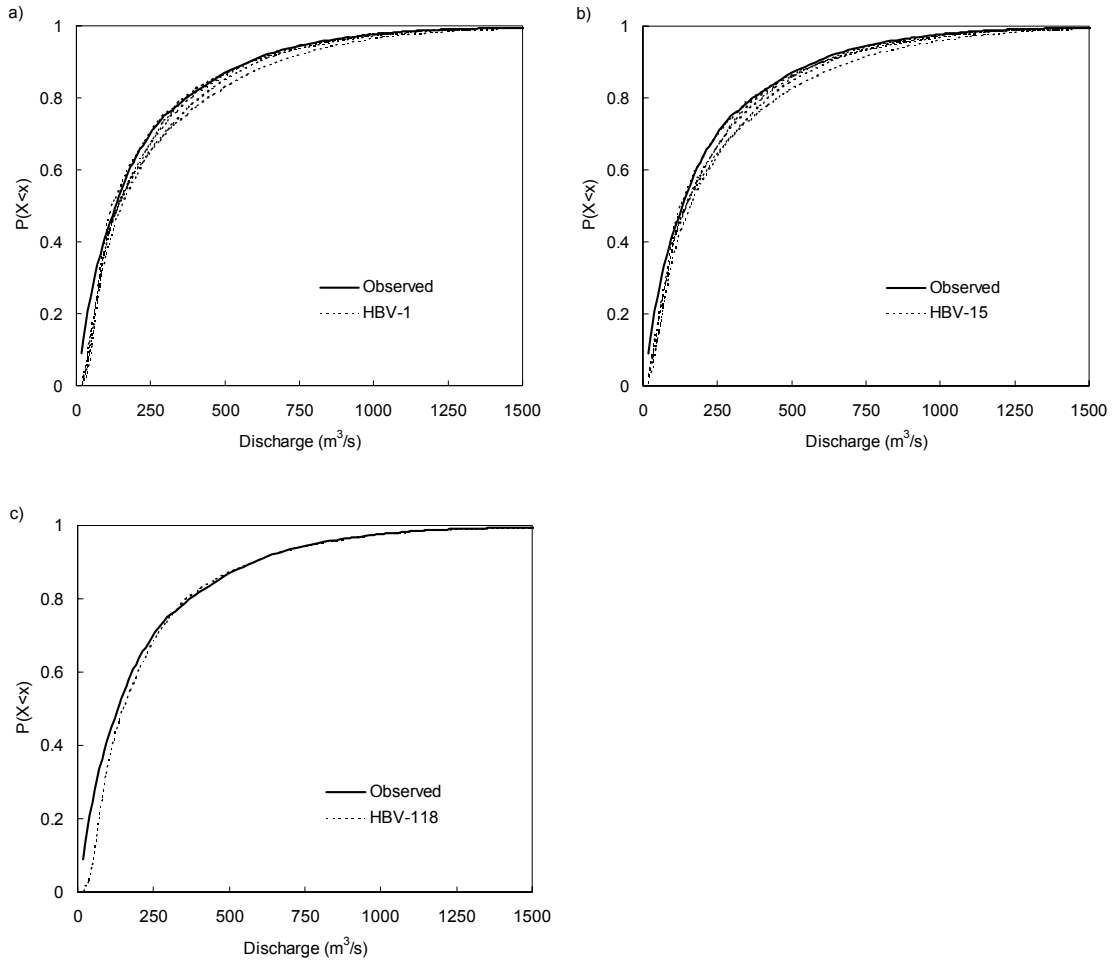

Figure 6.29 Cumulative frequency distribution $P(X<x)$ for daily discharges up to 1500 m^3s^{-1} for 30 years under current climate conditions for a) observed series and 5 precipitation realisations with HBV-1, b) observed series and 5 precipitation realisations with HBV-15 and c) observed series and 1 precipitation realisation with HBV-118.

The general trend from these figures and table is a small overestimation of average discharges and discharge variability and a considerable underestimation of extreme discharges in the case of HBV-1 and HBV-15. HBV-118 slightly underestimates the discharge variability and underestimates extreme discharges with respect to HBV-15. However, a general tendency for HBV-118 is hard to identify, because only one

precipitation realisation has been used for HBV-118. The small overestimation of average discharge behaviour can be explained by the small overestimation of average precipitation behaviour by the random cascade model (see Table 6.3, on average +8 % for mean precipitation and + 4 % for the standard deviation of precipitation). However, the underestimation of extreme discharges by HBV-1 and HBV-15 can not be explained by the statistics of the precipitation input. The random cascade model rather overestimates than underestimates extreme precipitation.

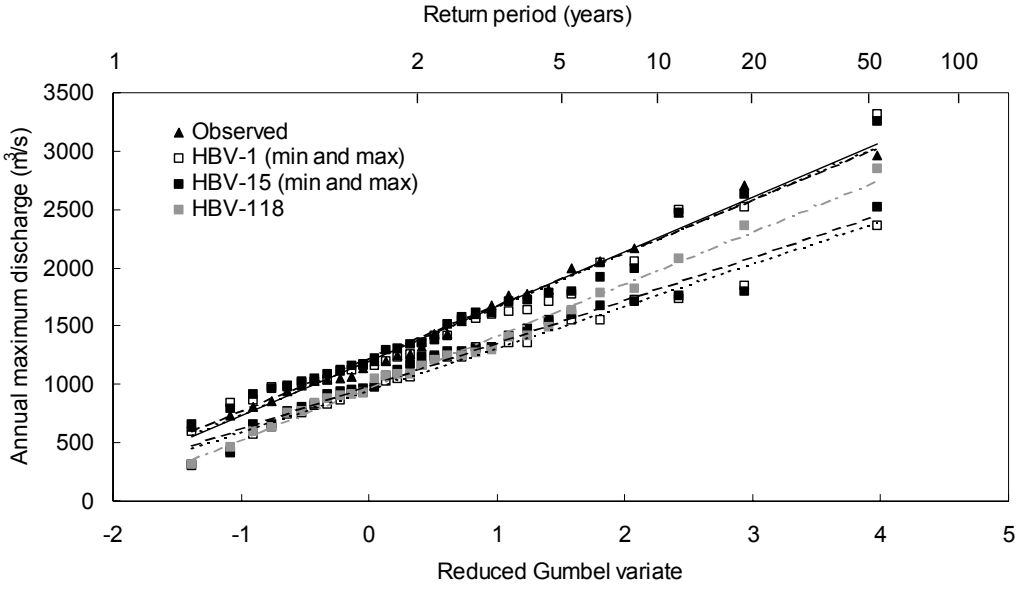

Figure 6.30 Gumbel plot for annual maximum discharges in m^3s^{-1} for a 30 year period as observed (1970-1999) and simulated with 5 precipitation realisations for HBV-1 and HBV-15 and 1 precipitation realisation for HBV-118 under current climate conditions. Only the minimum and maximum of the 5 HBV-1 and HBV-15 realisations are shown. Regression lines for observed (solid), HBV-1 simulated (dotted), HBV-15 simulated (dashed) and HBV-118 simulated (grey dashed-dotted) are given as well.

The main cause of this underestimation can be found in the transformation of observed precipitation at the point scale and simulated precipitation at the 20 km scale to areally averaged precipitation at the basin (HBV-1, ~150 km) or sub-basin scale (HBV-15, ~40 km and HBV-118, ~13 km). This is illustrated in Table 6.10 where the important statistics from Table 6.3 at the HBV-15 and HBV-118 sub-basin scales for the observed and simulated situation (1 realisation with *REVE* ≈ -20 %) are summarised. In particular, the 5-day, 8-day and 10-day 100-year precipitation return values are underestimated by the rainfall model at the HBV-15 (by about 20 %) and HBV-118 (by about 15 %) sub-basin scale, but also 1-day extreme values and variability are underestimated compared to the 20 km scale (where the rainfall model mainly overestimates these statistics). This underestimation of generated extreme precipitation at the sub-basin scale is in fact an overestimation of observed extreme precipitation at the sub-basin scale. Namely, the observed 5-day, 8-day and 10-day 100-year precipitation return values in Table 6.10 are approximately the corresponding observed point values, from which the multi-day extreme statistics in Table 6.3 have been derived.

The overestimation of observed precipitation variability and extreme behaviour is explained by the fact that for a lot of sub-basins, in particular for HBV-118, only one or two stations are used as precipitation input into the model. This results in observed input at the point scale compared to simulated input at the (correct) 20 km scale. Observed precipitation is considered as areally averaged precipitation, but is actually point precipitation. Consequently, observed precipitation shows too much variability and extreme behaviour, which will have implications for the parameter estimation during calibration. Parameters are estimated under too variable and extreme conditions, which may have consequences for simulations under changed conditions (e.g. land use and climate change). Unfortunately, insufficient precipitation stations are available to assess the areally averaged sub-basin scale precipitation in a right way and therefore this overestimation has occurred. The overestimation of precipitation variability and extreme behaviour seems to be common practice, because in most rainfall-runoff modelling studies station precipitation is used as input in stead of areally averaged precipitation at the sub-basin scale.

Table 6.10 Daily precipitation statistics at the sub-basin scale for observed and random cascade modelled current climate.

Sub-basin scale statistics		HBV-15			HBV-118		
		Observed	Modelled	Diff. (%) [A]	Observed	Modelled	Diff. (%) [A]
Average	mm	2.6	2.7	+4	2.6	2.7	+4
Standard deviation	mm	4.8	4.6	-4	5.0	4.9	-2
Wet day frequency	-	0.57	0.59	+3	0.53	0.51	-4
Temporal correlation cf. lag-1	-	0.31	0.29	-4	0.28	0.27	-4
20-year return value	mm	53.6	51.7	-4	57.6	55.4	-4
100-year return value	mm	66.3	63.7	-4	71.5	68.4	-4
5-day 100-year return value	mm	136	109	-20	139	117	-16
8-day 100-year return value	mm	173	139	-19	174	147	-15
10-day 100-year return value	mm	193	158	-18	194	164	-15

[A] difference in % between modelled and observed statistic.

The difference between HBV-15 and HBV-118 in Table 6.10 (-20 % and –15 %) can be explained by the fact that modelled precipitation is less averaged when transformed to the HBV-118 scale than when transformed to the HBV-15 scale. However, the difference in discharge 100-year return values for the HBV-15 and HBV-118 model using the same (maximum) precipitation realisation (respectively -2 % and –10 % in Table 6.8) can not be explained by these differences in precipitation at the sub-basin scale. This difference may be caused by differences in regionalisation techniques and related differences in parameter values (e.g. *FC* values in Table 6.5 cover a much broader range in the case of HBV-118). In this way, it gives some information about uncertainties due to parameter estimation, but it does not give information about uncertainties due to differences in processes incorporated or process formulations. Nevertheless, the calibration and validation results from HBV-15 and HBV-118 were comparable. Figure 6.30 shows a large difference (about 20 %) between the minimum and maximum of the modelled realisations, which illustrates the large impact of the stochasticity of the precipitation process.

6.5.4 Synthetic changed climate

The climate change situation will be considered by comparing the results obtained with input from the rainfall model for current and changed climate conditions. Figure 6.31 shows the cumulative frequency distribution of daily discharges for 5 realisations with HBV-1 and HBV-15 and 1 realisation with HBV-118 for the current and changed climate. Figure 6.32 gives the 20-year and 100-year return values for the current and changed climate. Quantitative figures are shown in Table 6.8.

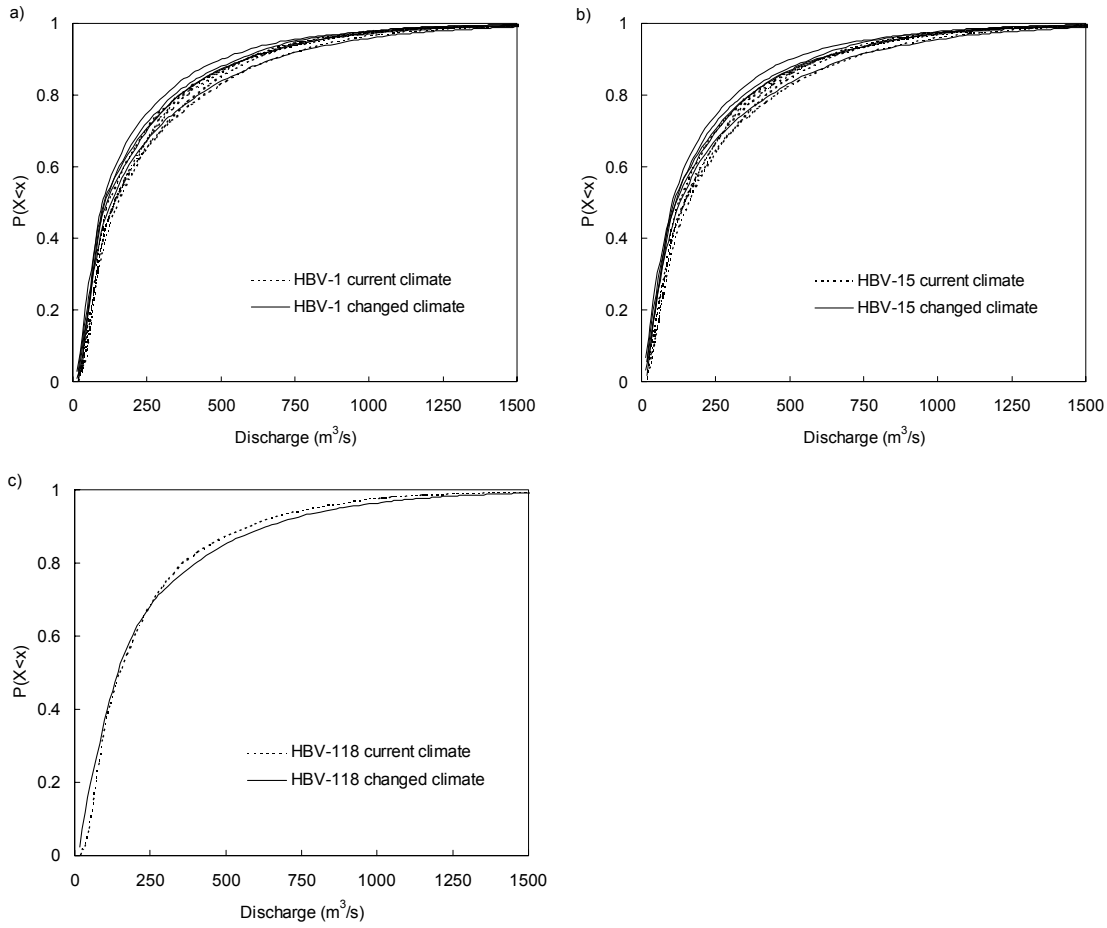

Figure 6.31 Cumulative frequency distribution $P(X<x)$ for daily discharges up to 1500 m^3s^{-1} under current and changed climate conditions for 5 realisations of 30 years for a) HBV-1 and b) HBV-15 and 1 realisation of 30 years for c) HBV-118.

The general trend is a small decrease of the average discharge and a small increase of the discharge variability and extreme discharges with climate change. The decrease of the average discharge has to do with the slight increase of modelled average precipitation with climate change (about 5 %, see Table 6.3) combined with the considerable increase of (potential) evapotranspiration (on average about 15 %, see Figure 6.2). The increase in discharge variability and extreme discharges is a result of the considerable increase of precipitation variability and extreme precipitation (10-20 %), but is less than would be expected on the basis of the changes in precipitation behaviour. There are even precipitation realisations which have resulted in a small decrease of the extreme value distribution for annual discharges derived from both

HBV-1 and HBV-15. As a consequence of this, the variability in extreme values has increased with respect to the simulations for current climate conditions. The HBV-118 model shows a similar increase in 20-year and 100-year return values with climate change as the corresponding realisations for HBV-1 and HBV-15.

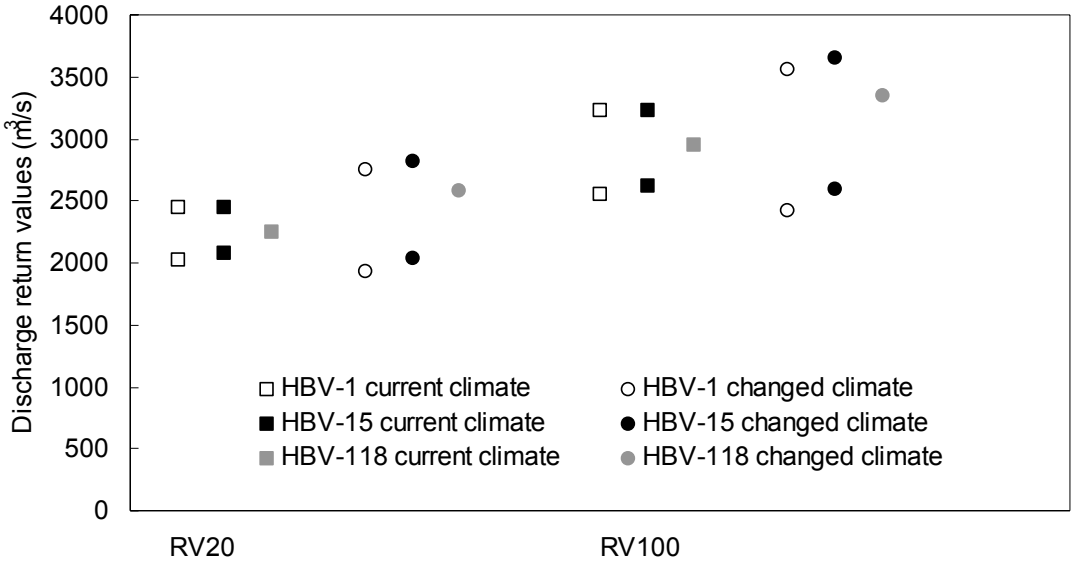

Figure 6.32 Discharge 20-year (RV20) and 100-year (RV100) return values in m^3s^{-1} from a 30 year period as simulated with 5 precipitation realisations for HBV-1 and HBV-15 and 1 precipitation realisation for HBV-118 under current and changed climate conditions. Only the minimum and maximum of the 5 HBV-1 and HBV-15 realisations are shown.

6.5.5 Uncertainties

The uncertainty in extreme discharges with climate change is caused by various sources of uncertainties of which the most important are: climatological input (precipitation, evapotranspiration), model structure, parameter values and extrapolation to large return periods.

The uncertainty in precipitation variability and extreme precipitation was found to be large in chapter 4 (30-50 %). This uncertainty consisted of climate model errors, inter-model uncertainties and an estimation of climate forcing uncertainties. The effect of inter-model uncertainties on extreme river discharges has been roughly assessed by using the results of each individual climate model for climate change conditions to assess a parameter set for the random cascade rainfall model. These parameter sets have been used to generate for each climate model one realisation which served as input into the HBV-15 model. The results are given in Figure 6.33, where the minimum and maximum of the 5 realisations of annual maximum discharges for a 30 year period are given. The results of Figure 6.32 for climate change conditions and HBV-15 are shown as well for comparison. These results can be regarded as uncertainties in extreme discharges due to the stochasticity of the precipitation process. It was found in Figure 6.33 that these uncertainties are even larger than the uncertainties in extreme discharges due to inter-model uncertainties. The uncertainties due to individual climate model

errors are unimportant here, because the climate model results have only been used to derive relative changes in observed precipitation statistics. It can be expected that the uncertainty in extreme discharges due to climate forcing uncertainties is at least as large as the two uncertainties in Figure 6.33.

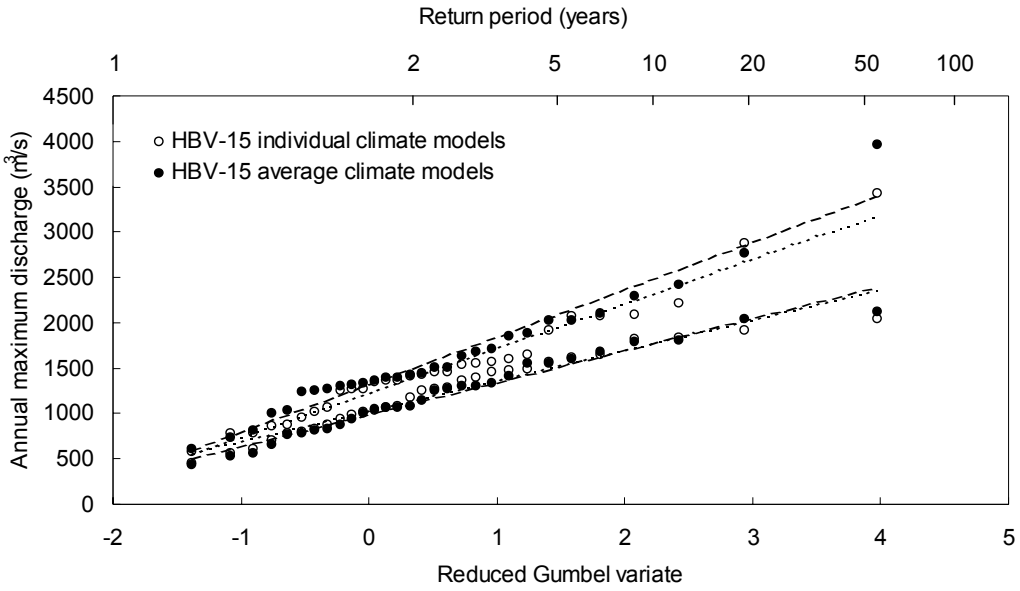

Figure 6.33 Gumbel plot for annual maximum discharges in m^3s^{-1} for a 30 year period as simulated with 5 precipitation realisations derived from the average of the 5 climate models and 5 precipitation realisations derived from the 5 individual climate models under changed climate conditions for HBV-15. Only the minimum and maximum of each of the 5 realisations are shown. Regression lines for the 'realisations' (dashed) and realisations from 'individual climate models' (dotted) are given as well.

The differences between the results of HBV-1, HBV-15 and HBV-118 give some indication about uncertainties in extreme discharges due to uncertainties in model structure, although these differences are mainly scale related. Small differences between results of these different models have been found in this section (5-10 %) and therefore this uncertainty source seems to be relatively unimportant.

The effect of different key parameter values on the results was investigated in the calibration phase of the model, but mainly using HBV-1 (see 6.5.1). In particular, variations of the parameters determining the fast runoff response (α and k_H) can have significant consequences for extreme discharges. For example a 50 % change of α can result in approximately a 8 % change in the 100-year return value (see Figure 6.21). However, this reduction of uncertainty in parameters by the hydrological model (50 % to 8 %) is much larger than the reduction of uncertainty in precipitation statistics by the hydrological model (e.g. 15 % to 6 %), i.e. the model sensitivity to changes in parameters is much smaller than the sensitivity to changes in precipitation. The uncertainty in α and k_H is estimated at 20 % resulting in a much smaller impact on the output uncertainty than for example the impact of precipitation uncertainty.

The uncertainty in extreme discharges due to extrapolation can be roughly assessed by using the formulations described in 2.3.5. The uncertainty in the estimation of the 100-

year return value is 20 % [one-sided, see equation (2.43)] using a 90% confidence interval and employing a 30-year series. The uncertainty is 25 % when using a 95% confidence interval. This uncertainty can only be reduced by employing longer time series as can be done for the observed series (about 90 years, 12 and 15 % uncertainty). This can not be performed with respect to the modelled series for current and changed climate, because the hydrological model needs to be calibrated with a sufficient number of precipitation series of sufficient length. In this respect, the 30-year series currently is the maximum simulation length which can be used without arriving at a too coarse spatial precipitation scale. Other extreme value distributions (GEV, Pearson type-III) may slightly reduce uncertainties due to extrapolation (see e.g. Gerretsen, 2001).

Overall, the uncertainties in extreme discharges due to precipitation errors and extrapolation errors seem to be more important (respectively more than 20 % and about 20 %) than uncertainties due to hydrological model errors and parameter estimation errors. These uncertainties should be quadratically summed, because of the general random character of the uncertainties resulting in an uncertainty of at least 30-40 %.

6.6 Summary and conclusions

One temperature and one evapotranspiration series have been used as input into the river basin model. Observed series have been employed for current climate conditions. Temperature differences between HadCM3 simulated current and changed climate and a relation between temperature change and evapotranspiration change have been taken to obtain temperature series respectively evapotranspiration series for changed climate conditions.

Precipitation for the current and changed climate has been modelled with a random cascade rainfall model. This model consists of a temporal model for the whole region and a spatial model for the disaggregation of this rainfall to the appropriate scale (20 km). The temporal model consists of a discrete first-order four-state Markov chain determining rainfall occurrence and a truncated two-parameter gamma distribution describing rainfall amount. The spatial disaggregation of the temporal rainfall series is done using a discrete random cascade approach with generators determined from a beta-lognormal distribution. The parameters of these models were determined from observed and GCM and RCM modelled rainfall. All relevant rainfall statistics except wet day frequency for current and changed climate are well simulated by the random cascade model.

An appropriate river basin model has been constructed by implementing the appropriate model components derived in chapter 5 into the existing modelling framework HBV. Additionally, two river basin models of differing complexities have been set up to evaluate the sensitivity of the model results to model complexity and to allow for a verification of the model appropriateness procedure. The supposedly appropriate model has 118 sub-basins (HBV-118) and the additional models have 1 and 15 sub-basin(s) (HBV-1 and HBV-15). The three models were calibrated and validated with equal data series (as far as possible). Generations of the rainfall model under current and changed climate conditions have been used to assess the climate change impacts.

The average and extreme discharge behaviour at the basin outlet (Borgharen) is well reproduced by the three models in the calibration and validation, the results become

somewhat better with increasing model complexity. The differences between the average discharge behaviour of the sub-basins modelled by the two distributed models are small. Extreme discharges are generally better simulated by HBV-118 in the calibration, where in the validation HBV-15 is somewhat better. The model results with synthetic precipitation under current climate conditions show a small overestimation of average discharge behaviour and a considerable underestimation of extreme discharge behaviour. The underestimation of extreme discharges can not be explained by the statistics of the synthetic precipitation input, but is caused by the observed precipitation input at the sub-basin scale. In most cases, this precipitation is not an areally averaged quantity, but rather a point quantity resulting in an overestimation of observed precipitation variability and extreme behaviour at the sub-basin scale compared to the generated precipitation. This seems to be a very frequently occurring problem, which can be dealt with by increasing the density of precipitation stations in a river basin in an efficient manner.

The general trend with climate change is a small decrease of the average discharge and a small increase of discharge variability and extreme discharges. The variability in extreme discharges for climate change conditions has increased with respect to the simulations for current climate conditions. This variability results both from the stochasticity of the precipitation process and the differences between the climate models. Other uncertainties include those related to the river basin model structure, the parameter values and the extrapolation to large return periods. Overall, it appeared that the uncertainties in extreme discharges due to precipitation errors and extrapolation errors are more important than uncertainties due to hydrological model errors and parameter estimation errors. The total uncertainty is estimated at 30-40 %.

Chapter 7

Conclusions and discussion

7.1 Conclusions

In this section, the answers to the five research questions will be formulated. The research questions were related to dominant processes and variables (research question 1), appropriate scales (research question 2), associated appropriate process formulations (research question 3), climate change (research question 4) and impacts of climate change on river flooding (research question 5).

7.1.1 Dominant processes and variables

Dominant climate variables have been considered in section 4.1 and were found to be precipitation, temperature and evapotranspiration. Dominant river basin processes have been derived from literature in section 5.2 and were infiltration and saturation excess overland flow, subsurface storm flow and subsurface flow in the soil matrix. The main associated variables are elevation, soil type and land use type.

7.1.2 Appropriate spatial and temporal scales

The appropriate spatial scale of each key variable was assumed to be equal to a fraction of the spatial correlation length of that variable. This fraction has been determined on the basis of relationships between statistics and scale accepting an error in the estimation of the statistic of 10 %, as described in section 2.3. This resulted in fractions varying between 0.20 and 0.25. The application to the climate variables in chapter 4 resulted in an appropriate spatial scale for precipitation of 20 km with a temporal scale of 1 day. The application to the river basin variables in section 5.3 revealed appropriate spatial scales for elevation, soil and land use of respectively 0.1, 5.3 and 3.3 km. The appropriate model scale has been determined by multiplying the appropriate variable scales with their associated weights. The weights were based on SCS curve number method relationships between the peak discharge and some specific parameters. The values of these parameters are dependent on the scale of each key variable. The resulting appropriate model scale was about 10 km with a temporal scale of 1 day.

In addition to this systematic scale analysis, the effects of spatial and temporal precipitation and model scales on peak discharges have been considered in chapter 3 by employing a simple stochastic rainfall model and a dimensionless river basin model. The resulting appropriate precipitation scales were assessed at 1-2 grid points/spatial correlation length and at most 1 time step/temporal correlation length. The appropriate model scales were estimated at 5-10 grid points/spatial correlation length and 7-10 time steps/temporal correlation length. The correlation lengths refer to precipitation.

7.1.3 Appropriate process formulations

Appropriate formulations related to these appropriate scales have been derived from literature and some rough estimations in section 5.4. The formulations of importance were those related to evapotranspiration, surface flow and subsurface (storm) flow. Relatively simple formulations were found to be sufficient for this model objective and appropriate spatial scale.

7.1.4 Climate change

The climate change effect has been assessed by analysing and comparing data from stations, re-analyses, global climate models (GCMs) and regional climate models (RCMs) for Western Europe. Average precipitation values do not show significant changes with climate change (a doubling of carbon dioxide), while standard deviations increase by about 10 %. Extreme precipitation may increase with climate change by about 15-20 % and correlation lengths by about 30-40 %. The differences between climate models can be considerable, in particular with respect to extreme values and correlation lengths. The RCMs and the Australian GCM simulate extreme precipitation behaviour under current climate conditions very well, while the re-analyses underestimate and the British and Canadian GCMs overestimate extreme precipitation. Model errors and inter-model differences in the estimation of extreme precipitation with climate change can amount up to 50 %, which is significantly larger than the simulated change. The average predicted temperature increase with climate change is 3.7 °C (2.9-4.7 °C). The temperature behaviour under current climate conditions is well simulated by the RCMs and the British GCM, but rather poorly by the Canadian and Australian GCM. The estimated uncertainty in average temperature with climate change is about 2-3 °C, which is comparable with the simulated change. The average increase in potential evapotranspiration with climate change has been derived from a relationship between temperature changes and evapotranspiration changes and is about 15 % (20 % in winter and 10 % in summer).

7.1.5 Impact of climate change on river flooding

The impact of climate change on river flooding has been evaluated by using the climate change information described above and river basin models of different complexities. The climate change information on temperature and evapotranspiration could directly be used. Precipitation with climate change has been generated with a space-time random cascade rainfall model in an acceptable way. An appropriate river basin model has been constructed by implementing the appropriate model components derived before into an existing modelling framework (HBV). Additionally, two river basin models of differing complexities have been set up to evaluate the sensitivity of the model results to model complexity and to allow for a verification of the model appropriateness procedure. The appropriate model has 118 sub-basins (HBV-118) and an associated model scale of about 13 km. This model scale is of the same order of magnitude as the one revealed in the scale analysis (10 km) and assumed to be sufficient for checking the appropriateness requirements. The additional models have 1 and 15 sub-basin(s) (HBV-1 and HBV-15). The three models were calibrated and validated with equal data series (as far as possible). Generations of the rainfall model under current and changed climate conditions have been used to assess the climate change impacts.

The average and extreme discharge behaviour at the basin outlet (Borgharen) is well reproduced by the three models in the calibration and validation, the results become somewhat better with increasing model complexity. The differences between the average discharge behaviour of the sub-basins modelled by the two distributed models are small. The model results with synthetic precipitation under current climate conditions show a considerable underestimation of extreme discharge behaviour. The underestimation of extreme discharges is caused by the observed precipitation input at the sub-basin scale. In most cases, this precipitation is not an areally averaged quantity, but rather a point quantity resulting in an overestimation of observed precipitation variability and extreme behaviour at the sub-basin scale compared to the generated precipitation. This seems to be a very frequently occurring problem, which can be improved by increasing the density of precipitation stations in a river basin in an efficient manner.

The general trend with climate change is a small decrease (~5 %) of the average discharge and a small increase (~5-10 %) of discharge variability and extreme discharges. The variability in extreme discharges for climate change conditions has increased with respect to the simulations for current climate conditions. This variability results both from the stochasticity of the precipitation process and the differences between the climate models. Other uncertainties include those related to the river basin model structure, the parameter values and the extrapolation to large return periods. Overall, it was found that the uncertainties in extreme discharges due to precipitation errors and extrapolation errors (both about 20 %) are more important than uncertainties due to hydrological model errors and parameter estimation errors (both less than 10 %).

7.2 Discussion

7.2.1 Appropriate modelling

The appropriate spatial precipitation scale derived on the basis of precipitation data (chapter 4; 4-5 grid points/correlation length) is smaller than the one derived on the basis of model sensitivities to varying spatial precipitation scales (chapter 3; 1-2 grid points/correlation length). More confidence can be placed on the former appropriate scale, because it is derived directly from the data. The other one is estimated from model sensitivities assuming the model is correct. This adds substantial uncertainty to the assessment of appropriate scales. Therefore, the appropriate scales of the other key variables have been directly determined from data as well. Only for the integration of these appropriate variable scales, model sensitivities have been used, which is considered to be inevitable.

The resulting appropriate model scale derived with the appropriateness procedure (chapter 5; 8-10 grid points/precipitation correlation length) is comparable with the one derived from model sensitivities to varying spatial model scales (chapter 3; 5-10 grid points/correlation length. This confirms, although roughly, the findings from the appropriateness procedure. Therefore, simulations with different river basin models have been performed to give additional information about the validity of the model appropriateness procedure and the sensitivity of model results to model complexity. In this way, an integrated approach of research objectives I and II has been achieved.

On the basis of the differences between the results of the three models in the calibration, validation and simulations under current climate conditions, it was found that HBV-118 is complex enough to simulate discharge behaviour and in particular extreme discharge behaviour for a river basin like the Meuse. In particular in the calibration, the results became somewhat better with increasing model complexity. This can be explained by the fact that in a complex model more parameters can be tuned in such a way, that a good agreement with observations is obtained. In the validation, the parameters can not be adjusted and, as a consequence, the differences between the model results are less obvious. This may be because of the data used in HBV-118 are more dependent on the calibration and validation period than the smaller amount of data in HBV-15. Another explanation for the small differences is that no additional discharge series have been used in the calibration and validation of HBV-118 compared to HBV-15. Additional series could have improved the calibration and validation of HBV-118 and thus increased the differences with HBV-15. Finally, the small discrepancies between the models are not surprising given the small differences in spatial model scales for HBV-15 and HBV-118 (37 km and 13 km).

The consistency criterion has been used in this thesis to assess model appropriateness rather than the output uncertainty criterion. A consistent model is defined as a model with scales and formulations at a balanced level, neither too coarse nor too detailed with respect to each other. Considering this criterion, HBV-118 is indeed an appropriate model for the assessment of climate change impacts on river flooding, because the application of the model appropriateness procedure results in an approximately consistent model. The model results discussed above and the accompanying explanations confirm, although not convincingly, the results of the model appropriateness procedure.

The observed precipitation input at the sub-basin scale was frequently found to be precipitation at the point scale instead of an areally averaged quantity. This is a common problem in hydrology since station precipitation is mostly used as input in rainfall-runoff models. Insufficient precipitation stations are generally available to assess the areally averaged sub-basin scale precipitation in a right way. Moreover, the Thiessen method used is not an interpolation method, but attributes precipitation from the closest gauge to a specific point and thus results in point precipitation for areas amounting up to sub-basin scales. First, this can be improved by employing more sophisticated interpolation methods like inverse distance interpolation or kriging. Second, the density of precipitation stations in a river basin can be increased in an efficient manner or the length of the time series can be shortened causing other disadvantages such as an increase in extrapolation uncertainty. A third possibility to avoid the differences between observed and generated sub-basin scale precipitation is the generation of precipitation at a smaller scale compared to the 20 km scale. In this way, both observed and generated precipitation are at the wrong, small scale. As a consequence, parameters are erroneously estimated in the calibration and incorrectly used in the simulations under current and changed climate conditions. The main conclusion is that when precipitation is modelled at the appropriate precipitation scale, observed precipitation (preferably areally averaged) should at least be available at this scale for a proper calibration and validation.

7.2.2 Uncertainties

The uncertainties in extreme discharges due to precipitation errors and extrapolation errors were found to be more important than uncertainties due to hydrological model errors and parameter estimation errors. It is therefore preferable to improve precipitation predictions with climate change and/ or decrease extrapolation errors by incorporating longer time series. The latter improvement will be difficult to obtain and therefore attention should be paid to the improvement of precipitation in climate models at the appropriate scale for hydrological impact assessment. However, this will only slightly reduce the total uncertainty, because of the remaining large extrapolation errors. Application of more complex hydrological models or parameter estimation techniques will probably not reduce the total uncertainty, before reductions in precipitation and extrapolation errors have been achieved. Obviously, for other research objectives, improvements in models and parameter estimation may have a much larger effect (e.g. flood forecasting in the short term).

The acceptable error in the determination of appropriate scales has been rather arbitrarily set at 10 %. The sensitivity of appropriate scales to varying accepted errors can be substantial, as illustrated in chapter 4 for precipitation, resulting in varying model scales. This confirms the fact that the applied model appropriateness procedure can be viewed as a methodology to obtain a consistent model rather than a model with a specific maximal uncertainty. However, the output uncertainty can serve as an additional criterion for model appropriateness. This output uncertainty was found to be at least 30-40 %, mainly consisting of precipitation and extrapolation uncertainties. Thus, although the model is appropriate when considering its consistency, it is inappropriate when solely taking into account its output uncertainty and an arbitrary uncertainty criterion of 25 %.

A limit on the accuracy of estimated extreme discharges is the amount of spatial and temporal data available. The spatial resolution of the data influences the model complexity to be employed and thus the accuracy of estimated flood frequencies. The temporal length of the data series imposes a limit on the accuracy of extrapolations to extreme values. These two data characteristics should be jointly viewed, because for example a long time series of precipitation at a too coarse spatial resolution will not serve as an appropriate input for the calibration and validation of a river basin model. Using synthetic precipitation at a finer, appropriate spatial resolution to assess flood frequencies will not completely solve this problem and will give a kind of apparent accuracy. This is because the parameters of the precipitation model are derived from observed precipitation statistics. Here, 39 stations with a daily precipitation time series of 30 years or more were available, where at least 76 stations are preferred. Some precipitation statistics can be reduced to a finer scale by means of the reduction functions. However, the parameters of the spatial precipitation model should be determined directly from precipitation data. Thus, the spatial resolution of the precipitation series for the calibration and validation was insufficient resulting in the differences found in chapter 6. Obviously, the spatial resolution could have been more appropriate if only time series of 15 years were adopted. Therefore, a not commonly used trade-off of the spatial and temporal accuracy should be made keeping the output uncertainty as small as possible.

7.2.3 Uncertainty and change

The uncertainty in river flooding with climate change (over 40 %) is much larger than the change with respect to current climate conditions (less than 10 %). One would therefore argue that river flooding will not change with climate change, because the changes fall completely within the uncertainty range. However, climate changes are systematic changes rather than random changes and thus the uncertainty range will be shifted to another level (about 5-10 % higher in this case). Obviously, there is a considerable amount of uncertainty (or variability in this respect), but the range of this uncertainty (and the expected value) will change due to systematic changes in the input of the system. This can be illustrated by the following example. Consider an average observed precipitation year representing current climate conditions and a wet observed precipitation year representing changed climate conditions (a temporal analog). The model is able to simulate for both years a correct discharge behaviour and thus the model can be supposed to do so for a changed climate as well assuming the predicted precipitation change is right. This is a temporal analog for one year of average discharge behaviour, similar analogs for flood frequencies can not be given, but are supposed to be comparable. Therefore, it can be assumed that the model simulates extreme discharges for a changed climate in a reasonable way, although the variability in these extreme discharges only increase with climate change. It is thus possible to see effects of changes in, for example input, on the model outcomes.

7.2.4 Generality of results

The results may be generalised to other geographical areas and research problems. The appropriateness procedure can be in principle applied to every arbitrary area in the world. The dominance of processes is area dependent, but in general, similar variables play an important role in flood generating rainfall-runoff processes. The appropriate scales of these variables depend on the region. For example, the appropriate spatial scale for precipitation will be much smaller for tropical, mountainous areas with large orographical effects than for temperate, relatively flat areas like the Meuse basin. Furthermore, the appropriate scales are influenced by the size of the basin. Small catchments require smaller time scales than large basins and consequently associated spatial scales will differ between small and large basins. The appropriate spatial scales were based on a daily time scale in this research for the Meuse basin, whereas the determination of appropriate spatial scales for a similar study in a research catchment of several km^2 should be based on a hourly or even minute time scale leading to smaller appropriate spatial scales. Similarly, scale analysis in a climate change study for the Amazon may be based on a weekly or monthly time scale probably resulting in larger appropriate spatial scales. Appropriate process formulations will change with these changes in scale as they are often scale dependent.

The type of research problem may influence the importance of processes and associated variables. For example, when studying the impact of climate change on low flows, evapotranspiration and groundwater flow become more important, whereas overland flow and subsurface storm flow may be less significant. Consequently, other variables are dominant and other appropriate spatial and temporal scales will prevail. Therefore, based on the results obtained here only very general guidelines with respect to appropriate models for other research objectives can be given.

7.2.5 Usefulness of model appropriateness

The idea of model appropriateness was introduced in chapter 1 in a search for an optimum model complexity for a specific research objective and area. At first, an appropriate model was defined as a model associated with minimal total costs or a minimal total uncertainty. Later on, its definition was rather based on a consistency criterion implying that a model should have scales and formulations at a balanced level. This criterion has been implemented in a model appropriateness procedure, which was mainly applied to assess the appropriate model scale. The processes to be incorporated and the process formulations to be used were determined more (semi-)qualitatively.

The usefulness of the appropriateness procedure is thus in its ability to assess the appropriate scales of the individual key variables before model construction and integrate them in a balanced way into an appropriate model scale. The procedure will not result in a model for a specific situation with a prescribed maximum uncertainty. Obviously, the model output uncertainty can be determined afterwards and compared with accuracy criteria formulated by model users or policy makers. This output uncertainty should consist of several uncertainties at a balanced level. It was found that uncertainties due to precipitation and extrapolation errors dominated over other uncertainties. However, the precipitation uncertainties are mainly caused by climate model errors and uncertainties about future climate. These uncertainties are not particularly related to scale and could therefore not been reduced to a balanced level in the model appropriateness procedure. The extrapolation uncertainties have to do with the length of the data series. These could neither be detected in the procedure, because the appropriateness of scales concerns support and spacing scale and not extent scale.

Another use of the procedure is that is provides a framework for decisions about the reduction or expansion of data networks and needs. Application of the framework to the dominant variables in a specific situation may reveal where possible data inconsistencies (e.g. a too sparse network) exist. Also, discrepancies between observations and model results may be explained with the help of the procedure, as has been done for example in chapter 4. Obviously, the adequacy of the integration function for a specific situation (the curve number method in this case) should be considered when applying the appropriateness procedure.

References

Abbott, M.B., Bathurst, J.C., Cunge, J.A., O'Connell, P.E. and Rasmussen, J.L., 1986. An introduction to the European hydrological system - Système Hydrologique Europeen, "SHE". 2. Structure of a physically-based, distributed modelling system. *J. Hydrol.*, **87**, 61-77.

Abrahart, R.J., Kirkby, M.J., McMahon, M.L., Bathurst, J.C., Ewen, J., Kilsby, C.G., White, S.M., Diamond, S. and Woodward, I., 1996. MEDRUSH - Spatial and temporal river-basin modelling at scales commensurate with global environmental change. In: K. Kovar and H.P. Nachtnebel (Eds.), *Application of geographic information systems in hydrology and water resources management*. Proc. HydroGIS'96 Conf., Vienna, Austria, 47-54.

Anderson, M.G. and Burt, T.P., 1990. Subsurface runoff. In: M.G. Anderson and T.P. Burt (Eds.), *Process studies in hillslope hydrology*. Wiley, Chichester, 365-400.

Arnell, N.W., 1999. A simple water balance model for the simulation of streamflow over a large geographical domain. *J. Hydrol.*, **217**, 314-335.

Arora, V.K. and Boer, G.J., 2001. Effects of simulated climate change on the hydrology of major river basins. *J. Geophys. Res.*, **106**, 3335-3348.

Baier, W. and Robertson, G.W., 1966. A new versatile soil moisture budget. *Can. J. Plant Sci.*, **46**, 299-315.

Bardossy, A., 1997. Downscaling from GCMs to local climate through stochastic linkages. *J. Environ. Manage.*, **49**, 7-17.

Bardossy, A. and Plate, E.J., 1992. Space-time model for daily rainfall using atmospheric circulation patterns. *Water Resour. Res.*, **28**, 1247-1259.

Bear, J., 1972. *Dynamics of fluids in porous media.* Dover Publ., New York, 784 pp.

Beck, M.B., 1987. Water quality modeling: A review of the analysis of uncertainty. *Water Resour. Res.*, **23**, 1393-1442.

Beersma, J., Agnew, M., Viner, D. and Hulme, M. (Eds.), 2000. *Climate scenarios for water-related and coastal impacts.* Proc. ECLAT-2 Workshop Report No.3 KNMI, De Bilt, the Netherlands. Climatic Research Unit, Norwich, 144 pp.

Bell, J., Duffy, P., Covey, C. and Sloan, L., 2000. Comparison of temperature variability in observations and sixteen climate model simulations. *Geophys. Res. Lett.*, **27**, 261-264.

Berger, H.E.J., 1992. *Flow forecasting for the river Meuse*. Ph.D.-thesis. Delft Univ. of Technol., Delft, 356 pp.

Bergström, S., 1990. *Parameter values for the HBV model in Sweden (in Swedish)*. SMHI rapporter hydrologi no. 28. Swedish Meteor. Hydrol. Inst., Norrköping, 35 pp.

Bergström, S., 1995. The HBV model. In: V.P. Singh (Ed.), *Computer models of watershed hydrology*. Water Resour. Publ., Highlands Ranch, 443-476.

Bergström, S. and Forsman, A., 1973. Development of a conceptual deterministic rainfall-runoff model. *Nord. Hydrol.*, **4**, 147-170.

Bergström, S. and Graham, L.P., 1998. On the scale problem in hydrological modelling. *J. Hydrol.*, **211**, 253-265.

Beven, K., 1989. Changing ideas in hydrology - The case of physically based models. *J. Hydrol.*, **105**, 157-172.

Beven, K., 1993. Prophecy, reality and uncertainty in distributed hydrological modelling. *Adv. Water Resour.*, **16**, 41-52.

Beven, K.J. and Kirkby, M.J., 1979. A physically based, variable contributing area model of basin hydrology. *Hydrolog. Sci. B.*, **24**, 43-69.

Beven, K.J., Calver, A. and Morris, E.M., 1987. *The Institute of Hydrology distributed model*. Tech. Rep. 98. Inst. Hydrol., Wallingford.

Binley, A.M. and Beven, K.J., 1991. Physically-based modelling of catchment hydrology: a likelihood approach to reducing predictive uncertainty. In: D.G. Farmer and M.J. Rycroft (Eds.), *Computer modelling in the environmental sciences*. Clarendon Press, Oxford, 75-88.

Binley, A.M., Beven, K.J., Calver, A. and Watts, L.G., 1991. Changing responses in hydrology: Assessing the uncertainty in physically based model predictions. *Water Resour. Res.*, **27**, 1253-1261.

Blaney, H.F. and Criddle, W.D., 1950. *Determining water requirements in irrigated areas from climatological and irrigation data*. TP-96. USDA, Washington, 48 pp.

Blazkova, S. and Beven, K., 1997. Flood frequency prediction for data limited catchments in the Czech Republic using a stochastic rainfall model and TOPMODEL. *J. Hydrol.*, **195**, 256-278.

Blom, G., 1958. *Statistical estimates and transformed beta variables*. Wiley, New York., 176 pp.

Blöschl, G. and Sivapalan, M., 1995. Scale issues in hydrological modelling: a review. In: J.D. Kalma and M. Sivapalan (Eds.), *Scale issues in hydrological modelling.* Wiley, Chichester, 9-48.

Blöschl, G. and Sivapalan, M., 1997. Process controls on regional flood frequency: Coefficient of variation and basin scale. *Water Resour. Res.*, **33**, 2967-2980.

Boer, G.J., Flato, G.M., Reader, M.C. and Ramsden, D., 2000a. A transient climate change simulation with greenhouse gas and aerosol forcing: experimental design and comparison with the instrumental record for the twentieth century. *Clim. Dynam.*, **16**, 405-426.

Boer, G.J., Flato, G.M. and Ramsden, D., 2000b. A transient climate change simulation with greenhouse gas and aerosol forcing: projected climate to the twenty-first century. *Clim. Dynam.*, **16**, 427-450.

Booij, M.J., 2000. Model appropriateness for simulation of climate change and river flooding. In: L.R. Bentley, J.F. Sykes, C.A. Brebbia, W.C. Gray and G.F. Pinder (Eds.), *Computational methods in water resources*. Balkema, Rotterdam, 1169-1176.

Booij, M.J., 2002a. Modelling the effect of spatial and temporal rainfall and catchment model resolution on extreme river discharge. *Hydrolog. Sci. J.*, **47** (2).

Booij, M.J., 2002b. Extreme daily precipitation in Western Europe with climate change at appropriate spatial scales. *Int. J. Climatol.*, **22**, 69-85.

Boorman, D.B. and Sefton, C.E.M., 1997. Recognising the uncertainty in the quantification of the effects of climate change on hydrological response. *Climatic Change,* **35**, 415-434.

Bossard, M., Steenmans, Ch., Feranec, J. and Otahel, J., 2000. *The revised and supplemented Corine land cover nomenclature*. Tech. Rep. 38. European Environment Agency, Copenhagen, 110 pp.

Brandsma, Th., 1995. *Hydrological impact of climate change: a sensitivity study for the Netherlands*. Ph.D.-thesis. Delft University of Technology, Delft, 391 pp.

Bras, R.L. and Rodriguez-Iturbe, I., 1976. Rainfall generation: A nonstationary time-varying multidimensional model. *Water Resour. Res.*, **12**, 450-456.

Brasington, J. and Richards, K., 1998. Interactions between model predictions, parameters and DTM scales for TOPMODEL. *Comput. Geosci.*, **24,** 299-314.

Brooks, R.H. and Corey, A.T., 1964. *Hydraulic properties of porous media*. Hydrology Paper 3. Colorado State University, Fort Collins.

Bruneau, P., Gascuel-Odoux, C., Robin, P., Merot, Ph. and Beven, K., 1995. Sensitivity to space and time resolution of a hydrological model using digital elevation data. *Hydrol. Process.*, **9**, 69-81.

Buckingham, E., 1907. *Studies on the movement of soil moisture*. USDA Bur. Soils Bull. 38. USDA.

Bultot, F., Coppens, A., Dupriez, G.L., Gellens, D. and Meulenberghs, F., 1988. Repercussions of a CO2 doubling on the water cycle and on the water balance - A case study for Belgium. *J. Hydrol.*, **99**, 319-347.

Bultot, F., Gellens, D., Spreafico, M. and Schädler, B., 1992. Repercussions of a CO2 doubling on the water balance - A case study in Switzerland. *J. Hydrol.*, **137**, 199-208.

Cacko, J., Bily, M. and Bukoveczky, J., 1988. *Random processes: measurement, analysis and simulation*. Elsevier, Amsterdam, 234 pp.

Cameron, D., Beven, K. and Tawn, J., 2000. An evaluation of three stochastic rainfall models. *J. Hydrol.*, **228**, 130-149.

Campbell, G.S., 1974. A simple method for determining unsaturated conductivity from moisture retention data. *Soil Sci.*, **117**, 311-314.

Carter, T.R., Hulme, M. and Lal, M., 1999. *Guidelines on the use of scenario data for climate impact and adaptation assessment*. Version 1. IPCC-TGCIA, Norwich, 69 pp.

Chapman, T.G., 1997. Stochastic models for daily rainfall in the western Pacific. *Math. Comput. Simulat.*, **43**, 351-358.

Chen, Z-Q., Govindaraju, R.S. and Kavvas, M.L., 1994a. Spatial averaging of unsaturated flow equations under infiltration conditions over areally heterogeneous fields. 1. Development of models. *Water Resour. Res.*, **30**, 523-533.

Chen, Z-Q., Govindaraju, R.S. and Kavvas, M.L., 1994b. Spatial averaging of unsaturated flow equations under infiltration conditions over areally heterogeneous fields. 2. Numerical simulations. *Water Resour. Res.*, **30**, 535-548.

Chiew, F. and McMahon, T., 1994. Application of the daily rainfall-runoff model MODHYDROLOG to 28 Australian catchments. *J. Hydrol.*, **153**, 383-416.

Chow, V.T., 1959. *Open channel hydraulics*. McGraw Hill, New York, 680 pp.

Christensen, J.H., Christensen, O.B., Lopez, P., Meijgaard, E. van and Botzet, M., 1996 *The HIRHAM4 regional atmospheric climate model.* Scientific Report 96-4. Danish Meteorological Institute, Copenhagen, 51 pp.

Christensen, J.H., Machenhauer, B., Jones, R.G., Schär, C., Ruti, P.M., Castro, M. and Visconti, G., 1997. Validation of present-day regional climate simulations over Europe: LAM simulations with observed boundary conditions. *Clim. Dynam.*, **13**, 489-506.

Commissie Boertien I, 1993. *Testing points of departure river dike reinforcements: Safety against flooding (in Dutch).* Report 1. Ministerie van Verkeer en Waterstaat, The Hague.

Commissie Rivierdijken, 1977. *Report committee on river dikes (in Dutch)*. Ministerie van Verkeer en Waterstaat, The Hague.

Cosh, M.H. and Brutsaert, W., 1999. Aspects of soil moisture variability in the Washita '92 study region. *J. Geophys. Res.*, **104**, 19751-19757.

Crawford, N.H. and Linsley, R.K., 1966. *Digital simulation in hydrology - Stanford watershed model IV*. Tech. Rep. 39. Stanford Univ., Stanford.

Cubasch, U., Waszkewitz, J., Hegerl, G. and Perlwitz, J., 1995. Regional climate changes as simulated in time-slice experiments. *Climatic Change*, **31**, 273-304.

Cunge, J.A., 1969. On the subject of a flood propagation computation method (Muskingum method). *J. Hydraul. Res.*, **7**, 205-230.

D'Agostino, R.B. and Stephens, M.A. (Eds.), 1986. *Goodness-of-fit-techniques*. Marcel Dekker Inc., New York, 560 pp.

Dawdy, D.R. and Bergmann, J.M., 1969. Effect of rainfall variability on streamflow simulation. *Water Resour. Res*., **5**, 958-966.

De Blois, C.J., 2000. *Uncertainty in large-scale models for decision support in water management*. Ph.D.-thesis. University of Twente, Enschede, 248 pp.

Déqué, M. and Piedelievre, J.-P., 1995. High resolution climate simulation over Europe. *Clim. Dynam*., **11**, 321-339.

Dickinson, R.E., 1989. Uncertainties of estimates of climate change: A review. *Climatic Change*, **15**, 5-13.

Diermanse, F.L.M., 2001. *Physically based modelling of rainfall-runoff processes.* Ph.D.-thesis. Delft University Press, Delft, 234 pp.

Doorenbos, J. and Pruitt, W.O., 1977. *Crop water requirements*. Irrigation and Drainage Paper 24. FAO, Rome.

Estrela, T. and Quintas, L., 1994. Use of GIS in the modelling of flows on floodplains. In: W.R. White and J. Watts (Eds.), *River flood hydraulics*. Proc. 2nd Int. Conf. York, England, 177-189.

Farajalla, N.S. and Vieux, B.E., 1995. Capturing the essential spatial variability in distributed hydrological modelling: infiltration parameters. *Hydrol. Process.*, **9**, 55-68.

Filliben, J.J., 1975. The probability plot correlation coefficient test for normality. *Technometrics*, **17**, 111-117.

Flato, G.M., Boer, G.J., Lee, W.G., McFarlane, N.A., Ramsden, D., Reader, M.C. and Weaver, A.J., 2000. The Canadian Centre for Climate Modelling and Analysis global coupled model and its climate. *Clim. Dynam.*, **16**, 451-467.

Franchini, M. and Pacciani, M., 1991. Comparative analysis of several conceptual rainfall-runoff models. *J. Hydrol.*, **122**, 161-219.

Freeze, R.A. and Harlan, R.A., 1969. Blueprint for a physically-based, digitally-simulated hydrologic response model. *J. Hydrol.*, **9**, 237-258.

Gabriel, K.K. and Neumann, J., 1962. A Markov chain model for daily rainfall occurrence at Tel Aviv. *Q. J. Roy. Meteor. Soc.*, **88**, 90-95.

Ganopolski, A., Rahmstorf, S., Petoukhov, V. and Claussen, M., 1998. Simulation of modern and glacial climates with a coupled global model of intermediate complexity. *Nature*, **391**, 351-356.

García-Ruiz, J.M., Arnáez, J., White, S.M., Lorente, A. and Beguería, S., 2000. Uncertainty assessment in the prediction of extreme rainfall events: an example from the central Spanish Pyrenees. *Hydrol. Process.*, **14**, 887-898.

Garen, D.C. and Burges, S.J., 1981. Approximate error bounds for simulated hydrographs. *J. Hydraul. Eng.-ASCE*, **107**, 1519-1534.

Gates, W.L., 1999. An overview of the results of the Atmospheric Model Intercomparison Project (AMIP I). *B. Am. Meteorol. Soc.*, **80**, 29-56.

Gellens, D. and Roulin, E., 1998. Streamflow response of Belgian catchments to IPCC climate change scenarios. *J. Hydrol.*, **210**, 242-258.

Germann, P.F. and Beven, K.J., 1986. A distribution function approach to water flow in soil macropores based on kinematic wave theory. *J. Hydrol.*, **83**, 173-183.

Gerretsen J.H., 2001. Return periods of floods in the Dutch Meuse at Borgharen. Submitted to J. Water Res. Pl.-ASCE.

Ghosh, B., 1951. Random distances within a rectangle and between two rectangles. *B. Calcutta Math. Soc.*, **43**, 17-24.

Gibson, J.K., Kalberg, P., Uppala, S., Hernandes, A., Nomura, A. and Serrano, E., 1997. *ECMWF Reanalysis report series 1 - ERA description*. ECMWF, Reading, 72 pp.

Giorgi, F., 1995. Perspectives for regional earth system modeling. *Global Planet. Change*, **10**, 23-42.

Giorgi, F. and Francisco, R., 2000. Uncertainties in regional climate change prediction: a regional analysis of ensemble simulations with the HADCM2 coupled AOGCM. *Clim. Dynam.*, **16**, 169-182.

Giorgi, F., Marinucci, M.R. and Visconti, G., 1992. A 2xCO2 climate change scenario over Europe generated using a limited area model nested in a general circulation model: 2. Climate change scenario. *J. Geophys. Res.*, **97**, 10011-10028.

Gleick, P.H., 1986. Methods for evaluating the regional hydrologic impacts of global climatic changes. *J. Hydrol.*, **88**, 97-116.

Gleick, P.H., 1987. Regional hydrologic consequences of increases in atmospheric CO2 and other trace gases. *Climatic Change*, **10**, 137-161.

Goel, N.K., Kurothe, R.S., Mathur, B.S. and Vogel, R.M., 2000. A derived flood frequency distribution for correlated rainfall intensity and duration. *J. Hydrol.*, **228**, 56-67.

Gordon, C., Cooper, C., Senior, C., Banks, H., Gregory, J., Johns, T., Mitchell, J. and Wood, R., 2000. The simulation of SST, sea ice extents and ocean heat transports in a version of the Hadley Centre coupled model without flux adjustments. *Clim. Dynam.*, **16**, 147-168.

Gordon, H.B. and O'Farrell, S.P., 1997. Transient climate change in the CSIRO coupled model with dynamic sea ice. *Mon. Weather Rev.*, **125**, 875-907.

Grabs, W. (Ed.), 1997. *Impact of climate change on hydrological regimes and water resources management in the Rhine basin*. Report CHR no. I-16. Int. Comm. Hydrol. Rhine Basin (CHR), Lelystad, 172 pp.

Green, W.H. and Ampt, G.A., 1911. Studies on soil physics. 1. Flow of air and water through soils. *J. Agr. Sci.*, **4**, 1-24.

Gregory, J.M. and Mitchell, J.F.B., 1995. Simulation of daily variability of surface temperature and precipitation over Europe in the current and 2 x CO2 climates using the UKMO climate model. *Q. J. Roy. Meteor. Soc.*, **121**, 1451-1476.

Grijsen, J.G. and Vreugdenhil, C.B., 1976. *Numerical representation of flood waves in rivers*. Paper presented at the International Symposium on unsteady flow in open channels, Newcastle-upon-Tyne, Publ. No. 165. WL|Delft Hydraulics, Delft, 13 pp.

Gringorten, I.I., 1963. A plotting rule for extreme probability paper. *J. Geophys. Res.*, **68**, 813-814.

Guo, S. and Ying, A., 1997. Uncertainty analysis of impact of climate change on hydrology and water resources. In: D. Rosbjerg (Ed.), *Sustainability of water resources under increasing uncertainty*. Proc. Int. Symp. S1 at Fifth Sci. Assem. IAHS, Rabat, Morocco, 331-338.

Gupta, V.K. and Waymire, E.C., 1993. A statistical analysis of mesoscale rainfall as a random cascade. *J. Appl. Meteorol.*, **32**, 251-267.

Gupta, V.K., Rodriguez-Iturbe, I. and Wood, E.F. (Eds.), 1986. *Scale problems in hydrology: runoff generation and basin response*. Reidel, Dordrecht, 246 pp.

Hall, F.J., 1987. Contributions of Robert E. Horton. In: E.R. Landa and S. Ince (Eds.), *History of geophysics*. Am. Geophys. Union, Washington.

Hamlin, M.J., 1983. The significance of rainfall in the study of hydrological processes at basin scale. *J. Hydrol.*, **65**, 73-94.

Hargreaves, G.L., Hargreaves, G.H. and Riley, J.P., 1985. Agricultural benefits for Senegal river basin. *J. Irrig. Drain. E.-ASCE*, **111**, 113-124.

Harlin, J and Kung, C-S, 1992. Parameter uncertainty and simulation of design floods in Sweden. *J. Hydrol.*, **137**, 209-230.

Hartmann, D.L., 1994. *Global physical climatology*. Academic Press, San Diego, 411 pp.

Henderson-Sellers, A., 1993. An antipodean climate of uncertainty. *Climatic Change*, **25**, 203-224.

Hirst, A.C., Gordon, H.B. and O'Farrell, S.P., 1997. Response of a coupled ocean-atmosphere model including oceanic eddy-induced advection to anthropogenic CO2 increase. *Geophys. Res. Lett.*, **23**, 3361-3364.

Holtan, H.N., 1961. *A concept for infiltration estimates in watershed engineering*. USDA Bull. USDA, 41-51.

Hoosbeek, M.R., 1998. Incorporating scale into spatio-temporal variability: applications to soil quality and yield data. *Geoderma*, **85**, 113-131.

Horton, R.E., 1940. An approach toward a physical interpretation of infiltration-capacity. *Soil Sci. Soc. Am. J.*, **5**, 399-417.

Hulme, M. and Carter, T.R., 1999. Representing uncertainty in climate change scenarios and impact studies. In: T.R. Carter, M. Hulme and D. Viner (Eds.), *Representing uncertainty in climate change scenarios and impact studies*. Proc. ECLAT-2 Helsinki Workshop, Helsinki, Finland, 11-37.

IPCC, 1996. *Climate change 1995. The science of climate change.* Contribution of Working Group I to the Second Assessment Report of the Intergovernmental Panel on Climate Change [J.T Houghton, L.G. Meiro Filho, B.A. Callander, N. Harris, A. Kattenberg and K. Maskell (Eds.)]. Cambridge Univ. Press, Cambridge, 572 pp.

IPCC, 2001. *Climate change 2001: The scientific basis*. Contribution of Working Group I to the Third Assessment Report of the Intergovernmental Panel on Climate Change [J.T. Houghton, Y. Ding, D.J. Griggs, M. Noguer, P.J. van der Linden, X. Dai, K. Maskell and C.A. Johnson (Eds.)]. Cambridge Univ. Press, Cambridge, 881 pp.

Jacobs, P., Blom, G. and Linden, G. van der, 2000. Climatological changes in storm surges and river discharges: The impact on flood protection and salt intrusion in the Rhine-Meuse delta. In: J. Beersma, M. Agnew, D. Viner and M. Hulme (Eds.), *Climate scenarios for water-related and coastal impacts.* Proc. ECLAT-2 Workshop Report No.3 KNMI, De Bilt, the Netherlands, 35-48.

Jakeman, A.J. and Hornberger, G.M., 1993. How much complexity is warranted in a rainfall-runoff model? *Water Resour. Res.*, **29**, 2637-2649.

Jimoh, O.D. and Webster, P., 1996. The optimum order of a Markov chain model for daily rainfall in Nigeria. *J. Hydrol.*, **185**, 45-69.

Johns, T.C., Carnell, R.E., Crossley, J.F. and Gregory, J.M., 1997. The second Hadley Centre coupled ocean-atmosphere GCM: model description, spinup and validation. *Clim. Dynam.*, **13**, 103-134.

Jones, R.G., Murphy, J.M. and Noguer, M., 1995. Simulation of climate change over Europe using a nested regional-climate model. I: Assessment of control climate, including sensitivity to location of lateral boundaries. *Q. J. Roy. Meteor. Soc.*, **121**, 1413-1449.

Jones, R.G., Murphy, J.M., Noguer, M. and Keen, A.B., 1997. Simulation of climate change over Europe using a nested regional climate model. Part II: Comparison of driving and regional model responses to a doubling of carbon dioxide concentration. *Q. J. Roy. Meteor. Soc.*, **123**, 265-292.

Jones, R.N., 2000. Managing uncertainty in climate change projections - Issues for impact assessment. An editorial comment. *Climatic Change*, **45**, 403-419.

Jothityangkoon, C., Sivapalan, M. and Viney, N.R., 2000. Tests of a space-time model of daily rainfall in southwestern Australia based on nonhomogeneous random cascades. *Water Resour. Res.*, **36**, 267-284.

Kacholia, K. and Reck, R.A., 1997. Comparison of global climate change simulations for 2 x CO2-induced warming. An intercomparison of 108 temperature change projections published between 1980 and 1995. *Climatic Change*, **35**, 53-69.

Kahane, J.P. and Peyriere, J., 1976. Sur certains martingales de Benoit Mandelbrot. *Adv. Math.*, **22**, 131-145.

Kalnay, E., Kanamitsu, M., Kistler, R., Collins, W., Deaven, D., Gandin, L., Iredell, M., Saha, S., White, G., Woollen, J., Zhu, Y., Chelliah, M., Ebisuzaki, W., Higgins, W., Janowiak, J., Mo, K.C., Ropelewski, C., Wang, J., Leetmaa, A., Reynolds, R., Jenne, R. and Joseph, D., 1996. The NCEP/NCAR 40-year reanalysis project. *B. Am. Meteorol. Soc.*, **77**, 437-471.

Katz, R.W., 1999. Techniques for estimating uncertainty in climate change scenarios and impact studies. In: T.R. Carter, M. Hulme and D. Viner (Eds.), *Representing uncertainty in climate change scenarios and impact studies.* Proc. ECLAT-2 Helsinki Workshop, Helsinki, Finland, 38-53.

Katz, R.W. and Brown, B.G., 1994. Sensitivity of extreme events to climate change: The case of autocorrelated time series. *Environmetrics*, **5**, 451-462.

Kavvas, M.L., Saquib, M.N. and Puri, P.S., 1987. On a stochastic description of the time-space behavior of extratropical cyclonic precipitation fields. *Stoch. Hydrol. Hydraul.*, **1**, 37-52.

Kent, K.M., 1972. Chapter 15. Travel time, time of concentration and lag. In: *SCS National Engineering Handbook, section 4: hydrology*. USDA, Washington, , 16 pp.

Kharin, V.V. and Zwiers, F.W., 2000. Changes in the extremes in an ensemble of transient climate simulations with a coupled atmosphere-ocean GCM. *J. Climate*, **13**, 3760-3788.

Kidson, J.W. and Thompson, C.S., 1998. A comparison of statistical and model-based downscaling techniques for estimating local climate variations. *J. Climate*, **11**, 735-753.

Killingtveit, A. and Sælthun, N.R., 1995. *Hydropower development: hydrology*. Norwegian Inst. Technol., Oslo.

King, D., Daroussin, J. and Tavernier, R., 1994. Development of a soil geographical database from the soil map of the European Communities. *Catena*, **21**, 37-56.

Kirby, W., 1972. Computer-oriented Wilson-Hilferty transformation that preserves the first three moments and the lower bound of the Pearson type 3 distribution. *Water Resour. Res.*, **8**, 1251-1254.

Kitanidis, P.K., 1997. *Introduction to geostatistics: Applications in hydrogeology*. Cambridge Univ. Press, Cambridge, 271 pp.

Kite, G.W. and Kouwen, N., 1992. Watershed modeling using land classifications. *Water Resour. Res.*, **28**, 3193-3200.

Kite, G.W. and Haberlandt, U., 1999. Atmospheric model data for macroscale hydrology. *J. Hydrol.*, **271**, 303-313.

Kite, G.W. and Droogers, P., 2000. Comparing evapotranspiration estimates from satellites, hydrological models and field data. *J. Hydrol.*, **229**, 3-18.

Kittel, T.G.F., Giorgi, F. and Meehl, G.A., 1998. Intercomparison of regional biases and doubled CO2-sensitivity of coupled atmosphere-ocean general circulation model experiments. *Clim. Dynam.*, **14**, 1-15.

Klemes, V., 1983. Conceptualisation and scale in hydrology. *J. Hydrol.*, **65**, 1-24.

Knox, J.C., 1993. Large increases in flood magnitude in response to modest changes in climate. *Nature*, **361**, 430-432.

Knox, J.C. and Kundzewicz, Z.W., 1997. Extreme hydrological events, palaeo-information and climate change. *Hydrolog. Sci. J.*, **42**, 765-779.

Kok, K. and Veldkamp, A., 2001. Evaluating impact of spatial scales on land use pattern analysis in Central America. *Agr. Ecosyst. Environ.*, **85**, 205-221.

Kok, K., Farrow, A., Veldkamp, A. and Verburg, P.H., 2001. A method and application of multi-scale validation in spatial land use models. *Agr. Ecosyst. Environ.*, **85**, 223-238.

Kostiakov, A.N., 1932. On the dynamics of the coefficient of water-percolation in soils and on the necessity for studying it from a dynamic point of view for purposes of amelioration. In: Trans. 6th Comm. Intern. Soil Sci. Soc. Russian, part A, 17-21.

Koutsoyiannis, D., Kozonis, D. and Manetas, A., 1998. A mathematical framework for studying rainfall intensity-duration-frequency relationships. *J. Hydrol.*, **206**, 118-135.

Krajewski, F.W., Lakshmi, V., Georgakos, K.P. and Subhash, C.J., 1991. A Monte Carlo study of rainfall sampling effect on a distributed catchment model. *Water Resour. Res*., **27**, 119-128.

Krysanova, V., Bronstert, A. and Müller-Wohlfeil, D.-I., 1999. Modelling river discharge for large drainage basins: from lumped to distributed approach. *Hydrolog. Sci. J.*, **44**, 313-331.

Kundzewicz, Z.W., Szamalek, K. and Kowalczak, P., 1999. The great flood of 1997 in Poland. *Hydrolog. Sci. J.*, **44**, 855-870.

Kurothe, R.S., Goel, N.K. and Mathur, B.S., 1997. Derived flood frequency distribution for negatively correlated rainfall intensity and duration. *Water Resour. Res.*, **33**, 2103-2107.

Kwadijk, J.C.J., 1993. *The impact of climate change on the discharge of the river Rhine*. Ph.D.-thesis. Univ. Utrecht, Utrecht, 201 pp.

Lamb, R., 1999. Calibration of a conceptual rainfall-runoff model for flood frequency estimation by continuous simulation. *Water Resour. Res.*, **35**, 3103-3114.

Lamb, R., Beven, K. and Myraboe, S., 1999. Use of spatially distributed water table observations to constrain uncertainty in a rainfall-runoff model. *Adv. Water Resour.*, **22**, 305-318.

Leavesley, G.H., 1994. Modeling the effects of climate change on water resources - A review. *Climatic Change*, **28**, 159-177.

Leavesley, G.H., Lichty, R.W., Troutman, B.M. and Saindon, L.G., 1983. *Precipitation-runoff modeling system*. User manual. USGS water resources investigations report 83-4238. USGS, Denver.

Legates, D.R. and McCabe Jr., G.J., 1999. Evaluating the use of "goodness-of-fit" measures in hydrologic and hydroclimatic model validation. *Water Resour. Res.*, **35**, 233-241.

Lei, J. and Schilling, W., 1994. Parameter uncertainty propagation analysis for urban rainfall runoff modelling. *Water Sci. Technol.*, **29**, 145-154.

Lei, J.H. and Schilling, W., 1996. Preliminary uncertainty analysis - A prerequisite for assessing the predictive uncertainty of hydrologic models. *Water Sci. Technol.*, **33**, 79-90.

Lindström, G., Johansson, B., Persson, M., Gardelin, M. and Bergström, S., 1997. Development and test of the distributed HBV-96 hydrological model. *J. Hydrol.*, **201**, 272-288.

Loague, K.M. and Freeze, K.A., 1985. A comparison of rainfall-runoff modeling techniques on small upland catchments. *Water Resour. Res.*, **21**, 229-248.

Lopes, V.L., 1996. On the effect of uncertainty in spatial distribution of rainfall on catchment modelling. *Catena*, **28**, 107-119.

Lovejoy, S. and Schertzer, D., 1985. Generalized scale invariance in the atmosphere and fractal models of rain. *Water Resour. Res.*, **21**, 1233-1250.

Lovejoy, S. and Schertzer, D., 1990. Multifractals, universality classes, and satellite and radar measurements of cloud and rain fields. *J. Geophys. Res.*, **95**, 2021-2034.

Machenhauer, B., Windelband, M., Botzet, M., Hesselbjerg Christensen, J., Déqué, M., Jones, R.G., Ruti, P.M. and Visconti, G., 1998. *Validation and analysis of regional present-day climate and climate change simulations over Europe*. Max Planck Institute for Meteorology, Hamburg, 87 pp.

Maidment, D.R. (Ed.), 1993. *Handbook of hydrology*. McGraw-Hill, New York, 1400 pp.

Mandelbrot, B.B., 1974. Intermittent turbulence in self-similar cascades: Divergence of high moments and dimension of the carrier. *J. Fluid. Mech.*, **62**, 331-358.

Marinucci, M.R. and Giorgi, F., 1992. A 2 X CO2 climate change scenario over Europe generated using a limited area model nested in a general circulation model. I: Present day simulation. *J. Geophys. Res.*, **97**, 9989-10009.

Marinucci, M.R., Giorgi, F., Beniston, M., Wild, M., Tschuck, P., Ohmura, A. and Bernasconi, A., 1995. High resolution simulations of January and July climate over the western Alpine region with a nested regional modeling system. *Theor. Appl. Climatol.*, **51**, 119-138.

Matalas, N.C., 1967. Mathematical assessment of synthetic hydrology. *Water Resour. Res.*, **3**, 937-945.

Mauser, W. and Schädlich, S., 1998. Modelling the spatial distribution of evapotranspiration on different scales using remote sensing data. *J. Hydrol.*, **212**, 250-267.

Mbagwu, J.S.C., 1995. Testing the goodness of fit of infiltration models for highly permeable soils under different tropical soil management systems. *Soil Til. Res.*, **34**, 199-205.

McCarthy, G.T., 1938. The unit hydrograph and flood routing. Conf. North Atlantic Div.

McGregor, J.L., Walsh, K.J. and Katzfey, J.J., 1993. Nested modelling for regional climate studies. In: A.J. Jakeman, M.B. Beck and M.J. McAleer (Eds.), *Modelling change in environmental systems.* Wiley, Chichester, 367-386.

Mearns, L.O., Giorgi, F., McDaniel, L. and Shields, C., 1995. Analysis of variability and diurnal range of daily temperature in a nested regional climate model: comparison with observations and doubled CO2 results. *Clim. Dynam.*, **11**, 193-209.

Mearns, L.O., Rosenzweig, C. and Goldberg, R., 1997. Mean and variance change in climate scenarios: methods, agricultural applications, and measures of uncertainty. *Climatic Change*, **35**, 367-396.

Meehl, G.A., 2000. Meeting summary - The Coupled Model Intercomparison Project (CMIP). *B. Am. Meteorol. Soc.*, **81**, 313-318.

Melching, C.S., 1992. An improved first-order reliability approach for assessing uncertainties in hydrologic modeling. *J. Hydrol.*, **132**, 157-177.

Melching, C.S., Yen, B.C. and Wenzel Jr., H.G., 1990. A reliability estimation in modeling watershed runoff with uncertainties. *Water Resour. Res.*, **26**, 2275-2286.

Middelkoop, H. and Parmet, B., 1998. Assessment of the impact of climate change on peak flows in the Netherlands - a matter of scale.. In: R. Lemmelä and N. Helenius (Eds.), *Proc. Sec. Int. Conf. on Climate and Water*, Espoo, Finland, 20-33.

Middelkoop, H., Daamen, K., Gellens, D., Grabs, W., Kwadijk, J.C.J., Lang, H., Parmet, B.W.A.H., Schädler, B. and Schulla, J., 2001. Impact of climate change on hydrological regimes and water resources management in the Rhine basin. *Climatic Change*, **49**, 105-128.

Mimikou, M., Kouvopoulos, Y., Cavadias, G. and Vayianos, N., 1991. Regional hydrological effects of climate change. *J. Hydrol.*, **123**, 119-146.

Minhas, B.S., Parikh, K.W. and Srinavasan, T.N., 1974. Toward the structure of a production function for wheat yields with dated input of irrigated water. *Water Resour. Res.*, **10**, 383-393.

Moody, A. and Woodcock, C.E.., 1995. The influence of scale and the spatial characteristics of landscapes on land-cover mapping using remote sensing. *Landscape Ecol.*, **10**, 363-379.

Moon, S-E., Ryoo, S-B. and Kwon, J-G., 1994. A Markov chain model for daily precipitation occurrence in South Korea. *Int. J. Climatol.*, **14**, 1009-1016.

Morgan, M.G. and Henrion, M., 1990. *Uncertainty. A guide to dealing with uncertainty in quantitative risk and policy analysis*. Cambridge Univ. Press, Cambridge, 344 pp.

Moussa, R. and Bocquillon, C., 1996a. Criteria for the choice of flood-routing methods in natural channels. *J. Hydrol.*, **186**, 1-30.

Moussa, R. and Bocquillon, C., 1996b. Fractal analyses of tree-like channel networks from digital elevation model data. *J. Hydrol.*, **187**, 157-172.

Murphy, J., 1999. An evaluation of statistical and dynamical techniques for downscaling local climate. *J. Climate*, **12**, 2256-2284.

Nandakumar, N. and Mein, R.G., 1997. Uncertainty in rainfall-runoff model simulations and the implications for predicting the hydrological effects of land-use change. *J. Hydrol.*, **192**, 211-232.

Nash, J.E. and Sutcliffe, J.V., 1970. River flow forecasting through conceptual models. Part I - A discussion of principles. *J. Hydrol.*, **10**, 282-290.

Nemec, J. and Schaake, J., 1982. Sensitivity of water resource systems to climate variation. *Hydrolog. Sci. J.*, **27**, 327-343.

Nikora, V.I., 1994. Self-similarity and self-affinity of drainage basins. *Water Resour. Res.*, **30**, 133-137.

NOAA (National Oceanic and Atmospheric Administration), 1999. *Global daily WMO weather station data*.

Obled, Ch., Wendling, J. and Beven, K., 1994. The sensitivity of hydrological models to spatial rainfall patterns: an evaluation using observed data. *J. Hydrol*., **159**, 305-333.

Oppenheimer, M., 1998. Global warming and the stability of the West Antartic Ice Sheet. *Nature*, **393**, 325-332.

Osborn, T.J., 1997. Areal and point precipitation intensity changes: Implications for the application of climate models. *Geophys. Res. Lett.*, **24**, 2829-2832.

Osborn, T.J. and Hulme, M., 1997. Development of a relationship between station and grid-box rainday frequencies for climate model evaluation. *J. Climate*, **10**, 1885-1908.

Osborn, T.J. and Hulme, M., 1998. Evaluation of the European daily precipitation characteristics from the atmospheric intercomparison project. *Int. J. Climatol.*, **18**, 505-522.

Over, T.M. and Gupta, V.K., 1994. Statistical analysis of mesoscale rainfall: Dependence of a random cascade generator on large-scale forcing. *J. Appl. Meteorol.*, **33**, 1526-1542.

Over, T.M. and Gupta, V.K., 1996. A space-time theory of mesoscale rainfall using random cascades. *J. Geophys. Res.*, **101**, 26319-26331.

Passchier, R.H., 1996. *Evaluation hydrologic model packages*. Q 2044. WL|Delft Hydraulics, Delft.

Patwardhan, A. and Small, M.J., 1992. Bayesian methods for model uncertainty analysis with application to future sea level rise. *Risk Analysis*, **12**, 513-523.

Philip, J.R., 1957. The theory of infiltration. 1. The infiltration equation and its solution. *Soil Sci.*, **83**, 345-357.

Priestley, C.H.B. and Taylor, R.J., 1972. On the assessment of surface heat flux and evaporation using large scale parameters. *Mon. Weather Rev.*, **100**, 81-92.

Räisänen, J., 1997. Objective comparison of patterns of CO2 induced climate change in coupled GCM experiments. *Clim. Dynam.*, **13**, 197-211.

Refsgaard, J.C., 1996. Terminology, modelling protocol and classification of hydrological models. In: M.B. Abbott and J.C. Refsgaard (Eds.), *Distributed hydrological modelling*. Water Sci. Technol. Libr., **22**, 17-39.

Renssen, H., Lautenschlager, M. and Schuurmans, C.J.E., 1996. The atmospheric winter circulation during the Younger Dryas stadial in the Atlantic/European sector. *Clim. Dynam.*, **12**, 813-824.

Richards, L.A., 1931. Capillary conduction of liquids in porous mediums. *Physics*, **1**, 318-333.

Rijkswaterstaat, 1998. *Daily Borgharen discharge data*.

RIZA, 2000. *Topographic data for the Meuse basin*. RIZA, Arnhem.

Rodriguez-Iturbe, I. and Mejia, J.M., 1974. On the transformation from point rainfall to areal rainfall. *Water Resour. Res.*, **10**, 729-735.

Rotach, M.W., Marinucci, M.R., Wild, M., Tschuck, P., Ohmura, A. and Beniston, M., 1997. Nested regional simulation of climate change over the Alps for the scenario of a doubled greenhouse forcing. *Theor. Appl. Climatol.*, **57**, 209-227.

Saint-Venant, B., 1871. Théorie du mouvement non permanent des eaux, avec application aux crues des rivières et à l'introduction des marées dans leurs lits. *C.R. Séan Acad. Sci.*, **73**, 147-154, 237-240.

Schubert, S.D., Rood, R.B. and Pfaendtner, J., 1993. An assimilated data set for earth science applications. *B. Am. Meteorol. Soc.*, **74**, 2331-2342.

Seibert, J., 1997. Estimation of parameter uncertainty in HBV model. *Nord. Hydrol.*, **28**, 247-262.

Seibert, J., 1999. Regionalisation of parameters for a conceptual rainfall-runoff model. *Agr. Forest Meteorol.*, **98**, 279-293.

Shackley, S., Young, P., Parkinson, S. and Wynne, B., 1998. Uncertainty, complexity and concepts of good science in climate change modelling: are GCMs the best tools? *Climatic Change*, **38**, 159-205.

Shah, S.M.S., O'Connell, P.E. and Hosking, J.R.M., 1996a. Modelling the effects of spatial variability in rainfall on catchment response. 2. Experiments with distributed and lumped models. *J. Hydrol.*, **175**, 89-111.

Shah, S.M.S., O'Connell, P.E. and Hosking, J.R.M., 1996b. Modelling the effects of spatial variability in rainfall on catchment response. 1. Formulation and calibration of a stochastic rainfall field model. *J. Hydrol.*, **175**, 67-88.

Shaw, E.M., 1994. *Hydrology in practice*. Chapman & Hall, London, 569 pp.

Sherman, L.K., 1932. Streamflow from rainfall by the unit-hydrograph method. *Eng. News. Rec.*, **108**, 501-505.

Sivapalan, M. and Blöschl, G., 1998. Transformation of point rainfall to areal rainfall: Intensity-duration-frequency curves. *J. Hydrol.*, **204**, 150-167.

Sivapalan, M., Beven, K.J. and Wood, E.F., 1990. On hydrologic similarity: 3. A dimensionless flood frequency model using a generalised geomorphologic unit hydrograph and partial area runoff generation. *Water Resour. Res.*, **26**, 43-58.

SMHI, 1999. *Integrated Hydrological Modelling System (IHMS)*. Manual version 4.3. SMHI, Norrköping.

Smith, J., 1996. Models and scale: up- and downscaling. In: A. Stein, F.W.T. Penning de Vries and P.J. Schotma (Eds.), *Models in action.* Proc. of a seminar series 1995-1996, Wageningen, 25-41.

Stol, Ph.Th., 1972. The relative efficiency of the density of rain-gage networks. *J. Hydrol.*, **15**, 193-208.

TAW, 2000. From exceedance probability to flood risk (in Dutch). TAW, Delft.

Todini, E., 1991. Hydraulic and hydrologic flood routing schemes. In: D.S. Bowles and P.E. O'Connell (Eds.), *Recent advances in the modeling of hydrologic systems.* Proc. NATO Adv. Stud. Inst., Sintra, Portugal, 389-405.

Tol, R.S.J. and Vos, A.F. de, 1998. A Bayesian statistical analysis of the enhanced greenhouse effect. *Climatic Change*, **38**, 87-112.

Turc, L., 1961. Evaluation des besoins en eau d'irrigation, evapotranspiration potentielle, formule climatique simplifice et mise a jour. *Ann. Agron.*, **12**, 13-49.

Uhlenbrook, S., Seibert, J., Leibundgut, C. and Rodhe, A., 1999. Prediction uncertainty of conceptual rainfall-runoff models caused by problems in identifying model parameters and structure. *Hydrolog. Sci. J.*, **44**, 779-797.

U.S. Geological Survey, 1993. *Digital elevation models*. Data user guide 5. U.S. Geological Survey, Reston, 50 pp.

U.S. Geological Survey, 1995. *Digital elevation model data from 7.5-minute quadrangle maps.* U.S. Geological Survey, Sioux Falls.

U.S. Geological Survey, 1996. *Global 30-arc second elevation data set.* U.S. Geological Survey, Sioux Falls.

Van der Wal, K.U., 2001. *Meuse model moulding. On the effect of spatial resolution*. MSc.-thesis. University of Twente, Enschede, 70 pp.

Van Genuchten, M.Th., 1980. A closed-form equation for predicting the hydraulic conductivity of unsaturated soils. *Soil Sci. Soc. Am. J.*, **44**, 892-898.

Veihe, A. and Quinton, J., 2000. Sensitivity analysis of EUROSEM using Monte Carlo simulation I: hydrological, soil and vegetation parameters. *Hydrol. Process.*, **14**, 915-926.

Velner, R.G.J., 2000. *Rainfall-runoff modelling of the Ourthe catchment with the HBV model. A study for extension of the lead time for flood forecasting in the Meuse (in Dutch)*. RIZA working document 2000.091X. Wageningen University, Wageningen, 116 pp.

Visser, H., Folkert, R.J.M., Hoekstra, J. and Wolff, J.J. de, 2000. Identifying key sources of uncertainty in climate change projections. *Climatic Change*, **45**, 421-457.

Vogel, R.M., Bell, C.J. and Fennessey, N.M., 1997. Climate, streamflow and water supply in the northeastern United States. *J. Hydrol.*, **198**, 42-68.

Vogel, R.W. and McMartin, D.E., 1991. Probability plot goodness-of-fit and skewness estimation procedures for the Pearson Type 3 distribution. *Water Resour. Res.*, **27**, 3149-3158.

Vogel, R.W. and McMartin, D.E., 1992. Correction to "Probability plot goodness-of-fit and skewness estimation procedures for the Pearson Type 3 distribution" by Richard M. Vogel and Daniel E. McMartin. *Water Resour. Res.*, **28**, 1757.

Vreugdenhil, C.B., 1989. *Computational hydraulics*. Springer-Verlag, Berlin, 180 pp.

Vreugdenhil, C.B. and Wijbenga, J.H.A., 1982. Computation of flow patterns in rivers. *J. Hydraul. Eng.-ASCE*, **108**, 1296-1310.

Walsh, S.J., Crawford, T.W., Welsh, W.F. and Crews-Meyer, K.A., 2001. A multiscale analysis of LULC and NDVI variation in Nang Rong district, northeast Thailand. *Agr. Ecosyst. Environ.*, **85**, 47-64.

Warrick, R.A., Barrow, E.M. and Wigley, T.M.L. (Eds.), 1993. *Climate and sea level change: observations, projections and implications.* Cambridge Univ. Press, Cambridge, 424 pp.

Waymire, E., Gupta, V.K. and Rodriguez-Iturbe, I., 1984. A spectral theory of rainfall at the meso-β scale. *Water Resour. Res.*, **20**, 1453-1465.

Weglarczyk, S., 1998. The interdependence and applicability of some statistical quality measures for hydrological models. *J. Hydrol.*, **206**, 98-103.

Weijers, E.P. and Vellinga, P., 1995. *Climate change and river flooding: Changes in rainfall processes and flooding regimes due to an enhanced greenhouse effect*. Tech. Rep. R-95/01. Amsterdam Free University, Amsterdam, 42 pp.

Western, A.W. and Blöschl, G., 1999. On the spatial scaling of soil moisture. *J. Hydrol.*, **217**, 203-224.

Western, A.W., Blöschl, G. and Grayson, R.B., 1998. Geostatistical characterisation of soil moisture patterns in the Tarrawarra catchment. *J. Hydrol.*, **205**, 20-37.

Whetton, P.H., Fowler, A.M., Haylock, M.R. and Pittock, A.B., 1993. Implications of climate change due to the enhanced greenhouse effect on floods and droughts in Australia. *Climatic Change*, **25**, 289-317.

Wilby, R.L. and Wigley, T.M.L., 1997. Downscaling general circulation model output: a review of methods and limitations. *Prog. Phys. Geog.*, **21**, 530-548.

Wilby, R.L. and Wigley, T.M.L., 2000. Precipitation predictors for downscaling: observed and general circulation model relationships. *Int. J. Climatol.*, **20**, 641-661.

Wilby, R., Greenfield, B. and Glenny, C., 1994. A coupled synoptic-hydrological model for climate change impact assessment. *J. Hydrol.*, **153**, 265-290.

Wilks, D.S., 1998. Multisite generalization of a daily stochastic precipitation generation model. *J. Hydrol.*, **210**, 178-191.

Willmott, C.J., 1981. On the validation of models. *Phys. Geog.*, **2**, 184-194.

Wilson, C.B., Valdes, J.B. and Rodriguez-Iturbe, I., 1979. On the influence of the spatial distribution of rainfall on storm runoff. *Water Resour. Res.*, **15**, 321-328.

Wind, H.G., Nierop, T.M., Blois, C.J. de and Kok, J-L. de, 1999. Analysis of flood damages from the 1993 and 1995 Meuse floods. *Water Resour. Res.*, **35**, 3459-3465.

Wit, M. de, Warmerdam, P., Torfs, P., Uijlenhoet, R., Roulin, E., Cheymol, A., Deursen, W. van, Walsum, P. van, Kwadijk, J., Ververs, M. and Buiteveld, H., 2001. *Effect of climate change on the hydrology of the river Meuse.* Draft NRP Report. Dutch National Research Programme on Global Air Pollution and Climate Change, Bilthoven, 92 pp.

Wojcik, R., Beersma, J.J. and Buishand, T.A., 2000. *Rainfall generator for the Rhine basin. Multi-site generation of weather variables for the entire drainage area.* KNMI-publication: 186-IV. KNMI, De Bilt, 38 pp.

Wolock, D.M. and McCabe, G.J., 2000. Differences in topographic characteristics computed from 100- and 1000-m resolution digital elevation model data. *Hydrol. Process.*, **14**, 987-1002.

Wood, E.F., Sivapalan, M., Beven, K. and Band, L., 1988. Effects of spatial variability and scale with implications to hydrologic modeling. *J. Hydrol.*, **102**, 29-47.

Yang, D., Herath, S. and Musiake, K., 2000. Comparison of different distributed hydrological models for characterization of catchment spatial variability. *Hydrol. Process.*, **14**, 403-416.

Ye, W., Bates, B.C., Viney, N.R., Sivapalan, M. and Jakeman, A.J., 1997. Performance of conceptual rainfall-runoff models in low-yielding ephemeral catchments. *Water Resour. Res.*, **33**, 153-166.

Yevjevich, V., 1972. *Probability and statistics in hydrology*. Water Resour. Publ., Fort Collins, 302 pp.

Zapert, R., Gaertner, P.S. and Filar, J.A., 1998. Uncertainty propagation within an integrated model of climate change. *Energ. Econ.*, **20**, 566-593.

Zong, Y. and Chen, X., 2000. The 1998 flood on the Yangtze, China. *Nat. Hazards*, **22**, 165-184.

Zwiers, F.W. and Kharin, V.V., 1998. Changes in the extremes of the climate simulated by CCC GCM2 under CO2 doubling. *J. Climate*, **11**, 2200-2222.

Symbols

a	side of square $\mathbf{\Lambda}$	[L]
a_1	parameter of rainfall correlation function representing nugget effect	[1]
a_m	empirical constant for macropore flow	$[LT^{-1}]$
a_t	uniform element in diagonal parameter matrix **A** in AR(1) model	[1]
A	surface area	$[L^2]$
A_h	energy advected to the water body in Penman-Monteith equation	$[LT^{-1}]$
b	number of subareas in each level of subdivision in random cascade model	[1]
b_1	parameter of rainfall correlation function describing correlation in x dimension	$[L^{-2}]$
b_2	parameter of rainfall correlation function describing correlation in y dimension	$[L^{-2}]$
b_3	parameter of rainfall correlation function describing correlation in time dimension	$[T^{-2}]$
b_{ij}	elements in parameter matrix **B** in AR(1) model	[1]
b_m	empirical constant for macropore flow	[1]
b_s	parameter determining elements b_{ij} in AR(1) model	[1]
BHETA	parameter in soil moisture routine of HBV model	[1]
c_0	nugget variance contribution	
c_1	spatial variance contribution	
c_2	temporal variance contribution	
C_m	melting factor in HBV model	$[LT^{-1}\theta^{-1}]$
C_r	refreezing factor in HBV model	[1]
CN	SCS curve number	[1]
CV	coefficient of variation	[1]
d	number of dimensions in random cascade model	[1]
d_1	parameter of random phase model	[1]
d_2	parameter of random phase model	$[L^3T^{-1}]$
$\mathrm{d}T$	difference between observed and simulated temperature	[θ]
D_E	vapour pressure deficit in Penman-Monteith equation	[F]
D_r	coefficient for wave attenuation in routing routine in HBV model	[1]
e	2.7183….	[1]
ET_a	actual evapotranspiration in HBV model	$[LT^{-1}]$
ET_p	potential evapotranspiration	$[LT^{-1}]$
f_1	empirical constant for random cascade model parameters	[1]
f_2	empirical constant for random cascade model parameters	[1]
f_3	empirical constant for random cascade model parameters	[1]
f_4	empirical constant for random cascade model parameters	[1]
f_5	empirical constant for random cascade model parameters	[1]

F	surface area of model cell	$[L^2]$
F_0^2	Froude number	[1]
FC	soil water holding capacity in HBV model	[L]
g	semi-variance	
g	acceleration due to gravity	$[LT^{-2}]$
G	uncertainty criterion	
h	lag distance in space	[L]
h	water depth	[L]
h_f	water depth of fast reservoir in HBV model	[L]
h_H	water depth of fast reservoir at high flow rate in HBV model	[L]
h_s	water depth of slow reservoir in HBV model	[L]
H	hydraulic head	[L]
k	lag distance in time	[T]
k	recession coefficient	$[T^{-1}]$
k_f	recession coefficient of fast reservoir in HBV model	$[T^{-1}]$
k_H	recession coefficient at high flow rate in HBV model	$[T^{-1}]$
k_s	recession coefficient of slow reservoir in HBV model	$[T^{-1}]$
K	relative lag constant	[1]
K_G	frequency factor of Gumbel distribution	[1]
K_H	hydraulic conductivity	$[LT^{-1}]$
l	hydraulic length	[L]
L	spatial scale	[L]
L_e	extent scale	
L_r	delay parameter of routing routine in HBV model	[T]
L_s	spatial range in spherical variogram model	[L]
L_{sp}	spacing scale	
L_{sup}	support scale	
LP	fraction between 0 and 1 in soil moisture routine in HBV model	[1]
M	moment	
$MAXBAS$	period over which is filtered in transformation routine in HBV model	[T]
p	water distribution function	[1]
p_e	rainfall excess intensity in SCS method	$[LT^{-1}]$
p_i	unconditional probability for state i	[1]
p_{ij}	conditional probability for state i given state j	[1]
P	precipitation	
P_C	continuous precipitation in random phase model	[1]
P_D	discrete precipitation in random phase model	[1]
P_e	rainfall excess volume in SCS method	[L]
P_{XY}	corrected, discrete precipitation in random phase model	$[L^3T^{-1}]$
PE	effective precipitation	
$PPCC$	probability plot correlation coefficient	[1]
$PPCC^*$	semi probability plot correlation coefficient	[1]
q	specific discharge	$[LT^{-1}]$
q_m	specific macropore discharge	$[LT^{-1}]$
q_p	peak discharge in SCS method	$[L^3T^{-1}]$
Q	discharge	
Q_{avg}	average observed discharge	$[LT^{-1}]$
Q_d	direct discharge over land in HBV model	$[LT^{-1}]$

Q_f	storm flow out of fast reservoir in HBV model	$[LT^{-1}]$
Q_H	high flow rate out of fast reservoir in HBV model	$[LT^{-1}]$
Q_{in}	indirect discharge through the soil layer in HBV model	$[LT^{-1}]$
Q_m	snow melt in HBV model	$[LT^{-1}]$
$Q_{\max}$	maximum discharge during period Ω_d	
Q_p	design discharge	$[L^3T^{-1}]$
Q_p	water from precipitation routine in HBV model	$[LT^{-1}]$
Q_{perc}	threshold for percolation in HBV model	$[LT^{-1}]$
Q_r	refreezing in HBV model	$[LT^{-1}]$
Q_s	subsurface flow out of slow reservoir in HBV model	$[LT^{-1}]$
Q_t	total discharge out of fast and slow reservoir in HBV model	$[LT^{-1}]$
Q_{tu}	upstream total discharge in HBV model	$[LT^{-1}]$
Q_{td}	downstream total discharge in HBV model	$[LT^{-1}]$
r	correlation coefficient	[1]
r^*	semi-correlation coefficient	[1]
rc	runoff coefficient	[1]
R_1	Osborn-Hulme reduction function for wet day frequency	[1]
R_2	Sivapalan-Blöschl reduction function for return values	[1]
R^2	Nash-Sutcliffe efficiency coefficient	[1]
R_n	net radiation exchange for the free water surface in Penman-Monteith equation	$[LT^{-1}]$
RE	relative error	[1]
$REVE$	relative extreme value error	[1]
RV	return value	
RVE	relative volume error	[1]
s	location in one, two or three dimension(s)	
S	number of locations in the space domain Λ_d	
S_0	slope of river bed or land surface	[1]
S_f	slope of energy line	[1]
S_L	spatial component of spherical variogram model	
S_m	sink source term for macropore flow	$[T^{-1}]$
S_s	sink source term for surface flow	$[LT^{-1}]$
S_{sm}	soil moisture depth in HBV model	[L]
S_{sub}	sink source term for subsurface flow	$[T^{-1}]$
S_T	temporal component of spherical variogram model	
SE	standard error	
t	time	[T]
T	number of time steps in the time domain Ω_d	
T_+	wave period in relation to wave damping time	[1]
T_a	air temperature	[θ]
T_b	threshold temperature for snowfall in HBV model	[θ]
T_l	lag from centroid of rainfall excess to peak discharge in SCS method	[T]
T_p	rainfall duration in SCS method	[T]
T_q	time of rise to the peak in SCS method	[T]
T_s	temporal range in spherical variogram model	[T]
u	Osborn-Hulme statistic	[1]
U_2	wind speed measured at 2 m in Penman-Monteith equation	$[LT^{-1}]$
v	flow velocity	$[LT^{-1}]$

v_c	characteristic velocity	[LT^{-1}]
V	capacity	[L^3]
V_p	volume of runoff under the hydrograph in SCS method	[L]
W	random cascade generator	
x	first horizontal dimension	[L]
y	second horizontal dimension	[L]
Y	model output	
Y_m	modelled values of Y	
Y_o	observed values of Y	
z	vertical dimension	[L]
α	measure of non-linearity of fast reservoir in HBV model	[1]
α_1	parameter representing spatial nugget effect	[1]
α_2	parameter representing temporal nugget effect	[1]
α_g	shape parameter of gamma distribution	[1]
α_{gs}	shape parameter of symmetrical gamma distribution in AR(1) model	[1]
β	parameter of beta distribution in random cascade model	[1]
β_1	parameter for Osborn-Hulme function R_1	[1]
β_2	parameter for Osborn-Hulme function R_1	[1]
β_e	scale parameter of exponential distribution	[1]
β_g	scale parameter of gamma distribution	[1]
β_{gs}	scale parameter of symmetrical gamma distribution in AR(1) model	[1]
β_G	scale parameter of Gumbel distribution	[1]
χ	Mandelbrot-Kahane-Peyriere (MKP) function	
Δ	subarea in random cascade model	
Δ_E	gradient of relation between saturated vapour pressure and temperature in Penman-Monteith equation	[Fθ^{-1}]
Δt	temporal resolution	[T]
Δx	spatial resolution	[L]
ϕ	soil porosity	[1]
γ	semi-variance function	
γ_2	kurtosis	
γ_E	psychometric constant dependent on air temperature	[Fθ^{-1}]
η	parameter of Gumbel distribution ≈ 0.5772	[1]
φ	frequency in x dimension	
κ	frequency in y dimension	
κ^2	variance reduction function	[1]
λ	spatial correlation length	[L]
λ_E	latent heat of vaporisation	[EM^{-1}]
λ_n	scale ratio in random cascade model	[1]
μ	average	
π	3.142….	[1]
θ	volumetric soil moisture content	[1]
θ_f	volumetric soil moisture content at field capacity	[1]
θ_m	volumetric macropore water content	[1]

θ_w	volumetric soil moisture content at wilting point	[1]
ρ	correlation function	[1]
σ	standard deviation	
σ^2	parameter of log-normal distribution in random cascade model	[1]
τ	temporal correlation length	[T]
τ	slope of log-log relationship between M and λ_n	
ω	frequency in time dimension	
ω_0	wave period	[T]
ξ_{gs}	location parameter of symmetrical gamma distribution in AR(1) model	[1]
ξ_G	location parameter of Gumbel distribution	[1]
υ	fitted function to Osborn-Hulme statistic as a function of lag; $u(h)$	[1]
υ_1	parameter for function υ	[1]
υ_2	parameter for function υ	[L]
$\overline{\upsilon}$	average Osborn-Hulme statistic	[1]
Ω	aggregation time period	[T]
Ω_d	time domain	[T]
ψ	pressure head for saturated flow/ tension head for unsaturated flow	[L]
ζ	random variable uniformly distributed in interval $\{0,2\pi\}$	[1]
$\mathbf{A}$	diagonal parameter matrix with uniform elements a in AR(1) model	
$\mathbf{B}$	parameter matrix with elements b_{ij} in AR(1) model	
$\mathbf{P}$	vector of spatially correlated precipitation	
$\mathbf{X}$	vector of model inputs, parameters and/ or processes	
$\mathbf{X_0}$	expected values of $\mathbf{X}$	
$\mathbf{X_m}$	modelled values of $\mathbf{X}$	
$\mathbf{X_o}$	observed values of $\mathbf{X}$	
$\mathbf{Z}$	vector of a spatially correlated variable	
$\boldsymbol{\varepsilon}$	vector of uncorrelated random numbers	[1]
$\boldsymbol{\Lambda}$	aggregation area	
$\boldsymbol{\Lambda}_d$	2-dimensional space domain	[L^2]

Acronyms and abbreviations

1XCO2	current 'equivalent' carbon dioxide concentration
2XCO2	twice the current 'equivalent' carbon dioxide concentration
AGCM	Atmospheric General Circulation Model
AMIP	Atmospheric Model Intercomparison Project
AOGCM	Atmospheric-Oceanic General Circulation Model
APIC	Antecedent Precipitation Index model (USA)
AR(1)	AutoRegressive lag-1
ARMA	AutoRegressive Moving Average
ARNO	Arno river model (Italy)
AVHRR	Advanced Very High Resolution Radiometer
BRMC	Bureau of Meteorology Research Centre (Australia)
CCC(ma)	Canadian Centre for Climate (modelling and analysis) (Canada)
CDF	Cumulative Distribution Function
CGCM	Canadian Global Coupled Model (Canada)
CMIP	Coupled Model Intercomparison Project
CO_2	carbon dioxide
CORINE	COoRdination of INformation on the Environment system (EU)
CSIRO	Commonwealth Scientific and Industrial Research Organisation (Australia)
DEM	Digital Elevation Model
DTED	Digital Terrain Elevation Data
ECHAM	ECMWF HAMburg AGCM (Germany)
ECMWF	European Center for Medium-Range Weather Forecasting
EDC DAAC	EROS Data Center Distributed Active Archive Center (USA)
EEA	European Environmental Agency (EU)
EROS	Earth Resources Observation Systems (USA)
FAO	Food and Agriculture Organisation (UN)
GCM	General Circulation Model or Global Climate Model
GEV	Generalised Extreme Value distribution
GIS	Geographic Information System
GSFB	Generalised Surface inFiltration Baseflow model (Australia)
GTOPO30	Global 30 arc-second DEM
HadAM	Hadley Centre Atmospheric Model (United Kingdom)
HadCM	Hadley Centre Coupled Model (United Kingdom)
HadRM	Hadley Centre Regional Model (United Kingdom)
HBV	Hydrologiska Byråns Vattenbalansavdelning model (Sweden)
HEC	Hydrologic Engineering Center (USA)
HIRHAM	HIRLAM-ECHAM
HIRLAM	HIgh Resolution Limited Area Model
HRU	Hydrological Response Unit

IDF	Intensity-Duration-Frequency
IHACRES	Identification of Hydrographs And Components from Rainfall, Evaporation and Streamflow data model (Australia)
IHDM	Institute of Hydrology Distributed Model (United Kingdom)
IPCC	Intergovernmental Panel on Climate Change
IRMB	Integrated Runoff Model-F. Bultot (Belgium)
KMI	Royal Meteorological Institute (Belgium)
LANDSAT	LAND SATellite
LASCAM	LArge Scale Catchment Model (Australia)
MAT1	dominant parent MATerial
MC	Monte Carlo
METEO F	Meteo France (France)
MKP	Mandelbrot-Kahane-Peyriere
OPYC	Ocean isoPYCnal model
NAPP	National Aerial Photography Program (USA)
NASA-GEOS	National Aeronautics and Space Administration-Goddard Earth Observation System (USA)
NATLAN	NATure LANd cover package
NCAR-CCM	National Center for Atmospheric Research-Community Climate Model (USA)
NCAR/PSU MM	National Center for Atmospheric Research/ Pennsylvania State University Mesoscale Model (USA)
NCEP-NCAR	National Centers for Environmental Prediction-National Center for Atmospheric Research (USA)
NOAA	National Oceanic and Atmospheric Administration (USA)
PDF	Probability Density Function
PRMS	Precipitation Runoff Modelling System (USA)
RCM	Regional Climate Model
REA	Representative Elementary Area
RegCM	Regional Climate Model (USA)
REV	Representative Elementary Volume
SA	Sensitivity Analysis
SACRAMENTO	Sacramento model (USA)
SCS	Soil Conservation Service (USA)
SHARE	Spatially Horizontally Averaged Richards Equation
SHE	Système Hydrologique Europeèn
SLURP	Simple LUmped Reservoir Parametric model (Canada)
SMHI	Swedish Meteorological and Hydrological Institute (Sweden)
SPOT	Système Probatoire d'Observation de la Terre (France)
SSARR	Streamflow Synthesis And Reservoir Regulation model (USA)
STANFORD	Stanford watershed model (USA)
SWAP	Soil Water Atmosphere Plant model (Netherlands)
SWMM	Storm Water Management Model (USA)
TEXT1	dominant surface TEXTural Class
TANK	Tank model (Japan)
TOPMODEL	TOPograhic MODEL (United Kingdom)
US7.5MIN	United States 7.5 minute DEM (USA)
USGS	United States Geological Survey (USA)
XINANJIANG	Xinanjiang model (China)

Summary

Global climate change is likely to increase temperatures, change precipitation patterns and probably raise the frequency of extreme events. Impacts of climate change on river flooding may be considerable and may cause enormous economical, social and environmental damage and even loss of lives. This necessitates the application of robust and accurate flood estimation procedures to provide a strong basis for investments in flood protection measures with climate change.

A broad palette of models is available to fulfil this requirement. More complex models generally have larger data requirements and computational costs, but may result in smaller model output uncertainties and associated costs. It would seem that an optimum complexity associated with minimum total costs or uncertainty exists. This raises the question what such an appropriate model should look like given the specific modelling objective and research area. Or which physical processes and data should be incorporated and which mathematical process formulations should be used at which spatial and temporal scale, to obtain an appropriate model level?

Therefore, the main objectives of this study are the determination of the appropriate model complexity dependent on modelling objective and research area and the assessment of the climate change impact on river flooding with an appropriate model. The Meuse basin in Belgium and France serves as an application area in this thesis. The first objective is dealt with in chapter 2, 3, 4 and 5 and constitutes the main part of this thesis. The second objective is mainly treated in chapter 4 and 6.

First, in **chapter 2** a preliminary model appropriateness procedure has been set up. This procedure was found to be inadequate, because of the simplified assumptions done and the necessity of selecting a model before the start of the procedure. Therefore, a more general model appropriateness framework was introduced comprising the determination of the dominant processes and variables, the appropriate scales and the associated appropriate process formulations. In this way, the characteristics of an appropriate model are determined beforehand and can be implemented in an existing or new model. Thus, an internally consistent model is obtained, although it depends on the criteria for the appropriateness of scales, the formulations used and the data availability whether the complete model is appropriate for the research objective. This can be revealed by comparing the output uncertainty of the appropriate model with a specific uncertainty criterion. The appropriateness framework is thus mainly based on a consistency criterion with an additional uncertainty criterion.

As part of the appropriateness framework, a methodology was described to assess the appropriate scale for a particular variable. This appropriate scale is assumed to be equal to a fraction of the correlation length of that variable. The fraction is determined on the

basis of relationships between statistics and scale accepting an error of 10 % in the estimation of the statistic. This results in fractions of the correlation length between 0.20 and 0.25 for different statistics such as the standard deviation and the return value. The integration of these appropriate variable scales to an appropriate model scale is done by multiplying the appropriate variable scales with associated weights. The weights are based on SCS curve number method relationships between the peak discharge and some specific parameters. The values of these parameters are dependent on the scale of each variable and in this way, relations between the peak discharge and the variable scale are developed. Finally, the weights are determined and multiplied with the appropriate variable scale to obtain the appropriate model scale.

In **chapter 3**, the issue of appropriate scales is further explored by considering the effect of different spatial and temporal rainfall input and a river basin model scales on extreme river discharges. This was done by employing a stochastic rainfall model and a dimensionless river basin model with varying scales. The main conclusion was that the effect of the model scale (resolution) on extreme river discharge is of major importance as compared with the effect of the input scale for the examined river basin and model. The highest model resolution (5-10 grid points/ spatial correlation length; 7-10 time steps/ temporal correlation length) seems to be appropriate in determining the extreme discharge for large river basins with a similar rainfall regime and runoff concentration pattern as used here. Furthermore, a relatively low spatial and temporal rainfall resolution (1-2 grid points/ spatial correlation length; at most 1 time step/ temporal correlation length) was sufficient to represent the rainfall input of a model for these large basins. These conclusions will not be significantly affected when using other parameter values in the river basin model as shown by the sensitivity analysis.

In **chapter 4**, climate data from stations, re-analyses, global climate models (GCMs) and regional climate models (RCMs) for Western Europe were analysed and compared. The differences between climate models can be considerable, in particular with respect to extreme values and correlation lengths. The RCMs and the Australian GCM simulate extreme precipitation behaviour under current climate conditions very well, while the re-analyses underestimate and the British and Canadian GCMs overestimate extreme precipitation. Average precipitation values do not show significant changes with climate change (a doubling of carbon dioxide), while standard deviations increase by about 10 %. Extreme precipitation may increase with climate change by about 15-20 % and correlation lengths by about 30-40 %. Model errors and inter-model differences in the estimation of extreme precipitation with climate change can amount up to 50 %. This is significantly larger than the simulated change. The temperature behaviour under current climate conditions is well simulated by the RCMs and the British GCM, but rather poorly by the Canadian and Australian GCM. The average predicted temperature increase with climate change is 3.7 °C (2.9-4.7 °C). The estimated uncertainty herein is about 2-3 °C, which is comparable with the simulated change. The application of the reduction methodology from chapter 2 resulted in an appropriate scale for extreme precipitation of 20 km with a temporal scale of 1 day.

Chapter 5 deals with the dominant processes and variables, appropriate scales and appropriate process formulations in the river basin. Dominant processes in the context of river flooding have been derived from literature and were infiltration and saturation excess overland flow, subsurface storm flow and subsurface flow in the soil matrix. The

associated key variables are elevation, soil type and land use type. The application of the reduction methodology resulted in appropriate scales for these key variables of respectively 0.1, 5.3 and 3.3 km. The appropriate model scale was about 10 km with a temporal scale of 1 day. Appropriate formulations related to these appropriate scales have been derived from literature and some rough semi-qualitative estimations. The formulations of importance were those related to evapotranspiration, surface flow and subsurface (storm) flow. Relatively simple formulations were found to be sufficient for this model objective and appropriate spatial scale.

In **chapter 6**, the impact of climate change on river flooding has been evaluated by using the climate change information and river basin models of different complexities. Precipitation with climate change was generated with a space-time random cascade rainfall model in an acceptable way. An appropriate river basin model has been constructed by implementing the appropriate model components derived before into an existing modelling framework (HBV). Additionally, two river basin models of differing complexities have been set up to evaluate the sensitivity of the model results to model complexity and to allow for a verification of the model appropriateness procedure. The appropriate model has 118 sub-basins (HBV-118) and an associated model scale of about 13 km. This model scale is of the same order of magnitude as the one revealed in the scale analysis (10 km) and assumed to be sufficient for checking the appropriateness requirements. The additional models have 1 and 15 sub-basin(s) (HBV-1 and HBV-15). The three models were calibrated and validated with identical data series as far as possible. Generations of the rainfall model under current and changed climate conditions have been used to assess the climate change impacts.

The average and extreme discharge behaviour at the basin outlet (Borgharen) is well reproduced by the three models in the calibration and validation, the results become somewhat better with increasing model complexity. The small differences between HBV-15 and HBV-118 are not surprising given the small differences in spatial model scales and the fact that no additional discharge series have been used in the calibration and validation of HBV-118. The model results with synthetic precipitation under current climate conditions show a considerable underestimation of extreme discharge behaviour. The underestimation of extreme discharges is caused by the observed precipitation input at the sub-basin scale. In most cases, this precipitation is not an areally averaged quantity, but rather a point quantity resulting in an overestimation of observed precipitation variability and extreme behaviour at the sub-basin scale compared to the generated precipitation. This seems to be a very frequently occurring problem, which can be improved by increasing the density of precipitation stations in a river basin in an efficient manner or employing more sophisticated interpolation methods.

The general trend with climate change is a small decrease (~5 %) of the average discharge and a small increase (~5-10 %) of discharge variability and extreme discharges. The variability in extreme discharges increased under climate change conditions. This variability results both from the stochasticity of the precipitation process and the differences between the climate models. Overall, it was found that the uncertainties in extreme discharges due to precipitation errors and extrapolation errors (both about 20 %) are more important than uncertainties due to hydrological model errors and parameter estimation errors (both less than 10 %).

Finally, in **chapter 7** the main conclusions are summarised and some specific issues are discussed. The two main objectives are achieved. First, a methodology to assess an appropriate model dependent on research objective and area has been developed. Its application to the issue of climate change impacts on flooding in the Meuse basin revealed dominant processes and variables, appropriate variable scales, an appropriate model scale of 10 km and appropriate process formulations. These appropriate model components have been used to construct the appropriate model.

Second, the impact of climate change on flooding in the river Meuse has been assessed with the appropriate model. The change in river flooding (5-10 %) was found to be much smaller than its associated uncertainty (more than 40 %). However, it has been argued that the changes have a systematic rather than a stochastic character and therefore are not completely cancelled out by the uncertainties.

Samenvatting

Door wereldwijde klimaatveranderingen zullen temperaturen waarschijnlijk gaan stijgen, neerslagpatronen veranderen en de frequenties van extreme gebeurtenissen toenemen. De effecten van deze klimaatveranderingen op hoogwater in rivieren kunnen aanzienlijk zijn en enorme economische, sociale en ecologische schade veroorzaken en zelfs doden tot gevolg hebben. Dit maakt het noodzakelijk om robuuste en nauwkeurige hoogwater voorspellingsmethoden te gebruiken, die als een stevige basis kunnen dienen voor investeringen in hoogwater beschermingsmaatregelen bij klimaatveranderingen.

Een breed scala aan modellen is beschikbaar om aan deze eisen te voldoen. Complexere modellen hebben in het algemeen meer data en rekentijd nodig, maar kunnen resulteren in kleinere modelonzekerheden en bijbehorende kosten. Het lijkt erop dat er een optimale modelcomplexiteit bestaat, die gepaard gaat met minimale totale kosten of onzekerheden. Dit roept de vraag op hoe zo'n geschikt model er uit moet zien gegeven een specifiek onderzoeksdoel en –gebied. Of welke fysische processen en data moet een model bevatten en welke mathematische procesformuleringen moeten worden gebruikt op welke ruimtelijke en temporele schaal, om een geschikt model te verkrijgen?

De belangrijkste doelstellingen in dit onderzoek zijn daarom de bepaling van een geschikte modelcomplexiteit afhankelijk van het onderzoeksdoel en –gebied en de schatting van het effect van klimaatveranderingen op hoogwater met een geschikt model. Het Maasstroomgebied in België en Frankrijk dient als een toepassingsgebied in dit proefschrift. De eerste doelstelling wordt behandeld in hoofdstuk 2, 3, 4 en 5 en vormt het grootste deel van dit proefschrift. De tweede doelstelling wordt voornamelijk in hoofdstuk 4 en 6 behandeld.

Ten eerste is in **hoofdstuk 2** een voorlopige procedure voor modelgeschiktheid opgezet. Deze procedure bleek niet aan de eisen te voldoen vanwege de vereenvoudigde aannames en de noodzaak tot het hebben van een model bij aanvang van de procedure. Daarom werd een meer algemeen raamwerk voor modelgeschiktheid geïntroduceerd, dat bestaat uit de bepaling van de dominante processen en variabelen, de geschikte schalen en de bijbehorende geschikte procesformuleringen. Op deze manier worden de karakteristieken van een geschikt model vooraf bepaald en kunnen worden geïmplementeerd in een bestaand of nieuw model. Zo wordt een intern consistent model verkregen, ofschoon het van de criteria voor de geschiktheid van schalen, de gebruikte formuleringen en de databeschikbaarheid afhangt of het gehele model geschikt is voor het onderzoeksdoel. Dit laatste kan worden uitgevonden door de totale onzekerheid van het geschikte model te vergelijken met een specifiek criterium. Het raamwerk voor modelgeschiktheid is dus hoofdzakelijk gebaseerd op een consistentiecriterium met een additioneel onzekerheidscriterium.

Als onderdeel van het raamwerk werd vervolgens een methode beschreven om de geschikte schaal voor een bepaalde variabele te bepalen. Aangenomen wordt dat deze geschikte schaal gelijk is aan een fractie van de correlatielengte van die variabele. De fractie wordt bepaald op basis van relaties tussen statistieken en schalen en acceptatie van een fout van 10 % in de schatting van de statistiek. Dit resulteert in fracties van de correlatieslengte tussen 0.20 en 0.25 voor verschillende statistieken zoals de standaarddeviatie en de herhalingswaarde. De integratie van deze geschikte schalen voor variabelen naar een geschikte modelschaal is tot stand gebracht door de geschikte schalen voor variabelen te vermenigvuldigen met de bijbehorende gewichten. Deze gewichten zijn gebaseerd op SCS curve-nummer relaties tussen de piekafvoer en enkele specifieke parameters. De waarden van deze parameters zijn afhankelijk van de schaal van elke variabele en op deze manier ontstaan relaties tussen de piekafvoer en de schaal voor een variabele. Uiteindelijk worden de gewichten bepaald en vermenigvuldigd met de geschikte schaal voor een variabele om zo de geschikte modelschaal te verkrijgen.

In **hoofstuk 3** wordt het probleem van geschikte schalen verder verkend door het effect van verschillende ruimtelijke en temporele schalen voor de neerslaginvoer en het stroomgebiedmodel op extreme afvoeren te bekijken. Hiervoor zijn een stochastisch neerslagmodel en een dimensieloos stroomgebiedmodel met variabele schalen gebruikt. De belangrijkste conclusie was dat het effect van de modelschaal (resolutie) op extreme rivierafvoeren veel belangrijker is dan het effect van de invoerschaal voor het beschouwde stroomgebied en model. De hoogste modelresolutie (5-10 roosterpunten/ ruimtelijke correlatielengte; 7-10 tijdstappen/ temporele correlatielengte) lijkt geschikt te zijn voor de bepaling van extreme afvoeren van grote stroomgebieden met een soortgelijk neerslagregime en afvoerconcentratie patroon. Verder was a relatief lage ruimtelijke en temporele neerslagresolutie (1-2 roosterpunten/ ruimtelijke correlatielengte; hoogstens 1 tijdstap/ temporele correlatielengte) voldoende om de neerslaginvoer van een model voor deze grote stroomgebieden te representeren. Deze conclusies zullen niet significant anders zijn wanneer andere parameterwaarden in het stroomgebiedmodel worden gebruikt, zoals aangetoond is door de gevoeligheidsanalyse.

In **hoofdstuk 4** werden klimaatdata afkomstig van stations, assimilaties, globale klimaatmodellen (GCMs) en regionale klimaatmodellen (RCMs) voor West Europa geanalyseerd en vergeleken. De verschillen tussen de klimaatmodellen kunnen aanzienlijk zijn, in het bijzonder met betrekking tot extreme waarden en correlatielengten. De RCMs en de Australische GCM simuleren extreem neerslaggedrag voor het huidige klimaat erg goed, terwijl de assimilaties extreme neerslag onderschatten en de Britse en Canadese GCMs extreme neerslag overschatten. Gemiddelde neerslagwaarden veranderen niet significant bij klimaatveranderingen (een verdubbeling van koolstofdioxide), terwijl de standaarddeviaties stijgen met ongeveer 10 %. Extreme neerslag kan als gevolg van klimaatveranderingen stijgen met 15-20 % en correlatielengten met 30-40 %. Modelfouten en verschillen tussen modellen onderling bij de schatting van extreme neerslag bij klimaatveranderingen kunnen oplopen tot 50 %. Dit is significant hoger dan de gesimuleerde verandering. Het temperatuurgedrag onder de huidige klimaatcondities wordt goed gesimuleerd door de RCMs en de Britse GCM, maar tamelijk slecht door de Canadese en Australische GCMs. De gemiddelde voorspelde temperatuurverandering bij klimaatveranderingen is 3.7 ºC (2.9-4.7 ºC). De geschatte onzekerheid hierin is 2-3 ºC, wat vergelijkbaar is met de gesimuleerde verandering. De toepassing van de reductiemethodologie van

hoofdstuk 2 resulteerde in een geschikte schaal voor extreme neerslag van 20 km bij een temporele schaal van 1 dag.

In **hoofdstuk 5** worden de dominante processen en variabelen, geschikte schalen en geschikte procesformuleringen in het stroomgebied beschouwd. Dominante processen in de context van hoogwater in rivieren zijn afgeleid uit de literatuur en waren oppervlakkige afstroming als gevolg van een infiltratie- of verzadigingsoverschot, ondergrondse 'storm'-afstroming en ondergrondse afstroming in de bodemmatrix. De bijbehorende 'sleutelvariabelen' zijn hoogte, bodemtype en landgebruiktype. De toepassing van de reductiemethodologie resulteerde in geschikte schalen voor deze sleutelvariabelen van respectievelijk 0.1, 5.3 en 3.3 km. De geschikte modelschaal was ongeveer 10 km bij een temporele schaal van 1 dag. Geschikte formuleringen gerelateerd aan deze geschikte schalen zijn verkregen uit de literatuur en enkele globale semi-kwalitatieve schattingen. De formuleringen van belang waren die gerelateerd aan evapotranspiratie, oppervlakkige afstroming en ondergrondse (storm) afstroming. Relatief simpele formuleringen bleken voldoende te zijn voor het onderhavige onderzoeksdoel en de geschikte ruimtelijke schaal.

In **hoofdstuk 6** is het effect van klimaatveranderingen op hoogwater geëvalueerd door de klimaatinformatie en stroomgebiedmodellen van verschillende complexiteiten te gebruiken. De neerslag bij klimaatveranderingen is op een acceptabele manier gegenereerd met een ruimte-tijd 'random cascade' neerslagmodel. Vervolgens is een geschikt stroomgebiedmodel geconstrueerd door de geschikte modelcomponenten van voorgaande hoofdstukken te implementeren in een bestaand modelraamwerk (HBV). Bovendien zijn twee extra stroomgebiedmodellen met afwijkende complexiteiten opgezet, om de gevoeligheid van de modelresultaten voor modelcomplexiteit te evalueren en om in staat te zijn om de procedure voor modelgeschiktheid te verifiëren. Het geschikte model heeft 118 deelstroomgebieden (HBV-118) en een bijbehorende modelschaal van ongeveer 13 km. Deze modelschaal is van dezelfde orde van grootte als die uit de schaalanalyse (10 km) en wordt geacht voldoende te zijn om de eisen voor geschiktheid te checken. De additionele modellen hebben 1 en 15 deelstroomgebied(en) (HBV-1 en HBV-15). De drie modellen werden gekalibreerd en gevalideerd met identieke datareeksen voor zover mogelijk. Generaties van het neerslagmodel onder huidige en toekomstige klimaatomstandigheden zijn gebruikt om de klimaateffecten te bepalen.

Het gemiddelde en extreme afvoergedrag bij het uitstroompunt (Borgharen) wordt goed gereproduceerd door de drie modellen in de kalibratie en validatie. De resultaten worden iets beter bij een toename van de modelcomplexiteit. De kleine verschillen tussen HBV-15 en HBV-118 zijn niet verassend gezien de kleine verschillen in de ruimtelijke modelschalen en het feit dat er geen extra afvoerreeksen zijn gebruikt in de kalibratie en validatie van HBV-118. De modelresultaten met synthetische neerslag onder huidige klimaatomstandigheden laten een aanzienlijke onderschatting van extreme afvoeren zien. De onderschatting van extreme afvoeren wordt veroorzaakt door de waargenomen neerslag op de schaal van de deelstroomgebieden. In de meeste gevallen is deze neerslag niet een gebiedsgemiddelde grootheid, maar meer een puntgrootheid wat resulteert in een overschatting van de waargenomen neerslagvariabiliteit en extreem neerslaggedrag op de schaal van de deelstroomgebieden vergeleken met de gegenereerde neerslag. Dit lijkt een veel voorkomend probleem te

zijn, dat kan worden verbeterd door de dichtheid van neerslagstations te vergroten op een efficiënte manier of door meer verfijnde interpolatiemethoden te gebruiken.

De algemene tendens bij klimaatveranderingen is een kleine afname (~5 %) van de gemiddelde afvoer en een kleine toename (~5-10 %) van de afvoervariabiliteit en extreme afvoeren. De variabiliteit in extreme afvoeren neemt toe bij klimaatveranderingen. Deze variabiliteit is afkomstig van de stochasticiteit van het neerslagproces en de verschillen tussen de klimaatmodellen. Globaal werd vastgesteld dat de onzekerheden in extreme afvoeren als gevolg van fouten in de neerslag en de extrapolatie (beide ongeveer 20 %) belangrijker zijn dan de onzekerheden als gevolg van hydrologische modelfouten en fouten in de parameterschattingen (beide minder dan 10 %).

Tenslotte worden in **hoofdstuk 7** de belangrijkste conclusies samengevat en worden enkele specifieke kwesties bediscussieerd. De twee belangrijkste doelstellingen zijn bereikt. Ten eerste is er een methodologie ontwikkeld om een geschikt model afhankelijk van het onderzoeksdoel en –gebied te bepalen. De toepassing van de methodologie op het probleem van klimaatseffecten op hoogwater in het Maasstroomgebied resulteerde in dominante processen en variabelen, geschikte schalen voor variabelen, een geschikte modelschaal van 10 km en geschikte procesformuleringen. Deze geschikte modelcomponenten zijn gebruikt om een geschikt model te construeren.

Ten tweede is het effect van klimaatveranderingen op hoogwater in de Maas bepaald met het geschikte model. De verandering in hoogwater (5-10 %) was veel kleiner dan de bijbehorende onzekerheid (meer dan 40 %). Echter, er is betoogd dat de veranderingen een meer systematisch dan stochastisch karakter hebben en daarom worden ze niet volledig tenietgedaan door de onzekerheden.

About the author

Martijn J. Booij was born on 27 October 1972 in Geldrop, the Netherlands. Here, he followed his secondary education at the Strabrecht College and received his VWO diploma in 1991. In the same year, he started his academic education at the Wageningen Agricultural University by studying Soil, Water and Atmosphere with a specialisation in Hydrology and Water Management. In 1996, the author fulfilled his traineeship at INTA in Santiago del Estero, Argentina on the subject of unsaturated groundwater flow and irrigation management. The first final masters project about soil quality in the floodplains of the Meuse was conducted at WL| Delft Hydraulics. His second masters project was about the simulation of coupled water flow and heat transport of a groundwater system on Svalbard and was partly carried out at the Agricultural University of Norway. After his graduation in 1997, the author worked as a hydrologist on short projects at the Service for the Rural Area of the Ministry of Agriculture in Utrecht. In the same year, he started his PhD research at the Water Resources Management group, Department of Civil Engineering of the University of Twente. The results of this research about appropriate modelling and climate change impacts on river flooding are described in this thesis. Since October 2001, Martijn Booij is working as a research fellow at the same Water Resources Management group. His current research is part of the EU project FLOCODS, and focuses on the development of a decision support system for flood control and ecosystem upgrading in the Red River basin, Vietnam.